Detailed Astrophysical Properties of Lyman Break Galaxies

Thesis by

Alice E. Shapley

In Partial Fulfillment of the Requirements

for the Degree of

Doctor of Philosophy

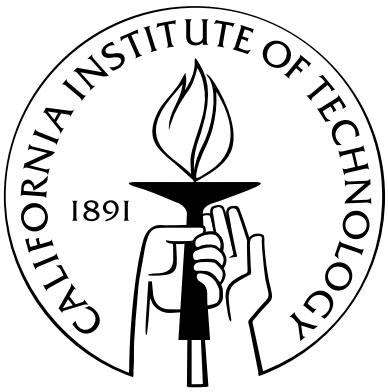

California Institute of Technology

Pasadena, California

2003

(Defended April 17th, 2003)

For my mother, father, and sister Nina

Acknowledgements

It is a rare and lucky thing to find an environment and group of people in which one feels truly comfortable and happy. I have been fortunate enough to find these things in the Caltech astronomy department. There are many people who deserve acknowledgement for their assistance in the completion of this thesis, and I would like to take this opportunity to thank them.

Data obtained with instruments on the Palomar 200-inch and Keck I and Keck II telescopes form the backbone of my thesis. For all of their assistance in the collection of this data, I would like to thank the members of the observatory staff at both the Palomar and Keck observatories. These individuals have contributed their expertise in operating the awesome telescopes, maintaining and supporting the instruments we use, and providing nourishment and peaceful observing environments. I would like to offer special thanks to John Cromer, who is the ultimate LRIS Black Belt, and has been a wonderful friend ever since the first year of graduate school. Also completely invaluable and generously helpful are the astronomy department system administrators Patrick Shopbell, Cheryl Southard, and Anu Mahabal. Diane Fujitani has been very sweet and helpful in dealing with numerous logistical issues.

The Caltech astronomy faculty are an extremely dynamic group of people, from whom I have learned a great deal about astronomy and the world of astronomers. I especially want to thank Wal Sargent and Anneila Sargent, for lots of interesting conversations on wide-ranging topics, both astronomy-related (and astronomy-gossip-related) and otherwise; my 2nd floor neighbor Richard Ellis, for always being so fun to talk to; and Marc Kamionkowski, for including graduate students on the admissions committee and giving us a taste of what it is like to be on the other side.

Though many of them have long-since graduated, I want to offer thanks to former Caltech graduate students Chris Fassnacht, David Hogg, Brad Behr, Andrew Baker, and Josh Bloom, all of whom served as excellent mentors and friends. I have been lucky enough to know several Caltech postdocs during my time here. Lori Lubin has been a fantastic role model, providing advice and insight into things ranging from careers, to personalities, to IRAF. With Crystal Martin I enjoyed many fun tennis games, scientific discussions, and, of course, Osterbrock. Pieter van Dokkum has been a great 2nd floor neighbor, and Todd Small is a terrific lunch-date, and the author of the all-important “redshift” program.

I would also like to thank fellow members of the "group," including Caltech graduate students Matt Hunt, Dawn Erb, and Naveen Reddy. We have been through many observing-, IRAF-, and data-reduction-related adventures together, and I look forward to all of our future adventures. Though not at Caltech, Mark Dickinson and Mauro Giavalisco have also been tremendously fun to observe with, and have provided lots of useful assistance during my time as a graduate student.

At this point, I would like to thank the incredible group of friends that I have found at Caltech, whom I hope to stay close to for the foreseeable future and beyond. I would like to thank Pat Udomprasert for being so supportive about everything imaginable, in every way, shape, and form, and for being such a close, thoughtful friend. I would like to thank Rob Simcoe for being a terrific, supportive friend, and officemate, and, as a fellow member of the Sargent Dynasty, for many helpful conversations about metals. I would like to thank Jon Sievers for his tolerance of excessive teasing and poking, for his ability to offer guidance on topics quite removed from what he usually studies, and for our rare serious conversations. I would like to thank Mike Santos, for our late night talks and impossibly specific mutual observations, his boundless considerateness, and patience in explaining things very well. And, finally, I would like to thank John Cartwright, for going through so many things together with me.

There are a couple of people who have been my guides over the last several years, and I am indebted to them for their generosity of insight, knowledge, and time. Max Pettini has served as a terrific mentor, teaching me about spectroscopic observations, the interpretation of galaxy spectra, and the construction of coherent discussions in research papers. I really appreciate all of the detailed feedback that he has given me about various stages of the work presented here, and only wish that we had spent more time in the same place. Despite the imposing physical distance between us, I have learned an enormous amount from Max, and have deeply enjoyed his friendship. I would also like to thank Kurt Adelberger for his infinite patience in fielding a relentless stream of questions during the first couple of years of this work. He is a wonderful teacher, who always gave me the detailed answers that I needed, and taught me a lot of the statistical and astronomical techniques used for this thesis work. I greatly admire his tremendous creativity and skepticism, and will always be thankful for the advice he gave me (and for his Hawaiian wayfaring spirit, which brought us to such wonders as the Mookini Heiau).

I don't think I can properly thank my thesis advisor, Chuck Steidel, but I will try. Being a part of such an active, exciting research group is a dream come true for me, and I am grateful to have experienced so many aspects of being in the "group": observing, reducing the data, initially finding something interesting from the observations and sharing it with each other, and exchanging feedback on papers. It always amazes and impresses me that Chuck is so available to talk about the details of any problem or discovery I think I've found, no matter how minor or incorrect it may turn out to be. What makes him such a great advisor is his simultaneous ability to discuss both the

details that often crowd the mind of the graduate student, and also the big picture that drives the work, suggesting ways to get to the heart of a problem without getting sidetracked in the minutiae. But, that is not all—he has also been there as a supportive friend during critical parts of this thesis work, especially in the face of adversity. So, maybe the best thing I can say is that Chuck is a very important person to me, one of my best friends, and I am deeply grateful to him and Sarah and the rest of the Steidel family for their friendship and support during the last six years.

And, finally, I would like to thank Steve Furlanetto for making the last few months of graduate school so sweet. And, finally, finally, I am lucky enough to have the best parents and sister in the whole universe. My mother, father, and sister Nina have been advisors, cheerleaders, therapists, and endless sources of love since way before I ever set foot in California. This thesis is dedicated to them with all my love.

Abstract

A large statistical sample of $z \sim 3$ galaxies has been efficiently UV-color-selected, and confirmed spectroscopically. Here we present additional observations providing insight into the physical conditions in these Lyman Break Galaxies (LBGs), selected to be rapidly forming stars when the universe was $\sim 15\%$ of its current age. In Part I, we present the results of an optical/IR survey of 118 LBGs. The distribution of LBG optical/IR colors is used in conjunction with the rest-frame UV luminosity function to construct the rest-frame optical luminosity function and luminosity density of LBGs. Broad-band optical/IR spectral energy distributions are used to model the stellar populations of LBGs, and an evolutionary sequence is proposed to explain the observations. In Part II, we utilize the large database of ~ 1000 individual rest-frame UV LBG spectra to construct high S/N composite spectra. The composite spectra provide information about hot stars, dust, ionized gas in H II regions, and the large-scale outflows of neutral and ionized interstellar material propelled out of the galaxies by the mechanical energy injected into the interstellar medium by frequent supernova explosions. An analysis of the composite LBG spectra uncovers strong trends among the continuum and spectroscopic properties of these star-forming galaxies, and highlights the importance of outflows in determining the overall UV spectroscopic appearance. While the composite spectra reveal many properties of the galaxies, they are limited by low spectral resolution and the loss of information incurred by averaging over large samples of galaxies. Therefore, in Part III, we present some new results from a pilot program to obtain deep, higher-resolution spectroscopic observations of individual bright LBGs. With these observations, we hope to place much tighter constraints on the properties of the outflows in LBGs, and the amount of mass, energy, and metals they return to the surrounding intergalactic medium. We also present other future directions to be pursued.

Contents

Acknowledgements **iv**

Abstract **vii**

1 Introduction **1**

1.1 $z \sim 3$ Stellar Populations 2

1.2 Star-formation Feedback and Outflows at $z \sim 3$ 5

I The Rest-Frame Optical Properties of Lyman Break Galaxies **9**

Abstract **10**

2 The Optical/IR Colors of Lyman Break Galaxies **11**

2.1 Introduction 11

2.2 Observations and Data Reductions 13

2.2.1 Optical Imaging 13

2.2.2 Near-IR Imaging 13

2.2.3 Optical/Near-IR Photometry 17

2.2.4 Photometric Uncertainties 17

2.3 The Optical/IR Colors of Lyman Break Galaxies 19

2.4 Rest-Frame Optical Luminosity Function 21

3 The Stellar Populations of Lyman Break Galaxies **35**

3.1 Introduction 35

3.2 Age-Dust Degeneracy 36

3.3 Population Synthesis Modeling 38

3.3.1 Spectroscopic Sample 38

3.3.2 Modeling Procedure 39

3.3.3 Comparison of Models 43

3.3.4 Anomalous Galaxies 45

3.4 Model Results . . . 48
3.4.1 Extinction and Luminosity . . . 53
3.4.2 Extinction and Age . . . 54
3.4.3 Stellar Mass . . . 58
3.5 "Young" and "Old" LBGs: Spectral Differences . . . 62
3.6 A Proposed Evolutionary Sequence for LBGs . . . 66

4 Summary and Conclusions **72**

II The Rest-Frame Ultraviolet Spectra of Lyman Break Galaxies **75**

Abstract **76**

5 The Lyman Break Galaxy Sample and Important UV Spectroscopic Features **77**
5.1 Introduction . . . 77
5.2 The LBG Spectroscopic Sample . . . 79
5.3 Generating the Composite Spectra . . . 80
5.3.1 Measuring Redshifts . . . 81
5.4 LBG Rest-frame UV Spectroscopic Features . . . 83
5.4.1 Stellar Features . . . 84
5.4.2 Outflow-related Features . . . 88
5.4.2.1 Low-ionization Lines Associated with Neutral Gas . . . 88
5.4.2.2 High-ionization Lines Associated with Ionized Gas . . . 89
5.4.2.3 Lyα . . . 91
5.4.3 Emission Lines . . . 92
5.4.3.1 AGN Contribution? . . . 92
5.4.3.2 C/O Abundance . . . 93
5.4.3.3 Si II* Lines . . . 96

6 Trends in Lyman Break Galaxy Spectra **100**
6.1 Introduction . . . 100
6.2 Selection Effects . . . 100
6.3 Uncertainties . . . 106
6.4 Lyα Dependences . . . 107
6.5 UV Color Dependences . . . 116
6.6 Kinematic $\Delta v_{\rm em-abs}$ Dependences . . . 118
6.7 Comparison with Local Starburst Results . . . 120

7 A Physical Picture Implied by the Spectra of Lyman Break Galaxies 124

7.1 Summary of Observational Results 124

7.2 A Physical Picture 124

7.3 The Absorbing Gas 127

7.4 Lyman Continuum Leakage 128

7.5 Future Observations 130

III Epilogue 132

8 A Deep Spectroscopic Survey of Lyman Break Galaxies 133

8.1 Introduction 133

8.2 Sample and Observations 134

8.3 Data Reductions 136

8.4 Early Results 137

List of Figures

1.1 The redshift distribution of spectroscopically confirmed $z \sim 3$ galaxies satisfying the LBG color criteria. This distribution is characterized by $\langle z \rangle = 2.96 \pm 0.29$, and is constructed from data presented in Steidel et al. (2003). 2

1.2 The moderately high-resolution spectrum of MS1512-cB58, obtained with the Echelle Spectrograph and Imager (ESI) on the Keck II telescope. The spectral resolution is 58 km s^{-1} and the S/N is > 30 per resolution element. A wealth of information about the physical conditions in cB58 has been gained from this high-quality spectrum, including details of the galaxy's stellar population, large-scale outflow kinematics, outflowing gas covering fraction and abundance pattern. Additional multiwavelength imaging and spectroscopic observations of cB58 have been used to gain further information about the nature of this actively star-forming galaxy. An analysis of the above Keck/ESI spectrum of cB58 is presented in Pettini et al. (2002). 3

1.3 Velocity offsets relative to nebular emission line redshifts. The circles and triangles correspond, respectively, to the values of Δv_{IS} and $\Delta v_{Ly\alpha}$. We see the indication of large-scale motions with respect to the systemic redshift defined by the [OIII], [OII], and Hβ nebular emission lines. From Pettini et al. (2001). 6

1.4 The large-scale distribution of LBGs relative to neutral intergalactic hydrogren and metals. Left: Mean intergalactic Lyα transmissivity as a function of comoving distance from LBGs. LBGs appear to be associated with intergalactic H I underdensities on the smallest spatial scales, as indicated by the increase in the Lyα forest transmissivity near LBGs. Right: The projected cross-correlation function of C IV systems and Lyman-break galaxies. The LBG-C IV cross-correlation function is similar to the LBG autocorrelation function, and it is inferred that LBGs reside in regions of enhanced C IV abundance relative to the intergalactic mean. From Adelberger et al. (2003). . 7

2.1 The distribution of $\mathcal{R}$ magnitudes for the NIRC LBG sample, relative to that of the LBG survey as a whole. The LBG total sample histogram has been normalized to the number of galaxies contained in the NIRC LBG subsample, for the purpose of comparison. Also indicated is the $\mathcal{R}$ distribution for the NIRC LBGs with measured redshifts, which comprise a slightly brighter sample than the NIRC LBG sample as a whole. 15

2.2 The distribution of $(G-\mathcal{R})_0$, the IGM-absorption-corrected $G-\mathcal{R}$ color, for galaxies in the NIRC LBG sample with redshifts, relative to that of the LBG spectroscopic sample as a whole. The total LBG histogram has been normalized to the number of objects in the NIRC LBG histogram. This figure shows that the NIRC LBG spectroscopic sample contains an excess of highly reddened galaxies, relative to the total LBG spectroscopic sample. 16

2.3 $\mathcal{R}$ and K_s images for two objects in the NIRC LBG sample. A bar indicating 10" is in the lower right-hand corner of each image. The N-E orientation of the $\mathcal{R}$ and K_s images for each object is indicated in the K_s images. NIRC orientations were chosen to locate a guide star on the guide camera, as well as to maximize the number of galaxies per pointing. Top: B20902-C6 has $\mathcal{R} = 24.13$ and $\mathcal{R} - K_s = 2.39$ which puts it in the bluer half of the sample of $\mathcal{R} - K_s$ measurements, with a fairly typical signal-to-noise ratio. Bottom: Westphal-MMD11 has $\mathcal{R} = 24.05$ and $\mathcal{R} - K_s = 4.54$, which gives it the reddest and highest signal-to-noise $\mathcal{R} - K_s$ measurement in the NIRC LBG sample. 18

2.4 The distribution of observed $\mathcal{R} - K_s$ colors for the NIRC LBG sample. Of the 118 galaxies, 107 have $\mathcal{R} - K_s$ detections, and 11 have upper limits, corresponding to the typical K_s detection limit of $K_s = 22.5$. Detections are indicated in the red (dark) shaded histogram, while upper limits are in the yellow (light) shaded bins. A dashed line at $\mathcal{R} - K_s = 1.82$ marks the color for a flat spectrum in F_ν. The average color in the sample is $< \mathcal{R} - K_s >= 2.85$. 81 of 118 galaxies in the NIRC LBG sample have measured redshifts, with $< z >= 2.996$. 20

2.5 $\mathcal{R} - K_s$ vs. $\mathcal{R}$. Dots indicate $\mathcal{R} - K_s$ detections, while down-arrows indicate upper limits. The diagonal line traces the typical sample detection limit of $K_s = 22.5$. There are three points below this detection line, representing galaxies in K_s images with more sensitive detection limits than the typical one. 23

2.6 Top: The rest-frame optical luminosity function of LBGs. The points and solid line indicate the magnitude range used for the Schechter function fit. The error bars on the points include the photometric uncertainties on the $\mathcal{R}$ and $\mathcal{R} - K_s$ measurements. The lower x-axis indicates the range in optical absolute magnitude, M_V, spanned by the K_s luminosity function (assuming $h = 1$). The dotted line indicates the locally determined 2dFGRS b_j luminosity function, offset by a color of $b_j - V = 0.5$ magnitudes (for comparison at the same rest wavelength as the LBG optical luminosity function). Bottom: The 68.3% confidence intervals for the best-fit Schechter function parameters. The covariance between the best-fit parameters is indicated by the confidence regions. As the faint-end slope (α) becomes steeper, the characteristic luminosity (m^*) increases, and the overall normalization (ϕ^*) decreases. 25

3.1 The Age-Dust Degeneracy. The points indicate the observed spectral energy distribution of 3C324-C2, a LBG at $z = 2.880$. Shown with the points are BC96 constant star-formation models of different ages, modified by the amount of dust extinction required to reproduce the observed $G - \mathcal{R}$ color. The dotted line is a 1 Gyr model with $E(B-V) = 0.149$; the dashed line is a 100 Myr model with $E(B-V) = 0.186$; and the solid line is a 1 Myr model with $E(B-V) = 0.263$. All of these models describe the observed optical photometry equally well. However, only the 1 Gyr model successfully describes the the observed $\mathcal{R} - K_s$ color. 37

3.2 The distribution of observed Lyman α equivalent widths. The median equivalent width is 0. However, there are extreme cases of observed equivalent widths greater than 300 Å in either emission or absorption. If unaccounted for, such large equivalent widths would bias the modeling of the stellar population—especially the estimate of the dust extinction, but, to a certain extent, the age as well. 40

3.3 The best-fit BC96 constant star-formation models for three galaxies in the NIRC LBG sample. These three examples span the range of properties in the sample. A young and dusty galaxy with very little evidence for a Balmer break, Westphal-CC63 is fit with a 10 Myr model with $E(B-V) = 0.355$ (while the formal best-fit age for CC63 is 4 Myr, we have restricted the best-fit age parameter space to values which are physically plausible ($\geq$ 10 Myr)). At the other extreme, B20902-D11 has a best-fit age of 1.3 Gyr and $E(B-V) = 0.09$—much older with much less dust extinction. Intermediate between these two extremes, B20902-M11 has a best-fit age of 140 Myr and $E(B-V) = 0.205$. Each plot shows the galaxy's redshift and best-fit parameters. The photometric measurements are plotted as magnitudes, yet the error bars on the G, J, and K_s points refer to the uncertainties in the $G-\mathcal{R}$, $\mathcal{R}-J$ and $\mathcal{R}-K_s$ colors, respectively. The U and I measurements are plotted, even though they were not used to determine the best-fit models. There is no I data for the Westphal field, hence the lack of an I point for CC63. 46

3.4 Confidence intervals in the $E(B-V) - t_{sf}$ parameter space for the three galaxies featured in Figure 3.3. Each confidence region is determined by generating a large sample of artificial colors for a galaxy (based on its measured colors and photometric uncertainties), and finding the best-fit $E(B-V)$ and t_{sf} for each set of artificial colors. The black region indicates the 68.3% confidence region; the red (dark grey) region indicates the 90% region, and the yellow (light grey) region indicates the remaining 10% of the realizations. Colors were assigned by probability density—i.e., the black points contain the highest density of realizations, while the red (dark grey) points contain intermediate densities, and the yellow (light grey) points have the lowest densities. Westphal-CC63 and B20902-D11 both have better determined optical/IR colors than B20902-M11, as demonstrated by the smaller confidence regions for those galaxies. . 47

3.5 Anomalous Galaxies. Westphal-MMD11 and DSF2237b-MD81 are not described by any of the simple models which successfully fit the majority of galaxies in the NIRC LBG sample. For both galaxies, there is no combination of dust and age which simultaneously fits the $G-\mathcal{R}$, $\mathcal{R}-J$ and $\mathcal{R}-K_s$ colors. The $\mathcal{R}-J$ and $\mathcal{R}-K_s$ colors are simply too red to be fit by any of the simple models, including models with different star-formation histories. 1 Myr and 1 Gyr BC96 constant star-formation models were fit to the observed $G-\mathcal{R}$ color alone, excluding other colors. Solid lines represent 1 Myr BC96 constant star-formation models, and dashed lines indicate 1 Gyr models. Dotted lines indicate fits to the $\mathcal{R}-J$ and $\mathcal{R}-K_s$ colors, excluding the $G-\mathcal{R}$ color. For both galaxies, the $\mathcal{R}-J$ and $\mathcal{R}-K_s$ colors alone are fit by large amounts of extinction ($E(B-V) \geq 0.6$) and very young ages ($t_{sf} \leq 10$ Myr). The extrapolation of the dotted line to shorter wavelengths significantly underpredicts the flux observed in the U_n and G filters. 49

3.6 Histograms of t_{sf} and $E(B-V)$ values derived from BC96 constant star-formation models. Top: The t_{sf} histogram. The cyan (light grey) bin indicates seven galaxies whose unconstrained best-fit t_{sf} values were older than the age of the universe at $z \sim 3$. Constraining each of these galaxies to have a best-fit t_{sf} younger than the age of the universe at its redshift (assuming an $\Omega_m = 0.3$, $\Omega_\Lambda = 0.7$, $h = 0.7$ cosmology) resulted in best-fit t_{sf} values of roughly 2 Gyr. The galaxy Q0201-B13 is at $z = 2.167$, so its best-fit t_{sf} of 2.5 Gyr (the oldest bin) does not pose a problem. Bottom: The $E(B-V)$ distribution, derived from both optical and near-IR photometry. This distribution probably over-represents the dustiest galaxies, relative to the LBG population as a whole, as shown by Figure 2.2. 51

3.7 Histograms of m_{star} and instantaneous star-formation rate, $\Psi(t_{sf})$, derived from the best-fit BC96 constant star-formation models. Top: The formed m_{star} distribution. The cyan (light grey) bins contain the seven galaxies with unconstrained best-fit t_{sf} values older than the age of the universe at $z \sim 3$. A significant fraction of the NIRC LBG sample have m_{star} values approaching the formed stellar mass in a current L^* galaxy ($4 \times 10^{10} h^{-2} M_\odot$), while a significant fraction have m_{star} values that are an order of magnitude smaller. Bottom: The distribution of instantaneous star-formation rates, determined by applying the inferred extinction corrections to the distribution of rest-frame UV luminosities. 52

3.8 M_{UV} and M_V vs. $E(B-V)$. M_{UV} and M_V refer to the rest-frame UV and optical (V) absolute magnitudes which are probed by the $\mathcal{R}$ and K_s apparent magnitudes, respectively, at $z \sim 3$. The two left-hand panels show the relationship of rest-frame UV and optical luminosities with best-fit $E(B-V)$. Both UV and optical luminosities are uncorrelated with $E(B-V)$. When the luminosities are corrected for dust-extinction (shown in the right-hand panels), strong correlations result between intrinsic luminosity and dust extinction. The correlation holds not only in the rest-frame UV but also in the rest-frame optical, where the effects of dust-extinction are less extreme (but clearly still important, as shown by the lower right-hand panel). The correlation between intrinsic luminosity and dust extinction is independent of the star-formation history used to fit the observed spectral energy distributions. 55

3.9 The Extinction-Age Correlation. This is the joint distribution of best-fit BC96 constant star-formation $E(B-V)$ and t_{sf} parameters. There is a significant correlation between the two best-fit parameters, which holds for all of the star-formation histories which we used to fit the observed spectral energy distributions. However, the strength of the correlation does depend on the assumed dust attenuation law. This plot assumes a Calzetti dust law, but if an SMC curve is used instead, the correlation is greatly reduced. Open circles indicate galaxies whose unconstrained best-fit t_{sf} values were older than the age of the universe at $z \sim 3$. Open squares indicate galaxies whose unconstrained best-fit ages are < 10 Myr. 56

3.10 m_{star} vs. M_{UV} and M_V. Relationships are shown between m_{star} derived from the best-fit BC96 constant star-formation models, and the UV and optical luminosities. M_{UV} and M_V refer to the rest-frame UV and optical (V) absolute magnitudes. The left-hand panels show the relationships for luminosity which is uncorrected for extinction, while the right-hand panels show the relationships for extinction-corrected luminosity. . . . 60

3.11 m_{vir} vs. m_{star}. This plot shows the relationship between the dynamical mass implied by nebular line widths, assuming virial equilibrium (m_{vir}), and the best-fit BC96 formed stellar mass (m_{star}), assuming constant star formation. The solid line describes $m_{vir} = m_{star}$. Horizontal error bars reflect the 1σ model confidence region of m_{star}, while vertical error bars reflect the uncertainties in the measured nebular line width and angular half-light radius. The inferred dynamical masses should reflect approximate upper limits to the formed stellar mass in the physical region probed by the NIRC observations. We find broad consistency between the mass scales inferred from near-infrared spectroscopic and photometric measurements. In the two cases where there are significant differences, the best-fit stellar mass is significantly smaller than the inferred dynamical mass. 61

3.12 Comparison of "young" and "old" LRIS spectra. The composite spectrum of a subsample of galaxies with best-fit constant star-formation $t_{sf} \leq 35$ Myr is shown in magenta (grey), while the composite spectrum of a subsample of galaxies with $t_{sf} \geq 1$ Gyr is shown in black. The most striking differences between the two composite spectra are the relative strengths of Lyman-α emission; the relative strengths of the interstellar features Si II 1192, 1260, 1526 Å, CII 1334 Å, and Al II 1670 Å; and the relative CIV 1549 Å P-Cygni profiles. 64

3.13 Zoomed in comparison of "young" and "old" LRIS spectra. Four regions of the composite young and old spectra are expanded for a more detailed view. The vertical axis of the detailed plot of Lyman-α spans a larger range in intensity than the other plots, for the purpose of showing the full extent of the strong Lyman-α emission in the old spectrum. 65

5.1 The distribution of velocity offsets between Lyα emission and low-ionization interstellar absorption. The most straightforward indication that LBGs are experiencing large-scale outflows of their interstellar material is the velocity offset measured in individual spectra between Lyα emission and interstellar absorption lines. This histogram shows the distribution of velocity offsets for the 323 galaxies with spectra in which both types of features are detected. The mean velocity offset (redshift difference) is $\Delta v = 650$ km s^{-1}($\Delta z = 0.008$). 82

5.2 A composite rest-frame UV spectrum constructed from 811 individual LBG spectra. Dominated by the emission from massive O and B stars, the overall shape of the UV continuum is modified shortward of Lyα by a decrement due to inter-galactic HI absorption. Several different sets of UV features are marked: stellar photospheric and wind, interstellar low- and high-ionization absorption, nebular emission from H II regions, Si II* fine-structure emission whose origin is ambiguous, and emission and absorption due to interstellar HI (Lyα and Lyβ). There are numerous weak features which are not marked, as well as several features bluewards of Lyα which only become visible by averaging over many sightlines through the IGM. The composite LBG spectrum is available in electronic form from http://www.astro.caltech.edu/∼aes/lbgspec/. 85

5.3 Four zoomed-in regions from the composite spectrum of Figure 5.2. The zoomed-in vertical scale allows a more detailed look at weak emission features such as Si II* $\lambda\lambda\lambda 1265, 1309, 1533$, and O III] $\lambda\lambda 1661, 1666$. The lower left-hand box shows the zoomed-in region near C IV $\lambda\lambda 1548, 1550$. The observed composite spectrum is plotted as a solid line, while the dashed line is a Starburst99 model spectrum for 300 Myr of continuous star-formation with $Z = \frac{1}{4} Z_{\odot}$ (Leitherer et al., 1999, 2001). The model and data agree well for the emission component of the C IV P-Cygni stellar wind line, but the model overpredicts the amount of broad, blue-shifted absorption. This may be due to the lower average metallicity or older age of the LBGs included in the composite spectrum, relative to the model. The lower right-hand box shows the zoomed-in region near the He II $\lambda 1640$ stellar wind line, whose large strength we have trouble reproducing using Starburst99 models with reasonable parameters. 86

5.4 log(C/O) vs. log(O/H) for local H II regions. Blue triangles are data from dwarf irregular galaxies and the Magellanic Clouds (Garnett et al., 1995, 1997; Kobulnicky & Skillman, 1998). Spiral galaxy data are shown with circles (Garnett et al., 1999). Red symbols assume a shallow ($R_V = 3.1$) Milky Way extinction curve, whereas green symbols indicate a steeper ($R_V = 5.0$) one. The solar abundances (Holweger, 2001; Allende Prieto et al., 2002) are indicated by the large bulls-eye. The horizontal (magenta) shaded area indicates the log(C/O) confidence region derived from the total composite LBG spectrum. The vertical (cyan) shaded area indicates the range of log(O/H) implied by the ratio of [O III], [O II], and Hβ line-strengths in a small sample of bright LBGs (Pettini et al., 2001). 95

6.1 The distribution of $E(B-V)$ values as a function of z. Due to the way in which LBGs are color-selected to have *observed* $G - \mathcal{R}$ colors which lie within a specific range, the increased IGM absorption affecting the G-band flux as a function of z limits the range of *intrinsic* colors of LBGs (parameterized by $E(B-V)$) at higher z. 102

6.2 Photometric and spectroscopic incompleteness of the LBG sample as a function of $\mathcal{R}$ magnitude. The empty histogram represents galaxies photometrically selected by their colors to be at $z \sim 3$. The blue histogram consists of galaxies from the photometric sample which were observed spectroscopically. The pink histogram indicates spectroscopically observed objects for which a redshift was successfully measured. The green histogram shows the small fraction of spectroscopically confirmed objects ($\sim 4\%$) which turn out to be stars or low-z galaxies. The dashed histogram shows the subset of spectroscopically confirmed objects which have secure redshifts confirmed by at least two independent members of our group. Non-AGN objects in this secure-z sample with $z > 2$ were included in composite spectra. 103

6.3 Photometric and spectroscopic incompleteness of the LBG sample as a function of $\mathcal{R}$ magnitude and spectroscopic type. The red histogram shows the number of galaxies observed spectroscopically. The cyan histogram shows the number of galaxies with redshifts measured from features which include Lyα emission. The blue dashed histogram shows the number of objects with no detectable Lyα emission and redshifts measured only from interstellar absorption lines. The green histogram shows the number of objects for which no redshift was successfully measured. The black dots indicate the ratio of galaxies with Lyα emission to those with only absorption line redshifts, which increases steeply as a function of $\mathcal{R}$ magnitude. Based on the assumption that the unidentified objects in the green histogram are $z \sim 3$ galaxies that have $W_{\mathrm{Ly}\alpha} < 0$ and spectra with insufficient S/N to identify absorption features, we see that the ratio of objects with Lyα emission to those with only absorption features remains roughly constant as a function of magnitude (pink dots). 104

6.4 The distribution of Lyα equivalent widths for the LBG spectroscopic sample. This sample contains a broad range of equivalent widths with a median of ~ 0 Å. Only 25% of the sample has rest-frame $W_{\mathrm{Ly}\alpha} \geq 20$ Å, large enough to be selected by narrow band excess techniques, given the depth of current surveys. There is a correlation between Lyα emission equivalent width and $\mathcal{R}$ magnitude among sources with $W_{\mathrm{Ly}\alpha} \geq 20$ Å, such that fainter galaxies have larger $W_{\mathrm{Ly}\alpha}$. 109

6.5 Bottom: A sequence of 4 continuum-normalized composite spectra, constructed from the 4 quartiles of LBG spectroscopic sample grouped according to Lyα equivalent width. The spectra have been offset by regular vertical intervals for easier viewing, in order of increasing $W_{\mathrm{Ly}\alpha}$. The lower left-hand panel zooms in on the region near Lyα, while the right-hand panel focuses on the region redwards of Lyα, where the strongest features are blue-shifted low-ionization and high-ionization interstellar absorption features associated with large-scale outflows of interstellar material. Top: The behavior of low- and high-ionization interstellar absorption lines as a function of Lyα equivalent width. These plots confirm quantitatively what the bottom panels indicate visually: the average low-ionization absorption equivalent width, W_{LIS}, decreases dramatically as $W_{\mathrm{Ly}\alpha}$ varies from strong absorption to strong emission, while the high-ionization Si IV absorption equivalent width, W_{SiIV}, remains roughly constant (except in the quartile of the sample with strong Lyα emission, in which W_{HIS} is slightly weaker). . 110

6.6 The dependence of UV continuum shape on Lyα equivalent width. Left: Plotted in blue, the composite spectrum of the quartile of galaxies with the strongest Lyα emission and the weakest low-ionization interstellar absorption lines is also significantly bluer in spectral slope than the composite spectrum of the quartile of galaxies with the strongest Lyα absorption and strongest low-ionization interstellar absorption lines, which is plotted in red. Right: The visual difference between the two extreme spectra in the left-hand panel is confirmed by the mean $E(B-V)$ for each of the four Lyα quartiles, which decreases as a function of increasing Lyα emission. 112

6.7 The dependence of $\Delta v_{\mathrm{em-abs}}$ on Lyα equivalent width. Velocity offsets between Lyα emission and the strongest low-ionization interstellar absorption lines were measured directly from the composite spectra of each of the four Lyα subsamples. As Lyα emission strength increases, the kinematic offset decreases. The error bars on the velocity offsets represent the scatter among the velocities of the different individual interstellar absorption features. 113

6.8 The dependence of O III] and C III] nebular emission strength on Lyα equivalent width. The composite spectrum constructed from the quartile of galaxies with $W_{\mathrm{Ly}\alpha} \geq 20$ Å has significantly stronger nebular emission than the rest of the sample. 114

6.9 The dependence of $W_{\mathrm{Ly}\alpha}$ on apparent UV luminosity. Restricting the comparison to galaxies with $W_{\mathrm{Ly}\alpha} \geq 20$ Å, which should not be prone to magnitude-dependent selection effects, we construct composite spectra for faint (right panel) and bright (left panel) galaxies. Equivalent widths are measured directly from the continuum-normalized composite spectra and indicate that fainter galaxies have larger Lyα emission equivalent widths than brighter galaxies. 115

6.10 Strong Lyα-dependent trends at fixed $\mathcal{R}$ magnitude. Galaxies with $\mathcal{R} = 24 - 24.5$ are divided into four subsamples based on Lyα equivalent width, and black triangles indicate measurements from the corresponding composite spectra. Left: $W_{\rm Ly\alpha}$ vs. $W_{\rm LIS}$. Colored symbols are as in Figure 6.5. Galaxies with $\mathcal{R} = 24 - 24.5$ follow the same trend as the total sample. Right: $E(B-V)$ vs. $W_{\rm Ly\alpha}$. Colored symbols are as in Figure 6.6, and galaxies with $\mathcal{R} = 24 - 24.5$ obey the same correlation. 116

6.11 The dependence of low-ionization interstellar absorption strength, $W_{\rm LIS}$, on both Lyα equivalent width and dust reddening. These plots show the results of dividing LBG spectroscopic sample into quartiles, according to either Lyα equivalent width (left) or $E(B-V)$ (right). While $W_{\rm LIS}$ depends strongly on both $W_{\rm Ly\alpha}$ and $E(B-V)$, there is more variance in $W_{\rm LIS}$ when the sample is sorted by $W_{\rm Ly\alpha}$. This suggests a stronger statistical link between $W_{\rm LIS}$ and $W_{\rm Ly\alpha}$, though the correlation between $W_{\rm LIS}$ and $E(B-V)$ is strong enough that there may be a direct physical connection among all three quantities. 118

6.12 Dependences of $W_{\rm LIS}$, $W_{\rm Ly\alpha}$, and $E(B-V)$ on $\Delta v_{\rm em-abs}$. These plots show the average $W_{\rm LIS}$, $W_{\rm Ly\alpha}$, and $E(B-V)$ values measured from each of the 3 subsets of galaxies sorted by $\Delta v_{\rm em-abs}$, and their associated composite spectra. $W_{\rm LIS}$ and $E(B-V)$ are not significantly dependent on Δv, while $W_{\rm Ly\alpha}$ is smaller for the subsample with the highest Δv (≥ 800 km s^{-1})). This trend is consistent with the fact that the Δv measured in the composite spectrum with the strongest Lyα absorption is larger than the Δv measured in the spectrum with the strongest Lyα emission. However, the change in $W_{\rm Ly\alpha}$ with Δv is small compared with the total variance of Lyα across the whole LBG spectroscopic sample. 121

7.1 Continuum-normalized spectra of the two highest S/N LBGs in the spectroscopic sample: MS1512-cB58 and Q0000-D6. cB58 (plotted in black) belongs in the quartile of LBGs with the strongest Lyα absorption, while Q0000-D6 (plotted in magenta) is in the 30% of the sample with the strongest Lyα emission. The contrast between Lyα profiles is clear, as is the contrast between $W_{\rm LIS}$ absorption strengths. On the other hand, the strength of the high-ionization absorption lines is roughly comparable. In this case, where we know the spectral resolution accurately for both spectra, we can show that the intrinsic velocity widths of the absorption lines are comparable, and that the difference in $W_{\rm LIS}$ between cB58 and Q0000-D6 is due to a difference in the covering fraction of neutral gas. 129

8.1 Four examples of deep LRIS-R spectra. Each spectrum represents a total of 18 hours of integration time, and has been shifted into the rest frame and continuum-normalized. This figure contains spectra with strong low-ionization interstellar absorption lines, at least one of which in each spectrum reaches zero intensity at line center. The object name and interstellar absorption redshift are indicated at the top of each figure. Both low- and high-ionization interstellar absorption features are indicated with dotted lines, and the weak S V stellar photospheric absorption line is indicated as well. One striking property of these spectra is the large variation in the widths of the high-ionization Si IV absorption features. 138

8.2 Four examples of deep LRIS-R spectra. Each spectrum represents a total of 18 hours of integration time, and has been shifted into the rest frame and continuum-normalized. This figure contains spectra with weaker low-ionization interstellar absorption lines than those shown in Figure 8.1. The weakest lines are observed in the spectrum of SSA22a-C32 (bottom), with depths at line-center barely reaching down to 50% of the continuum level. The object name and interstellar absorption redshift are indicated at the top of each figure. Both low- and high-ionization interstellar absorption features are indicated with dotted lines, and the weak S V stellar photospheric absorption line is indicated as well. Of special note is the spectrum of SSA22a-C47 (top), which actually contains two redshifts. We have adopted the rest frame of the $z = 3.064$ galaxy and marked the spectral features accordingly, but a set of strong absorption lines is apparent for the $z = 3.019$ galaxy as well. 139

8.3 A comparison of low-ionization velocity widths. This figure illustrates the difference in low-ionization absorption profiles for two galaxies with deep spectroscopic observations: SSA22a-C16 (plotted in black), and SSA22a-C32 (plotted in magenta). The absorption features in the spectrum of C32 are not only significantly shallower, but also significantly narrower than the features in the spectrum of C16. This difference cannot be attributed to differences in spectral resolution. 141

8.4 A comparison of high-ionization velocity widths. This figure illustrates the difference in high-ionization absorption profiles for two galaxies with deep spectroscopic observations and very similar low-ionization absorption profiles: SSA22a-C24 (plotted in black), and SSA22a-C35 (plotted in magenta). While the C II low-ionization profiles are almost identical in the spectra of C24 and C35, the widths of the Si IV absorption profiles are almost 3 times larger in the spectrum of C24. 142

8.5 Zoomed-in region of the spectrum of SSA22a-C35 at $z = 3.098$. We detect the stellar photospheric line, S V λ 1501, in this spectrum, along with several other stellar features. Measuring the redshifts of the stellar features allows us to characterize the complete velocity field of the outflowing neutral and ionized gas, referenced to the systemic velocity of the stars. 143

List of Tables

2.1 NIRC Lyman-Break Galaxy Fields 27
2.2 NIRC Observations and Integration Times 28
2.2 NIRC Observations and Integration Times 29
2.3 Lyman-Break Galaxy Optical/Near-IR Photometry 30
2.3 Lyman-Break Galaxy Optical/Near-IR Photometry 31
2.3 Lyman-Break Galaxy Optical/Near-IR Photometry 32
2.3 Lyman-Break Galaxy Optical/Near-IR Photometry 33
2.3 Lyman-Break Galaxy Optical/Near-IR Photometry 34

3.1 Lyman-Break Galaxy Constant SFR Best-Fit Parameters 69
3.1 Lyman-Break Galaxy Constant SFR Best-Fit Parameters 70
3.1 Lyman-Break Galaxy Constant SFR Best-Fit Parameters 71

5.1 Strong LBG Interstellar Absorption Features 98
5.2 Weak LBG Emission Features 99

6.1 Spectroscopic Properties of Lyα Subsamples 123

8.1 LRIS-R Observations of Bright Lyman-Break Galaxies in the SSA22a Field 145
8.1 LRIS-R Observations of Bright Lyman-Break Galaxies in the SSA22a Field 146

Chapter 1

Introduction

The spectroscopic confirmation of a large population of UV-selected star-forming galaxies at $z \sim 3$ represented an important step forward in the study of galaxy formation (Steidel et al., 1996b, Figure 1.1). Essential early observations of color-selected Lyman Break Galaxies (LBGs) included the determinations of their redshifts, large-scale clustering, rest-frame UV colors and luminosities, and contribution to the universal star-formation rate density at $z \sim 3$. These discoveries characterized the overall properties of the LBG sample, providing valuable information about their bias with respect to the underlying matter distribution, model-dependent dark-matter halo masses, and their input into the global energy budget at high redshift.

While such information is vital to the comparison between LBGs and the predictions of galaxy formation models, there are other lines of inquiry that are complementary and also quite valuable. Imaging and spectroscopic observations of the gravitationally-lensed LBG, MS1512-cB58 (Yee et al., 1996), span in wavelength from the submillimeter to the X-ray, and have been used to perform a detailed analysis of the stellar population, dust-content, chemical abundance pattern, large-scale velocity field, and mass-outflow rate in a single high-redshift star-forming galaxy (see Figure 1.2). The observations of cB58 are of excellent quality but cB58 is still only one galaxy, and we would like to obtain more general results. Although the same quality of high-S/N information used in the analysis of cB58 cannot be obtained routinely for typical unlensed LBGs, the goal of this thesis is to use multi-wavelength imaging and composite rest-frame UV spectra to learn more about the intrinsic physical properties of galaxies selected as LBGs. We hope to determine the ages, dust-content, stellar masses, morphologies, outflow-properties, H II region metallicities and temperatures, and a plausible evolutionary scenario for LBGs, in order to understand how these galaxies fit into models of galaxy formation, how they relate to local starburst galaxies, what the descendants of LBGs are, and how LBGs impact their surrounding environments through the effects of powerful star-formation feedback.

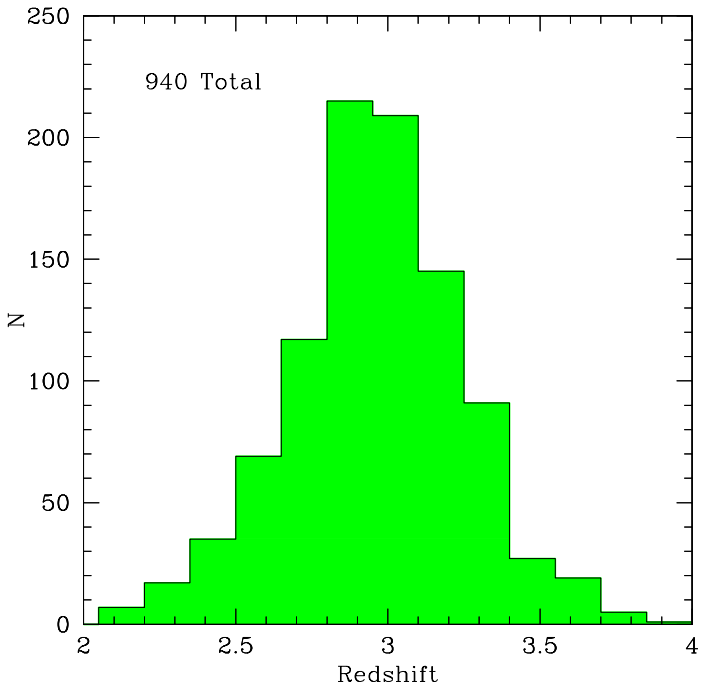

Figure 1.1 The redshift distribution of spectroscopically confirmed $z \sim 3$ galaxies satisfying the LBG color criteria. This distribution is characterized by $\langle z \rangle = 2.96 \pm 0.29$, and is constructed from data presented in Steidel et al. (2003).

1.1 $z \sim 3$ Stellar Populations

At the time this thesis work was begun, a definite dichotomy existed in the theoretical descriptions of LBGs. According to one model, these galaxies are bright in the rest-frame UV (and strongly clustered) due to the fact that they are the central galaxies of the most massive dark matter halos at $z \sim 3$. They have been forming stars steadily over long time scales and will ultimately form as many stars as bright and massive elliptical and spirals in the local universe (Mo et al., 1999; Baugh et al., 1998). Alternatively, LBGs are simply UV-bright due to the event of strong merger-induced starbursts (Somerville et al., 2001). In this latter scenario, LBGs will be UV-bright for much shorter time-periods, and should therefore typically have younger stellar populations. They will form much less stellar mass before fading to become *sub* L^* galaxies, or else repeatedly merge to become present-day luminous galaxies (Sawicki & Yee, 1998; Lowenthal et al., 1997). In the merger-induced starburst scenario, the $z \sim 3$ LBGs are not the direct progenitors of present-day massive elliptical and spiral galaxies, as proposed by the Mo et al./Baugh et al. model.

Aiming to determine the range of ages, star-formation histories, and dust-extinction in LBGs, and to address the dichotomy of models described above, we carried out a near-IR survey of UV-selected LBGs using the near-IR camera (NIRC) on the Keck I telescope. The results of this survey

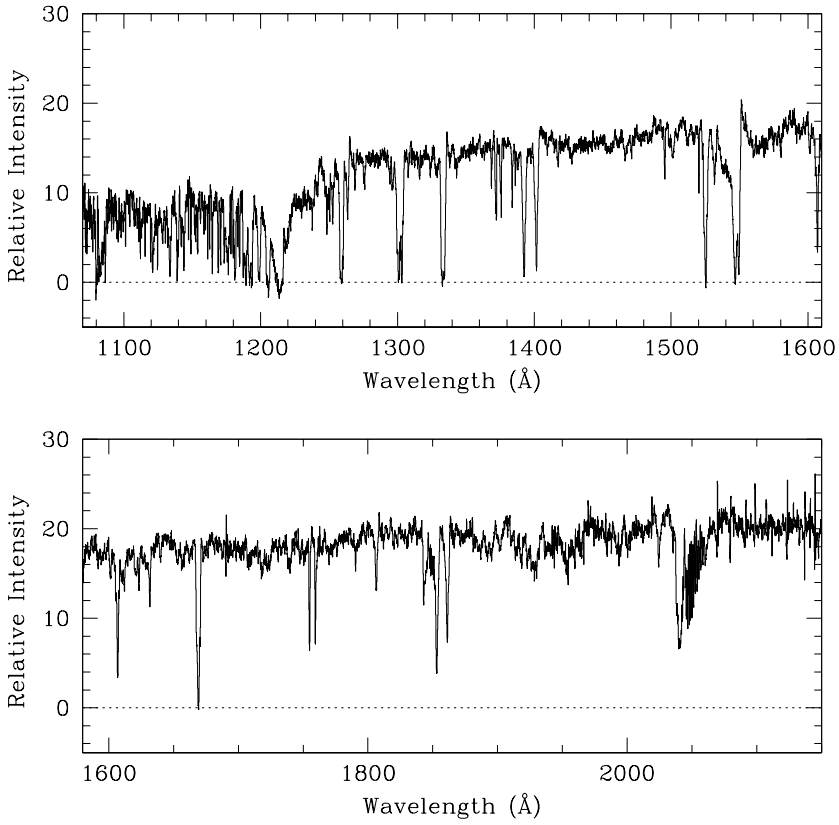

Figure 1.2 The moderately high-resolution spectrum of MS1512-cB58, obtained with the Echelle Spectrograph and Imager (ESI) on the Keck II telescope. The spectral resolution is 58 km s^{-1} and the S/N is > 30 per resolution element. A wealth of information about the physical conditions in cB58 has been gained from this high-quality spectrum, including details of the galaxy's stellar population, large-scale outflow kinematics, outflowing gas covering fraction and abundance pattern. Additional multiwavelength imaging and spectroscopic observations of cB58 have been used to gain further information about the nature of this actively star-forming galaxy. An analysis of the above Keck/ESI spectrum of cB58 is presented in Pettini et al. (2002).

are presented in Part I. Chapter 2 includes the distribution of optical/IR colors of LBGs and the rest-frame optical luminosity function. Models of LBG stellar populations based on their broad-band colors are presented in Chapter 3, and the conclusions are summarized in Chapter 4. The stellar population models used simple prescriptions tuned to detect the strength of the age-sensitive "Balmer Break" at rest-frame $\lambda = 3648$ Å, which required the addition of the near-IR photometry. Optical photometry of the rest-frame UV that is entirely bluewards of the Balmer Break offers us little information about the relative importance of the degenerate effects of age and dust, even assuming a given star-formation history.

Analysis based on a moderately large sample of near-IR observations enabled a considerable advance in our understanding of LBG stellar populations. At the same time, we found that, even with the addition of the near-IR photometry redwards of the Balmer Break, most of the galaxies have star-formation histories, and therefore star-formation ages, that are only weakly constrained by the photometric observations without limiting parameter space using external constraints on the assumed extinction law and relatively simple forms for the star-formation history. Also, light from the most recent episode of star formation can dominate observations in the rest-frame optical, swamping the light from previous episodes of star formation. In a related study, Papovich et al. (2001) found that the stellar mass formed during a maximally old burst—as much as $\sim 3-8$ times the stellar mass associated with the current star-formation episode—can be present without without significantly affecting the rest-frame UV/optical colors of an actively star-forming galaxy at $z > 2$. Observations of the rest-frame near-IR will provide much better constraints on the star-formation histories of $z \sim 3$ galaxies, and the amount of stellar mass they contain. These observations will be performed in the near future as part of the GOODS SIRTF Legacy Science Project (Dickinson & Giavalisco, 2002). More than ~ 80 spectroscopically confirmed $z > 2$ galaxies in the Hubble Deep Field (HDF) will be observed at 3.6, 4.5, 5.8, and 8.0 μm using the InfraRed Array Camera (IRAC) on the Space InfraRed Telescope Facility (SIRTF), providing much better constraints on the stellar populations and stellar mass content of galaxies at high redshift.

While understanding the limitations of our modeling procedure in constraining the exact past star-formation histories of LBGs, we proceeded with reasonable assumptions for the important model parameters that were motivated by recent observational evidence. Applying constant star-formation models reddened by the Calzetti (1997) starburst attenuation relation to the whole sample, we found some intriguing strong correlations. Most striking is the correlation between the inferred dust extinction and stellar population age, in the sense that younger, more rapidly star-forming galaxies are also dustier than older, more quiescent (though still actively star-forming) galaxies. There are also systematic differences in the rest-frame UV spectroscopic properties of the youngest ($t_{sf} \leq 35$ Myr) and the oldest ($t_{sf} \sim 1$ Gyr) galaxies, in that older galaxies have stronger Lyα emission and weaker interstellar absorption lines. Part I includes a model for the evolution of the

star-formation rates and dust-extinction properties of LBGs that accounts for the strong correlations observed between their stellar population parameters.

1.2 Star-formation Feedback and Outflows at $z \sim 3$

As the research for this thesis progressed, so did our understanding of the importance and ubiquity of star-formation induced outflows in high-redshift LBGs. These outflows, or superwinds, had been extensively observed in local starburst galaxies over the preceding decade (Heckman et al., 2000, and references therein). When the rest-frame UV spectra of LBGs were first collected, one of the remarkable properties immediately apparent were the large widths of the strong low-ionization interstellar absorption lines, FWHM $= 400 - 700$ km s^{-1} (Steidel et al., 1996b; Lowenthal et al., 1997). One proposed explanation for these large widths was the impact of non-gravitational processes such as interstellar shocks and supernova winds, rather than the effects of gravitational virial dynamics. Franx et al. (1997) first noted the blueshift of interstellar absorption lines relative to redshifted Lyα emission in the spectrum of a $z = 4.92$ gravitationally lensed arc, and compared this redshift offset with observations and models of galactic-scale outflows in local starburst galaxies. The evidence for outflows was again presented by Steidel et al. (1998), who found that the average redshift offset between Lyα and interstellar absorption lines for a sample of galaxies in the SSA22 field was $\Delta z_{Ly\alpha-abs} = 0.008 \pm 0.004$, corresponding to $\Delta v = 600 \pm 300$ km s^{-1}. Neither redshifted Lyα emission or blueshifted interstellar absorption provide accurate estimates of the true systemic redshifts of the galaxies in most cases, as Pettini et al. (2001) demonstrated for a sample of 17 LBGs with near-infrared spectroscopic measurements (see Figure 1.3). In this sample, the rest-frame optical emission lines such as [OIII] and Hβ, which are produced in H II regions and should therefore be fairly reliable tracers of the systemic velocity of a galaxy, yielded redshifts which most of the time fell somewhere in between the Lyα emission and interstellar absorption measurements (These near-IR spectroscopic results were preceded by the earlier related work of Pettini et al., 1998, which contained a much smaller sample of objects).

Roughly concurrent with the observations of rest-frame optical nebular lines, a detailed analysis of the velocity field associated with interstellar gas in the gravitationally lensed $z = 2.73$ LBG, MS1512-cB58, also revealed the signatures of a large-scale outflow (Pettini et al., 2000, 2002). These high-resolution rest-frame UV spectroscopic observations showed that neutral and ionized interstellar gas was blueshifted by as much as ~ 600 km s^{-1} relative to the stellar systemic velocity, while the peak of the Lyα emission profile was redshifted by $\sim 400-500$ km s^{-1}relative to the stars, with Lyα emission extending redwards to $\sim +1000$ km s^{-1}. Based on the measurement of the outflow neutral H I column density from the damped Lyα profile in cB58, and based on an assumption of a spherical geometry and plausible radius for the location of the absorbing gas, it was also shown that the

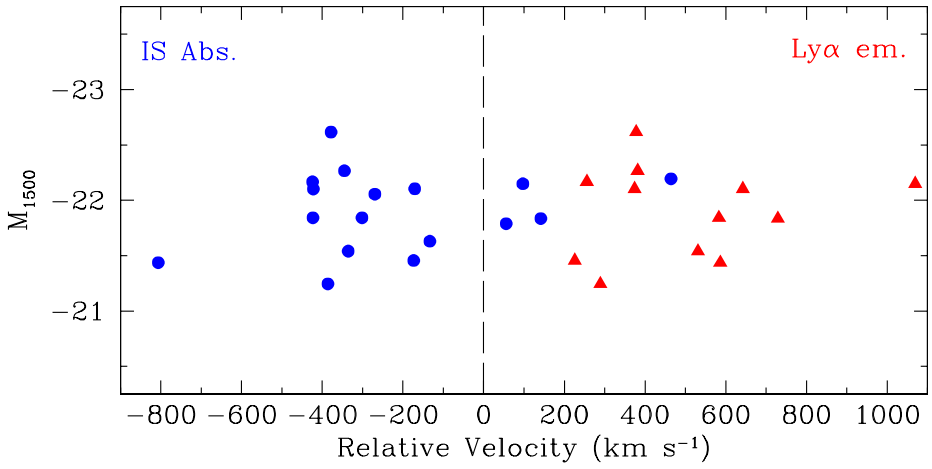

Figure 1.3 Velocity offsets relative to nebular emission line redshifts. The circles and triangles correspond, respectively, to the values of Δv_{IS} and $\Delta v_{Ly\alpha}$. We see the indication of large-scale motions with respect to the systemic redshift defined by the [OIII], [OII], and Hβ nebular emission lines. From Pettini et al. (2001).

mass outflow rate in cB58 is comparable to the star-formation rate (Pettini et al., 2000). Therefore, not only in the sample of LBGs with near-IR observations of rest-frame optical emission lines, but also in the best-studied high-redshift star-forming galaxy with the most detailed and high-quality data, there is evidence for the large-scale outflow of interstellar material. Furthermore, based on simple physical arguments, given their typical star-formation rates and physical sizes (Shapley et al., 2001; Giavalisco et al., 1996b), LBGs easily satisfy and exceed the necessary criteria for driving a superwind: $\Sigma_* \geq 0.1 M_\odot\ \mathrm{yr}^{-1}\mathrm{kpc}^{-2}$ (Heckman, 2002).

Most recently, an entirely complementary study underscores the importance of outflows in LBGs. Comparing the large-scale distributions of LBGs, intergalactic neutral hydrogen, and metals in the same cosmic volumes, Adelberger et al. (2003) find evidence that superwinds from LBGs clear out large ($r \sim 0.5$ comoving Mpc) regions in the intergalactic medium, and enrich the galaxies' surroundings with heavy elements (see Figure 1.4). This claim stems from the apparent deficit of neutral hydrogen within $r \sim 0.5$ comoving Mpc of LBGs (unlikely to be caused by escaping Lyman Continuum radiation), and the strong cross-correlation between the locations of LBGs and C IV absorption systems. The newest, complementary evidence for superwinds emphasizes the significance of feedback, not only in the evolution of galaxies (if they are losing material at the same rate as they are forming stars) but also in the enrichment and physical conditions in the intergalactic medium (IGM).

Part II of this thesis describes our efforts to extract physical information from the large sample of individually low S/N LBG spectra by constructing much higher S/N composite spectra, each containing hundreds of individual spectra. Chapter 5 describes the method of constructing the composite spectra, and the set of features contained in LBG rest-frame UV spectra. While there

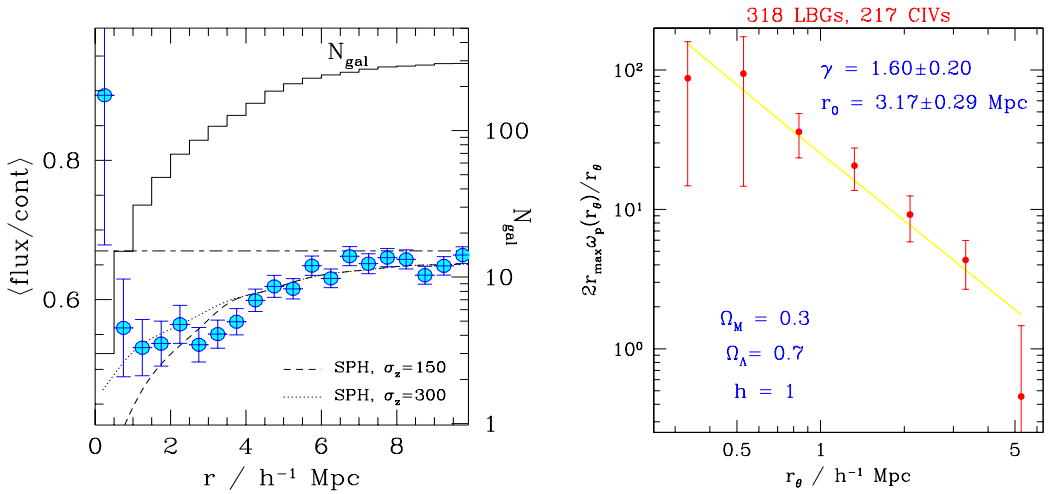

Figure 1.4 The large-scale distribution of LBGs relative to neutral intergalactic hydrogren and metals. Left: Mean intergalactic Lyα transmissivity as a function of comoving distance from LBGs. LBGs appear to be associated with intergalactic H I underdensities on the smallest spatial scales, as indicated by the increase in the Lyα forest transmissivity near LBGs. Right: The projected cross-correlation function of C IV systems and Lyman-break galaxies. The LBG-C IV cross-correlation function is similar to the LBG autocorrelation function, and it is inferred that LBGs reside in regions of enhanced C IV abundance relative to the intergalactic mean. From Adelberger et al. (2003).

are relatively weak absorption and emission features providing information about massive stars and H II regions, by far the strongest absorption features (and Lyα in emission) in LBG rest-frame UV spectra are those low- and high-ionization transitions associated with neutral and ionized outflowing gas. Therefore, the study of the properties of the outflows became one of the most important goals of constructing the composite LBG spectra. Chapter 6 describes some of the important spectroscopic trends observed among the spectroscopic properties of LBGs, and Chapter 7 attempts to explain these correlations in the context of the galactic-scale outflow model.

A lot of information was gained from the high S/N composite spectra about the way in which outflowing gas affects the spectroscopic appearance of LBGs in the rest-frame UV (Shapley et al., 2003). A combination of the covering fraction and velocity distribution of the outflowing gas controls the observed strength of the saturated low-ionization interstellar absorption lines, which in turn is strongly correlated with the UV continuum slope (a proxy for dust-extinction) and the emergent Lyα profile. We were limited from further interpreting these intriguing observational results by the low and somewhat uncertain spectral resolution of our composite spectra, and were unable to determine unequivocally which physical parameter of the outflowing gas was the strongest controlling factor. We also encountered difficulties explaining the relative behaviors of the low- and high-ionization absorption transitions, and the significance of the set of weak Si II* excited fine-structure emission features (in terms of their association with either outflowing gas or with H II regions). Therefore, in Part III, we describe some preliminary results based on deep and higher-resolution spectra of bright

LBGs. The improved quality and higher spectral resolution of these new observations will indicate much more precisely the physical properties of the multiple phases of gas involved in the outflows. The new observations will also provide new constraints on the escape of Lyman Continuum radiation in LBGs, and how that escape fraction is related to other galaxy properties. Ultimately, we would like to understand how a galaxy's evolutionary state (star-formation history, age, stellar mass), and morphology determine the observed outflow properties, and therefore the escape of gas, metals, dust, and ionizing radiation. With such an understanding we will be able to trace the evolution of feedback in star-forming galaxies and how this feedback in turn affects the surrounding environments of galaxies.

A Note on the Contents of this Thesis: The contents of Part I (Chapters 2, 3, and 4) have appeared as Shapley et al. 2001, ApJ, 562, 95 (© 2001. The American Astronomical Society. All rights reserved. Printed in U.S.A.), while the contents of Part II (Chapters 5, 6, and 7) have appeared as Shapley et al. 2003, ApJ, 588, 65 (© 2003. The American Astronomical Society. All rights reserved. Printed in U.S.A.). Figure 1.3 originally appeared in Pettini et al. 2001, ApJ, 554, 981 (© 2001. The American Astronomical Society. All rights reserved. Printed in U.S.A.), and Figure 1.4 originally appeared in Adelberger et al. 2003, ApJ, 584, 45 (© 2003. The American Astronomical Society. All rights reserved. Printed in U.S.A.).

Part I

The Rest-Frame Optical Properties of Lyman Break Galaxies

Abstract

We present the results of a near-infrared imaging survey of $z \sim 3$ Lyman Break Galaxies (LBGs). The survey covers a total of 30 arcmin^2 and includes 118 photometrically selected LBGs with K_s band measurements, 63 of which also have J band measurements, and 81 of which have spectroscopic redshifts. Using the distribution of optical $\mathcal{R}$ magnitudes from previous work and $\mathcal{R} - K_s$ colors for this subsample, we compute the rest-frame optical luminosity function of LBGs. This luminosity function is described by an analytic Schechter fit with a very steep faint end slope of $\alpha = -1.85 \pm 0.15$, and it strikingly exceeds locally determined optical luminosity functions at brighter magnitudes, where it is fairly well constrained. The V-band luminosity density of only the observed bright end of the $z \sim 3$ LBG luminosity function already approaches that of all stars in the local universe.

For the 81 galaxies with measured redshifts, we investigate the range of LBG stellar populations implied by the photometry which generally spans the range 900–5500 Å in the rest frame. The parameters under consideration are the star-formation rate as a function of time, the time since the onset of star formation, and the degree of reddening and extinction by dust. While there are only weak constraints on the parameters for most of the individual galaxies, there are strong trends in the sample as a whole. With a wider wavelength baseline than most previous studies at similar redshifts, we confirm the trend that intrinsically more luminous galaxies are dustier. We also find that there is a strong correlation between extinction and the age of the star-formation episode, in the sense that younger galaxies are dustier and have much higher star-formation rates. The strong correlation between extinction and age, which we show is unlikely to be an artifact of the modeling procedure, has important implications for an evolutionary sequence among LBGs. A unified scenario which accounts for the observed trends in bright LBGs is one in which a relatively short period of very rapid star formation (hundreds of $M_\odot$ yr^{-1}) lasts for roughly 50–100 Myr, after which both the extinction and star-formation rate are considerably reduced and stars are formed at a more quiescent, but still rapid, rate for at least a few hundred Myr. In our sample, a considerable fraction ($\sim 20\%$) of the LBGs have best-fit star-formation ages $\gtrsim 1$ Gyr, implied stellar masses of $\gtrsim 10^{10}$ $M_\odot$, and are still forming stars at ~ 30 $M_\odot$ yr^{-1}.

Chapter 2

The Optical/IR Colors of Lyman Break Galaxies

2.1 Introduction

In the past few years, considerable progress has been made in our understanding of the nature of high redshift galaxies, driven mostly by the availability of large samples that have been photometrically selected using rest-frame UV spectral features. The largest existing sample at present is at $z \sim 3$, where it is efficient to use ground-based imaging through optical filters designed to isolate the Lyman limit spectral discontinuity at 912 Å in the rest frame, and where the spectroscopic follow-up has proved to be straightforward because many important spectral features are well placed at wavelengths where optical spectrographs are most sensitive (Steidel et al., 1996b, 1999). Very deep *Hubble Space Telescope (HST)* imaging such as that provided by the Hubble Deep Fields has also proved to be very effective, using similar techniques for $z \gtrsim 2$ (Steidel et al., 1996a; Madau et al., 1996; Lowenthal et al., 1997). The *HST* data reach much deeper into the high redshift galaxy UV luminosity function, but are confined to very small areas on the sky; as such, the ground-based and space-based surveys have been largely complementary (cf. Steidel et al., 1999).

To date, most of the work on these high redshift galaxy samples has focused on the large-scale clustering properties of the galaxies (e.g., Adelberger et al., 1998; Giavalisco et al., 1998; Steidel et al., 1998; Giavalisco & Dickinson, 2001), on the properties of individual galaxies as deduced from their spectra (e.g., Pettini et al., 1998, 2000, 2001), or on inferences concerning the universal star-formation history as deduced from the global UV luminosity density (e.g., Madau et al., 1996; Steidel et al., 1999; Meurer et al., 1999; Adelberger & Steidel, 2000). The strong clustering of the bright Lyman Break Galaxies (LBGs) has generally been interpreted as indirect evidence that the observed galaxies reside in relatively massive dark matter halos, but how these galaxies are linked to present-day galaxies is far from clear, and has been quite controversial. While considerable, the directly-observed UV luminosity of LBGs is clearly very significantly modified by extinction (see

Adelberger & Steidel, 2000, hereafter AS2000, for an extensive discussion of this topic) and at best provides information on the instantaneous formation rate of O and B stars.

While the far-UV properties of the LBGs are the most straightforward to study observationally, it is also of interest to explore additional properties of these galaxies that require longer wavelength observations, to be used in concert with the existing far-UV measurements. For example, one would like to determine the distribution of rest-frame optical luminosities, and the star-formation histories, ages, dust content, and stellar masses—all necessary for understanding the range of objects selected with the typical Lyman Break photometric criteria, and the relationship of these objects to galaxies in the lower redshift universe. Indeed, different models provide quite divergent descriptions of the nature and fate of the objects which are identified as LBGs. According to one model, the galaxies selected as LBGs are bright in the rest-frame UV because they are experiencing merger-induced starburst events. The intense starburst events occur on relatively short timescales (less than 100 Myr), and produce 10-100 times less stellar mass than what is seen in a typical L^* galaxy. Such low-mass bursting objects would then be the precursors of local low-mass spheroids, unless they merge with similar objects to form more massive systems (Lowenthal et al., 1997; Sawicki & Yee, 1998; Somerville et al., 2001). Alternatively, LBGs are the central objects in relatively massive dark matter halos, which form stars steadily but relatively quiescently over longer than 1 Gyr timescales, accumulate $\geq 10^{10} M_{\odot}$ by $z \sim 3$, and evolve eventually into the ellipticals and spiral galaxies at the bright end of the local luminosity function (Steidel et al., 1996b; Baugh et al., 1998).

It is not possible to determine the nature of LBG stellar populations—and thereby distinguish between the above scenarios—with only optical observations probing the rest-frame UV. Both an aging stellar population and increasing dust extinction result in redder rest-frame UV colors, so that the effects of age and dust are degenerate without longer wavelength data. Recent studies (Sawicki & Yee, 1998; Dickinson, 2000; Papovich et al., 2001) have shown that the addition of near-IR photometric measurements at rest wavelengths longer than the location of an age-sensitive spectral break at ~ 3600 Å removes some of the degeneracy between dust and age in the modeling of LBG stellar populations. Here we present the results of a moderately large near-IR survey of optically selected LBGs, designed to determine the distribution of rest-frame optical luminosities of LBGs, and, where possible, information about their star-formation histories. In § 2.2, we present the details of the optical and near-IR observations and data reduction. § 2.3 summarizes the distribution of optical/IR colors of LBGs. In § 2.4, we describe the derivation of the LBG rest-frame optical luminosity function, and compare it to local galaxy luminosity functions. Chapter 3 presents the procedure and results of population synthesis modeling of the LBG spectral energy distributions between 900 Å and 5500 Å in the rest frame, using the measured optical/IR colors. Extensions of the model results to rest-frame UV spectroscopy are also discussed in Chapter 3, and an evolutionary sequence for LBGs is proposed. Our general conclusions from the survey are summarized in Chapter 4.

2.2 Observations and Data Reductions

2.2.1 Optical Imaging

Optical images were obtained for all the fields included here as part of our extensive survey for $z \sim 3$ galaxies; the field centers are given in Table 2.1. The optical imaging data were collected during the interval 1995–1998 at the William Herschel Telescope (3C 324, B2 0902+34, and CDFa), the Palomar 200-inch Hale Telescope (CDFa, DSF2237a, DSF2237b, HDF, Q0201, Q0256, SSA22a, and SSA22b), and the Kitt Peak Mayall 4-meter Telescope (Westphal). The details of our survey have been presented elsewhere (Steidel et al., 1996b; Giavalisco et al., 1998; Steidel et al., 1999), so here we present only a summary of its relevant features. In deep U_n, G, $\mathcal{R}$ (Steidel & Hamilton, 1993) images, with typical 1σ surface brightness limits of 29.1, 29.2, 28.6 AB magnitudes per arcsec^2, respectively, we identify $z \sim 3$ galaxy candidates by their distinctive colors. To select the objects in the sample centered at $z \sim 3$, the photometric criteria consist of the following:

$$\mathcal{R} \leq 25.5, \quad G - \mathcal{R} \leq 1.2, \quad U_n - G \geq G - \mathcal{R} + 1$$

These criteria effectively isolate star-forming galaxies whose redshifts place the Lyman continuum discontinuity within the U_n band, and result in a redshift distribution that is reasonably well described by a Gaussian with $\langle z \rangle = 2.97$ and a standard deviation of $\sigma(z) = 0.27$. The various biases inherent in such photometric selection have been discussed extensively by Steidel et al. (1999). At the time of this writing, there are approximately 1000 LBGs in this redshift range that have been spectroscopically confirmed using the Low Resolution Imaging Spectrometer (LRIS; Oke et al., 1995) at the W. M. Keck Observatory. The full optical survey and spectroscopic catalogs will be presented elsewhere.

2.2.2 Near-IR Imaging

To explore the range of optical/near-IR colors present in our sample of high redshift galaxy candidates and spectroscopically confirmed $z > 2$ galaxies, a subset of objects was selected for follow-up near-IR imaging. Objects bright in $\mathcal{R}$ were preferentially selected for near-IR imaging, as can be seen by the relative distributions of $\mathcal{R}$ apparent magnitude in the near-IR sample and that in our $z \sim 3$ sample as a whole (Figure 2.1). We deliberately selected objects whose rest-frame UV inferred extinction properties (see Steidel et al. 1999 and AS2000 for a discussion) spanned the entire range seen in the full LBG survey, from zero to several magnitudes of extinction in the rest-frame UV. Within the LBG $z \sim 3$ selection function, galaxies with higher redshifts suffer greater absorption by intergalactic H I, resulting in systematically redder $G - \mathcal{R}$ colors for a fixed intrinsic spectral energy distribution (SED). Figure 2.2 shows the distributions of $(G - \mathcal{R})_0$, the $G - \mathcal{R}$ color statistically

corrected for IGM absorption, for both the near-IR LBG sample and the LBG $z \sim 3$ sample as a whole. This figure shows that, in an effort to target galaxies with extreme values of implied extinction with NIRC, we over-sampled the reddest $(G - \mathcal{R})_0$ bins by roughly a factor of 2 relative to the rest of the distribution.

All of the near-IR data were obtained with the facility near-IR camera (NIRC) (Matthews & Soifer, 1994) on the W. M. Keck I Telescope during the course of 9 separate observing runs in the interval 1997 May - 1999 May. NIRC has a 256×256 InSb array, with a pixel scale of $0.15''$/pixel, resulting in a $38.4''$ field. This field size represents less than 1% of the large optical pointings used to find LBGs (typically $9' \times 9'$) which contain 100-150 $z \sim 3$ candidates to $\mathcal{R} = 25.5$. To maximize efficiency, we preferentially targeted objects having at least one other LBG within $\sim 40''$. A typical pointing included 2–3 LBGs, but this number varied from 1 to 7 LBGs per pointing. Each NIRC pointing contained at least one primary target galaxy with a spectroscopic redshift, and, in many cases, additional LBG candidates for which spectra have not yet been obtained. There are spectroscopic redshifts for about 75% of the full $\mathcal{R} - K_s$ sample.

We observed at 1.25μm and 2.15μm, using the standard J and K_s filters. Using integration times of 4×15 seconds (J) and 6×10 seconds (K_s) per exposure, we dithered the telescope between exposures to form a 9-point box pattern on the sky, each box position separated by a few arcseconds. In most cases, we aimed to complete 6 or more sets of the 9-point dither pattern for each NIRC pointing. During the dither pattern the telescope was guided with an off-set CCD camera, with the orientation of the NIRC detector chosen so that a suitable guide star would fall on the guider chip. Table 2.1 summarizes the coverage of the NIRC survey with respect that of the optical survey for LBGs, listing the angular area and number of LBGs covered in K_s and J for each optical survey field. The optical fields listed in Table 2.1 do not represent the entire optical LBG survey, but only the fields which contain NIRC pointings. Table 2.2 summarizes all of the NIRC target pointings, the objects contained in each pointing, and the total integration times for each pointing.

The data were reduced using standard procedures with the aid of the DIMSUM[1] package. On clear nights, we determined the photometric zeropoints for the J and K_s bandpasses with observations of faint (11th - 12th magnitude) near-infrared standard stars from the list of Persson et al. (1998). During 5 of our 9 NIRC runs, we experienced stable, photometric conditions, while the remaining 4 runs contained variable cirrus. On runs with variable conditions, we carefully calibrated observing sequences with observations obtained when the conditions were judged to be photometric. As measured from the FWHM of standard stars, the seeing during our several NIRC runs ranged from $0.3''$ to $0.7''$ in both J and K_s, with FWHM$\simeq 0.5''$ being typical. Figure 2.3 shows two different examples of $\mathcal{R}$ and K_s images of LBGs surveyed with NIRC. Westphal-MMD11 has the reddest

[1]Deep Infrared Mosaicing Software, a package of IRAF scripts by Eisenhardt, Dickinson, Stanford, and Ward, available at ftp://iraf.noao.edu/contrib/dimsumV2/.

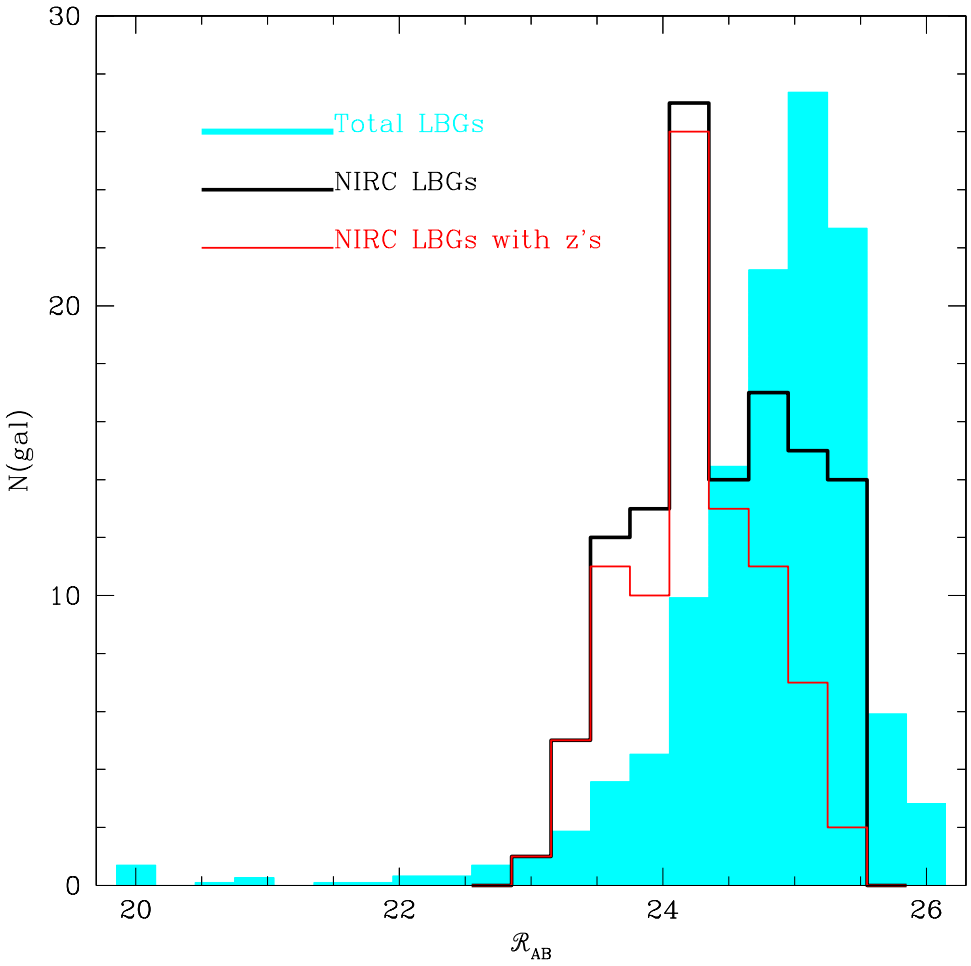

Figure 2.1 The distribution of $\mathcal{R}$ magnitudes for the NIRC LBG sample, relative to that of the LBG survey as a whole. The LBG total sample histogram has been normalized to the number of galaxies contained in the NIRC LBG subsample, for the purpose of comparison. Also indicated is the $\mathcal{R}$ distribution for the NIRC LBGs with measured redshifts, which comprise a slightly brighter sample than the NIRC LBG sample as a whole.

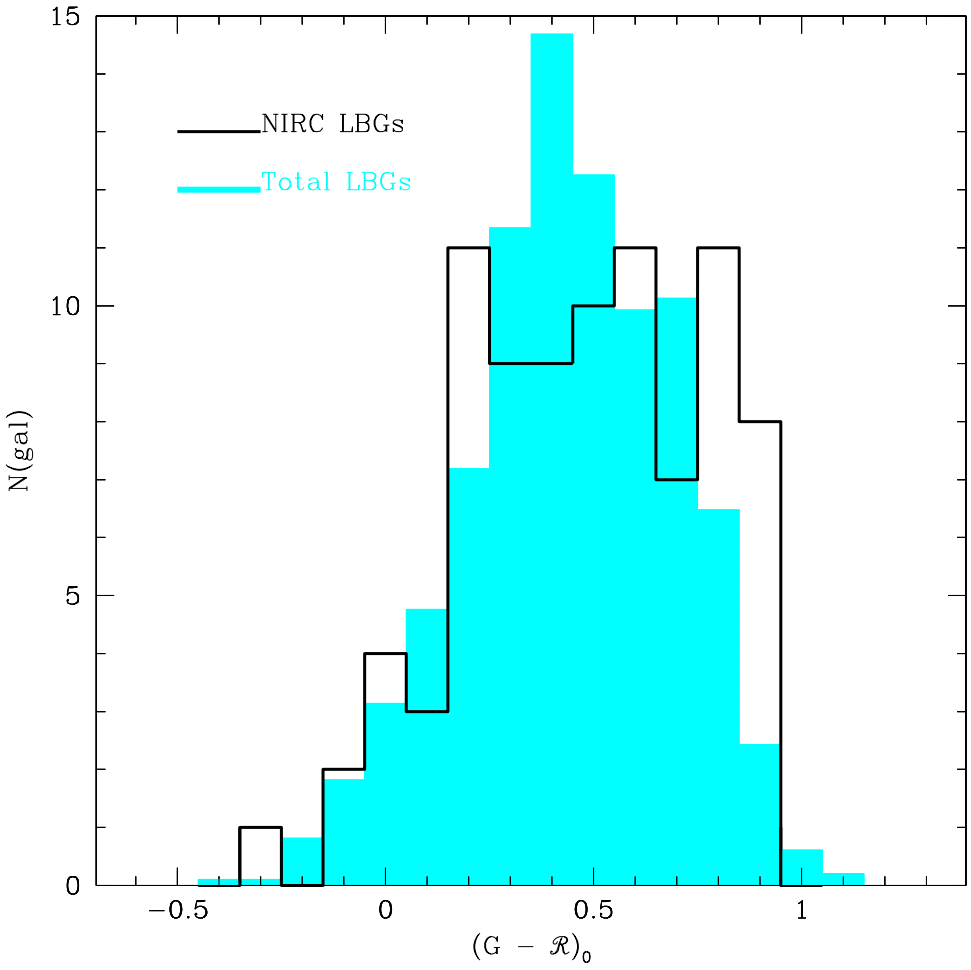

Figure 2.2 The distribution of $(G-\mathcal{R})_0$, the IGM-absorption-corrected $G-\mathcal{R}$ color, for galaxies in the NIRC LBG sample with redshifts, relative to that of the LBG spectroscopic sample as a whole. The total LBG histogram has been normalized to the number of objects in the NIRC LBG histogram. This figure shows that the NIRC LBG spectroscopic sample contains an excess of highly reddened galaxies, relative to the total LBG spectroscopic sample.

$\mathcal{R}-K_s$ color and brightest K_s magnitude in the NIRC LBG sample, while B20902-C6 is in the bluer and fainter half of the NIRC LBG sample.

2.2.3 Optical/Near-IR Photometry

Prior to the measurement of optical/near-IR colors, each NIRC frame was smoothed with a Gaussian to match the image quality in the corresponding optical images, which generally had $FWHM \simeq 1.0''$. The photometry was then performed in a manner analogous to that used for $z \sim 3$ galaxy searches, described elsewhere (Steidel et al., 1995; Steidel & Hamilton, 1993). In brief, using a modified version of the FOCAS (Valdes 1982) image detection and analysis routines, a catalog of isophotal and "total" object detections was generated in the $\mathcal{R}-$ band (where "total" refers to the FOCAS definition, which is the flux measured within an aperture grown to twice the area of the initial detection isophote). The $\mathcal{R}-$ band isophotal detection apertures were applied to the J and K_s images, to measure $\mathcal{R}-J$ and $\mathcal{R}-K_s$ colors. Table 2.3 lists the $\mathcal{R}$ *total* magnitudes, $G-\mathcal{R}$, $\mathcal{R}-J$, $\mathcal{R}-K_s$ *isophotal* colors, and redshifts for all objects in the NIRC sample. Optical magnitudes (G and $\mathcal{R}$) and colors are referenced to the AB system, whereas the near-IR magnitudes (J and K_s) are on the Vega system. [2]

2.2.4 Photometric Uncertainties

To quantify the uncertainties in the measured $\mathcal{R}-J$ and $\mathcal{R}-K_s$ colors, we ran Monte Carlo simulations mimicking the actual process used to measure magnitudes and colors from the real data. Artificial galaxies, with a reasonable range of intrinsic sizes and with $\mathcal{R}$ magnitudes and $\mathcal{R}-K_s$ colors drawn randomly from the observed range of both quantities, were added to the images after convolution with the seeing disk. We then produced detection catalogs in $\mathcal{R}$ and measured the $\mathcal{R}-K_s$ colors with matched apertures in the K_s image. The process of adding fake galaxy sets (the number of galaxies added in a given trial was kept small enough so as not to alter the systematics of the observed data frames) and recovering the magnitudes and colors using the same procedures used for the real data was repeated until enough detections were obtained to study the scatter between true and recovered $\mathcal{R}-K_s$ color as a function of recovered $\mathcal{R}$ and $\mathcal{R}-K_s$. The Monte-Carlo generated photometric uncertainties are significantly larger than those that would result from the application of simple Poisson counting statistics that neglect systematics.

The detections of artificial objects were binned in 0.5 mag steps in measured $\mathcal{R}$ magnitude and 0.2 mag steps in measured $\mathcal{R}-K_s$ color. The mean and standard deviation were then computed for the distribution of $\Delta(\mathcal{R}-K_s) = (\mathcal{R}-K_s)_{true} - (\mathcal{R}-K_s)_{measured}$ in each $(\mathcal{R}, \mathcal{R}-K_s)$ bin. In

[2] To convert from Vega magnitudes to AB magnitudes, we adopt the transformations: $K_s(AB) = K_s(Vega)+1.82$, $J(AB) = J(Vega) + 0.90$. The standard relation between AB magnitude and flux-density, f_ν, is: $m_{AB} = -48.6 - 2.5 \log f_\nu$ where f_ν is in units of ergs s^{-1} cm^{-2} Hz^{-1}.

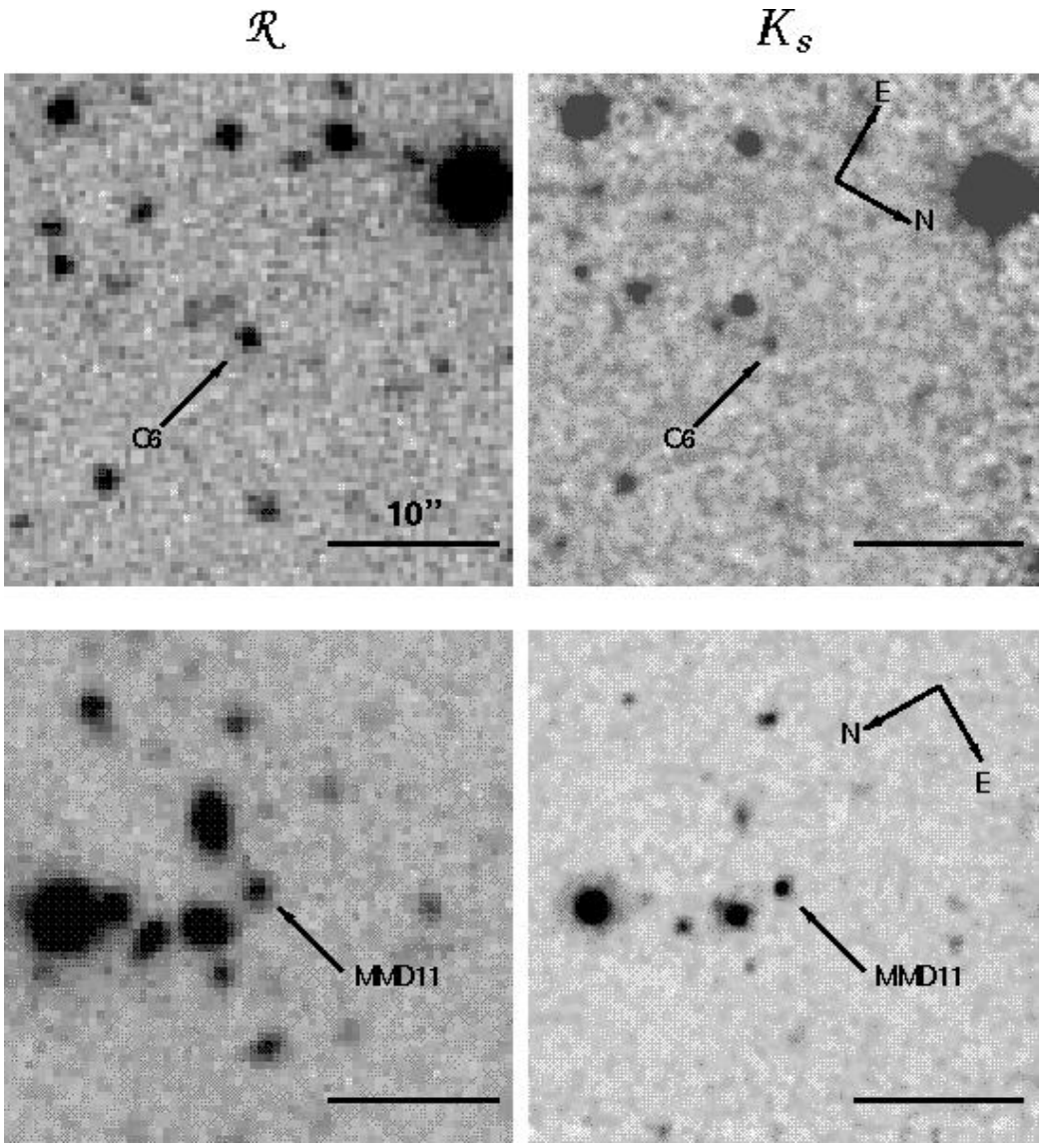

Figure 2.3 $\mathcal{R}$ and K_s images for two objects in the NIRC LBG sample. A bar indicating 10” is in the lower right-hand corner of each image. The N-E orientation of the $\mathcal{R}$ and K_s images for each object is indicated in the K_s images. NIRC orientations were chosen to locate a guide star on the guide camera, as well as to maximize the number of galaxies per pointing. Top: B20902-C6 has $\mathcal{R} = 24.13$ and $\mathcal{R} - K_s = 2.39$ which puts it in the bluer half of the sample of $\mathcal{R} - K_s$ measurements, with a fairly typical signal-to-noise ratio. Bottom: Westphal-MMD11 has $\mathcal{R} = 24.05$ and $\mathcal{R} - K_s = 4.54$, which gives it the reddest and highest signal-to-noise $\mathcal{R} - K_s$ measurement in the NIRC LBG sample.

general we did not find a significant systematic offset between the measured and true colors, so the color uncertainties are treated as symmetric. Accordingly, we adopted the standard deviation of the $\Delta(\mathcal{R} - K_s)$ distribution as the 1σ color uncertainty, $\sigma(\mathcal{R} - K_s)$ for each $(\mathcal{R}, \mathcal{R} - K_s)$ bin.

To be conservative, we initially treated each NIRC pointing independently for the estimation of photometric uncertainties in order to explore possible variations due to slightly different depths, seeing conditions, and sky background. We subsequently determined that the trend of $\sigma(\mathcal{R}-K_s)$ with $(\mathcal{R}, \mathcal{R} - K_s)$ was similar enough in all K_s NIRC pointings that we simply combined the simulation results from all pointings to calculate an average trend of $\sigma(\mathcal{R} - K_s)$ with $(\mathcal{R}, \mathcal{R} - K_s)$ for our entire $\mathcal{R} - K_s$ sample. Uncertainties were then assigned to the measured $\mathcal{R} - K_s$ colors in the NIRC sample, based on the magnitude and color of each object.

An identical procedure was used to generate uncertainties in the $\mathcal{R} - J$ colors of all of the observed galaxies. The $G - \mathcal{R}$ uncertainties were computed from a separate, but similar, set of Monte Carlo simulations (Adelberger, 2002). All the color uncertainties are listed along with the optical/IR photometry in Table 2.3.

2.3 The Optical/IR Colors of Lyman Break Galaxies

The distribution of measured optical/IR colors for the 118 galaxies with NIRC K_s data is shown in Figure 2.4. 107 of these measurements are K_s detections significant at the 5σ level, while 11 of them are only upper-limits, whose $\mathcal{R} - K_s$ limits correspond to the typical 5σ detection limit of $K_s = 22.5$ in our images. We find a mean $\mathcal{R} - K_s$ color of $< \mathcal{R} - K_s >= 2.85$ and a standard deviation $\sigma(\mathcal{R} - K_s) = 0.59$. Of these 118 galaxies, 81 have measured redshifts, with a mean of $< z >= 2.996$. There are J band measurements for 63 of the galaxies in the $\mathcal{R} - K_s$ sample. The mean $J - K_s$ color is $< J - K_s >= 1.52$ with $\sigma(J - K_s) = 0.77$. At $z \sim 3$, the J and K_s filters correspond to $\lambda_{eff}(J) = 3100$ Å, and $\lambda_{eff}(K_s) = 5400$ Å in the rest frame, respectively, whereas the optical passbands U_n, G, and $\mathcal{R}$ sample the galaxies at rest-frame $\lambda_{eff} \simeq 900$, 1200, and 1700 Å, respectively.

Clearly, there is a wide range of optical/near-IR color among the rest-UV selected $z \sim 3$ LBGs; the bluest galaxies in $\mathcal{R} - K_s$ have colors that are essentially flat in f_ν units from the far-UV to the optical in the rest frame, whereas the reddest LBGs approach the colors of "extremely red objects." The typical $\mathcal{R} - K_s$ color of $z \sim 3$ LBGs is more than 2.5 magnitudes redder than that expected for an unreddened instantaneous burst of star-formation at the mean redshift of our sample ($\mathcal{R} - K_s = 0.30$), but is significantly bluer than most galaxies in the present-day universe (cf. Papovich et al., 2001). Unfortunately, in the absence of high quality spectra covering the same large wavelength range, the interpretation of the colors of LBGs in the context of understanding their stellar populations and extinction must rely heavily on models. In Chapter 3, we use the full

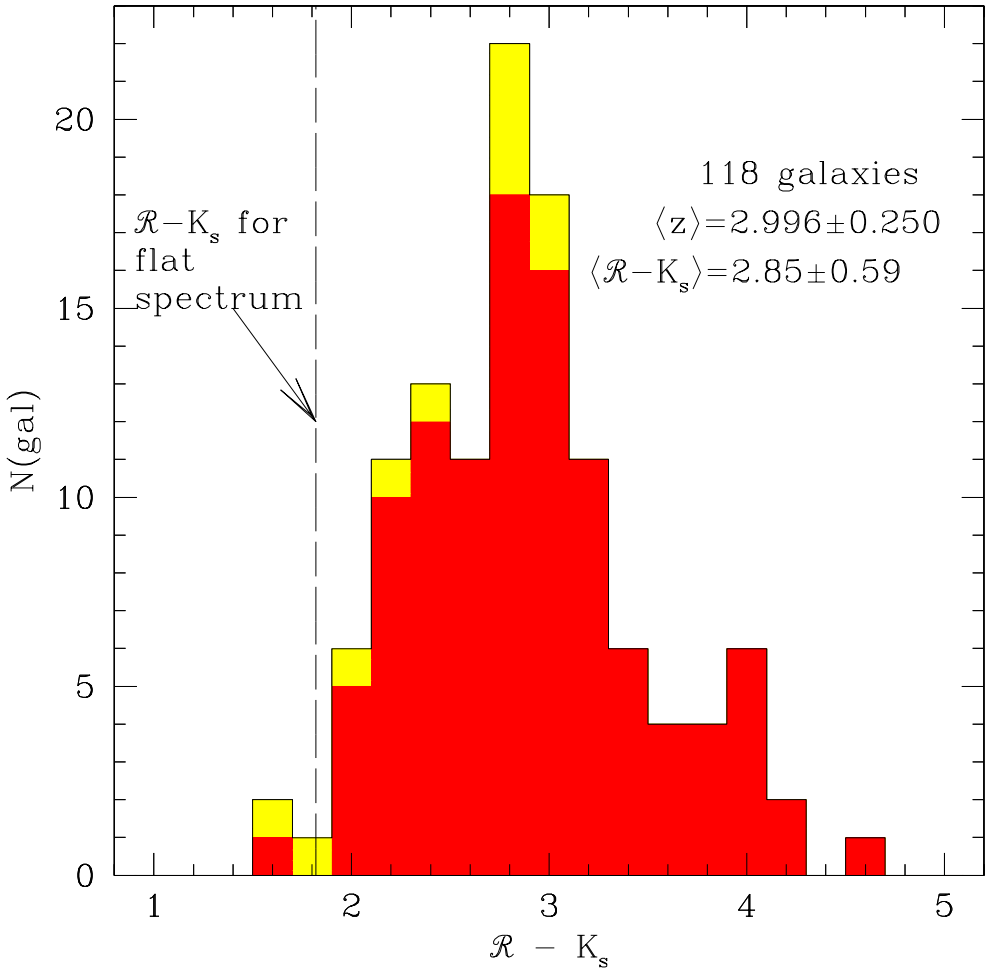

Figure 2.4 The distribution of observed $\mathcal{R} - K_s$ colors for the NIRC LBG sample. Of the 118 galaxies, 107 have $\mathcal{R} - K_s$ detections, and 11 have upper limits, corresponding to the typical K_s detection limit of $K_s = 22.5$. Detections are indicated in the red (dark) shaded histogram, while upper limits are in the yellow (light) shaded bins. A dashed line at $\mathcal{R} - K_s = 1.82$ marks the color for a flat spectrum in F_ν. The average color in the sample is $< \mathcal{R} - K_s >= 2.85$. 81 of 118 galaxies in the NIRC LBG sample have measured redshifts, with $< z >= 2.996$.

set of optical/IR colors ($G-\mathcal{R}, \mathcal{R}-J$, and $\mathcal{R}-K_s$) of LBGs in the NIRC sample in an attempt to disentangle the degenerate effects of dust and age on LBG broadband spectral energy distributions.

2.4 Rest-Frame Optical Luminosity Function

The distribution of redshifts and observed $\mathcal{R}$ and I magnitudes have been used to construct rest-frame far-UV luminosity functions for LBGs at $z \sim 3$ and $z \sim 4$ respectively (Steidel et al., 1999). With near-IR K_s magnitudes and optical/IR $\mathcal{R}-K_s$ colors for a sample of 118 LBGs, we have the necessary information to construct the rest-frame *optical* luminosity function of $z \sim 3$ LBGs, which is much more easily compared with galaxies in the present-day universe. Optical emission is much less attenuated than far-UV light by the presence of dust, and expected to be less directly linked to the instantaneous star-formation rate, as the stars giving rise to the optical emission sample a larger swath of the main sequence and include stars with longer lifetimes than the O/B stars producing the far-UV light. Thus, one might hope that the optical luminosities provide more information on the integrated stellar populations of the LBGs than can be obtained from far-UV measurements.

At $z \simeq 3$, the mean redshift of the LBG spectroscopic sample (and of the NIRC sample as well), the K_s-band central wavelength of 2.15μm is quite a good match to the central wavelength of the standard V optical filter. While the NIRC sample contains galaxies with a range of redshifts, the K_s-band central wavelength falls within the rest-wavelength range $5100-5700$ Å for the bulk of the sample. Furthermore, the "photometric depth" of the LBG redshift selection function corresponds to a difference in absolute magnitude of only $\Delta M_V \sim 0.30$ magnitudes for a given apparent magnitude; consequently, given our typical measurement uncertainties, we view it as a reasonable approximation for this analysis to treat all the galaxies in the NIRC sample as if they were located at the mean redshift of the entire LBG spectroscopic sample. This of course allows us to use the whole NIRC sample, and not just the objects with spectroscopic redshifts, for the luminosity function analysis.

Two pieces of information are required to construct the rest-frame optical luminosity function for LBGs at $z \sim 3$: the LBG rest-frame UV luminosity function (i.e., the distribution of $\mathcal{R}$ apparent magnitudes), and the LBG distribution of $\mathcal{R}-K_s$ as a function of $\mathcal{R}$ magnitude for the NIRC sample. The best-fit $\mathcal{R}$ apparent magnitude luminosity function parameters for LBGs (uncorrected for the effects of dust extinction) are a faint-end slope of $\alpha = -1.57$, a characteristic apparent magnitude of $m^*_{\mathcal{R}} = 24.54$, and an overall normalization of $\phi^* = 4.4 \times 10^{-3} h^3 \mathrm{Mpc}^{-3}$ (AS2000).[3] In § 2.3, we presented the overall distribution of $\mathcal{R}-K_s$ colors for the NIRC sample. A correlation with 98% confidence (better than 2σ) is detected between $\mathcal{R}-K_s$ color and $\mathcal{R}$ magnitude, such that fainter galaxies have redder $\mathcal{R}-K_s$ colors (see Figure 2.5). This correlation probability was computed including the 11 upper limits in the sample of 118 galaxies with $\mathcal{R}-K_s$ measurements, so the

[3] These parameters were fit assuming the currently favored cosmology of $\Omega_m = 0.3, \Omega_\Lambda = 0.7$.

result should not be biased by our typical detection limit of $K_s = 22.5$. The trend of $\mathcal{R} - K_s$ with $\mathcal{R}$ is included in the luminosity function analysis by using the relationship implied by the best-fit regression slope to the correlation: $\frac{d\langle \mathcal{R}-K_s \rangle}{d\mathcal{R}} = 0.17$. There is a lot of scatter around this regression slope, but it provides a means of encoding the trend between the two variables.

We generated a large sample (15000) of LBG $\mathcal{R}$ apparent magnitudes between $\mathcal{R} = 22.5$ and $\mathcal{R} = 27$, by randomly drawing luminosities from the LBG $z \sim 3$ rest-frame UV luminosity function placed at z=2.972, the mean redshift of the current $z \sim 3$ LBG spectroscopic sample. An $\mathcal{R} - K_s$ color was then assigned to each of the $\mathcal{R}$ magnitudes, drawn randomly from the distribution of $\mathcal{R} - K_s$ colors for galaxies in the NIRC sample with $24 \leq \mathcal{R} \leq 24.5$, and then shifted by the amount, $\Delta(\mathcal{R} - K_s) = 0.17 \times (\mathcal{R} - 24.25)$, according to the correlation between $\mathcal{R}$ and $\mathcal{R} - K_s$. The fiducial $(\mathcal{R}, \mathcal{R} - K_s)$ distribution was restricted to $\mathcal{R} = 24.0 - 24.5$ because this 0.5 magnitude range contained the largest number of $\mathcal{R} - K_s$ measurements (36). Also, the $\mathcal{R} - K_s$ measurements for $\mathcal{R} = 24.0 - 24.5$ were virtually all detections, rather than mixture of upper limits and detections. Combining each randomly generated pair of $\mathcal{R}$ and $\mathcal{R} - K_s$ measurements, we obtained an ensemble of K_s magnitudes, which were grouped into 0.5 magnitude bins.

To determine how the photometric uncertainties of both the $\mathcal{R}$ magnitudes and $\mathcal{R} - K_s$ colors translated into uncertainties in the derived K_s luminosity function, the procedure of generating an ensemble of random ($\mathcal{R}$, $\mathcal{R} - K_s$) pairs was repeated a large number (10000) of times. In each trial, we perturbed the sample of actual ($\mathcal{R}$, $\mathcal{R} - K_s$) measurements by random amounts consistent with the photometric uncertainties. In so doing, we assumed that the errors in $\mathcal{R}$ and $\mathcal{R} - K_s$ were uncorrelated, which is a valid approximation since the error in $\mathcal{R} - K_s$ for galaxies in our sample is dominated by the K_s photometric error. Due to the slight differences in the sample of $\mathcal{R}$ magnitudes drawn from the LBG $\mathcal{R}$ apparent luminosity function, and the more significant differences of the perturbed ($\mathcal{R}$, $\mathcal{R} - K_s$) measurements, a different K_s distribution was produced in each trial. The analytic Schechter function (1976) was fit to each perturbed distribution of K_s-band apparent magnitudes. We restricted the fitted region to span only $19 \leq K_s \leq 22.5$, reflecting the K_s range for which we have actual measurements. The average number from all the trials was adopted for each K_s 0.5 magnitude bin, and the adopted 1σ uncertainty was the standard deviation among the realizations (which does not include the uncertainties in the LBG $\mathcal{R}$-band luminosity function best-fit parameters (AS2000)).

The Schechter function was then fit to the average luminosity function values. The best-fit parameters we obtain are an overall normalization of $\phi^* = 1.8 \pm 0.8 \times 10^{-3}\ h^3\mathrm{Mpc}^{-3}$, a faint end slope of $\alpha = -1.85 \pm 0.15$, and a characteristic apparent magnitude of $m^*_{K_s} = 20.70 \pm 0.25$. The uncertainties on the fitted parameters represent the confidence intervals generated by fitting the Schechter function to each perturbed K_s distribution. Since it was assumed that all the galaxies comprising the K_s luminosity function were at the mean redshift of the LBG spectroscopic sample,

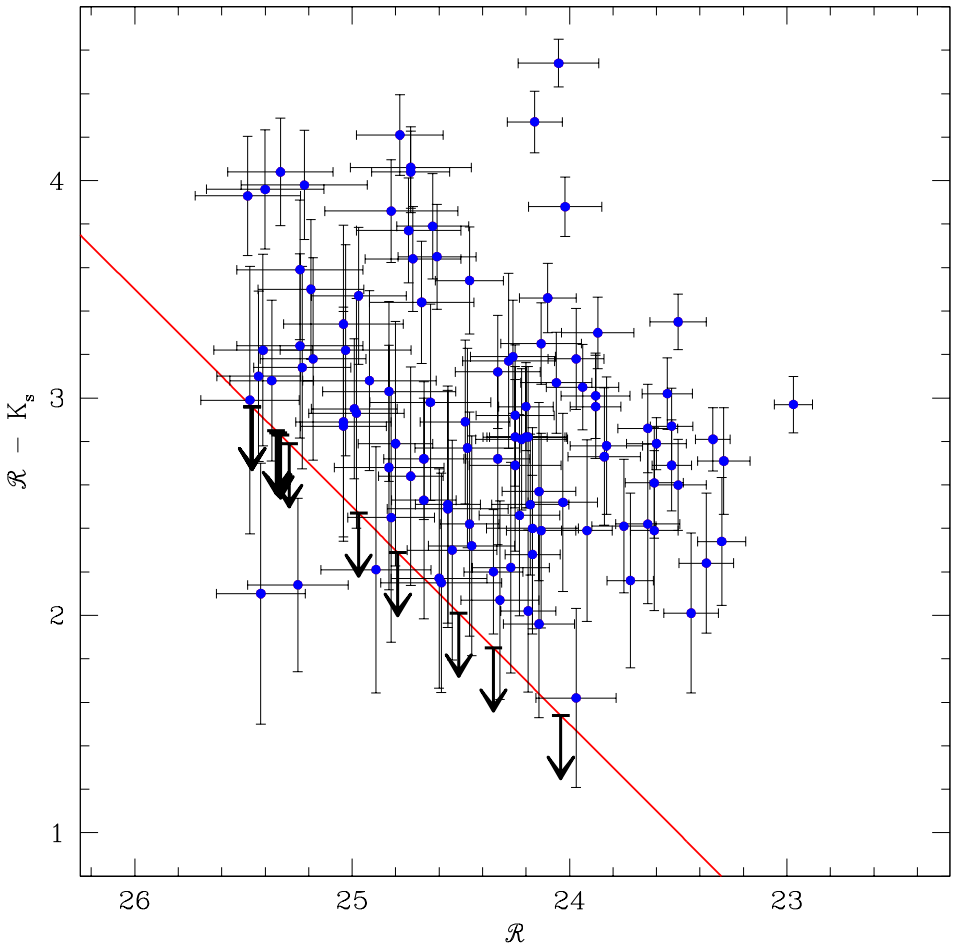

Figure 2.5 $\mathcal{R} - K_s$ vs. $\mathcal{R}$. Dots indicate $\mathcal{R} - K_s$ detections, while down-arrows indicate upper limits. The diagonal line traces the typical sample detection limit of $K_s = 22.5$. There are three points below this detection line, representing galaxies in K_s images with more sensitive detection limits than the typical one.

it is straightforward to convert the distribution of K_s apparent magnitudes into a 5400 Å (i.e., rest-frame V-band) absolute magnitude distribution. With our adopted $\Omega_m = 0.3, \Omega_\Lambda = 0.7$ cosmology, $m^*_{K_s} = 20.70$ corresponds to $M^*_V = -22.21 + 5\log h$. The overall shape of the rest-frame optical luminosity function is determined by the way in which the $\mathcal{R} - K_s$ distribution as a function of $\mathcal{R}$ magnitude redistributes $\mathcal{R}$ magnitudes into K_s magnitudes. Accordingly, the faint end slope of the LBG rest-frame optical luminosity function is steeper than that of the UV luminosity function, due to the positive correlation between $\mathcal{R}$ and $\mathcal{R} - K_s$. Figure 2.6 shows the apparent K_s luminosity function (and the absolute optical magnitudes to which it corresponds), as well as the confidence intervals on the best-fit Schechter luminosity function parameters. Immediately apparent from Figure 2.6 is the fact that the well-constrained bright end of the LBG luminosity function greatly exceeds locally determined optical luminosity functions.

To calculate the rest-frame optical co-moving luminosity density for LBGs brighter than $K_s = 22.5$, we integrate over the luminosity-weighted luminosity function in the appropriate magnitude range to obtain $\rho_{5400\mathring{A}} = 6.86 \times 10^{26}\,\mathrm{erg\,s^{-1}Hz^{-1}}h\,\mathrm{Mpc^{-3}}$. We use the V-band absolute magnitude of the Sun, $M_{V\odot} = 4.83$ (Binney & Merrifield, 1998), to express this quantity in solar units: $\rho_V = 1.35\times10^8 L_\odot h\mathrm{Mpc}^{-3}$. If the luminosity function were integrated to $K_s = 25.0$, the derived luminosity density would be more than 2 times larger than the value determined down to the typical survey detection limit of $K_s = 22.5$. However, such an extrapolation depends sensitively on the value of the faint end slope of the luminosity function, which is poorly constrained by our observed sample. Fukugita et al. (1998) summarize recent local determinations of the B-band luminosity density, most of which are in the range $\rho_B = (1.8-2.2)\times10^8 L_\odot\,\mathrm{Mpc}^{-3}$. Thus, the LBG V-band optical luminosity density down to only $K_s = 22.5$ is within a factor of 2 of local measurements of the B-band optical luminosity density, which were obtained by integrating over the entire B-band luminosity function.

The optical luminosity function of local galaxies has been computed from numerous surveys over the past thirty years. Some recent determinations from magnitude-limited redshift surveys include the Two-Degree Field Galaxy Redshift Survey (2dFGRS) b_j luminosity function (Folkes et al., 1999), the Las Campanas Redshift Survey (LCRS) R-band luminosity function (Lin et al., 1996), and the Sloan Digital Sky Survey (SDSS) luminosity functions in five optical bands (Blanton et al., 2001). These local optical luminosity functions have much shallower faint end slopes (α), fainter characteristic luminosities (M^*), and higher overall normalizations (ϕ^*) than the rest-frame optical luminosity function of LBGs. To demonstrate these differences, we plot the 2dFGRS b_j luminosity function in Figure 2.6 along with the LBG rest-frame optical luminosity function. The best-fit parameters of the 2dFGRS luminosity function are $\phi^* = 1.69 \pm 0.17 \times 10^{-2}\ h^3\mathrm{Mpc}^{-3}$, $\alpha = -1.28\pm0.05$, and $M^* = -19.73\pm0.06+5\log h$. For a direct comparison with the LBG luminosity function, which specifically probes the rest-frame V band, the 2dFGRS luminosity function has been shifted 0.5 magnitudes brighter (i.e., $M^* = -20.23 + 5\log h$), reflecting the typical $b_j - V$ color of

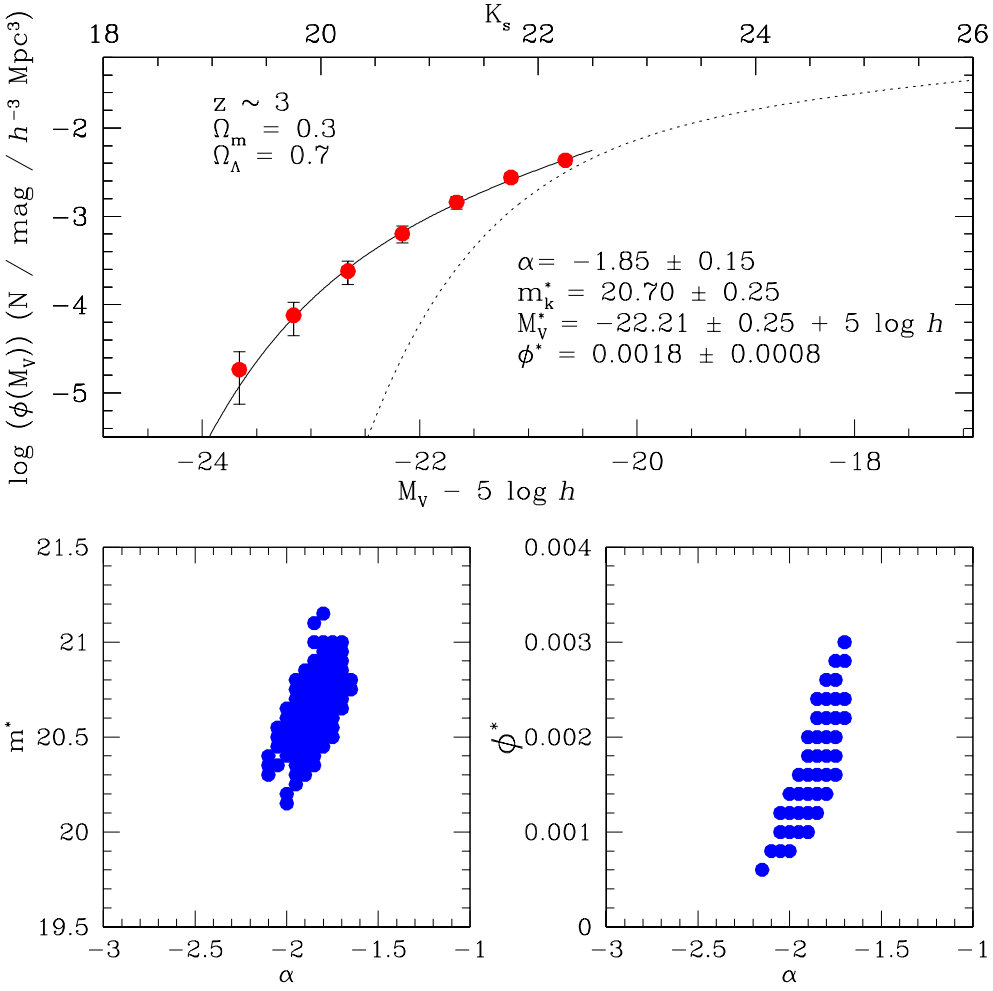

Figure 2.6 Top: The rest-frame optical luminosity function of LBGs. The points and solid line indicate the magnitude range used for the Schechter function fit. The error bars on the points include the photometric uncertainties on the $\mathcal{R}$ and $\mathcal{R} - K_s$ measurements. The lower x-axis indicates the range in optical absolute magnitude, M_V, spanned by the K_s luminosity function (assuming $h = 1$). The dotted line indicates the locally determined 2dFGRS b_j luminosity function, offset by a color of $b_j - V = 0.5$ magnitudes (for comparison at the same rest wavelength as the LBG optical luminosity function). Bottom: The 68.3% confidence intervals for the best-fit Schechter function parameters. The covariance between the best-fit parameters is indicated by the confidence regions. As the faint-end slope (α) becomes steeper, the characteristic luminosity (m^*) increases, and the overall normalization (ϕ^*) decreases.

local galaxies.

At the brightest absolute magnitudes, where the LBG V-band luminosity function is well constrained by our observations, the $z \sim 3$ LBG V-band luminosity function greatly exceeds the local function, and has a different shape. For this reason, we caution against over-interpreting the differences in the best-fit Schechter function parameters relative to other luminosity functions; for example, the very steep faint end slope, very bright value of M^*, and relatively low value of ϕ^* may well result from fitting the function over a small range of luminosity that does not actually extend as faint as the true "knee" in the luminosity distribution. In practice, it will be extremely difficult to extend this distribution to much fainter near-IR magnitudes from the ground, but it should be quite possible from space.

The obvious implication of the bright end of the V-band luminosity function of LBGs is that the mass-to-light ratio M/L_V of LBGs must be very different from that of galaxies in the local universe. Since the co-moving optical luminosity density in the $z \sim 3$ universe is evidently as large or larger than that in the $z \sim 0$ universe despite the fact that most of the stars observed in the local universe probably formed after $z \sim 3$, the V band light at $z \sim 3$ is apparently dominated by relatively massive stars associated with greatly enhanced current star-formation rates, and carries little information about total stellar mass. Unfortunately, this also means that no observations from the ground are likely to act as a direct proxy for stellar mass in objects that are actively forming stars at high redshift. Indeed, these observations, at 2.15 μm, are still dominated by the light from ongoing star-formation. In any case, *the V-band luminosity density of LBGs at $z \sim 3$ probably exceeds that of all stars in the present-day universe.*

Table 2.1. NIRC Lyman-Break Galaxy Fields

Field Name	Field Center (J2000)	Area ($\mathcal{R}$) (arc min)^2	Area (K_s) (arc min)^2	# Galaxies (K_s)	Area (J) (arc min)^2	# Galaxies (J)
CDFa	00 53 23.7 +12 34 00	78.42	1.72	7	1.18	5
Q0201	02 03 51.6 +11 34 09	75.77	1.35	3	1.21	3
Q0256	02 59 08.6 +00 11 41	72.28	1.17	6	...	...
B2 0902+34	09 05 30.2 +34 07 55	41.93	2.63	10	1.77	6
HDF	12 36 52.3 +62 12 59	75.32	2.96	14	2.29	10
WESTPHAL	14 17 14.5 +52 24 36	226.93	9.03	30	4.12	15
3C324	15 49 49.6 +21 29 07	44.29	1.85	6	0.56	2
SSA22a	22 17 34.2 +00 15 01	77.75	5.75	22	1.73	6
SSA22b	22 17 34.2 +00 06 18	77.60	0.59	2	...	...
DSF2237a	22 40 08.5 +11 52 34	83.38	0.64	1	0.61	1
DSF2237b	22 39 34.3 +11 51 44	81.62	2.43	17	1.71	15
TOTAL		935.29	30.12	118	15.18	63

Table 2.2. NIRC Observations and Integration Times

Pointing	Objects	Exposure (K_s) (sec)	Exposure (J) (sec)
CDFa-C8	C8,MD10	2400	···
CDFa-C1	C1,MD2	3780	1620
CDFa-C22	C22,M19,C19	3780	4620
Q0201-C6	C6,MMD21	3480	3780
Q0201-B13	B13	2700	2400
Q0256-M13	M13,C15,MD22	5220	···
Q0256-M17	M17,MD32,MD34	4260	···
B20902-C6	C6,M11,MD31	3780	3240
B20902-MD21	MD21	3240	3240
B20902-D11	D11,D12,MD32	1080	1620
B20902-MD11	MD11,MD14,MD18	2160	···
HDF-MM23	MM23,oC37,oMD49	6000	4680
HDF-DD15	DD15,MM28	3780	1620
HDF-CC24	CC24,oC38,oM5,MM25	2160	···
HDF-DD3	DD3,MM9,MM7	3120	3240
HDF-MM18	MM18,MM17	3240	3240
WESTPHAL-CC70	CC70,MM69,DD49	3240	3240
WESTPHAL-DD8	DD8,MMD14,MMD16,MM8	3240	3240
WESTPHAL-C11	C11	3240	···
WESTPHAL-CC13	CC13	2700	···
WESTPHAL-CC32	CC32,MMD53,MMD54	3240	···
WESTPHAL-CC79	CC79,MMD115	3000	···
WESTPHAL-MMD17	MMD17,MMD20,MM13	6420	2520
WESTPHAL-CC63	CC63,MMD91	3240	3180
WESTPHAL-MMD11	MMD11	1080	1620
WESTPHAL-CC1	CC1	3240	···
WESTPHAL-CC43	CC43,CC45,DD29	3180	3240
WESTPHAL-MMD109	MMD109,MMD112	1620	···
WESTPHAL-MMD113	MMD113,MMD111	1080	···
WESTPHAL-MMD23	MMD23,MM11	1620	···
3C324-C1	C1,C2,MD5	4200	···

Table 2.2 (cont'd)

Pointing	Objects	Exposure (K_s) (sec)	Exposure (J) (sec)
3C324-D7	D7,C12	1080	1380
3C324-C3	C3	1620	···
SSA22a-D14	D14,MD42,MD40,M31	1860	···
SSA22a-D3	D3,MD3	7800	2700
SSA22a-MD46	MD46,MD50	3360	···
SSA22a-aug96D1	aug96D1,M8	3780	···
SSA22a-C16	C16,M13,M11	3240	···
SSA22a-C36	C36	3240	3240
SSA22a-C6	C6,M4,MD4	6960	4860
SSA22a-blob1	C11,C15,M10	2160	···
SSA22a-blob2	M14,MD14	2160	···
SSA22b-oct96D8	oct96D8,MD11	2880	···
DSF2237a-C2	C2	1860	2700
DSF2237b-M20	M20,C26,M19,MD56,MD57,M17,M18	7380	7920
DSF2237b-MD2	MD2,MD10	3240	···
DSF2237b-D28	D28,MD81,MD80,C43	3240	3240
DSF2237b-D3	D3,D4,MD9,C1	6480	4860

Table 2.3. Lyman-Break Galaxy Optical/Near-IR Photometry

Object Name	RA (J2000)	Dec (J2000)	$\mathcal{R}_{\rm AB}$	$(G-\mathcal{R})_{\rm AB}$	$(\mathcal{R}_{\rm AB}-J_{\rm Vega})$	$(\mathcal{R}_{\rm AB}-K_{s\rm Vega})$	z
CDFa-C22	00 53 09.42	+12 36 00.5	23.97	0.73 ± 0.08	0.90 ± 0.50	3.18 ± 0.23	3.046
CDFa-M19	00 53 11.04	+12 36 12.3	25.29	0.84 ± 0.15	0.93 ± 0.75	$<$ 2.79	···
CDFa-C19	00 53 11.27	+12 35 39.9	24.63	0.81 ± 0.13	1.96 ± 0.30	3.79 ± 0.24	2.667
CDFa-C8	00 53 32.85	+12 32 11.4	23.72	0.96 ± 0.08	···	2.16 ± 0.40	3.071
CDFa-MD10	00 53 32.22	+12 31 56.3	25.42	0.48 ± 0.16	···	2.10 ± 0.60	···
CDFa-C1	00 53 34.74	+12 30 30.6	23.53	0.69 ± 0.06	1.29 ± 0.18	2.69 ± 0.21	3.110
CDFa-MD2	00 53 36.31	+12 30 31.2	23.88	0.75 ± 0.06	1.52 ± 0.23	2.96 ± 0.24	2.871
Q0201-C6	02 03 41.81	+11 34 41.5	23.92	0.62 ± 0.07	0.40 ± 0.55	2.39 ± 0.42	3.052
Q0201-MMD21	02 03 41.66	+11 34 44.8	24.67	0.51 ± 0.12	1.46 ± 0.47	2.72 ± 0.28	···
Q0201-B13	02 03 49.23	+11 36 10.8	23.34	0.03 ± 0.08	1.72 ± 0.13	2.81 ± 0.15	2.167
Q0256-C15	02 59 00.02	+00 11 38.6	24.23	0.69 ± 0.09	···	2.46 ± 0.46	3.385
Q0256-M13	02 58 58.83	+00 11 25.4	24.48	0.96 ± 0.12	···	2.89 ± 0.38	3.227
Q0256-M17	02 59 19.86	+00 12 32.4	24.04	1.10 ± 0.11	···	$<$ 1.54	···
Q0256-MD22	02 59 00.79	+00 11 40.3	24.54	0.74 ± 0.11	···	2.30 ± 0.51	···
Q0256-MD32	02 59 18.11	+00 12 41.5	23.61	0.89 ± 0.07	···	2.61 ± 0.25	···
Q0256-MD34	02 59 20.21	+00 13 02.9	24.02	0.72 ± 0.08	···	3.88 ± 0.14	···
B20902-D11	09 05 23.01	+34 09 40.1	22.97	0.29 ± 0.06	0.89 ± 0.27	2.97 ± 0.13	2.837
B20902-D12	09 05 23.45	+34 09 45.0	25.46	-0.12 ± 0.10	$<$ -0.23	$<$ 2.96	···
B20902-MD32	09 05 26.24	+34 09 28.8	24.03	0.73 ± 0.10	1.25 ± 0.37	2.52 ± 0.41	2.860
B20902-C6	09 05 20.58	+34 09 07.7	24.13	0.45 ± 0.08	0.73 ± 0.54	2.39 ± 0.45	3.098
B20902-M11	09 05 19.58	+34 09 04.0	24.19	1.18 ± 0.16	1.36 ± 0.43	2.82 ± 0.32	3.300
B20902-MD31	09 05 20.27	+34 09 29.6	24.74	0.55 ± 0.12	···	3.77 ± 0.24	···
B20902-MD21	09 05 20.08	+34 07 19.7	24.18	1.06 ± 0.16	1.03 ± 0.49	2.51 ± 0.32	3.017
B20902-MD11	09 05 35.20	+34 06 25.2	24.27	1.04 ± 0.16	···	2.22 ± 0.48	3.392

Table 2.3 (cont'd)

Object Name	RA (J2000)	Dec (J2000)	$\mathcal{R}_{\rm AB}$	$(G-\mathcal{R})_{\rm AB}$	$(\mathcal{R}_{\rm AB}-J_{\rm Vega})$	$(\mathcal{R}_{\rm AB}-K_{s\rm Vega})$	z
B20902-MD14	09 05 36.58	+34 06 37.0	24.68	0.97 ± 0.14	···	3.44 ± 0.28	···
B20902-MD18	09 05 35.23	+34 06 53.2	24.51	0.41 ± 0.12	···	$<$ 2.01	2.869
HDF-CC24	12 36 51.81	+62 15 16.3	24.33	0.76 ± 0.12	···	2.72 ± 0.40	3.333
HDF-DD3	12 36 47.60	+62 10 54.1	24.25	0.58 ± 0.09	1.45 ± 0.30	2.82 ± 0.32	2.942
HDF-DD15	12 36 48.97	+62 15 43.4	23.61	0.62 ± 0.07	0.36 ± 0.49	2.39 ± 0.37	3.135
HDF-MM7	12 36 47.75	+62 10 32.9	24.79	0.67 ± 0.17	1.02 ± 0.68	$<$ 2.29	2.985
HDF-MM9	12 36 51.45	+62 10 42.7	24.73	0.78 ± 0.16	···	4.04 ± 0.19	2.972
HDF-MM17[a]	12 36 47.67	+62 12 56.8	24.46	1.00 ± 0.15	1.52 ± 0.45	3.54 ± 0.25	2.931
HDF-MM18[b]	12 36 44.01	+62 13 11.9	24.10	1.00 ± 0.11	1.63 ± 0.21	3.46 ± 0.16	2.929
HDF-MM23	12 37 02.64	+62 14 27.0	24.61	1.09 ± 0.16	1.58 ± 0.47	3.65 ± 0.24	3.214
HDF-MM25	12 36 50.72	+62 14 45.6	24.82	0.74 ± 0.17	···	2.45 ± 0.57	3.105
HDF-MM28	12 36 46.64	+62 15 18.1	25.04	0.70 ± 0.18	1.01 ± 0.70	2.89 ± 0.53	3.371
HDF-oC37	12 37 03.18	+62 14 52.1	25.25	0.40 ± 0.16	0.99 ± 0.75	2.14 ± 0.40	2.925
HDF-oC38	12 36 48.81	+62 15 03.6	24.97	0.67 ± 0.18	-0.81 ± 0.61	3.47 ± 0.32	3.114
HDF-oMD49	12 37 04.25	+62 14 47.2	24.78	-0.09 ± 0.11	2.20 ± 0.24	4.21 ± 0.19	2.212
HDF-oM5	12 36 50.46	+62 14 45.5	24.98	0.93 ± 0.16	···	2.93 ± 0.53	3.097
WESTPHAL-CC79	14 17 13.70	+52 36 16.5	24.28	0.87 ± 0.14	···	3.17 ± 0.40	3.061
WESTPHAL-MMD115	14 17 15.48	+52 36 12.6	23.97	0.65 ± 0.11	···	1.62 ± 0.41	3.203
WESTPHAL-MMD109	14 17 27.43	+52 35 49.0	23.94	0.84 ± 0.11	···	3.05 ± 0.20	2.715
WESTPHAL-MMD112	14 17 26.57	+52 35 59.2	25.34	0.63 ± 0.20	···	$<$ 2.84	···
WESTPHAL-MMD113	14 18 24.85	+52 36 10.0	23.29	0.45 ± 0.08	···	2.71 ± 0.24	2.730
WESTPHAL-MMD111	14 18 23.71	+52 36 09.2	25.03	0.08 ± 0.15	···	3.22 ± 0.49	···
WESTPHAL-CC70	14 17 31.43	+52 34 25.6	23.75	0.55 ± 0.08	1.28 ± 0.24	2.41 ± 0.31	2.992
WESTPHAL-MM69	14 17 30.62	+52 34 17.2	25.24	0.83 ± 0.21	1.49 ± 0.57	3.24 ± 0.42	···

Table 2.3 (cont'd)

Object Name	RA (J2000)	Dec (J2000)	$\mathcal{R}_{\rm AB}$	$(G-\mathcal{R})_{\rm AB}$	$(\mathcal{R}_{\rm AB}-J_{\rm Vega})$	$(\mathcal{R}_{\rm AB}-K_{s\rm Vega})$	z
WESTPHAL-DD49	14 17 29.23	+52 34 31.5	23.50	0.17 ± 0.06	1.33 ± 0.18	3.35 ± 0.13	2.806
WESTPHAL-CC63	14 18 23.10	+52 32 46.9	23.50	1.14 ± 0.12	1.83 ± 0.14	2.60 ± 0.21	3.133
WESTPHAL-MMD91	14 18 22.93	+52 32 35.9	23.84	0.49 ± 0.09	1.11 ± 0.35	2.73 ± 0.32	2.738
WESTPHAL-CC43	14 17 25.47	+52 29 37.9	23.87	1.04 ± 0.15	1.24 ± 0.33	3.30 ± 0.16	3.081
WESTPHAL-CC45	14 17 27.68	+52 29 50.4	24.83	0.67 ± 0.18	1.59 ± 0.53	3.03 ± 0.41	2.758
WESTPHAL-DD29	14 17 25.92	+52 29 32.1	24.82	0.32 ± 0.13	1.60 ± 0.42	3.86 ± 0.24	3.240
WESTPHAL-CC32	14 18 14.45	+52 28 04.7	24.17	0.55 ± 0.11	···	2.40 ± 0.46	3.197
WESTPHAL-MMD53	14 18 12.63	+52 28 06.6	25.22	0.36 ± 0.16	···	3.98 ± 0.25	···
WESTPHAL-MMD54	14 18 14.46	+52 28 16.0	24.64	0.45 ± 0.13	···	2.98 ± 0.45	3.017
WESTPHAL-MMD23	14 17 21.95	+52 23 39.1	24.22	0.82 ± 0.14	···	2.81 ± 0.32	2.857
WESTPHAL-MM11	14 17 22.02	+52 23 27.0	25.24	0.61 ± 0.20	···	3.59 ± 0.32	···
WESTPHAL-CC13	14 18 02.47	+52 24 36.5	23.64	1.06 ± 0.14	···	2.42 ± 0.37	3.396
WESTPHAL-MMD17	14 18 09.56	+52 23 32.1	24.56	0.91 ± 0.17	2.04 ± 0.24	2.49 ± 0.55	2.869
WESTPHAL-MMD20	14 18 09.63	+52 23 37.2	24.59	0.63 ± 0.16	1.87 ± 0.30	2.15 ± 0.50	2.799
WESTPHAL-MM13	14 18 12.15	+52 23 30.4	25.40	0.69 ± 0.21	···	3.96 ± 0.27	2.856
WESTPHAL-west3-C11	14 18 17.63	+52 23 46.2	24.25	1.22 ± 0.16	···	2.69 ± 0.40	3.137
WESTPHAL-DD8	14 18 25.44	+52 23 22.4	24.47	0.68 ± 0.14	1.09 ± 0.56	2.77 ± 0.46	2.841
WESTPHAL-MMD14	14 18 24.72	+52 23 19.8	24.92	0.82 ± 0.20	1.62 ± 0.42	3.08 ± 0.41	···
WESTPHAL-MMD16	14 18 23.61	+52 23 28.8	24.73	0.92 ± 0.17	1.88 ± 0.30	4.06 ± 0.19	···
WESTPHAL-MM8	14 18 23.92	+52 23 07.7	24.13	1.04 ± 0.16	1.74 ± 0.21	3.25 ± 0.19	2.829
WESTPHAL-MMD11	14 18 09.73	+52 22 01.3	24.05	1.04 ± 0.16	2.67 ± 0.10	4.54 ± 0.11	2.979
WESTPHAL-CC1	14 18 21.98	+52 21 22.0	23.83	1.02 ± 0.15	···	2.78 ± 0.32	2.984
3C324-D7	15 49 52.96	+21 30 59.1	23.88	0.52 ± 0.08	0.78 ± 0.49	3.01 ± 0.20	···
3C324-C12	15 49 53.95	+21 31 06.7	25.04	0.54 ± 0.15	0.78 ± 0.71	3.34 ± 0.45	···

Table 2.3 (cont'd)

Object Name	RA (J2000)	Dec (J2000)	$\mathcal{R}_{\rm AB}$	$(G-\mathcal{R})_{\rm AB}$	$(\mathcal{R}_{\rm AB}-J_{\rm Vega})$	$(\mathcal{R}_{\rm AB}-K_{s\rm Vega})$	z
3C324-C3	15 49 47.10	+21 27 05.5	24.14	0.85 ± 0.13	···	2.57 ± 0.41	3.283
3C324-C1	15 49 54.27	+21 26 33.2	24.33	0.62 ± 0.14	···	3.12 ± 0.26	2.873
3C324-C2	15 49 53.98	+21 26 35.6	24.26	0.54 ± 0.10	···	3.19 ± 0.26	2.880
3C324-MD5	15 49 54.46	+21 26 34.6	25.48	-0.08 ± 0.24	···	3.93 ± 0.27	···
SSA22a-MD46	22 17 27.28	+00 18 09.9	23.30	0.42 ± 0.09	···	2.34 ± 0.29	3.090
SSA22a-MD50	22 17 26.83	+00 18 30.2	25.18	0.20 ± 0.17	···	3.18 ± 0.47	···
SSA22a-D14	22 17 35.29	+00 17 24.1	24.32	0.19 ± 0.14	···	2.07 ± 0.46	3.018
SSA22a-MD42	22 17 35.83	+00 17 19.8	25.33	0.06 ± 0.17	···	4.04 ± 0.25	···
SSA22a-MD40	22 17 35.96	+00 17 08.3	24.89	0.70 ± 0.19	···	2.21 ± 0.57	3.015
SSA22a-M31	22 17 36.87	+00 17 12.4	25.41	0.42 ± 0.18	···	3.22 ± 0.44	···
SSA22a-C36	22 17 46.10	+00 16 43.1	24.06	0.78 ± 0.13	1.23 ± 0.37	3.07 ± 0.23	3.065
SSA22a-C16	22 17 31.96	+00 13 16.1	23.64	0.98 ± 0.10	···	2.86 ± 0.20	3.061
SSA22a-M13	22 17 31.46	+00 12 55.2	25.46	0.74 ± 0.24	···	< 2.96	···
SSA22a-M11	22 17 31.77	+00 12 51.3	25.35	0.50 ± 0.18	···	< 2.85	···
SSA22a-M14	22 17 39.05	+00 13 30.1	25.47	0.75 ± 0.24	···	2.99 ± 0.62	3.091
SSA22a-MD14	22 17 37.93	+00 13 44.2	24.14	0.86 ± 0.14	···	1.96 ± 0.43	···
SSA22a-C11	22 17 25.68	+00 12 35.3	24.20	0.47 ± 0.12	···	2.82 ± 0.32	3.108
SSA22a-C15	22 17 26.12	+00 12 55.3	25.19	0.55 ± 0.19	···	3.50 ± 0.32	3.092
SSA22a-M10	22 17 26.79	+00 12 21.1	24.45	1.03 ± 0.18	···	2.32 ± 0.51	3.098
SSA22a-aug96D1	22 17 24.00	+00 12 02.8	23.60	0.32 ± 0.09	···	2.79 ± 0.12	2.202
SSA22a-M8	22 17 25.11	+00 11 56.8	24.72	0.89 ± 0.19	···	3.64 ± 0.24	···
SSA22a-D3	22 17 32.42	+00 11 33.0	23.37	0.97 ± 0.10	-0.60 ± 0.40	2.24 ± 0.32	3.086
SSA22a-MD3	22 17 31.89	+00 11 38.3	24.60	0.15 ± 0.13	1.40 ± 0.47	2.17 ± 0.50	2.483
SSA22a-C6	22 17 40.93	+00 11 26.0	23.44	0.79 ± 0.09	0.36 ± 0.44	2.01 ± 0.37	3.099

Table 2.3 (cont'd)

Object Name	RA (J2000)	Dec (J2000)	$\mathcal{R}_{\rm AB}$	$(G-\mathcal{R})_{\rm AB}$	$(\mathcal{R}_{\rm AB}-J_{\rm Vega})$	$(\mathcal{R}_{\rm AB}-K_{s\rm Vega})$	z
SSA22a-M4	22 17 40.92	+00 11 27.9	24.83	0.76 ± 0.19	0.93 ± 0.68	2.68 ± 0.56	3.091
SSA22a-MD4	22 17 39.95	+00 11 39.6	24.25	0.24 ± 0.12	1.03 ± 0.49	2.92 ± 0.32	2.611
SSA22b-MD11	22 17 23.07	+00 03 42.2	25.23	0.37 ± 0.15	···	3.14 ± 0.47	···
SSA22b-oct96D8	22 17 23.52	+00 03 57.3	23.53	0.77 ± 0.08	···	2.87 ± 0.18	3.323
DSF2237a-C2	22 40 08.30	+11 49 04.9	23.55	1.13 ± 0.10	1.47 ± 0.20	3.02 ± 0.17	3.318
DSF2237b-D28	22 39 20.25	+11 55 11.4	24.46	0.32 ± 0.08	1.34 ± 0.49	2.42 ± 0.52	2.934
DSF2237b-MD81	22 39 21.72	+11 55 10.5	24.16	0.31 ± 0.07	2.23 ± 0.17	4.27 ± 0.14	2.819
DSF2237b-MD80	22 39 22.23	+11 55 08.3	25.37	0.94 ± 0.20	1.16 ± 0.77	3.08 ± 0.37	···
DSF2237b-C43	22 39 21.57	+11 54 44.9	24.35	0.70 ± 0.11	1.73 ± 0.34	< 1.85	2.885
DSF2237b-M20	22 39 38.88	+11 52 22.1	24.20	1.12 ± 0.13	1.33 ± 0.43	2.96 ± 0.20	3.156
DSF2237b-C26	22 39 38.02	+11 52 11.4	24.73	0.57 ± 0.12	1.03 ± 0.60	2.64 ± 0.50	3.251
DSF2237b-M19	22 39 38.04	+11 52 20.6	24.80	0.96 ± 0.18	1.47 ± 0.53	2.79 ± 0.56	3.259
DSF2237b-MD56	22 39 39.00	+11 52 19.2	25.43	0.65 ± 0.17	1.81 ± 0.41	3.10 ± 0.39	···
DSF2237b-MD57	22 39 39.92	+11 52 27.2	24.56	0.73 ± 0.13	0.95 ± 0.66	2.51 ± 0.55	···
DSF2237b-M17	22 39 39.87	+11 52 06.5	24.67	1.03 ± 0.18	1.06 ± 0.60	2.53 ± 0.55	···
DSF2237b-M18	22 39 40.16	+11 52 16.0	25.33	0.76 ± 0.16	0.78 ± 0.72	< 2.83	···
DSF2237b-MD2	22 39 29.89	+11 47 12.5	24.17	0.90 ± 0.12	···	2.28 ± 0.36	2.505
DSF2237b-MD10	22 39 30.58	+11 47 34.3	25.04	1.01 ± 0.19	···	2.87 ± 0.53	3.115
DSF2237b-D3	22 39 18.91	+11 47 40.4	24.19	0.51 ± 0.09	1.07 ± 0.49	2.02 ± 0.37	2.931
DSF2237b-D4	22 39 18.75	+11 47 40.5	24.35	0.17 ± 0.10	1.13 ± 0.56	2.20 ± 0.29	2.935
DSF2237b-MD9	22 39 17.68	+11 47 39.2	24.97	0.45 ± 0.07	0.31 ± 0.56	< 2.47	···
DSF2237b-C1	22 39 16.90	+11 47 47.5	24.99	0.37 ± 0.12	1.60 ± 0.51	2.95 ± 0.32	3.064

[a]This galaxy is in the central Hubble Deep Field (HDF), and is referred to as "4-52.0" in Williams et al. (1996) and "HDF/NIC 813/814" in Papovich et al. (2001).

[b] This galaxy is in the central HDF, and is referred to as "1-54.0" in Williams et al. (1996) and "HDF/NIC 522" in Papovich et al. (2001).

Chapter 3

The Stellar Populations of Lyman Break Galaxies

3.1 Introduction

Given photometry that extends from $\sim 900 - 5500$ Å in the rest-frame for a reasonably large sample of $z \sim 3$ LBGs, it is of interest to use the data to constrain the star-formation histories and extinction properties of the galaxies with reference to models. Because the galaxy luminosity at even the longest wavelengths observed in our sample is still dominated by stars with small mass-to-light ratios, it is impossible to constrain the integrated stellar mass of galaxies without understanding something about the star-formation history. As it turns out, our sensitivity to the star-formation history using optical and near-IR data is coarse, at best—at the corresponding rest-frame far-UV to optical wavelengths, active star-formation can easily mask the evidence for previous generations of stars (e.g., Papovich et al., 2001), and dust extinction has a significant effect on the emergent SED. In order to interpret the color information of the LBGs in terms of interesting constraints on physical parameters, we must rely on models of both dust extinction *and* the intrinsic spectral energy distributions of stellar populations as a function of metallicity, initial mass function (IMF), star-formation history, and age. There is a large range of possible parameterizations of the extinction law and the intrinsic stellar population, and in general these cannot be well-constrained independently from fits to the galaxy SEDs. Consequently, in what follows, we adopt simple models for the attenuation law, and for the metallicity, IMF, and star-formation history of the stellar population, which external observations have shown to be reasonable for star-forming galaxies in the nearby and high redshift universe. Where relevant, we point out where different assumptions yield significantly different results. Extensive grids of models have been fitted to (generally fainter) LBGs observed in the HDF-North by Papovich et al. (2001); we refer the reader to that paper for a more detailed discussion of the effects of varying the modeling assumptions.

3.2 Age-Dust Degeneracy

With only optical (U_n, G, $\mathcal{R}$, and I) photometry for $z \sim 3$ galaxies, it is not possible to distinguish between a young galaxy spectral energy distribution ($\leq$ 30 Myr) which is considerably reddened by dust, and the spectral energy distribution of a galaxy which has been continuously forming stars over a much longer timescale ($\sim$ 1 Gyr), but with much less dust extinction (Sawicki & Yee, 1998). Figure 3.1 shows the results of fitting only the $G - \mathcal{R}$ color of the galaxy 3C324-C2 with Bruzual & Charlot (1996) constant star-formation galaxy spectral templates of different ages. As the template age increases, the amount of dust reddening necessary to fit the observed $G - \mathcal{R}$ color decreases. Both the 1 Myr model with $A_{1600} = 2.84$ and the 1 Gyr model with $A_{1600} = 1.61$ fit the observed optical photometry equally well (where A_{1600} is magnitudes of extinction at 1600 Å rest-frame). Indeed, the model rest-frame UV slope can be modified to match the observed (U_n, G, $\mathcal{R}$, I) colors, by simultaneously tuning its age and dust-content. The degeneracy results from the fact that, at $z \sim 3$, commonly used optical filters probe a short-wavelength region of the rest-frame spectrum which does not contain any age-sensitive features that can be easily recognized from broadband photometry. However, there is an age-sensitive break in the spectral energy distributions of actively star-forming galaxies that occurs near 3648 Å, often referred to as the "Balmer break." The Balmer break feature, which is age sensitive over star-formation timescales of $\sim$ 50 Myr$-$1 Gyr, cannot be described equally well by any combination of stellar population aging and dust-content. Longer wavelength photometry which includes the discontinuity can in principle be used to break the degeneracy between model fits.

The Balmer break feature in galaxy spectra is due to the stellar bound-free absorption coefficient, which has a sharp edge at 3648 Å, (the wavelength of the $n = 2 \longrightarrow$ *continuum* transition in neutral hydrogen), causing photons with wavelengths shortward of the edge to be absorbed much more efficiently than those with longer wavelengths. The prominence of this feature in a stellar spectrum depends on the temperature and gravity of the stellar atmosphere, which determines the form of hydrogen that is prevalent in the stellar atmosphere, and therefore which component of the total stellar absorption coefficient is dominant. In cooler late-type stars (such as F, G, and K), H^- opacity dominates the total absorption coefficient, and the Balmer decrement is not very pronounced. In the early-type massive O and B stars the high temperatures result in the increased ionization of hydrogen, so again, the Balmer absorption coefficient is reduced. The Balmer break is most prominent in A-stars with temperatures around $10,000^\circ$K (Gray, 1976).

At the onset of star-formation, a galaxy spectrum is dominated in the rest-frame UV and blue by the most-massive (O and B) stars, most of which have lifetimes shorter than 10 Myr. In a continuous star-formation model, after roughly 10 Myr, the rate at which O stars are being formed balances the rate at which they are dying, and the number of O stars levels off to a constant value (Leitherer

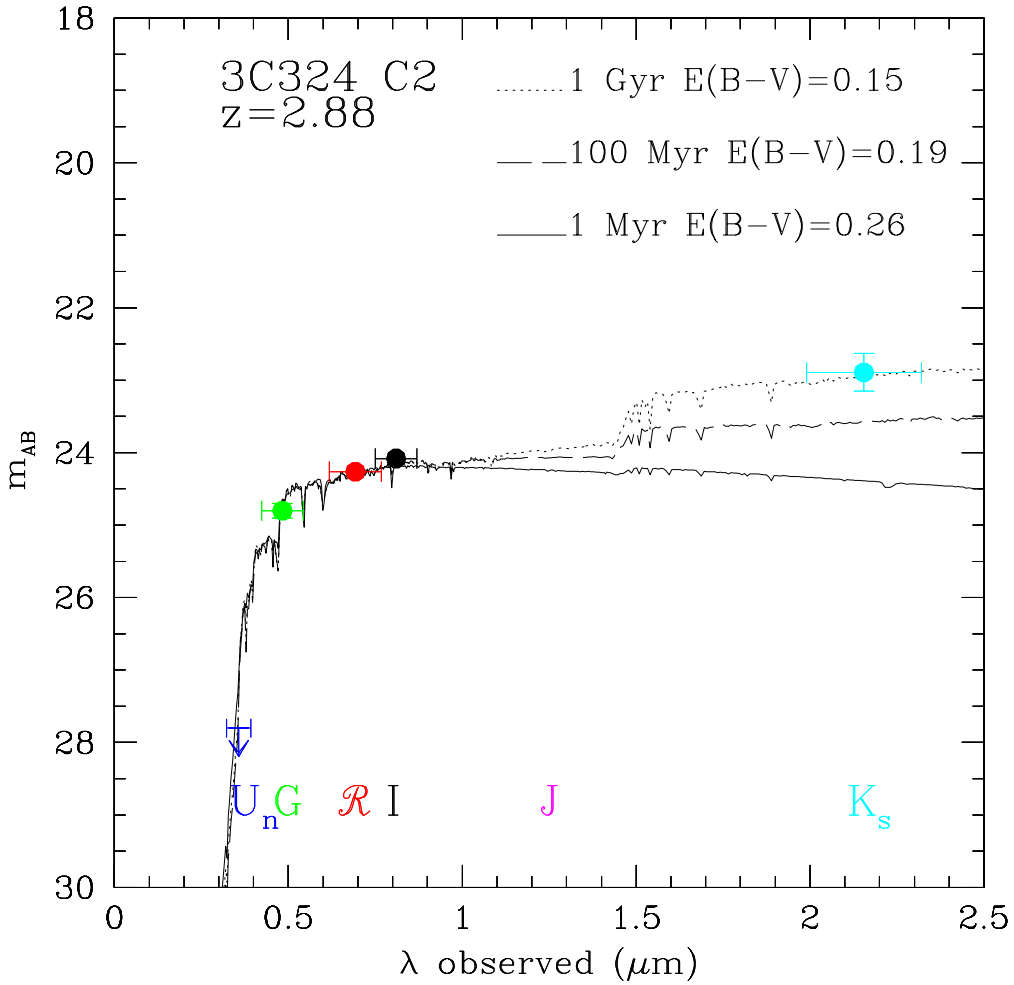

Figure 3.1 The Age-Dust Degeneracy. The points indicate the observed spectral energy distribution of 3C324-C2, a LBG at $z = 2.880$. Shown with the points are BC96 constant star-formation models of different ages, modified by the amount of dust extinction required to reproduce the observed $G - \mathcal{R}$ color. The dotted line is a 1 Gyr model with $E(B - V) = 0.149$; the dashed line is a 100 Myr model with $E(B - V) = 0.186$; and the solid line is a 1 Myr model with $E(B - V) = 0.263$. All of these models describe the observed optical photometry equally well. However, only the 1 Gyr model successfully describes the the observed $\mathcal{R} - K_s$ color.

et al., 1999). Meanwhile, the lifetimes of less massive A stars range from several hundred Myr to 1 Gyr. Therefore, as the O star population levels off, the number of A stars continues to increase. At the age where the increasing number of A stars relative to the constant number of O stars causes the galaxy spectrum at ~ 3600Å to be dominated by an A-star spectrum, we start to see an increasing Balmer break in the galaxy spectrum. After 100 Myr the magnitude difference on either side of the Balmer break in an unreddened galaxy model is 0.3 mag, and by 1 Gyr, the break has increased to a 0.6 magnitudes.

Thus, the strength of the Balmer break can be used as a rough guide to the duration of the current episode of star-formation on timescales $\lesssim 1$ Gyr. The details will depend on the star-formation history (e.g., whether the star-formation rate (SFR) is an increasing, or declining, function of time), the shape of the initial mass function, and the metallicity of the stellar population. Because the Balmer break even at its strongest is a relatively subtle spectral feature, and because only broadband photometry is available for the galaxies, a measurement of the Balmer break strength requires removing the effects of continuum reddening. This requirement introduces some covariance into the simultaneous estimates of extinction and the age of the star-formation episode; we discuss this covariance extensively in § 3.4.2.

3.3 Population Synthesis Modeling

3.3.1 Spectroscopic Sample

In order to examine the range of stellar population properties present in the NIRC sample of LBGs, we considered only the subsample of galaxies with measured redshifts and near-IR detections at least in K_s. The spectroscopic sample so defined consists of 81 galaxies. We included the $G - \mathcal{R}$, $\mathcal{R} - J$, and $\mathcal{R} - K_s$ colors of these galaxies in the modeling; the U_n band is strongly affected by H I absorption in both the galaxy and the IGM. A substantial fraction of the spectroscopic sample also has available I band photometry, but for these high redshift objects the I band adds little information because of its proximity to $\mathcal{R}$ and because the measurements are generally noisier than in other bands. Nevertheless, U_n and I data points (when they exist) are included in figures indicating the best-fit spectral template with respect to the observed LBG photometry,

The model galaxy templates used to fit the LBG photometry include no Lyman α emission, and typically contain Lyman α absorption with observed equivalent widths of $40 - 60$ Å ($10 - 15$ Å in the rest frame). However, the sample of LBGs for which there are rest-frame UV spectra exhibit a wide range of Lyman α equivalent widths, some of which are ten times larger than the model line widths, and appear in either absorption, emission, or a combination of both. The *observed* Lyman α equivalent width was used to correct the $G - \mathcal{R}$ color for line emission for each of the 81 galaxies in the spectroscopic sample. Figure 3.2 displays the distribution of Lyman α observed equivalent

widths for the LBGs with both NIRC data and Keck LRIS spectra (cf. Steidel et al., 2000).

Nebular line emission redshifted into the K_s-band might also bias the results of population synthesis modeling. The [OIII] $\lambda 5007, 4959$ Å doublet and Hβ $\lambda 4861$ Å line all fall within the K_s-band window for $z \geq 3.094$. In the NIRC LBG spectroscopic sample, 49 out of 81 galaxies (60%) have $z \geq 2.974$ such that at least [OIII] $\lambda 5007$ Å, the strongest of the three lines, is located within the K_s-band. Nebular line strengths have been measured for only a small sample of LBGs at the current time (see Pettini et al., 2001), nine of which are in the NIRC sample. The combined equivalent width from all the nebular lines affecting the K_s magnitude was calculated by comparing the line fluxes from Pettini et al. (2001) to the continuum flux, measured with NIRC. For each galaxy, the total nebular equivalent width in the K_s filter was compared to the effective width of the K_s filter, $\Delta\lambda(K_s)_{eff} = 3300$ Å, to evaluate the necessary correction to the K_s magnitude and $\mathcal{R} - K_s$ color. In every case, the indicated corrections for nebular emission reduce the K_s continuum flux, resulting in a bluer $\mathcal{R} - K_s$ color. The $\mathcal{R} - K_s$ corrections ranged from $0.03 - 0.27$ magnitudes with a median $\Delta(\mathcal{R} - K_s) = 0.14$ mag.

In order to determine the effect of these $\mathcal{R} - K_s$ color corrections on best-fit model parameters, we fit Bruzual & Charlot (1996) constant star-formation models to the colors of the nine galaxies with measured nebular equivalent widths. Models were fit to both the uncorrected colors and the colors corrected for nebular line emission. The $\mathcal{R} - K_s$ correction resulted in little or no change to the best-fit $E(B-V)$ value (since most of the lever arm for extinction estimation comes from the rest-UV data). The effect on the best-fit age was more significant, in that the nebular line correction will result in a systematically younger inferred age. The median correction for the nebular line contamination results in stellar population ages that are $\sim$35% younger than if no corrections for line emission are applied. It should be emphasized that nebular line contamination is negligible for the 40% of the spectroscopic NIRC sample with $z < 2.974$. With such a small subsample having near-IR spectroscopy at the time of this writing, there is not enough information available to determine how corrections for emission line contamination should be implemented for objects without near-IR spectroscopic measurements. We have chosen, therefore, not to apply these corrections, but to emphasize that in some cases the inferred ages may be influenced by the emission line contamination of the broadband K_s measurements.

3.3.2 Modeling Procedure

The two main theoretical elements which we used were (1) model galaxy spectra generated with the Bruzual & Charlot (1996, hereafter BC96) population synthesis code, and (2) a dust effective attenuation law empirically derived by Calzetti (1997) for local starbursts. [1] There are few con-

[1]The Calzetti attenuation law relates the observed flux, F_λ, in units of ergs s^{-1}Å^{-1}, to the intrinsic flux, $F_{0\lambda}$, with the relation: $F_\lambda = F_{0\lambda} 10^{-0.4E(B-V)k(\lambda)}$, where $k(\lambda)$ is a decreasing function of wavelength, reflecting the fact

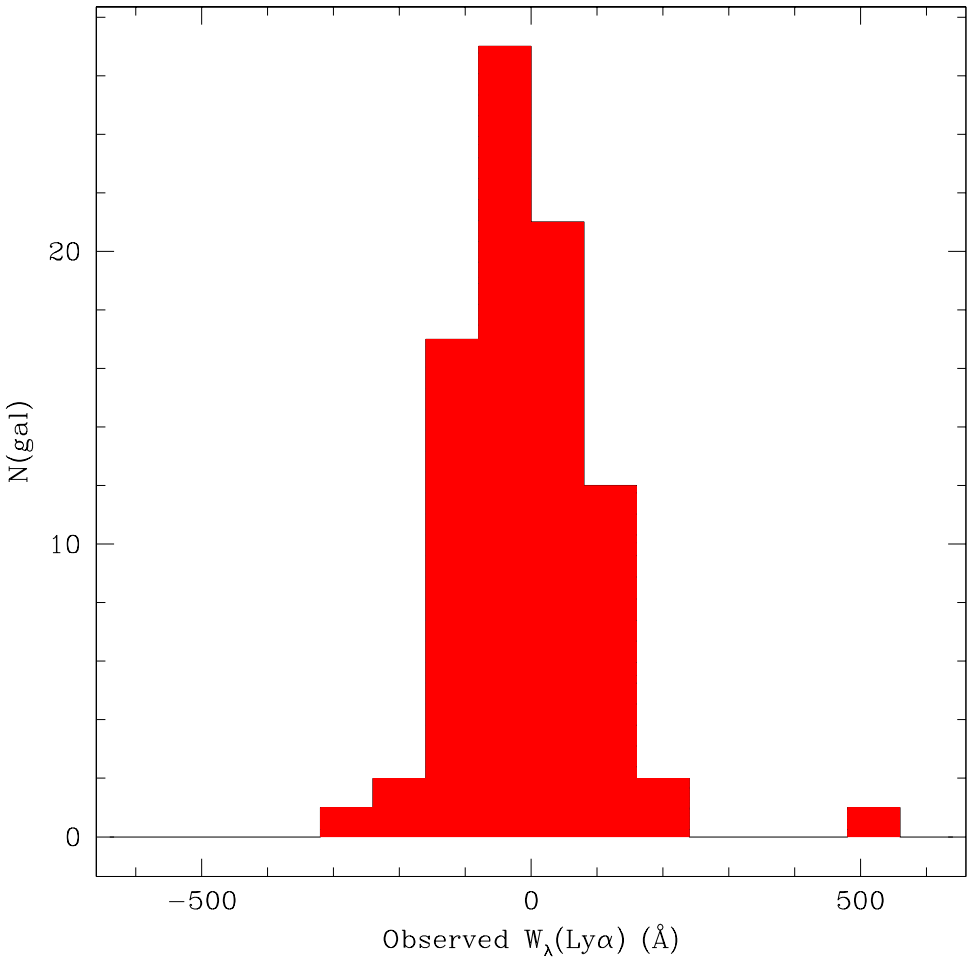

Figure 3.2 The distribution of observed Lyman α equivalent widths. The median equivalent width is 0. However, there are extreme cases of observed equivalent widths greater than 300 Å in either emission or absorption. If unaccounted for, such large equivalent widths would bias the modeling of the stellar population—especially the estimate of the dust extinction, but, to a certain extent, the age as well.

straints on the appropriate reddening model to use for high redshift star forming galaxies, and so we have adopted the form that works quite well for local starburst galaxies, which are arguably the best local analogs of LBGs. The validity of this reddening/extinction law at high redshift has yet to be tested adequately, due to the difficulty in measuring bolometric star-formation luminosities at high redshift (see AS2000; Meurer et al., 1999). We simply use it as the most realistic representation of the attenuation in $z \sim 3$ LBGs; we will briefly discuss how the results depend on the assumed attenuation law in § 3.4.2.

At the time this work began, the newest Bruzual and Charlot software available to us was the BC96 version, so that the results discussed in detail are based on BC96 model fits. In order to verify that the population synthesis fits did not change significantly with the most recent version of the Bruzual and Charlot package, BC2000 (Charlot 2000, private communication; Liu et al., 2000), we compared the BC96 and BC2000 results for a subset of models. BC96 results were also compared with those from the Starburst99 models (Leitherer et al., 1999).

Models with both solar and sub-solar metallicity were fit to the observed colors of LBGs, but we discuss results for only solar metallicity models. Recent measurements of LBG metallicities are not very well constrained, ranging from $0.1 - 0.5 Z_{\odot}$ (Pettini et al., 2001), indicating that these galaxies are more metal-rich than Damped Lyman α systems at the same redshift, but have slightly lower metallicites than H II regions in the Milky Way near the Sun. Even so, we prefer to use solar metallicity stellar models, since they are the only models which have been directly calibrated against empirical stellar spectra of many spectral types. Specifically, in the grid of theoretical stellar spectra compiled by Lejeune & Cuisinier (1996); Lejeune et al. (1997), which was used for the BC96 modeling, the only spectra which have been extensively tested against empirical stellar spectra are those with solar abundance. Papovich et al. (2001) report that the effects of using $0.2\ Z_{\odot}$ rather than solar metallicity models to fit LBG colors include best-fit ages systematically younger by a factor of 2, best-fit UV extinction factors systematically higher by a factor of 3, and derived stellar masses smaller by a factor of 2. These effects stem from the fact that the uncalibrated sub-solar metallicity models have intrinsically bluer UV continuum slopes and slightly larger Balmer breaks than solar metallicity models, for a given stellar population age. However, Leitherer et al. (2001) recently presented observations of O stars in the Large and Small Magellanic clouds with an average metallicity of $Z = \frac{1}{4} Z_{\odot}$, showing that metallicity does not have very drastic effects on the empirical rest-frame UV spectra of hot stars. Leitherer et al. concluded that modeling the spectra of $\sim \frac{1}{4} Z_{\odot}$ galaxies with solar metallicity models is an approximately valid approach. Until theoretical stellar libraries are updated with empirically calibrated sub-solar metallicity models of many spectral types, we believe that solar metallicity models are preferable.

that shorter wavelengths suffer more extinction than longer wavelengths. The attenuation curve is parameterized by an overall normalization, $E(B-V)$.

For all of the BC96 models, a Salpeter IMF extending from $0.1M_{\odot}$ to $125M_{\odot}$ was assumed. Papovich et al. (2001) have investigated the effects of varying the IMF on the estimated stellar population parameters. Acceptable model fits are obtained for IMFs with various slopes and lower mass cutoffs, with slightly different results. For example, use of the steeper Scalo IMF results in younger ages, lower attenuation values, higher star-formation rates, and larger formed stellar masses. The effect of changing the IMF on the formed stellar mass is small, however, compared with the associated uncertainties. We choose not to include the form of the IMF as another parameter in our model, although clearly the shape of the IMF, if allowed to vary arbitrarily, can have a very significant effect on the stellar population parameters.[2]

Evolutionary tracks distributed by the "Padova School" (the default for BC96) were used to describe the evolution of all the formed stars through the H-R diagram. Several different simple star-formation histories were considered: a continuous star-formation rate, $\Psi(t) = \Psi_0$; and exponentially declining star-formation rates, $\Psi(t) = \Psi_0 \exp(-t/\tau)$, with $\tau = 100, 50, 10$ Myr. The set of time constants, τ, was chosen to span the range between the two extremes of an instantaneous burst and continuous star-formation. For each star-formation history, two parameters were allowed to vary: 1) the *extinction*, parameterized by $E(B-V)$, and 2) the *age* since the onset of the most recent episode of star-formation, t_{sf}.

The model dust-attenuated, rest-frame galaxy spectra were shifted to the measured redshift of the actual galaxy, and further attenuated in a manner simulating absorption by the intergalactic medium of neutral hydrogen (Madau, 1995). Each internally reddened, redshifted, IGM-absorbed galaxy spectrum was then integrated through the ($G, \mathcal{R}$, J, and K_s) filter transmission curves to calculate its predicted colors. For each $(E(B-V), t_{sf})$ combination, the predicted ($G-\mathcal{R}$, $\mathcal{R}-J$, and $\mathcal{R}-K_s$) colors were compared with the observed colors using the χ^2 statistic. The best-fit $(E(B-V), t_{sf})$ combination was chosen to minimize χ^2, and the intrinsic instantaneous star-formation rate was determined by normalizing the best-fit model to the observed $\mathcal{R}$ magnitude (taking into account the best-fit extinction). By our definition, the "formed stellar mass" m_{star} is simply the integral of the star-formation rate and the age of the star-formation episode obtained from the best-fit model.

Once the best-fit $E(B-V)$, t_{sf}, $\Psi(t_{sf})$, and m_{star}, were obtained for the galaxies in the spectroscopic sample, we computed the 68.3% and 90% confidence intervals associated with each parameter. For each galaxy we generated a large sample of fake "observed" colors, by perturbing the observed colors in a manner consistent with the photometric errors. We assumed the errors were Gaussian, based on the results of Monte Carlo simulations (§ 2.2.4). We also assumed that the color errors were uncorrelated, a valid assumption given that the near-IR uncertainties tend to be much larger

[2]An analysis of the gravitationally-lensed LBG MS 1512-cB58 by Pettini et al. (2000) has shown that a Salpeter IMF is very successful in reproducing the details of the far-UV spectrum.

than the $\mathcal{R}$ uncertainty. The large sample of fits to the perturbed colors indicated the region of $(E(B-V), t_{sf}, \Psi(t_{sf}), m_{star})$ parameter space allowed by each galaxy's observed colors and photometric uncertainties.

3.3.3 Comparison of Models

As described above, a range of BC96 star-formation histories was considered, and the differences between BC96, BC2000, and Starburst99 were investigated. For the purpose of this analysis, and given our relatively large photometric uncertainties, the BC96 and BC2000 model fits are virtually indistinguishable. For the solar metallicity constant star-formation models, the BC2000 model SEDs have slightly bluer rest-frame far-UV slopes and slightly larger Balmer breaks than the BC96 SEDs for a given star-formation history. Therefore, best-fit ages from BC2000 are typically 70% as old, while extinction values are larger ($\Delta E(B-V) \lesssim 0.06$). The BC2000 best-fit extinction-corrected star-formation rates $\Psi(t_{sf})$ are typically 25% larger than in the BC96 models, and so the BC2000 m_{star} is typically 85% of the BC96 m_{star}. These differences are insignificant, given the large confidence intervals allowed for the best-fit and derived parameters for any given set of models.

The differences between the BC96 and the Starburst99 constant star-formation models were also explored. The Starburst99 models use stellar evolutionary tracks from the "Geneva School," and the model atmosphere grid of Lejeune et al. (1997). For the sake of consistency, we chose solar metallicity Starburst99 templates with a Salpeter IMF, which we re-normalized by roughly a factor of 0.5 in luminosity, to remove the effects of the larger minimum mass cutoff in the Starburst99 Salpeter IMF ($1\ M_{\odot}$). As in the case of BC2000, the Starburst99 best-fit $E(B-V)$ and t_{sf} parameters tended towards younger ages (45% of the BC96 t_{sf}), and slightly larger values of $E(B-V)$, ($0 < \Delta E(B-V) \leq 0.07$). The higher $E(B-V)$ values in the Starburst99 fits lead to extinction-corrected $\Psi(t_{sf})$ values which are 65% larger than the BC96 values on average, and therefore the m_{star} values for the Starburst99 models were typically 70% of the BC96 m_{star} values. The differences between the BC96 and Starburst99 $E(B-V)$ and t_{sf} parameters are also small compared with the allowed confidence intervals.

For all three sets of models: BC96, BC2000, and Starburst99, the relative ordering of $E(B-V)$ and t_{sf} is preserved—galaxies best described by higher $E(B-V)$ [t_{sf}] in the BC96 models also have higher $E(B-V)$ [t_{sf}] according to the Starburst99 and BC2000 models. Finally, we note that for each galaxy in our sample, the BC96, BC2000, and Starburst99 constant star-formation models all provide statistically indistinguishable fits—i.e., there are no cases where one set of models has significantly lower χ^2 values than the others. Evidently, even for identical star-formation histories, there are significant differences in the predictions of each of the models that can amount to a factor of 2 in inferred age and a factor somewhat less than 2 in formed stellar mass. Thus, it would be a mistake to take the results from any of the models as anything but approximate until both the

models and the data improve.

The model results for different BC96 star-formation histories were also compared in detail. We did not consider a very large number of star-formation histories, but enough to bracket a range of star-formation decay time (τ) parameter space. For the majority of the galaxies successfully modeled, *all* of the star-formation histories considered yielded best-fit models with χ^2 values allowed at the 90% level. For 8 of the galaxies we were able to rule out the models with time constants smaller than $\tau = 100$ Myr—this subsample is comprised of galaxies which are simultaneously blue in $G - \mathcal{R}$ and red in $\mathcal{R} - K_s$, and which have among the largest inferred continuous star-formation ages.

For the rest of the galaxies, whose star-formation histories cannot be usefully constrained, the best-fit $E(B-V)$ and, especially, t_{sf}, parameters demonstrate quite a large spread depending on which star-formation history is chosen to fit the photometry. In contrast, the formed stellar mass, m_{star}, derived from such best-fit parameters is a more robust quantity (e.g., Papovich et al., 2001). We investigated the m_{star} implied by each best-fit $(E(B-V), t_{sf})$ combination as a function of star-formation history, and find that for the $\tau = 100\,\mathrm{Myr}$ and $\tau = 50\,\mathrm{Myr}$ models, the m_{star} derived is typically within a factor of 2 of the m_{star} derived for the constant star-formation model. For the $\tau = 10\,\mathrm{Myr}$ models (these are effectively equivalent to an "instantaneous burst" model), the derived m_{star} is typically a factor of four smaller than the constant star-formation prediction—this relatively large difference is caused mostly by the degeneracy between an aging starburst and one which is relatively strongly reddened by dust. Star-formation histories with star-formation rates that are *increasing* functions of time pose even more significant problems for the models; for example, Papovich et al. (2001) have shown that an underlying maximally old stellar population (hidden by the most recent episode of star-formation) can contain up to $5\times$ the stellar mass derived from the rest-frame UV/optical SED. In this sense, as emphasized by Papovich et al., the inferred m_{star} based on the modeling should be treated as lower limits on the total stellar mass of the galaxies.

In short, broadband photometry is not particularly effective in constraining star-formation histories—the root cause of this problem is that the far-UV flux is determined solely by the instantaneous rate of O and B star-formation, whereas the rest-frame optical flux is dominated by previous star-formation if the SFR is declining, and by the instantaneous star-formation if the rate is increasing. There is of course no good *a priori* reason to favor declining star formation rates over increasing ones. The simplest assumption is that the observed instantaneous star-formation rate is representative of the rate since the onset of the current episode of star-formation. Under these simplifying assumptions, short-lived "bursts" of star-formation for which the SFRs are much higher than the past average, will appear "young," and protracted periods of star-formation with relatively constant SFRs on timescales $\gtrsim 100$ Myr will have significant Balmer breaks that can be recognized in the broadband photometry.

We summarize the best-fit and derived parameters for each galaxy assuming the BC96 constant star-formation models in Table 3.1. In Figure 3.3, the measured photometry for three NIRC LBGs is plotted along with the best-fit constant star-formation models for the galaxies. These examples demonstrate the range of stellar population parameter space which is probed with NIRC LBGs. Figure 3.4 shows the $E(B-V)-t_{sf}$ confidence regions for these three galaxies.

3.3.4 Anomalous Galaxies

Most of the NIRC LBG spectroscopic sample was adequately described by the simple models detailed above. Statistically acceptable fits were obtained for 74 of the 81 LBGs in the NIRC sample with redshifts. Three of the remaining seven galaxies have suspect J and K_s photometry upon closer inspection,[3] and fourth galaxy has a clear Seyfert-2-like spectrum. The remaining galaxies have colors that defy the simple models considered above. Two of the most anomalous galaxies are Westphal-MMD11 and DSF2237b-MD81. MMD11 and MD81 are the two reddest galaxies in $\mathcal{R}-K_s$ and $\mathcal{R}-J$ in the entire NIRC LBG sample, with $\mathcal{R}-K_s$ colors of 4.54 and 4.27, respectively, and $\mathcal{R}-J$ colors of 2.67 and 2.23. MMD11 is also in the reddest quartile of IGM-absorption-corrected $G-\mathcal{R}$ measurements for the sample, while MD81 is in the bluest quartile (see Figure 2.2). Neither MMD11 nor MD81 has a LRIS rest-frame UV spectrum with anomalously strong Lyman α emission or absorption, or notable interstellar or stellar features (though the signal-to-noise ratio in these spectra does not enable a quantitative examination). As discussed by AS2000, at $S_{850}=5.5\pm1.4$mJy (Chapman et al., 2000), the 850μm flux of MMD11 is the strongest detection from the sample of optically selected LBGs that have been observed with SCUBA. Furthermore, MMD11 has a complex [OIII] 5007 nebular line profile, extended into two components along the spatial direction. While there is substructure present, the [OIII] equivalent width is one of the smallest which has been measured in LBGs (Pettini et al., 2001), and could not have contaminated the $\mathcal{R}-K_s$ colors by any significant amount. MD81 is not detected at 850μm at the $\sim$ 3mJy level (Chapman *et al.* , in preparation), and has not been studied with near-IR spectroscopy.

When we attempt to fit simultaneously the $G-\mathcal{R}$, $\mathcal{R}-J$, and $\mathcal{R}-K_s$ colors for either MMD11 or MD81, we are unsuccessful, mainly due to the extremely red optical/IR colors. Since MMD11 and MD81 are so bright in the near-IR, their well-determined colors have more power to discriminate the quality of a model fit than the more poorly determined optical/IR photometry for the majority of the NIRC sample. However, even if MMD11 and MD81 had $\mathcal{R}-J$ and $\mathcal{R}-K_s$ uncertainties which were more typical of the NIRC LBG sample, no satisfactory model fits would be obtained for MD81, and only marginally acceptable fits would be obtained for MMD11. Figure 3.5 shows various attempts to fit the colors of these anomalous galaxies. Estimates of dust reddening are obtained

[3]The "suspect" photometry was obtained during variable observing conditions. an attempt was made to flux calibrate these measurements, but the optical/IR SED's for the relevant galaxies still indicate anomalous near-IR photometric points.

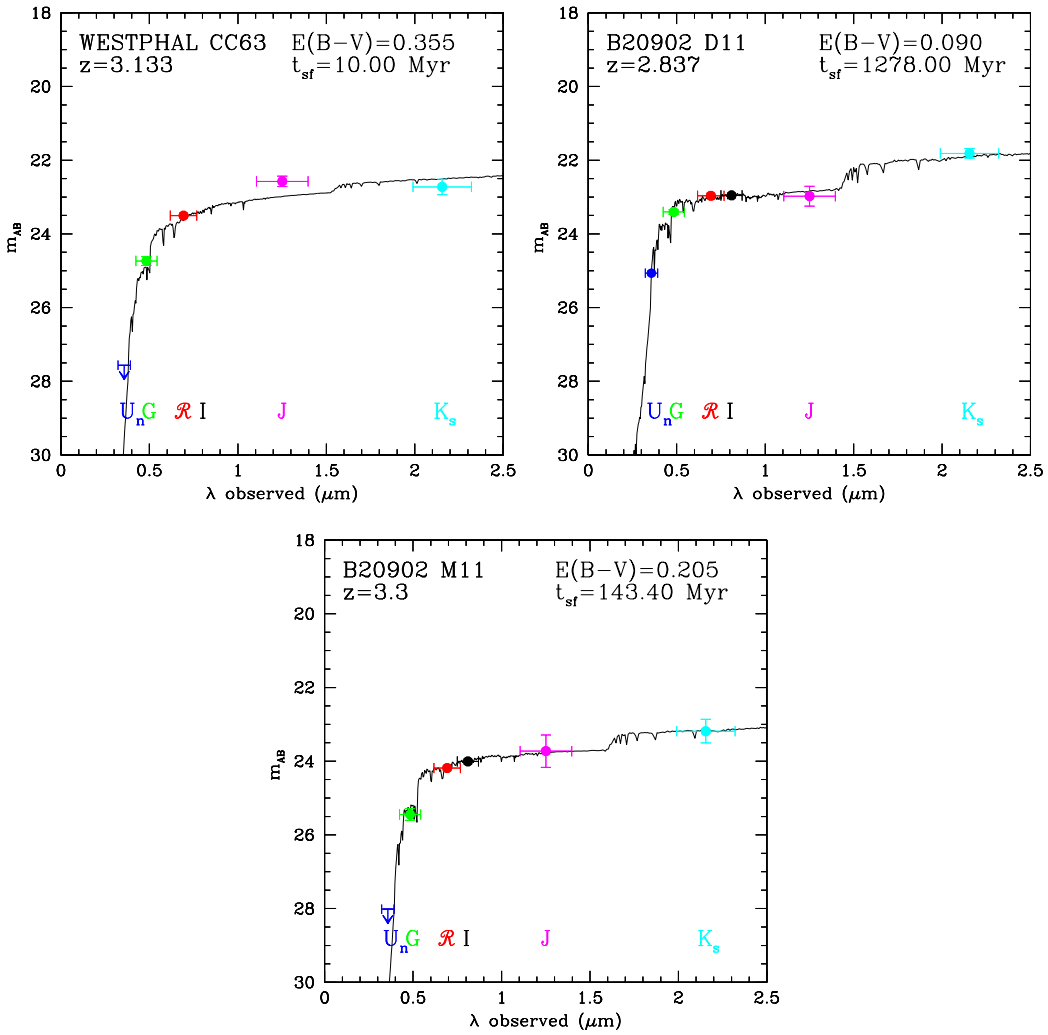

Figure 3.3 The best-fit BC96 constant star-formation models for three galaxies in the NIRC LBG sample. These three examples span the range of properties in the sample. A young and dusty galaxy with very little evidence for a Balmer break, Westphal-CC63 is fit with a 10 Myr model with $E(B-V) = 0.355$ (while the formal best-fit age for CC63 is 4 Myr, we have restricted the best-fit age parameter space to values which are physically plausible ($\geq$ 10 Myr)). At the other extreme, B20902-D11 has a best-fit age of 1.3 Gyr and $E(B-V) = 0.09$—much older with much less dust extinction. Intermediate between these two extremes, B20902-M11 has a best-fit age of 140 Myr and $E(B-V) = 0.205$. Each plot shows the galaxy's redshift and best-fit parameters. The photometric measurements are plotted as magnitudes, yet the error bars on the G, J, and K_s points refer to the uncertainties in the $G-\mathcal{R}$, $\mathcal{R}-J$ and $\mathcal{R}-K_s$ colors, respectively. The U and I measurements are plotted, even though they were not used to determine the best-fit models. There is no I data for the Westphal field, hence the lack of an I point for CC63.

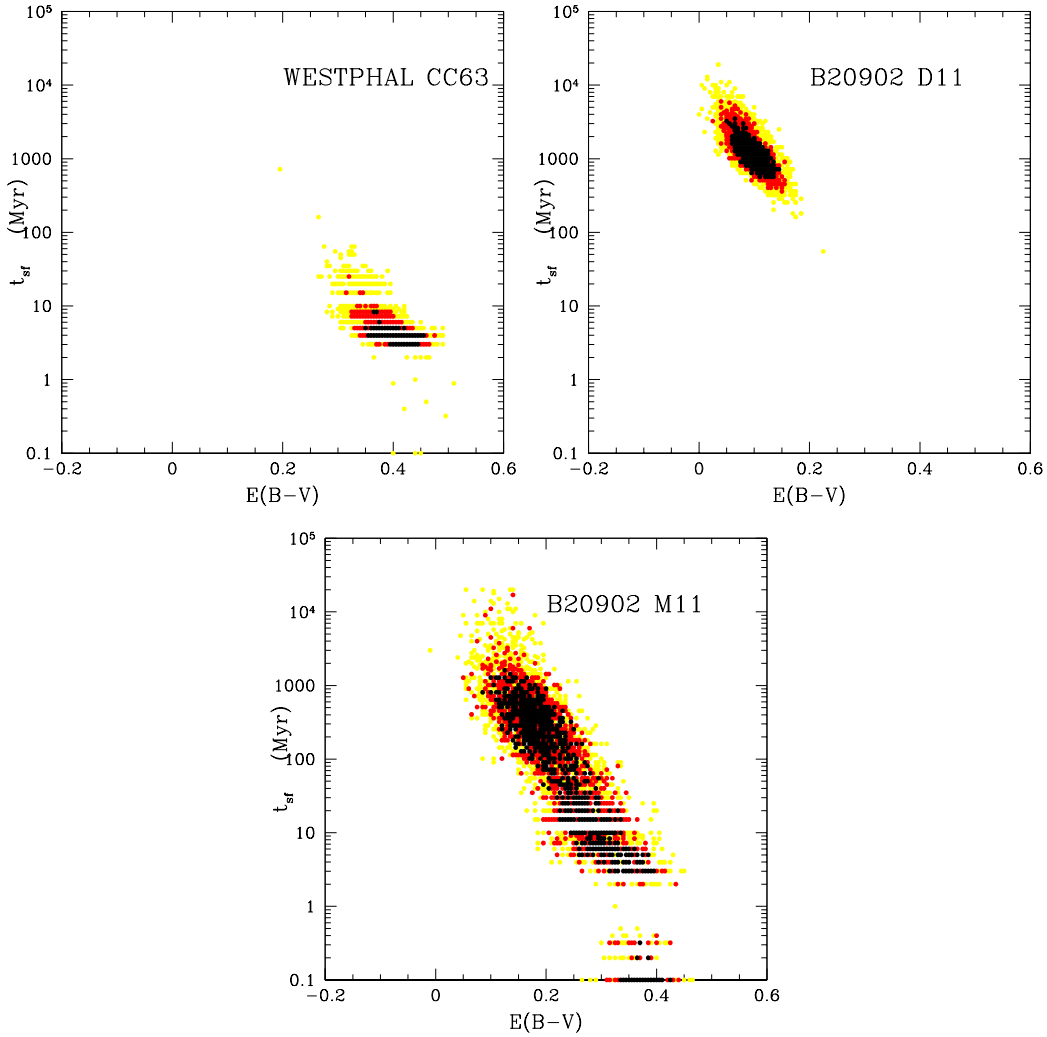

Figure 3.4 Confidence intervals in the $E(B-V)-t_{sf}$ parameter space for the three galaxies featured in Figure 3.3. Each confidence region is determined by generating a large sample of artificial colors for a galaxy (based on its measured colors and photometric uncertainties), and finding the best-fit $E(B-V)$ and t_{sf} for each set of artificial colors. The black region indicates the 68.3% confidence region; the red (dark grey) region indicates the 90% region, and the yellow (light grey) region indicates the remaining 10% of the realizations. Colors were assigned by probability density—i.e., the black points contain the highest density of realizations, while the red (dark grey) points contain intermediate densities, and the yellow (light grey) points have the lowest densities. Westphal-CC63 and B20902-D11 both have better determined optical/IR colors than B20902-M11, as demonstrated by the smaller confidence regions for those galaxies.

from fitting only the $G-\mathcal{R}$ color, assuming BC96 constant star-formation, and ages of 1 Myr and 1 Gyr. Clearly, the J and K_s points for both galaxies are significantly brighter than the predictions for even the 1 Gyr model. While a model with an age older than 1 Gyr might be able to fit the K_s points, the Balmer break present between J and K_s in such an old template spectrum would not be consistent with the well-determined, and bright, J measurements. For most of the galaxies in the NIRC LBG sample, this is not the case—even when fitting the $G-\mathcal{R}$ color alone, it is easy to find a model with the appropriate age and dust extinction to describe all of the photometry within the errors.

If we neglect the $G-\mathcal{R}$ color, and fit $\mathcal{R}-J$ and $\mathcal{R}-K_s$ alone, the best-fit models predict more than 7 magnitudes of extinction in the rest-frame UV and would significantly under-predict the rest-frame far-UV fluxes. The very red optical/IR colors of these galaxies may indicate a problem with the Calzetti extinction law in cases where dust extinction is very extreme. In these cases, as in the case of local ultra-luminous infrared galaxies (ULIRGs), the details of the geometry and distribution of the dust relative to where star-formation is occurring become more important and the simple recipe for extinction breaks down (Trentham et al., 1999; Meurer & Seibert, 2001). For example, based on the $G-\mathcal{R}$ color alone, we would infer a moderate to low amount of dust extinction in MD81 (which may still be true). But such a small amount of extinction, with any age or star-formation history considered in this work, cannot account for the very red $\mathcal{R}-J$ and $\mathcal{R}-K_s$ colors of MD81. Alternatively, the inability to model these unusual galaxies might be due to the over-simplified nature of the star-formation histories considered.

3.4 Model Results

Using the sample of 74 galaxies for which acceptable BC96 continuous star-formation fits were obtained, we explore the trends present among observed and modeled quantities. These galaxies, all of which have redshifts, are brighter by an average of ~ 0.2 magnitudes in $\mathcal{R}$ than the NIRC LBG sample as a whole, and brighter by ~ 0.5 mag than the larger optical LBG photometric sample. It should be emphasized that the sample of HDF-N LBGs recently analyzed by Papovich et al. (2001) includes only four (of 33) galaxies brighter than L^* in the rest-frame UV LBG luminosity function, whereas 75% of the galaxies in the sample analyzed here are brighter than L^*. Differences between the two samples might then be ascribed to UV-luminosity-dependent effects, although we see only subtle trends with UV luminosity within our full ground-based sample spanning a factor of ~ 10 in UV luminosity.

Steidel et al. (1999) and AS2000 have computed the distribution of LBG $E(B-V)$ values based on IGM-absorption-corrected $G-\mathcal{R}$ colors alone, assuming a fixed intrinsic stellar population that corresponds to a BC96 continuous star-formation model with $t_{sf} = 1$ Gyr. With the addition of

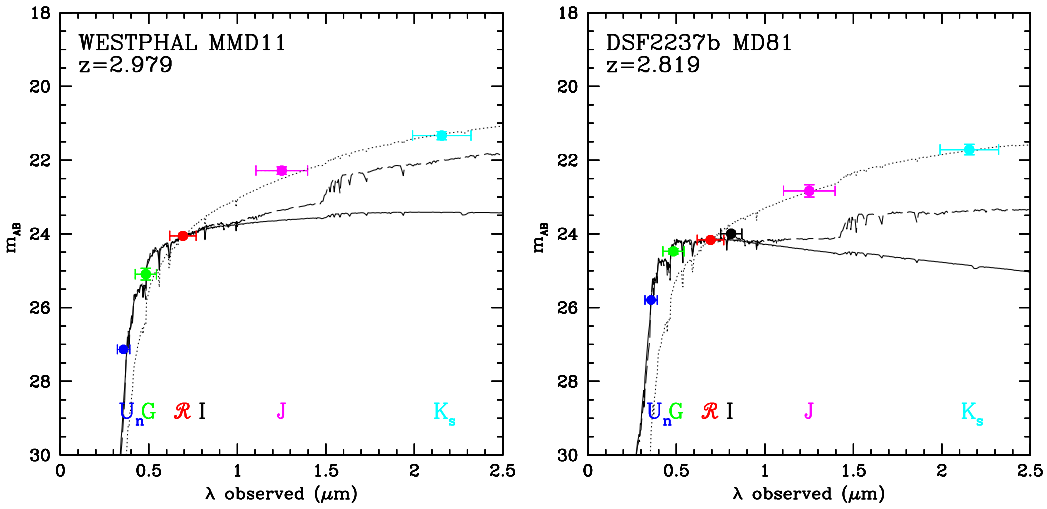

Figure 3.5 Anomalous Galaxies. Westphal-MMD11 and DSF2237b-MD81 are not described by any of the simple models which successfully fit the majority of galaxies in the NIRC LBG sample. For both galaxies, there is no combination of dust and age which simultaneously fits the $G-\mathcal{R}$, $\mathcal{R}-J$ and $\mathcal{R}-K_s$ colors. The $\mathcal{R}-J$ and $\mathcal{R}-K_s$ colors are simply too red to be fit by any of the simple models, including models with different star-formation histories. 1 Myr and 1 Gyr BC96 constant star-formation models were fit to the observed $G-\mathcal{R}$ color alone, excluding other colors. Solid lines represent 1 Myr BC96 constant star-formation models, and dashed lines indicate 1 Gyr models. Dotted lines indicate fits to the $\mathcal{R}-J$ and $\mathcal{R}-K_s$ colors, excluding the $G-\mathcal{R}$ color. For both galaxies, the $\mathcal{R}-J$ and $\mathcal{R}-K_s$ colors alone are fit by large amounts of extinction ($E(B-V) \geq 0.6$) and very young ages ($t_{sf} \leq 10$ Myr). The extrapolation of the dotted line to shorter wavelengths significantly underpredicts the flux observed in the U_n and G filters.

near-IR data, we have been able to model the extinction and variations in the stellar populations simultaneously. The inferred distribution of reddening, assuming the starburst attenuation relation of Calzetti (1997) and a suite of BC96 continuous star-formation models, has a median $E(B-V) = 0.155$, corresponding to $A_{1600} = 1.62$ magnitudes, similar to the median extinction presented in the earlier works. This reflects the fact that the previously-assumed galaxy SED is a reasonable approximation for the bulk of the sample in the rest-frame UV, and that most of the information on reddening comes from the far-UV data points even for a relatively "gray" extinction law.

The median age for our sample is $t_{sf} = 320$ Myr. More than 40% of the galaxies have $t_{sf} > 500$ Myr, while 25% have $t_{sf} < 40$ Myr. There were nine galaxies with formal best-fit t_{sf} values smaller than 10 Myr. Such small ages are not physically plausible for episodes of star-formation, given the dynamical timescales of the star-forming regions (see § 3.6). Furthermore, the conversion between extinction-corrected UV luminosity and star-formation rate becomes highly non-linear at ages shorter than 10 Myr. On these grounds, we restricted the best-fit constant-star-formation t_{sf} parameter space to ages of at least 10 Myr, which still provides acceptable fits for the nine youngest galaxies. We also applied the constraint that best-fit t_{sf} values could not be older than the age of the universe at $z \sim 3$ (assuming an $\Omega_m = 0.3$, $\Omega_\Lambda = 0.7$, $h = 0.7$ cosmology), which affected the fits for seven galaxies whose formal best-fit t_{sf} values were then too old. These galaxies, however, all had colors which were statistically consistent with being younger than the age of the universe at $z \sim 3$. As discussed in § 3.3.3, the t_{sf} values for the NIRC LBG sample are affected in a systematic way by varying the star-formation history or the population synthesis models, but the sample as a whole should broadly represent the significant range in these parameters spanned by the LBGs at $z \sim 3$. We have noted that the distribution of t_{sf} values does not reflect corrections to the $\mathcal{R} - K_s$ color for nebular line emission for the 60% of the galaxies in the NIRC LBG sample which are at high enough redshift that the K_s measurement could be affected. However, there is no apparent systematic offset towards higher t_{sf} values for the higher-redshift portion of the sample as might be expected if the higher redshift objects were significantly biased due to nebular line contamination. Histograms of best-fit t_{sf} and $E(B-V)$ are shown in Figure 3.6.

The median derived star-formation rate for the sample is $\Psi(t_{sf}) = 45h^{-2}M_\odot \mathrm{yr}^{-1}$, and the distribution of values is quite broad, ranging from $\sim 5h^{-2}M_\odot \mathrm{yr}^{-1}$ to as high as $\sim 940h^{-2}M_\odot \mathrm{yr}^{-1}$. Multiplying the best-fit t_{sf} and $\Psi(t_{sf})$ yields a distribution of m_{star}, with a median of $m_{star} = 1.2 \times 10^{10}h^{-2}M_\odot$, smaller but comparable to the present-day L^* stellar mass, $m_{star}(L^*) \sim 4.0 \times 10^{10}h^{-2}M_\odot$ (Cole et al., 2001; Papovich et al., 2001). However, we find that about 20% of the sample have m_{star} smaller than $4 \times 10^9 h^{-2}M_\odot$ (roughly the same sample with best-fit $t_{sf} < 40$Myr). Histograms of the inferred m_{star} and $\Psi(t_{sf})$ distributions are shown in Figure 3.7.

As mentioned above, a similar modeling technique for extracting physical parameters from observed colors of LBGs was used in recent work by Papovich et al. (2001); their sample of 33 galaxies

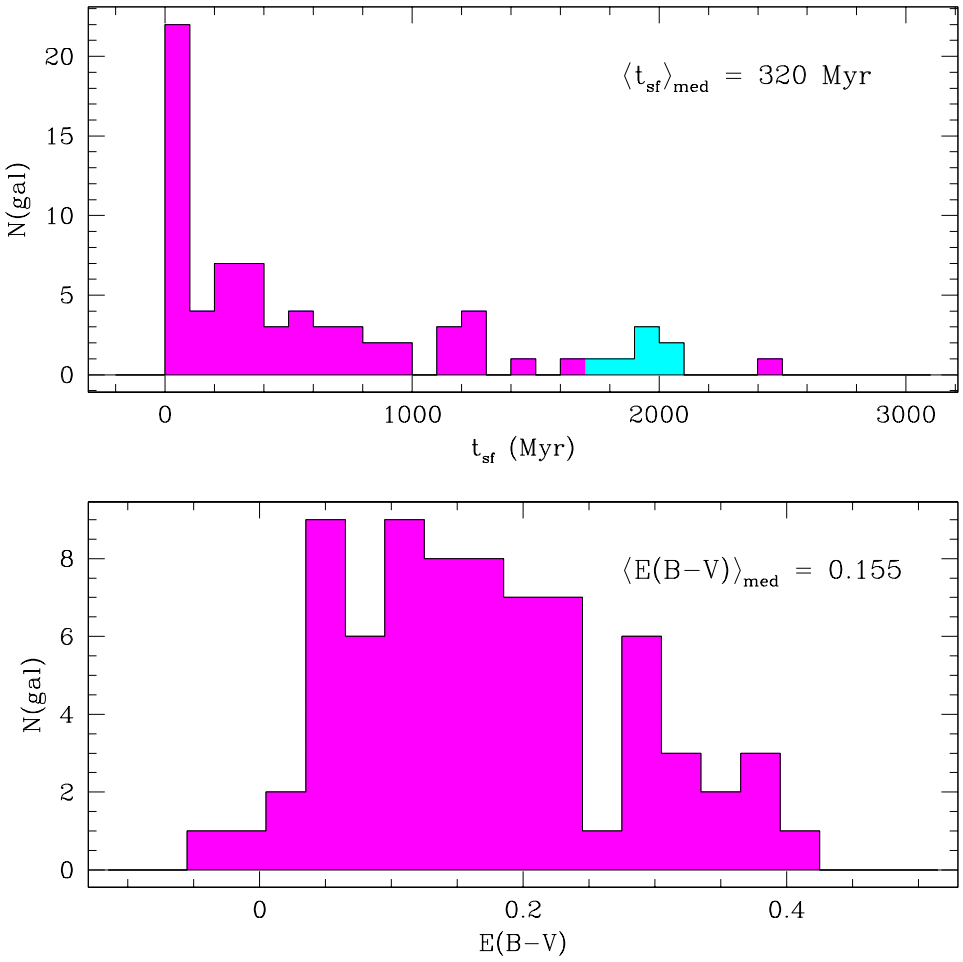

Figure 3.6 Histograms of t_{sf} and $E(B-V)$ values derived from BC96 constant star-formation models. Top: The t_{sf} histogram. The cyan (light grey) bin indicates seven galaxies whose unconstrained best-fit t_{sf} values were older than the age of the universe at $z \sim 3$. Constraining each of these galaxies to have a best-fit t_{sf} younger than the age of the universe at its redshift (assuming an $\Omega_m = 0.3$, $\Omega_\Lambda = 0.7$, $h = 0.7$ cosmology) resulted in best-fit t_{sf} values of roughly 2 Gyr. The galaxy Q0201-B13 is at $z = 2.167$, so its best-fit t_{sf} of 2.5 Gyr (the oldest bin) does not pose a problem. Bottom: The $E(B-V)$ distribution, derived from both optical and near-IR photometry. This distribution probably over-represents the dustiest galaxies, relative to the LBG population as a whole, as shown by Figure 2.2.

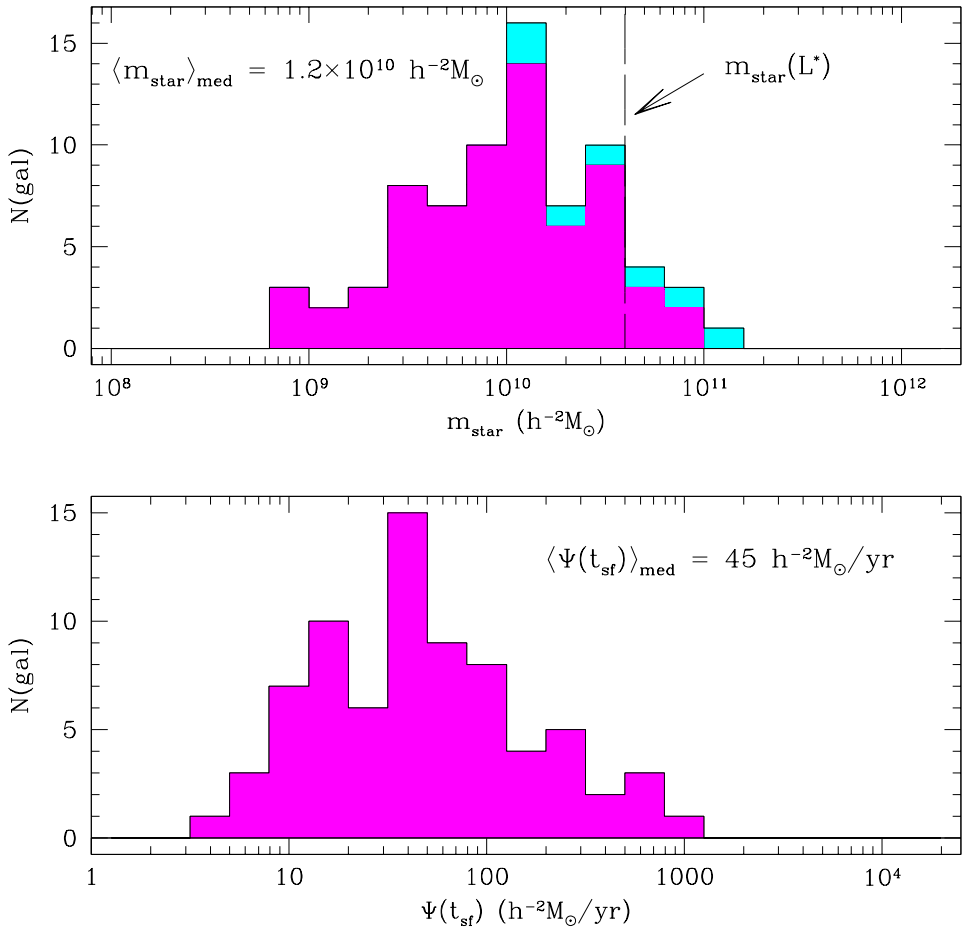

Figure 3.7 Histograms of m_{star} and instantaneous star-formation rate, $\Psi(t_{sf})$, derived from the best-fit BC96 constant star-formation models. Top: The formed m_{star} distribution. The cyan (light grey) bins contain the seven galaxies with unconstrained best-fit t_{sf} values older than the age of the universe at $z \sim 3$. A significant fraction of the NIRC LBG sample have m_{star} values approaching the formed stellar mass in a current L^* galaxy ($4 \times 10^{10} h^{-2} M_{\odot}$), while a significant fraction have m_{star} values that are an order of magnitude smaller. Bottom: The distribution of instantaneous star-formation rates, determined by applying the inferred extinction corrections to the distribution of rest-frame UV luminosities.

in the HDF-N is a superset of earlier work by Sawicki & Yee (1998) on 17 HDF-N galaxies. The Papovich et al. HDF study, while containing all of the Sawicki & Yee galaxies, finds somewhat different results from Sawicki & Yee, including lower typical extinction factors, older ages, and larger formed stellar masses. The authors attribute some of these differences to their higher-quality *HST* NICMOS J and H data (compared to the Sawicki & Yee ground-based J and H), more accurate matching of optical and infrared photometry to compute colors, and larger galaxy sample. Here and above we have focused primarily on the more recent HDF-N analysis of Papovich et al. (2001).

The main difference between our modeling procedure and that of Papovich et al. is that the latter work allowed τ, the exponential star-formation decay time constant, to vary as a free parameter in fitting the models. As discussed above, there were few cases in which our data could discriminate between different values of τ that were significant compared to the inferred value of t_{sf}. However, a direct comparison of the model results is possible for 19 of the 33 galaxies in the Papovich et al. work because the best-fit τ values are longer than the inferred t_{sf}, so that the star-formation history is essentially indistinguishable from a constant star-formation model. For these 19 HDF-N galaxies, the median inferred age is $t_{sf} = 453\,\mathrm{Myr}$, and the median $E(B-V) = 0.095$. The median t_{sf} is thus higher, while similar, to the NIRC LBG median t_{sf}, and the median $E(B-V)$ is slightly smaller than that of the NIRC LBG sample. The remaining 14 HDF-N galaxies have best-fit $t_{sf} > \tau$, and t_{sf} values which are systematically lower than the $t_{sf} < \tau$ sample. However, the τ values for these galaxies are not very well constrained, and larger τ values also provide acceptable fits. The older t_{sf} values resulting from larger τ parameters would be roughly consistent with the t_{sf} values for the other 19 galaxies. Thus, given the uncertainties, it is probably fair to compare broadly the whole Papovich et al. sample to the NIRC-LBG sample. Our results are consistent with the inferred parameters for the small subset of the brightest HDF galaxies, including two galaxies in common between the two samples (see Table 2.3). Generally speaking, the UV-brighter NIRC LBG sample has a higher proportion of objects with large inferred extinction and with large values of the inferred stellar mass (these are generally distinct sets of objects, as discussed further below), both of which may be due to the different range of UV luminosity spanned within the two samples.

3.4.1 Extinction and Luminosity

Using observed optical and far-infrared (FIR) data, AS2000 and Meurer et al. (1999) demonstrated that at both low and high redshifts, there appears to be a correlation between dust-obscuration and bolometric luminosity ($L_{\mathrm{bol,dust}}/L_{UV} \approx L_{\mathrm{bol,dust}}$). The results of our modeling of the LBG SEDs support the assertion that more heavily obscured galaxies have larger bolometric luminosities; however, because many of our assumptions are similar—most notably, the adopted starburst attenuation relation, our new results cannot be taken as independent evidence. As in AS2000, we find that the rest-frame UV luminosity is uncorrelated with the inferred value of $E(B-V)$, so that applying the

inferred extinction correction naturally results in a strong correlation between bolometric luminosity and extinction. As emphasized by AS2000, inferences about extinction in the high redshift galaxies are very difficult to test observationally, but the trends are very similar to what is observed for star-forming galaxies in the local universe and, so far, the starburst attenuation relation is consistent with available cross-checks at high redshift. We note in passing that internally consistent application of the inferred extinction corrections to the rest-frame optical luminosities results in a similar correlation of dust obscuration and optical luminosity, and a net correction to the V-band luminosity density of a factor of ~ 2 compared to the uncorrected numbers presented in § 2.4. The correlations of the UV and optical luminosities with best-fit $E(B-V)$ are shown in Figure 3.8 for BC96 continuous star-formation models. These correlations hold for the all of the star-formation histories used in this work to model the galaxy colors, and would hold for any assumed extinction relation that is correlated with rest-UV color.

3.4.2 Extinction and Age

In Figure 3.9 we plot the best-fit $E(B-V)$ and t_{sf} parameters for the 74 galaxies successfully fit with BC96 constant-star-formation models. There is a very strong anti-correlation between $E(B-V)$ and t_{sf} in the sense that younger galaxies are more heavily extinguished than older galaxies. Given the strong correlation between $\Psi(t_{sf})$ and $E(B-V)$ discussed in § 3.4.1, the relationship between extinction and age translates into a link between age and star-formation rate, where the youngest galaxies also have the highest star-formation rates. The correlation in the sample between $E(B-V)$ and t_{sf} falls roughly in the same direction as the observed covariance of the $(E(B-V), t_{sf})$ parameters for each individual galaxy. The covariance of $E(B-V)$ and t_{sf} is dominated in most cases by response of the fitted parameters to perturbations in the $G-\mathcal{R}$ color. Typically, a positive perturbation to the $G-\mathcal{R}$ results in a *positive* perturbation to the best-fit $E(B-V)$ and a *negative* perturbation to the best-fit t_{sf}, the latter due to the effect of the extinction estimate on the predicted $\mathcal{R}-K$ color for a given t_{sf}. The covariance of the two parameters is clearly demonstrated by the NIRC LBG confidence regions shown in Figure 3.4.

Given the strong covariance between best-fit $E(B-V)$ and t_{sf} parameters inherent in the modeling procedure, further tests are necessary to evaluate whether the trend of increasing extinction with decreasing t_{sf} is significant. In other words, does the apparent correlation arise solely due to objects' covariant confidence regions in $E(B-V)-t_{sf}$ space, because measurement errors can scatter intrinsically uncorrelated points along the same direction as an $E(B-V)-t_{sf}$ correlation? In order to test the strength of such an apparent correlation, we constructed a sample of 74 uncorrelated $E(B-V)$ and t_{sf} pairs (to match the size of the observed sample of 74 galaxies). This sample was generated by randomly selecting $E(B-V)$ and t_{sf} values independently from the *intrinsic* marginal distributions of each of the parameters. These *intrinsic* marginal distributions were estimated by

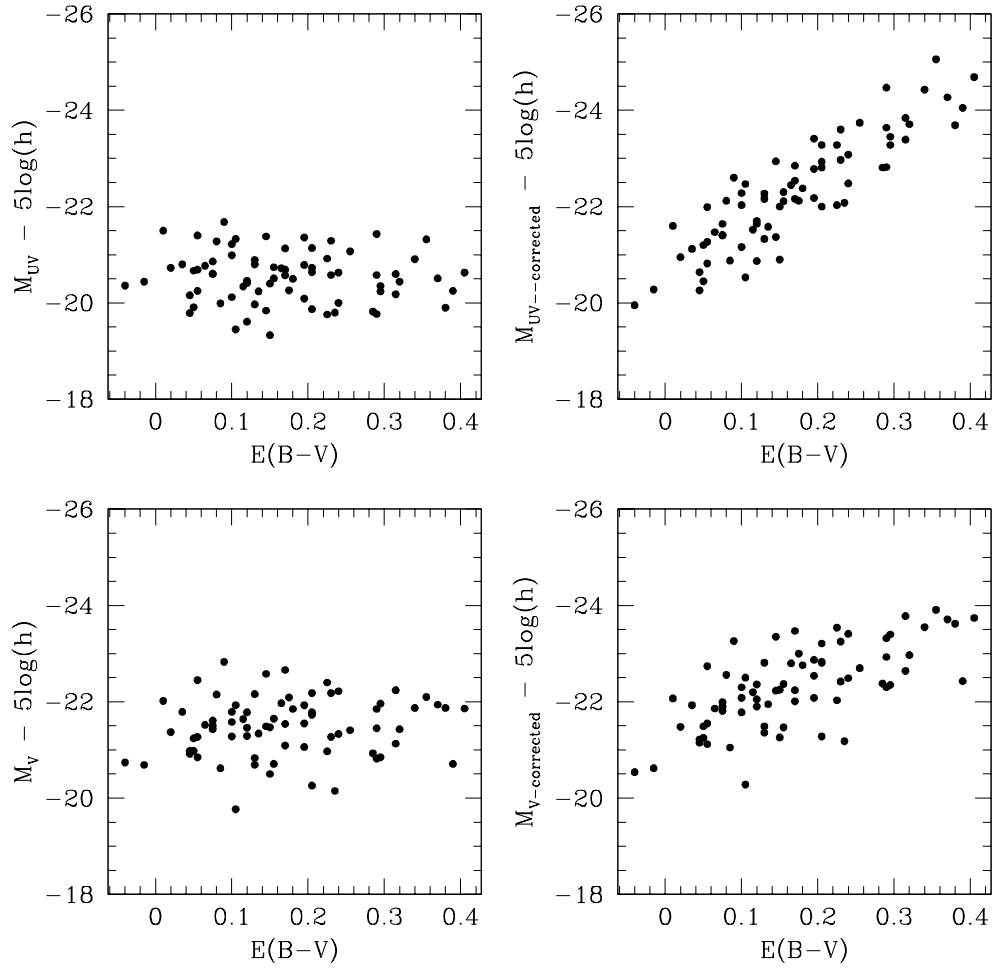

Figure 3.8 M_{UV} and M_V vs. $E(B-V)$. M_{UV} and M_V refer to the rest-frame UV and optical (V) absolute magnitudes which are probed by the $\mathcal{R}$ and K_s apparent magnitudes, respectively, at $z \sim 3$. The two left-hand panels show the relationship of rest-frame UV and optical luminosities with best-fit $E(B-V)$. Both UV and optical luminosities are uncorrelated with $E(B-V)$. When the luminosities are corrected for dust-extinction (shown in the right-hand panels), strong correlations result between intrinsic luminosity and dust extinction. The correlation holds not only in the rest-frame UV but also in the rest-frame optical, where the effects of dust-extinction are less extreme (but clearly still important, as shown by the lower right-hand panel). The correlation between intrinsic luminosity and dust extinction is independent of the star-formation history used to fit the observed spectral energy distributions.

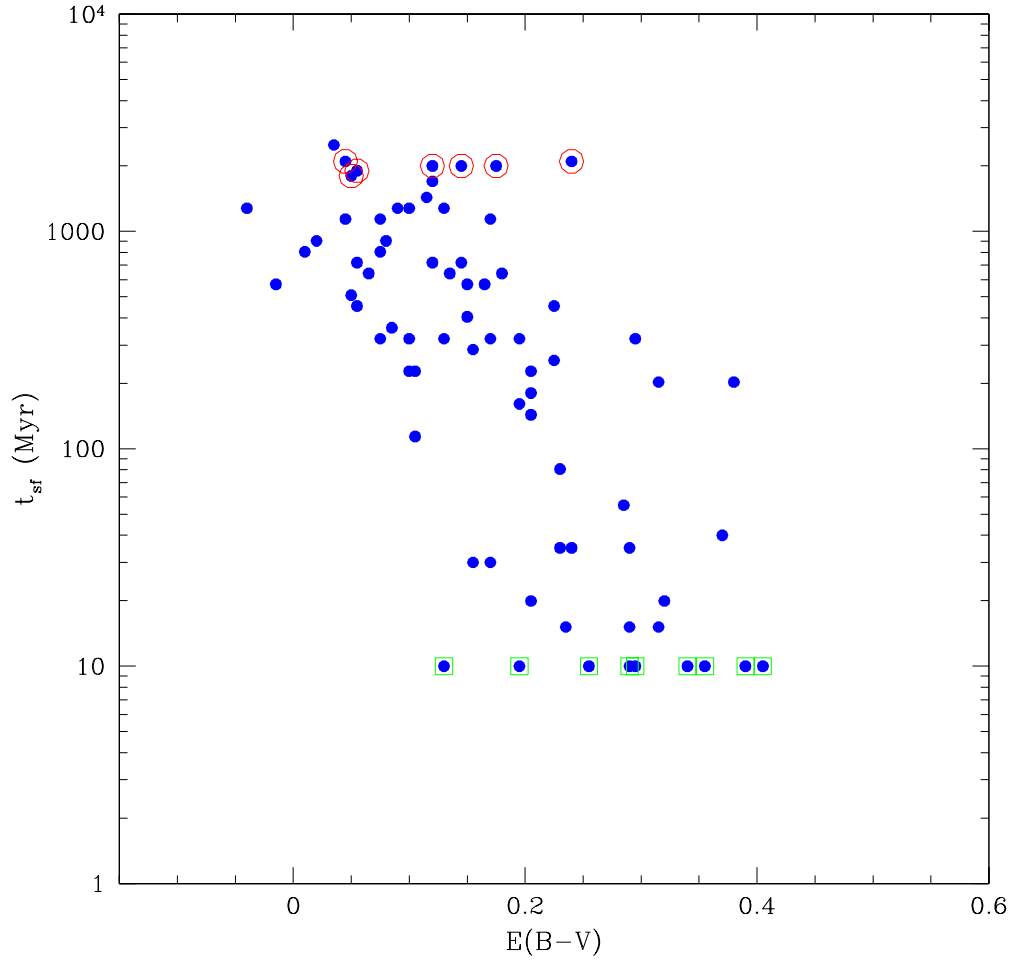

Figure 3.9 The Extinction-Age Correlation. This is the joint distribution of best-fit BC96 constant star-formation $E(B-V)$ and t_{sf} parameters. There is a significant correlation between the two best-fit parameters, which holds for all of the star-formation histories which we used to fit the observed spectral energy distributions. However, the strength of the correlation does depend on the assumed dust attenuation law. This plot assumes a Calzetti dust law, but if an SMC curve is used instead, the correlation is greatly reduced. Open circles indicate galaxies whose unconstrained best-fit t_{sf} values were older than the age of the universe at $z \sim 3$. Open squares indicate galaxies whose unconstrained best-fit ages are < 10 Myr.

assuming that the *observed* marginal distributions (shown in Figure 3.6) represented the *intrinsic* marginal distributions broadened by photometric measurement errors. In addition to $E(B-V)$ and t_{sf}, $\mathcal{R}$ apparent magnitude and z were randomly selected from the observed distributions of $\mathcal{R}$ and z for NIRC LBGs, in order to compute the colors that would be observed from a galaxy with the randomly selected $E(B-V)$ and t_{sf} parameters. A fake galaxy was retained only if its $E(B-V)$ and t_{sf} parameters implied a $G-\mathcal{R}$ color satisfying the LBG selection criterion of $G-\mathcal{R} \leq 1.2$, and a K_s magnitude brighter than the typical NIRC LBG detection limit of $K_s = 22.5$. Photometric uncertainties were assigned to each fake galaxy's predicted set of colors, based on the galaxy's $\mathcal{R}$ magnitude and colors, and the previously determined functions of $\sigma(\mathcal{R}, G-\mathcal{R})$, $\sigma(\mathcal{R}, \mathcal{R}-J)$, and $\sigma(\mathcal{R}, \mathcal{R}-K_s)$ (see § 2.2.4).

The sample of fake galaxies was then "observed" a large number (1000) of times. Each time, the colors of the fake galaxies were perturbed in a manner consistent with their photometric errors (a process similar to the one used to construct the confidence intervals for the 74 real observed galaxies). The result of observing the fake galaxies numerous times with measurement errors was a large distribution of best-fit $E(B-V)$ and t_{sf} values (the number of fake galaxies (74) multiplied by the number of trials (1000)). The marginal distributions of $E(B-V)$ and t_{sf} for this large simulated distribution matched the observed marginal distributions of $E(B-V)$ and t_{sf} in Figure 3.6—which verifies that our estimate of the intrinsic marginal distribution was reasonable. We then randomly selected a large number of groups of 74 best-fit $E(B-V) - t_{sf}$ pairs from the sample of 74,000 "observed" galaxies, and computed the correlation coefficient between $E(B-V)$ and t_{sf} for each randomly selected sample. In 1000 random samples of 74 fake best-fit $E(B-V) - t_{sf}$ values, *no* sample had a correlation coefficient as strong as the one seen in the real sample. Thus, *it appears that the age/extinction correlation for NIRC LBGs has less than a* 0.1% *chance of being the result of correlated measurement errors alone.*

A related question is whether the detection limits and selection criteria for the sample could have created an apparent dearth of young, unreddened galaxies, and old, dusty galaxies, which would mimic a real correlation between $E(B-V)$ and t_{sf}. For the redshift range of the sample, the BC96 constant star-formation models with $E(B-V) \sim 0$ and $t_{sf} \leq 100$ Myr have $G-\mathcal{R}$ within the range for LBGs ($-0.02 < G-\mathcal{R} < 0.35$), but also very blue $\mathcal{R}-K_s$ colors ($\mathcal{R}-K_s \leq 1.86$). A detection limit in K_s translates into a limit in $\mathcal{R}-K_s$ as a function of $\mathcal{R}$. However, since there are $\mathcal{R}-K_s$ limits rather than detections for only 3 out of 81 galaxies with redshifts in the NIRC sample, we conclude that our K_s detection limit has not prevented us from detecting a significant population of young, unreddened galaxies. At any redshift in the NIRC sample, old and reddened galaxies, with $E(B-V) > 0.15$ and $t_{sf} \geq 1$ Gyr, have predicted $\mathcal{R}-K > 3.00$, which means that all such galaxies with $\mathcal{R} < 25.5$, should be detected in $\mathcal{R}-K_s$. At the median redshift of the NIRC sample, the LBG selection limit of $G-\mathcal{R} < 1.20$ implies that we should be able to detect old galaxies with

$E(B-V) \leq 0.30$, which is more than one standard deviation to the red of the mean of the sample. At increasing redshift, the upper limit on $E(B-V)$ decreases until at the highest redshift in the NIRC sample, $z = 3.396$, it is only possible to select a 1 Gyr model with $E(B-V) \leq 0.14$ as a LBG, based on $G - \mathcal{R}$. Such a redshift-dependent effect discriminates against old and very dusty objects at the high redshift end of the LBG redshift selection function. To test the significance of such an effect, the sample of 74 galaxies was divided into low and high redshift subsamples, using the median redshift as a discriminator. All of the galaxies in the low redshift sample have $z \leq 3.061$, at which redshift a 1 Gyr stellar population could be detected with $E(B-V) \leq 0.300$. Despite the fact that $E(B-V)$ is barely restricted for the low redshift sample, a strong correlation between $E(B-V)$ and t_{sf} is recovered from this sample, as well as from the high redshift and total samples. We conclude that the redshift-dependent bias against detecting old and dusty galaxies cannot account for the strong correlation found between $E(B-V)$ and t_{sf} in the NIRC sample either.

The inferred strong correlation between age and extinction does depend on the details of the attenuation law applied to correct observed galaxy colors and magnitudes to their intrinsic, unobscured values. At low redshift, relatively "gray" starburst galaxy attenuation relations such as that of Calzetti (1997) provide a much better predictor of bolometric luminosity from far-UV observations than the reddening curves derived from observations of single stars, such as the SMC, LMC, and Galactic reddening curves (Meurer et al., 1999). There are very few observations to constrain the nature of dust extinction in galaxies at high redshift; however, the limited information which exists favors the starburst attenuation relation over a much steeper curve such as the SMC law (AS2000; Meurer et al., 1999). Nevertheless, if the SMC law is used with the BC96 constant star-formation models, instead of the Calzetti relation, the best-fit extinction values at 1600 Å (A_{1600}) are systematically smaller, by a median factor of 2.7, and the t_{sf} values are systematically larger. The ratio between SMC and Calzetti t_{sf} values increases as a function of increasing extinction, but the median ratio is 3.7. Qualitatively, the larger SMC t_{sf} values result from interpreting a larger fraction of the $\mathcal{R} - K_s$ color as due to the Balmer break (aging stellar population), and a smaller fraction as due to the effects of dust extinction.[4] The result of using the SMC law is that the correlation between inferred extinction and inferred age is very much diminished.

3.4.3 Stellar Mass

The formed stellar mass, m_{star}, for the constant star-formation models is simply the product of the best-fit t_{sf} and $\Psi(t_{sf})$. Figure 3.10 shows the relationship between m_{star} and observed and intrinsic (extinction-corrected) luminosity values. When the sample is restricted to galaxies with best-fit $t_{sf} > 320$ Myr (the median for NIRC LBGs), there are significant correlations between

[4] In fact, the inverse effects on extinction and age from using an SMC law tend to cancel out in the calculation of formed stellar mass, which is typically only 30% larger when using the SMC rather than Calzetti law.

both UV and optical extinction-corrected luminosities and m_{star}. However, when the whole NIRC LBG sample is considered, the extinction-corrected UV and optical luminosities are only weakly correlated with m_{star}, indicating that, for the wide range of extinction and age parameters found in the NIRC LBG sample, even rest-frame optical luminosities (the longest accessible wavelengths for $z \sim 3$ galaxies until the Space Infrared Telescope Facility (SIRTF) flies) often have more to do with current star-formation rates than with formed stellar masses. Thus, as emphasized by Papovich et al. (2001), the estimates of the formed stellar mass associated with the most recent star-formation episode must rely on the IMF-dependent population synthesis modeling until longer wavelength observations are possible. However, Papovich et al. also explored the dependence of inferred m_{star} on the modeling assumptions for a given observed galaxy SED, concluding that, while variation of the modeling parameters yields highly variable results for parameters such as age and extinction, the combination of best-fit pairs of these parameters generally results in much more tightly constrained m_{star} estimates for the modeled star formation episode. While exploring a smaller volume of parameter space, we confirm this trend for the formed stellar mass values (cf. § 3.3.3).

Our results should be compared directly with the solar metallicity, Salpeter IMF models of Papovich et al. (2001) (their Figure 17), where the characteristic formed stellar mass is $\sim$ a few $\times 10^{10}$ $M_{\odot}$ for objects with UV luminosities of L^* in the far-UV luminosity function of Steidel et al. (1999). Our NIRC sample, which has a median luminosity of somewhat brighter than L^*, has a median inferred stellar mass of 2.5×10^{10} $M_{\odot}$ using the $h = 0.7$ cosmology adopted by Papovich et al.. Thus, in the small region of overlap, the ground-based sample yields results similar to the brightest HDF-N galaxies. In contrast to Papovich et al., who found that the UV luminosity was well correlated with the inferred stellar mass, we find that the UV luminosity is uncorrelated with the inferred m_{star}. This may reflect a real difference between the brighter and fainter samples. One possible explanation could be that we see a wider range of extinction among the NIRC LBGs than is found at fainter UV luminosities (e.g., objects of a given UV luminosity can be either heavily extinguished very luminous objects, or modestly extinguished, much less luminous objects) such that the relationship between UV luminosities uncorrected and corrected for extinction is much less tight (see AS2000). Because of the very small overlap in UV luminosity between the two samples, the differences are at present statistically insignificant.

There are 9 objects[5] from the NIRC sample which also have nebular line width measurements from near-IR spectroscopy (Pettini et al., 2001). We use the nebular line widths and the measured near-IR half-light radii to compute the dynamical mass enclosed within the half-light radius. The mass inferred from the nebular line widths is probably not indicative of the total mass in the dark-

[5]One is Westphal MMD11, which we were unable to model successfully, and so it has not been included in this discussion.

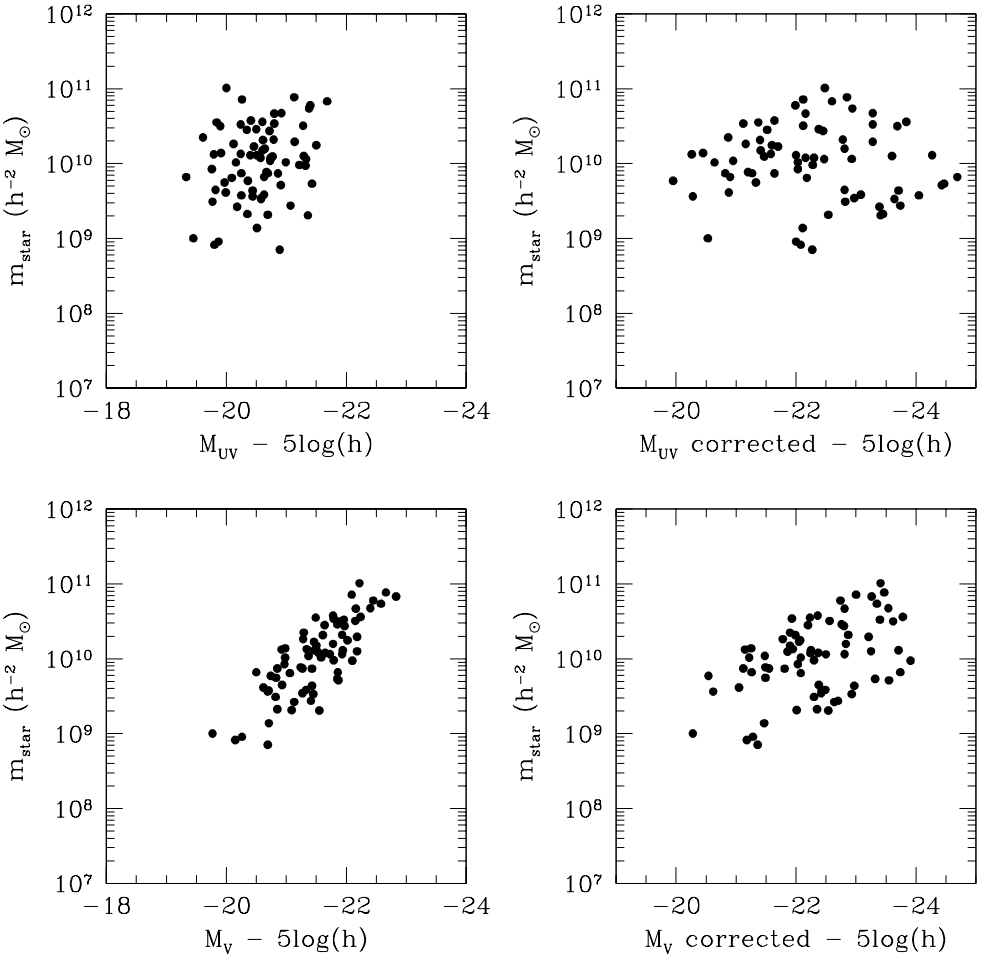

Figure 3.10 m_{star} vs. M_{UV} and M_V. Relationships are shown between m_{star} derived from the best-fit BC96 constant star-formation models, and the UV and optical luminosities. M_{UV} and M_V refer to the rest-frame UV and optical (V) absolute magnitudes. The left-hand panels show the relationships for luminosity which is uncorrected for extinction, while the right-hand panels show the relationships for extinction-corrected luminosity.

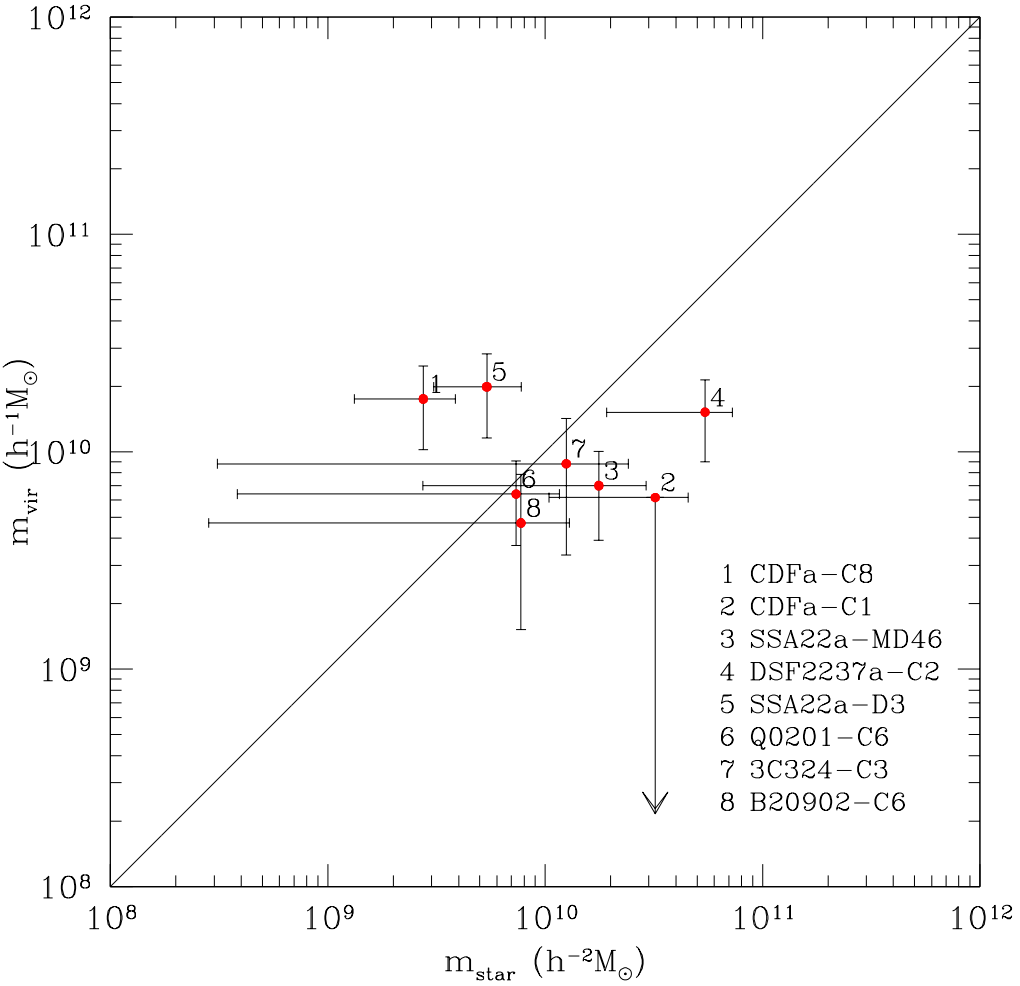

Figure 3.11 m_{vir} vs. m_{star}. This plot shows the relationship between the dynamical mass implied by nebular line widths, assuming virial equilibrium (m_{vir}), and the best-fit BC96 formed stellar mass (m_{star}), assuming constant star formation. The solid line describes $m_{vir} = m_{star}$. Horizontal error bars reflect the 1σ model confidence region of m_{star}, while vertical error bars reflect the uncertainties in the measured nebular line width and angular half-light radius. The inferred dynamical masses should reflect approximate upper limits to the formed stellar mass in the physical region probed by the NIRC observations. We find broad consistency between the mass scales inferred from near-infrared spectroscopic and photometric measurements. In the two cases where there are significant differences, the best-fit stellar mass is significantly smaller than the inferred dynamical mass.

matter halo containing the LBG, but is likely to represent a lower limit (see Pettini et al., 2001). Similarly, since the inferred stellar mass estimates are only sensitive to the most recent episode of star-formation, they should also represent lower limits on the total stellar mass present. However, the near-infrared spectroscopic and photometric measurements generally span the same physical region, which contains not only stellar mass, but also gas and dark matter. The spectroscopic line widths should be sensitive to all this matter, while the photometry only probes the luminous stellar matter. Therefore, the mass inferred from the nebular line widths should represent a rough upper limit to the m_{star} values derived from the BC96 model fits. We would suspect a problem in the population synthesis modeling technique if the derived m_{star} values were much larger and statistically discrepant with the inferred dynamical masses. As shown in Figure 3.11, for the majority of the galaxies, the m_{star} value is consistent with the inferred dynamical mass; in two cases where it is not, the best-fit stellar mass is significantly smaller than the inferred dynamical mass. We refrain from drawing conclusions from Figure 3.11, given the very large uncertainties in both mass estimates, but there is no evidence that the two mass scales are wildly inconsistent with one another.

3.5 "Young" and "Old" LBGs: Spectral Differences

One of the more striking results from the modeling of LBG stellar populations is the strong correlation between extinction and age, such that the galaxies best fit by younger stellar populations are also best described by larger amounts of extinction and reddening. As discussed in § 3.4.2, we believe that this correlation is significant, despite the tendency for the individual $(E(B-V), t_{sf})$ covariance intervals to lie in a similar direction to the observed sample correlation, and despite a $G - \mathcal{R}$ selection criterion which prevents a galaxy older than 1 Gyr with significant amounts of dust extinction from being classified as a LBG at the highest redshifts in the sample. With the assumption that the correlation is real, there are implications for interpreting the range of LBG best-fit stellar populations and extinction parameters. It appears that the distributions of LBG star-formation ages, extinction, and inferred stellar masses fall along a continuum in the parameter space, the extremes of which might be viewed as separate "populations." To illustrate this point, we isolate 16 galaxies with best-fit $t_{sf} \geq 1$ Gyr, and 16 galaxies with $t_{sf} \leq 35$ Myr. In the discussion which follows, the ~ 1 Gyr subsample is referred to as the "old" sample, and the ≤ 35 Myr subsample is labeled "young." The "young" sample has $\langle E(B-V) \rangle = 0.260$, $\langle \Psi(t_{sf}) \rangle = 210 h^{-2} M_{\odot} \mathrm{yr}^{-1}$, and $\langle m_{star} \rangle = 2.9 \times 10^9 h^{-2} M_{\odot}$. In contrast, the "old" sample has $\langle E(B-V) \rangle = 0.100$, $\langle \Psi(t_{sf}) \rangle = 25 h^{-2} M_{\odot} \mathrm{yr}^{-1}$, and $\langle m_{star} \rangle = 4.0 \times 10^{10} h^{-2} M_{\odot}$. The young sample is characterized by 2 magnitudes more dust extinction in the rest-frame UV than the old sample, star-formation rates at least an order of magnitude higher (even when restricting the best-fit t_{sf} values to be above a reasonable minimum age), and formed stellar masses more than an order of

magnitude smaller.

To investigate further the distinctions between galaxies in the young, dusty subsample and those in the older, less reddened group, we drew from our database of LBG rest-frame far-UV spectra, collected by our group between October 1995 and November 1999 (Steidel et al., 1996a,b, 1998, 1999). By combining individual rest-frame UV spectra of galaxies in the "young" and "old" subsamples described above, we constructed "young" and "old" composite spectra following a method similar to that described in Steidel et al. (2001).

The young and old composite spectra are plotted in Figure 3.12, and Figure 3.13 shows an expanded view of four specific regions of the spectra for more detailed comparison. There are several clear differences to note, the most dramatic of which is in the relative Lyman α line profiles. The old spectrum has strong Lyman α emission with rest-frame $W_\lambda = 20$ Å, whereas the young spectrum has a broad absorption trough plus much weaker emission which combine to give roughly $W_\lambda = 0$. The radiative transfer of Lyman α photons in galaxies is a complex process which depends not only on the amount of dust present in the ISM but also, and perhaps more importantly, on the geometry and kinematics of the neutral interstellar hydrogen gas (Charlot & Fall, 1993; Chen & Neufeld, 1994; Kunth et al., 1998; Tenorio-Tagle et al., 1999). However, due to resonant scattering, Lyman α photons will on average traverse a much longer path before escaping the galaxy than nearby continuum photons, so that they are more prone to absorption by dust in the ISM. Therefore, the amount of dust present in the ISM should have a non-negligible effect on the emergent Lyman α profile. The fact that the composite "young" spectrum exhibits a Lyman α profile with a combination of absorption and only weak emission, while the composite "old" spectrum has very strong Lyman α emission, offers independent support for a scenario in which the youngest galaxies have significantly dustier interstellar media than more mature LBGs.

Additionally, the young spectrum has much stronger Lyman β absorption, stronger low-ionization interstellar metal absorption lines of Si II λ1192, 1260, and 1526, C II λ1334, Fe II λ1608, and a stronger P-Cygni C IV λ1549 profile. The only interstellar metal absorption line which is stronger in the old spectrum is Al II λ1670. While the S/N ratios of the composite spectra represent large improvements over that of the individual spectra, the significance of the differences in line strengths between the old and young spectra is still difficult to quantify, given the noise in the composite spectra and the relatively small sample of objects whose spectra were combined. We therefore choose to make more qualitative observations. The low-ionization interstellar absorption lines are probably optically thick, and therefore on the flat part of the curve of growth, where equivalent width is determined mainly by velocity width, and not column density (Steidel et al., 1996b; Gonzalez Delgado et al., 1998; Heckman & Leitherer, 1997). Accordingly, the stronger interstellar absorption lines in the young spectrum may indicate interstellar medium velocity widths larger than those in the old spectrum. Larger velocity widths are consistent with a scenario in which a higher supernova rate

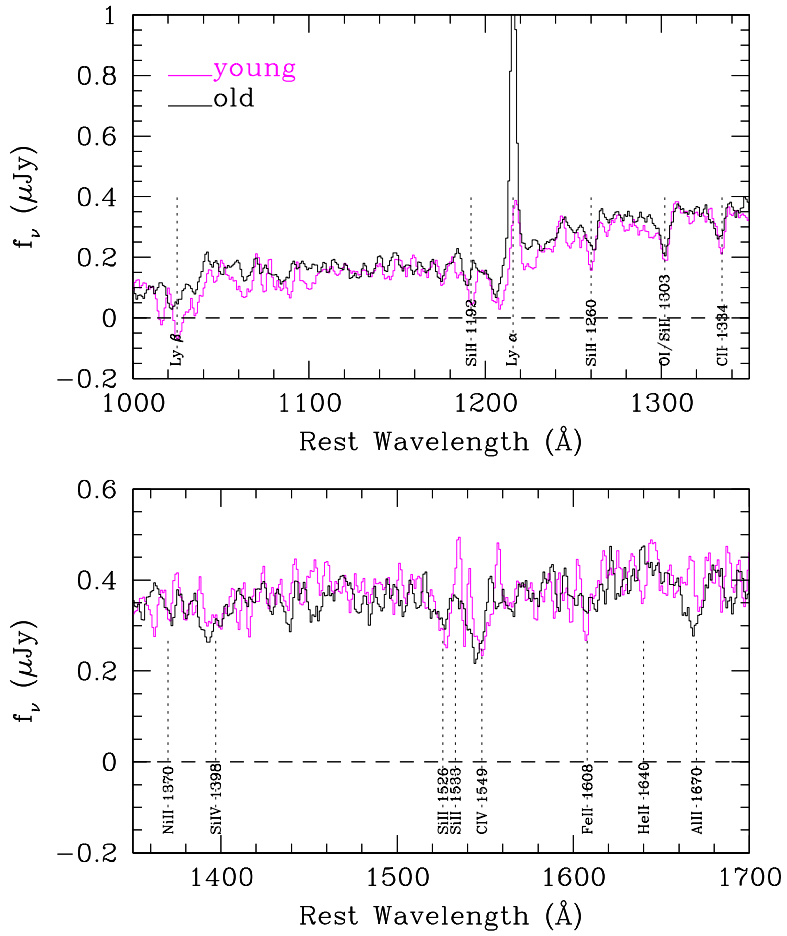

Figure 3.12 Comparison of "young" and "old" LRIS spectra. The composite spectrum of a subsample of galaxies with best-fit constant star-formation $t_{sf} \leq 35\,\mathrm{Myr}$ is shown in magenta (grey), while the composite spectrum of a subsample of galaxies with $t_{sf} \geq 1\,\mathrm{Gyr}$ is shown in black. The most striking differences between the two composite spectra are the relative strengths of Lyman-α emission; the relative strengths of the interstellar features Si II 1192, 1260, 1526 Å, CII 1334 Å, and Al II 1670 Å; and the relative CIV 1549 Å P-Cygni profiles.

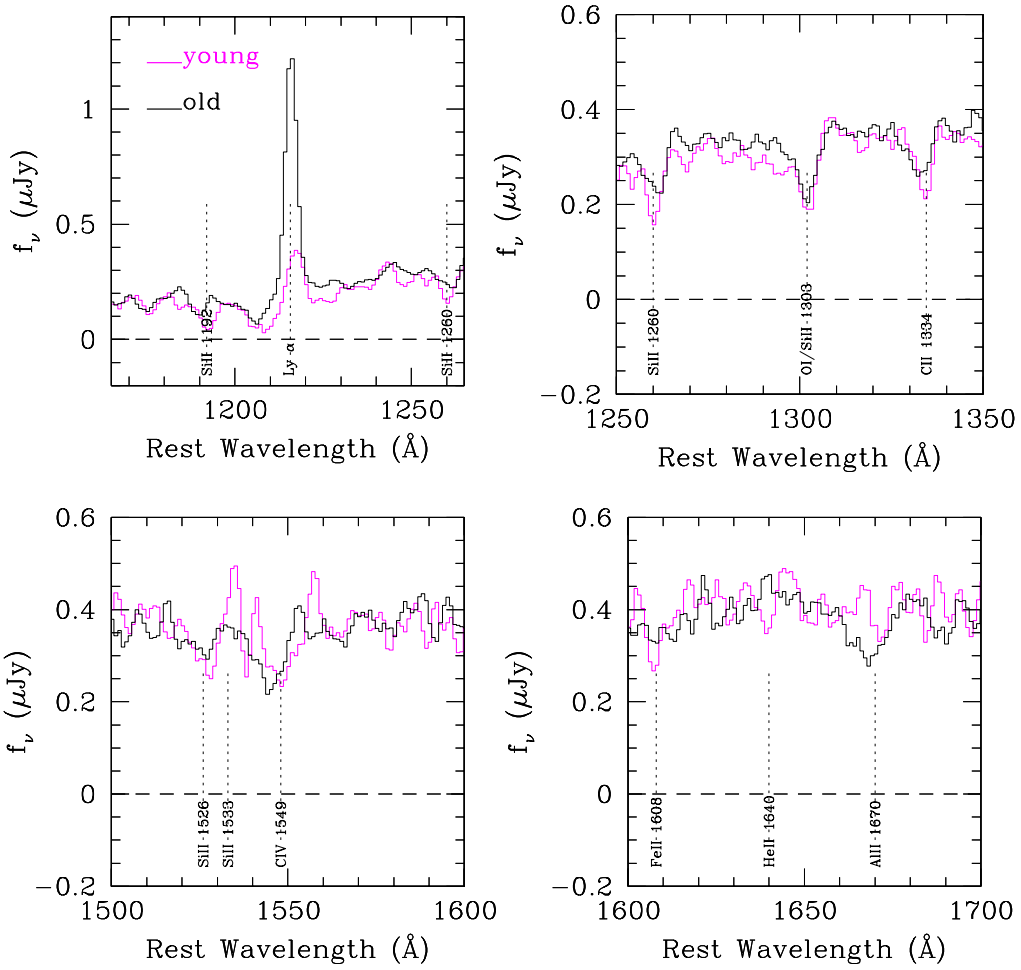

Figure 3.13 Zoomed in comparison of "young" and "old" LRIS spectra. Four regions of the composite young and old spectra are expanded for a more detailed view. The vertical axis of the detailed plot of Lyman-α spans a larger range in intensity than the other plots, for the purpose of showing the full extent of the strong Lyman-α emission in the old spectrum.

(based on the higher $\Psi(t_{sf})$) deposits larger amounts of mechanical energy into the ISM, accelerating the interstellar gas to higher velocities.

3.6 A Proposed Evolutionary Sequence for LBGs

A picture begins to emerge from the range of stellar populations observed in the NIRC LBG sample. At one extreme of the continuum, there is a group of galaxies with best-fit ages younger than or equal to the dynamical timescale associated with the luminous portions of LBGs. Based on NIRC and *HST*-WFPC2 observations, the typical LBG angular half-light radius is $0''.25$ (Giavalisco et al., 1996b; Pettini et al., 1998). This angular size translates into $r_{hl} = 1.3h^{-1}$ kpc at $z = 3$. Furthermore, from near-IR spectroscopic measurements of a sample of 15 LBGs, the typical nebular line widths are $\sigma \simeq 80$ km s^{-1}(Pettini et al., 2001). The associated dynamical timescale is $t_{dyn} \simeq \frac{2r_{hl}}{\sigma}$. With typical values for r_{hl} and σ, this calculation yields $t_{dyn} \simeq 30\, h^{-1}$ Myr. A starburst cannot occur on timescales shorter than the dynamical timescale of the region experiencing star-formation, for reasons of causality. Since a constant star-formation model with an age less than or equal to the dynamical timescale is indistinguishable from a bursting mode with a decay time, τ, limited to be greater than or equal to the dynamical timescale, the young, dusty galaxies in the NIRC LBG sample might well be described as galaxies undergoing bursts of star-formation. Whatever the cause of the burst of star-formation, we see intense star-formation and enhanced dust extinction in the youngest galaxies. At the other extreme are the galaxies whose best-fit constant star-formation t_{sf} values are close to a Hubble time at $z \sim 3$, whose dust extinction is only moderate, and whose star-formation rates are more quiescent. The NIRC LBG sample also contains galaxies with ages, dust-extinction, and star-formation rates which are intermediate between these two extremes.

Since the range of NIRC LBG stellar populations is controlled by two strong correlations—one between dust and age, and another between dust and intrinsic star-formation rate—we use these correlations to construct a unified evolutionary model for LBGs at high redshift. According to this model, the "young" and "old" samples discussed in this section constitute different evolutionary stages of the same population, which are both selected as LBGs. The "young" galaxies represent objects in the first stage, where the star-formation rate is very active ($\geq 200h^{-2}M_{\odot}$ yr^{-1}), large amounts of dust obscure the sites of star-formation, and a stellar mass on the order of $10^9 M_{\odot}$ is formed in a dynamical timescale. As time passes, dust is either destroyed or blown out, (or both), resulting in lower extinction, and the star-formation rate decays on a $\sim 50 - 100$ Myr timescale to reach the more quiescent rates seen in the "old" sample ($\sim 25h^{-2}M_{\odot}$ yr^{-1}). The "old" sample then represents the most advanced stage of the evolution which we observe in $z \sim 3$ LBGs, by which stage a stellar mass of $\gtrsim 10^{10} M_{\odot}$ has formed. As discussed earlier, for most "old" LBGs, it is not possible to distinguish from a strong Balmer break whether constant star-formation has continued for at least

1 Gyr, or whether exponentially declining star-formation has continued well past the age of the time constant, τ. If the relatively quiescent star-formation rates of the old galaxies are extrapolated back to the ages of the young/dusty sample assuming an exponentially declining star-formation rate with a time constant on the order of the dynamical timescale for LBGs, the star-formation rates obtained are on the order of the active rates in the young-dusty sample.

Such a simple evolutionary picture for LBGs is qualitatively consistent with the strong correlations we see in the NIRC LBG stellar population parameters. This evolutionary picture predicts a relatively flat distribution of t_{sf} values, which is broadly consistent with the observed t_{sf} histogram (Figure 3.6) except for the smallest t_{sf} bin, which is "over-sampled" in the NIRC LBG data set by about a factor of two (§ 2.2.2). While correcting the youngest bin by this amount makes the t_{sf} distribution flatter, the youngest bin still contains more galaxies than the other bins, implying that some fraction of the young, dusty, actively star-forming galaxies may fade to star-formation rates which are too low to be detected with the (ground-based) LBG criteria.

There are several interesting issues which accompany the above scenario. First, there is the question of what process produces the initial, rapid star-formation phase. Some obvious possibilities are major or minor merger events (e.g., Somerville et al., 2001; Mihos & Hernquist, 1996), or even the initial collapse of the baryonic component of the galaxy. Second, there is the question of how the large amount of dust in the significantly reddened "young" galaxies forms, given the relatively short timescales implied by the ages of these galaxies—how much of the dust is formed in the current star-formation episode, and how much originated in previous generations of stars?

Another important issue is the process by which dust is depleted as "young" LBGs evolve into "old" galaxies. There are a few proposed mechanisms for the removal of dust from galaxies. The first is radiation pressure, by which dust grains (especially larger ones $\sim 0.1\,\mu$m in size) can be expelled by the general radiation field of a galaxy. Davies et al. (1998) have numerically modeled the removal of dust from a present-day L^* spiral galaxy by radiation pressure, and have shown that up to 90% of the dust formed in such a galaxy may be ejected from the disk. While the relevant physical conditions might not be identical in local spiral galaxies and the high redshift LBGs, radiation pressure provides one viable mechanism by which dust can be removed from galaxies. Perhaps more relevant to the conditions in LBGs is the observational evidence for galactic-scale outflows, so-called "superwinds," in actively star-forming local galaxies. These outflows are due to the combined mechanical energy input from supernovae and winds from massive stars, which sweeps up interstellar material and accelerates it to speeds of several hundred km s^{-1} or greater (Heckman et al., 1990, 2000). There is strong kinematic evidence for such outflows in LBGs at high-redshift as well (Franx et al., 1997; Steidel et al., 1998; Pettini et al., 1998, 2000, 2001). Relative to the nebular emission lines representing the systemic velocity of the galaxy, low-ionization interstellar absorption lines in LBG rest-frame UV spectra are blue-shifted by ~ 300 km s^{-1}, and Lyman-α emission is redshifted

by $200 - 1100\,\mathrm{km\,s^{-1}}$ (Pettini et al., 2001). The implied typical outflow velocities are $\sim 400 - 500$ km $\mathrm{s^{-1}}$, and in the best studied case (Pettini et al., 2000) the implied mass outflow rate equals or exceeds the current star-formation rate (similar to what is seen in local starburst galaxies—e.g., Martin, 1999).

Recently, there has been direct observational evidence that dust, as well as gas, has been swept up by starburst superwinds and is contained in the material outflowing from local starburst galaxies (Heckman et al., 2000; Alton et al., 1999). Heckman et al. (2000) determine a typical outflowing dust mass of $10^6 - 10^7 M_\odot$ with a typical dust outflow rate of $0.1 - 1 M_\odot\,\mathrm{yr^{-1}}$ for the starbursts in their sample. While there are no direct observations of dust in LBG outflows, the presence of dust in the ISM of LBGs is required by their broadband colors. It seems very reasonable that the dust in the ISM of LBGs becomes entrained in the outflows implied by the kinematics of UV interstellar and nebular spectral features. The process of dust being expelled in superwinds from starburst galaxies at high redshift is qualitatively consistent with the observed trend between extinction and star-formation age in LBGs. Indeed, the superwind phenomenon has important implications not only for the enrichment of the intergalactic medium, but also for the evolution of dust opacity in galaxies.

Table 3.1. Lyman-Break Galaxy Constant SFR Best-Fit Parameters

Object Name	$E(B-V)$	t_{sf} (Myr)	SFR ($h^{-2}M_{\odot}\mathrm{yr}^{-1}$)	$\log(m_{star}(h^{-2}M_{\odot}))$
CDFa-C1	0.08	905	35	10.5
CDFa-C19	0.38	203	156	10.5
CDFa-C22	0.13	1278	36	10.7
CDFa-C8[b]	0.26	10	275	9.4
CDFa-MD2	0.20	321	65	10.3
Q0201-C6	0.08	321	23	9.9
Q0201-B13	0.04	2500	14	10.5
Q0256-C15	0.02	905	12	10.0
Q0256-M13	0.15	404	32	10.1
B20902-C6	0.05	509	15	9.9
B20902-D11	0.09	1278	53	10.8
B20902-M11	0.21	143	80	10.1
B20902-MD11	0.17	30	69	9.3
B20902-MD21	0.23	35	99	9.5
B20902-MD32	0.24	35	110	9.6
HDF-CC24	0.08	806	19	10.2
HDF-DD15	0.10	227	42	10.0
HDF-DD3	0.12	719	23	10.2
HDF-MM17	0.30	321	104	10.5
HDF-MM18	0.32	203	179	10.5
HDF-MM23[a]	0.18	2000	36	10.8
HDF-MM25	0.09	360	11	9.6
HDF-MM28[a]	0.05	1800	8	10.1
HDF-MM9[a]	0.24	2100	49	11.0
HDF-oC37	0.11	114	9	9.0
HDF-oC38[a]	0.15	2000	18	10.5
HDF-oM5	0.29	55	81	9.6
WESTPHAL-CC1[b]	0.34	10	516	9.7
WESTPHAL-CC13	0.11	227	51	10.1
WESTPHAL-CC32	0.06	454	16	9.9
WESTPHAL-CC43	0.23	454	104	10.6
WESTPHAL-CC45	0.23	255	33	9.9

Table 3.1 (cont'd)

Object Name	$E(B-V)$	t_{sf} (Myr)	SFR ($h^{-2}M_{\odot}\mathrm{yr}^{-1}$)	$\log(m_{star}(h^{-2}M_{\odot}))$
WESTPHAL-CC70	0.10	321	32	10.0
WESTPHAL-CC79	0.18	641	45	10.4
WESTPHAL-DD49	0.17	1139	68	10.9
WESTPHAL-CC63[b]	0.36	10	942	10.0
WESTPHAL-DD8	0.32	15	175	9.4
WESTPHAL-MM8	0.37	40	324	10.1
WESTPHAL-MMD109[b]	0.41	10	662	9.8
WESTPHAL-MMD113	0.23	81	156	10.1
WESTPHAL-MMD115[b]	0.13	10	71	8.9
WESTPHAL-MMD23	0.32	20	219	9.6
WESTPHAL-MMD54	0.10	1278	14	10.3
WESTPHAL-MMD91	0.16	286	42	10.1
WESTPHAL-west3-C11	0.29	15	223	9.5
3C324-C1	0.12	1434	20	10.4
3C324-C2	0.12	1700	22	10.6
3C324-C3	0.07	641	19	10.1
SSA22a-aug96D1	0.17	321	37	10.1
SSA22a-C11	0.08	1139	18	10.3
SSA22a-C15[a]	0.12	2000	11	10.3
SSA22a-C16	0.21	181	109	10.3
SSA22a-C36	0.17	571	48	10.4
SSA22a-C6[b]	0.20	10	204	9.3
SSA22a-D14	-0.01	571	6	9.6
SSA22a-M10[b]	0.30	10	212	9.3
SSA22a-M14	0.15	571	12	9.8
SSA22a-M4	0.13	321	17	9.7
SSA22a-D3[b]	0.29	10	540	9.7
SSA22a-MD3	0.24	15	54	8.9
SSA22a-MD4	0.14	641	21	10.1
SSA22a-MD40	0.21	20	45	9.0
SSA22a-MD46	0.01	806	22	10.2
SSA22b-oct96D8[a]	0.06	1900	32	10.8

Table 3.1 (cont'd)

Object Name	$E(B-V)$	t_{sf} (Myr)	SFR ($h^{-2}M_{\odot}\mathrm{yr}^{-1}$)	$\log(m_{star}(h^{-2}M_{\odot}))$
DSF2237a-C2	0.15	719	76	10.7
DSF2237b-C1[a]	0.05	2100	6	10.1
DSF2237b-C26	0.05	1139	9	10.0
DSF2237b-D28	0.06	719	10	9.9
DSF2237b-D3	0.16	30	46	9.1
DSF2237b-D4	-0.04	1278	5	9.8
DSF2237b-M19	0.20	161	40	9.8
DSF2237b-M20	0.21	227	69	10.2
DSF2237b-MD10	0.29	35	88	9.4
DSF2237b-MD2[b]	0.39	10	377	9.6

[a]The best-fit ages for marked galaxies, when unconstrained, were older than the age of the universe at the galaxy's redshift. The best-fit quantities listed for these galaxies reflect the constraint that the age of a galaxy should not be older than the age of the universe. Such a constraint still provides statistically acceptable fits for marked galaxies.

[b]The best-fit ages for the marked galaxies, when unconstrained, were younger than 10 Myr. Such young ages are physically implausible, and therefore we restricted the best-fit ages to be at least 10 Myr. The best-fit quantities listed for marked galaxies reflect this constraint, and provide statistically acceptable fits for marked galaxies.

Chapter 4

Summary and Conclusions

We have presented the results of a near-IR survey of optically selected $z \sim 3$ LBGs. The survey includes 118 galaxies with K_s measurements, 63 of which also have J measurements. We combined the new near-IR data with previously obtained optical data to compute the distributions of optical/IR colors of LBGs. We have used the photometric data, spanning typical rest-frame wavelengths of 900–5500 Å to obtain the following results:

1. The rest-frame optical luminosity function of UV-selected LBGs greatly exceeds locally determined luminosity functions at the bright end. A Schechter function fit formally yields a very steep ($\alpha = -1.85 \pm 0.15$) faint-end slope, but part of this could be due to the fact that at our detection limit of $K_s = 22.5$ ($M_V = -20.41 + 5\log h$ at $z \sim 3$) the data do not extend significantly beyond the knee in the luminosity function and the overall shape of the luminosity distribution is quite different from the local functions. Independent of the fitted parameters, the $z \sim 3$ optical luminosity function has a large excess of luminous galaxies relative to locally determined luminosity functions. Down to our detection limit of $K_s = 22.50$ (or a luminosity equivalent to $\sim 1.2L^*$ in the present-day V-band luminosity function), the rest-frame optical co-moving luminosity density of LBGs (uncorrected for dust extinction) is $\rho_V = 1.35 \times 10^8 L_\odot h\,\mathrm{Mpc}^{-3}$. This value is already within a factor of 2 of values determined by integrating local luminosity functions down to arbitrarily small luminosities. Thus, the optical light from LBGs at $z \sim 3$ likely exceeds that produced by all stars in the local universe.

2. We have modeled the stellar populations and extinction of the LBGs with both spectroscopic redshifts and near-IR measurements (81 galaxies) using relatively simple prescriptions. Most of the galaxies have star-formation histories, star-formation rates, and star-formation ages that are only weakly constrained by the photometric observations without limiting parameter space using external constraints on the assumed extinction law and relatively simple forms for the star-formation history. We have chosen to report the results assuming the solar-metallicity Bruzual & Charlot (1996) models, a Salpeter IMF, the Calzetti (1997) starburst attenuation relation, and a constant star-formation history. The systematic effects of changing the any of these assumptions have been summarized.

3. When the interpretation of LBG stellar populations is restricted to BC96 constant star-

formation models, we find a large spread of inferred ages, ranging from several Myr to more than 1 Gyr. The median best-fit constant star-formation age is $t_{sf} = 320$ Myr. In model-independent terms, the distribution of best-fit ages indicates that a significant fraction of LBGs have been forming stars on timescales long enough that a detectable Balmer break exists in their spectral energy distributions. Although the specific age assigned to the Balmer break depends on the star-formation history used to fit the colors, we note that very recent work indicates that winds from LBGs similar to those modeled above have shock-heated the intergalactic medium on physical scales of $100 - 200h^{-1}$ kpc (Adelberger et al., 2003). Such a large sphere of influence, with typical outflow velocities of a few hundred km s^{-1}, suggests star-formation timescales of at least a few hundred million years for typical LBGs. This constitutes completely independent support for the timescales resulting from the stellar population modeling presented in this work. The BC96 constant star-formation distribution of best-fit $E(B-V)$ ranges from $\sim 0.0-0.45$ with a median of 0.155. This distribution depends less on star-formation history than the distribution of best-fit ages. The median implied extinction for this sample corresponds to a factor of ~ 4.5 attenuation in the rest-frame UV (1600 Å) and a factor of $\sim$2 in the rest-frame optical. Derived from the distributions of $E(B-V)$ and t_{sf}, the best-fit star-formation rate, $\Psi(t_{sf})$, ranges from $5-940h^{-2}M_{\odot}\,\mathrm{yr}^{-1}$, with a median of $45h^{-2}M_{\odot}\,\mathrm{yr}^{-1}$. The distribution of formed stellar masses, m_{star}, ranges over more than 2 orders of magnitude with a median of $\sim 10^{10}h^{-2}M_{\odot}$. We note that the above parameter distributions and median values may not be completely general to LBGs at $z \sim 3$, since the way in which the NIRC LBGs were selected tended to enhance the number of young, dusty, intensely star-forming, low m_{star} objects, relative to the full LBG sample.

4. Regardless of the star-formation history used in this work to model the colors of the NIRC LBGs, we find a strong correlation between dust extinction and intrinsic luminosity, such that dustier galaxies are intrinsically more luminous. This correlation has been reported by other authors (AS2000; Meurer et al., 1999), but here the extinction estimates are supported by observations over a wider wavelength baseline, spanning on average from 900−5500 Å in the rest frame. This dependence of extinction on luminosity is consistent with a similar relation seen for star-forming galaxies in the local universe, and has the implication that, for the range of galaxies which we select as LBGs, those which are more heavily obscured by dust are as easy to detect in the rest-frame UV and optical as galaxies which are less dusty, because they are also intrinsically more luminous.

5. For most galaxies, we find that the formed stellar mass derived from the integral of the best-fit star-formation rate over time depends relatively weakly on the star-formation history applied to fit the observed colors (cf. Papovich et al., 2001). Regardless of star-formation history, the inferred formed stellar mass is only weakly correlated with extinction corrected UV and optical luminosities for our total ground-based sample. This fact, together with the results on the rest-frame optical luminosity function of LBGs, shows that even at observed wavelengths of 2.15 μm, the luminosities

are poor proxies for stellar mass in general. Therefore, inferences on stellar mass from optical/near-IR photometry are highly IMF-dependent and will apply only to the stars that have formed in the last several hundred Myr prior to observation. Longer-wavelength observations with SIRTF should improve the situation considerably.

6. We find a strong correlation between inferred star-formation age and extinction in LBGs, such that younger galaxies are dustier than older galaxies, and have higher star-formation rates. Establishing the significance of this correlation is difficult because of the covariance of $E(B-V)$ and t_{sf} in our fits, but we have been unable to reproduce a similarly strong observed correlation from any intrinsically uncorrelated distributions of $E(B-V)$ and t_{sf}. The correlation might be made to vanish with a suitable choice of star-formation histories or dust attenuation curve (i.e., SMC), but its existence appears secure for the most plausible choices of both. We also present evidence that this correlation is not an artifact of either the LBG $G-\mathcal{R}$ selection criteria, or of the typical detection limit of $K_s = 22.5$ for the NIRC observations.

7. Composite rest-frame UV spectra of "young" and "old" subsamples of NIRC LBGs exhibit differences, most dramatically in their respective Lyman-α profiles, offering independent evidence that the youngest galaxies have more dust extinction and/or more active interstellar media. We interpret the dust-age correlation in the context of a unified picture of LBGs in which the younger, dustier, more actively star-forming galaxies evolve into the older, less reddened, and more quiescent galaxies. The evolution of the dust extinction towards lower values is probably governed by the outflow of dust which is entrained in a "superwind" powered by the energy from supernovae explosions and the winds from massive stars. Objects at various points along this evolutionary sequence are identified by the LBG optical selection criteria. The timescale for the evolution of the young-dusty galaxies into the older-less-reddened galaxies is on the order of $50-100\,\mathrm{Myr}$, while the more quiescent phase can last a Gyr or more.

We would like to thank the staff members of the Palomar, La Palma, Kitt Peak, and Keck Observatories for their assistance in both optical and near-IR observations. We would also like to thank Matthew Hunt, for assistance with the near-IR data reduction, and Stephane Charlot for helpful discussions and assistance in implementing the most up-to-date Bruzual and Charlot spectral synthesis codes. Finally, we wish to extend special thanks to those of Hawaiian ancestry on whose sacred mountain we are privileged to be guests. Without their generous hospitality, most of the observations presented herein would not have been possible. CCS, KLA, and AES have been supported by grants AST95-96229 and AST-0070773 from the U.S. National Science Foundation and by the David and Lucile Packard Foundation.

Part II

The Rest-Frame Ultraviolet Spectra of Lyman Break Galaxies

Abstract

We present the results of a systematic study of the rest-frame UV spectroscopic properties of Lyman Break Galaxies (LBGs). The database of almost 1000 LBG spectra proves useful for constructing high S/N composite spectra. The composite spectrum of the entire sample reveals a wealth of features attributable to hot stars, H II regions, dust, and outflowing neutral and ionized gas. By grouping the database according to galaxy parameters such as Lyα equivalent width, UV spectral slope, and interstellar kinematics, we isolate some of the major trends in LBG spectra that are least compromised by selection effects. We find that LBGs with stronger Lyα emission have bluer UV continua, weaker low-ionization interstellar absorption lines, smaller kinematic offsets between Lyα and the interstellar absorption lines, and lower star-formation rates. There is a decoupling between the dependence of low- and high-ionization outflow features on other spectral properties. Additionally, galaxies with rest-frame $W_{\mathrm{Ly}\alpha} \geq 20$ Å in emission have weaker than average high-ionization lines, and nebular emission lines which are significantly stronger than in the sample as a whole. Most of the above trends can be explained in terms of the properties of the large-scale outflows seen in LBGs. According to this scenario, the appearance of LBG spectra is determined by a combination of the covering fraction of outflowing neutral gas which contains dust, and the range of velocities over which this gas is absorbing. In contrast, the strengths of collisionally excited nebular emission lines should not be affected by the nature of the outflow, and variations in these lines may indicate differences in the temperatures and metallicities in H II regions of galaxies with very strong Lyα emission. Higher sensitivity and spectral resolution observations are still required for a full understanding of the covering fraction and velocity dispersion of the outflowing neutral gas in LBGs, and its relationship to the escape fraction of Lyman continuum radiation in galaxies at $z \sim 3$.

Chapter 5

The Lyman Break Galaxy Sample and Important UV Spectroscopic Features

5.1 Introduction

Until now, the rest-frame UV spectra of Lyman Break Galaxies (LBGs) have been used primarily to measure redshifts. At first, the spectra were used to confirm the cosmologically distant nature of galaxies photometrically selected with the Lyman Break Technique to be at $z \sim 3$ (Steidel et al., 1996a,b; Lowenthal et al., 1997). Spectroscopic redshifts were also necessary to study the large-scale spatial distribution and clustering properties of LBGs (Adelberger et al., 1998; Steidel et al., 1998; Giavalisco et al., 1998). Furthermore, the determination of the $z \sim 3$ rest-frame UV luminosity function required knowledge of the redshifts of LBGs, combined with the optical apparent magnitudes and colors (Steidel et al., 1999). Most recently, the redshifts measured from rest-frame UV spectra have been used to study the cross-correlation of the large-scale distributions of galaxies and the inter-galactic medium within the same cosmic volume (Adelberger et al., 2003). Given the faint nature of LBGs (most have $\mathcal{R}_{AB} = 24 - 25.5$), the desire to observe a large sample results in individual spectra with low signal-to-noise (S/N) ratios and spectral resolution. In most cases, the low S/N of LBG spectra precludes any analysis more detailed than the determination of redshifts.

One notable exception is the galaxy MS1512-cB58, an L^* LBG at $z = 2.73$ with an apparent magnitude of $V = 20.6$ due to lensing by a foreground cluster at $z = 0.37$ (Yee et al., 1996). Cluster lensing boosts the apparent luminosity of cB58 by a factor of ~ 30, enabling relatively high-resolution ($R \simeq 5000$) studies of its rest-frame UV spectrum (Pettini et al., 2000, 2002). The velocity profiles of low and high-ionization interstellar metal absorption features have been characterized in detail; the weakest interstellar metal transitions have been used together with the damped Lyα absorption profile to determine the abundance pattern in cB58 (an α/Fe enhancement indicative of a young

stellar population, and an abundance of $\sim 0.4Z_{\odot}$ for the α elements); C IV and Si IV P-Cygni stellar wind profiles have been used as independent probes of the stellar population and metallicity; weak stellar absorption features have been used to precisely measure the systemic velocity of the stars, relative to which the redshifts of Lyα emission and interstellar absorption indicate offsets of several hundred km s^{-1}; finally, the strengths of the strongest interstellar absorption features (which have zero transmission at line center) have been used to infer a high covering fraction of outflowing neutral material, through which negligible Lyman continuum emission can escape. For the vast majority of unlensed LBGs, it is unfortunately not possible to obtain individual spectra that contain the same high-quality information about physical conditions. Since cB58 is only one object, we need to worry about how "typical" its continuum and spectroscopic properties are, relative to the range seen in the entire sample of LBGs.

Even from the low S/N spectra used to measure redshifts, we discern a large variation in the types of spectra associated with LBGs. Most obviously, there are large ranges of Lyα profile shapes and UV continuum slopes. There are also variations among the equivalent widths of the few strong interstellar absorption lines that we detect most of the time in individual spectra, and of the redshift offset measured between Lyα emission and interstellar absorption (for spectra in which both types of features are detected). While there is no hope of collecting data of comparable quality to the cB58 spectra for individual unlensed LBGs, we have assembled a sample of almost 1000 spectroscopically confirmed $z \sim 3$ galaxies over the past six years. By dividing our spectroscopic database into subsamples according to specific criteria, and creating high S/N composite spectra of each subsample, we hope to understand how the LBG spectroscopic properties depend in a systematic way on other galaxy properties.

Past uses of composite LBG spectra have proven very illustrative. For example, a composite of 29 individual LBG spectra at $\langle z \rangle = 3.4 \pm 0.09$ shows significant residual flux shortward of the Lyman limit at 912 Å (Steidel et al., 2001). If this composite spectrum is taken to be representative of LBGs at $z \sim 3$, the LBG contribution to the ionizing background could exceed that of QSOs at similar redshifts by as much as a factor of 5. The appearance of this composite spectrum is very different from that of cB58, with strong Lyα emission, a continuum slope in the bluest quartile of the total LBG sample, and interstellar absorption lines roughly half the strength of those in the cB58 spectrum. Determining the relative numbers of LBGs that resemble this composite versus those that more closely resemble cB58 is important for determining the overall contribution of LBGs to the ionizing background. Composite LBG spectra were also constructed for galaxy subsamples grouped by the stellar population age inferred from optical/near-IR photometry (Shapley et al., 2001). The "young" ($t \leq 35$ Myr) and "old" ($t \sim 1$ Gyr) composite spectra exhibited systematic differences, including significantly stronger Lyα emission in the "old" spectrum, and stronger interstellar absorption and stellar P-Cygni wind features in the "young" spectrum. Such differences may indicate

an evolutionary sequence for the appearance of the rest-frame UV spectra.

Based on the promise of these specific composite studies, we are motivated to undertake a more general study of the spectroscopic properties of the entire LBG sample. This systematic study is in some ways a high-redshift analog to the work of Heckman et al. (1998), which characterized the region of UV spectroscopic parameter space inhabited by local starburst galaxies. In particular, we would like to gain more detailed information about the properties of the large-scale outflows of interstellar material which are inferred in LBGs from blueshifted interstellar absorption and redshifted Lyα emission, relative to the systemic stellar redshift (Pettini et al., 2001, 2002; Franx et al., 1997; Lowenthal et al., 1997). The outflows represent not only an important feedback process that affects galaxy formation and evolution, but also may have a profound impact on the metal enrichment, ionization, and physical state of the surrounding intergalactic medium (Adelberger et al., 2003; Adelberger, 2003; Steidel et al., 2001). So far, most of the information about the nature of outflows at high redshift comes from high-quality observations of a single galaxy—cB58—and from studies of the metal content and HI opacity of the Lyα forest near LBGs. The current survey provides information that is complementary to both types of observations, as it explores outflow properties from the galaxy perspective, but is based on a much larger (if lower spectral resolution) sample of galaxies.

The LBG spectroscopic sample is described in § 5.2, while § 5.3 presents the method of generating composite spectra and defining the "rest-frame" in the presence of large-scale velocity fields. § 5.4 gives an overview of the types of stellar and interstellar spectroscopic features that appear in high S/N composite LBG spectra, *some of which have not previously been observed in UV spectra of local star-forming regions.* In Chapter 6, we present some of the important trends observed in LBG spectra, with particular attention to outflow-related properties. Finally, in Chapter 7, we present a physical picture that is broadly consistent with the observations, and highlight the need for several future observations to test this picture.

5.2 The LBG Spectroscopic Sample

The individual galaxy spectra used to construct the composite spectra in this paper were drawn from the Lyman Break Galaxy (LBG) survey of $z \sim 3$ galaxies. The details of our survey have been presented elsewhere (Steidel et al., 1996a,b, 1999) and will be extensively summarized in a future work (Steidel et al., 2003), so here we present only a few relevant features. The full LBG photometric sample consists of 2347 galaxies in 17 separate fields with optical colors satisfying the following criteria:

$$\mathcal{R} \leq 25.5, \quad G - \mathcal{R} \leq 1.2, \quad U_n - G \geq G - \mathcal{R} + 1 \tag{5.1}$$

plus an additional 180 galaxies with the same color criteria, but $\mathcal{R}$ magnitudes that are as faint as $\mathcal{R} = 26$ (which are located in the LBG survey field containing the bright quasar, Q1422+239, for which we obtained significantly deeper photometry, allowing an extension of the LBG selection technique to fainter magnitudes).

We have spectroscopically observed 1320 of these photometric candidates using the Low Resolution Imaging Spectrometer (LRIS) at the W. M. Keck Observatory (Oke et al., 1995). Most of the spectra were obtained using a 300 lines mm^{-1} grating blazed at 5000 Å, and a multi-object slit mask with $1''.4$ slits, providing a spectral resolution of $8 - 12$ Å, depending on the seeing. Recent spectroscopic data, including some of the observations in the Q0933+288 and Q1422+2309 fields, and all of the data in the Q0302−003 field, were obtained with the new blue arm of LRIS (LRIS-B; McCarthy et al. 1998; Steidel et al. 2003, in preparation), and dispersed by a 300 lines mm^{-1} grism blazed at 5000 Å. This setup provided slightly higher spectral resolution than the 300-line grating setup, and much higher throughput. Typical exposure times for both setups were 3×1800 sec with $1''.0$ dithers between exposures to provide for adequate sky-subtraction. The two-dimensional, sky-subtracted, and coadded spectra were then extracted to one-dimension, and wavelength calibrated using a HgNeAr arc-lamp spectrum. Spectra were flux-calibrated with observations of standard stars taken close to the time of the science observations. Finally, air wavelengths were converted to vacuum wavelengths, in order to measure redshifts in the vacuum frame. The average S/N ratio of spectra in the sample is ~ 4 per resolution element.

From this sample of spectra, we identify 36 stars, 2 absorption-line galaxies at $z \sim 0.5$, 2 galaxies with $z \simeq 1.98$, 957 objects at $z > 2$, and 292 objects for which we cannot measure a redshift. Of the 957 galaxies at $z > 2$, 12 are identified as broad-lined AGN due to the presence of emission lines with FWHM > 2000 km s^{-1}, while 16 are identified as narrow-lined AGN with strong Lyα emission accompanied by significant C IV λ1549 emission, but FWHM < 2000 km s^{-1}(Steidel et al., 2002). We exclude from the spectroscopic sample the 28 objects identified as AGN on an individual basis (though we may have included galaxies with low-level AGN activity that is undetected in individual spectra but may become evident in the composites. We will treat this point further in section 5.4.3.1). Furthermore, we include only galaxies whose redshifts were independently and securely confirmed by at least two members of our group. This last criterion limits our composite sample to 811 spectra.

5.3 Generating the Composite Spectra

There are several steps required to generate the composite galaxy spectra presented in this work. The first step consists of carefully defining a sample of galaxy spectra to be combined. Each extracted, one-dimensional, flux-calibrated spectrum in the sample is then shifted into the rest frame. The

spectra are then averaged, after being scaled to a common mode in the wavelength range 1250-1500 Å and rebinned to a common dispersion of 1 Å per pixel. In order to exclude both positive and negative sky subtraction residuals and cosmic ray events, an equal number of positive and negative outliers are rejected at each dispersion pixel, totaling less than 10% of the data.

5.3.1 Measuring Redshifts

One of the non-trivial aspects of generating the composite spectra consists of defining a systemic rest frame for each galaxy. The low S/N ratio of typical LBG spectra precludes much more than measuring redshifts from the very strongest rest-frame UV features. These features include H I Lyα, seen either in emission, absorption, or a combination of both; low-ionization resonance interstellar metal lines such as Si II λ1260, O I λ1302 + Si II λ1304, C II λ1334, Si II λ1526, Fe II λ1608, and Al II λ1670, which are associated with the neutral interstellar medium; and high-ionization metal lines such as Si IV $\lambda\lambda 1393, 1402$ and C IV $\lambda\lambda 1548, 1550$ associated with ionized interstellar gas and P-Cygni stellar wind features. In 28% of the rest-frame UV LBG spectra in our spectroscopic sample, the only spectral feature visible is Lyα emission. In 32% of the spectra, Lyα appears only as broad absorption, and multiple low- and/or high- ionization interstellar absorption lines are used to measure the redshift (broad Lyα absorption is not very precise as a redshift indicator). Finally, in the remaining 40% of the spectra, both Lyα emission and interstellar absorption lines are visible and both can be used to measure redshifts. In 95% of the cases where both Lyα emission and interstellar absorption lines have been used to measure the redshift of the galaxy, the Lyα emission redshift is higher than the interstellar absorption redshift. Figure 5.1 shows the distribution of $\Delta v_{\rm em-abs}$, which has $\langle \Delta v_{\rm em-abs} \rangle \sim 650$ km s^{-1}. This velocity difference indicates that at least one of the two sets of features is not at rest with respect to the stars in the galaxy. Such kinematics suggest that LBGs are experiencing large-scale outflows caused by the mechanical energy input from supernova explosions that are the result of vigorous massive star-formation rates. It has been shown that, in the local universe, any galaxy with a star-formation rate surface-density $\Sigma_* \geq 0.1 M_\odot$ yr^{-1}kpc^{-2} is capable of driving a superwind (Heckman, 2002). Given their typical star-formation rates and physical sizes, LBGs easily satisfy and exceed the criteria for driving a superwind (Shapley et al., 2001; Giavalisco et al., 1996b).

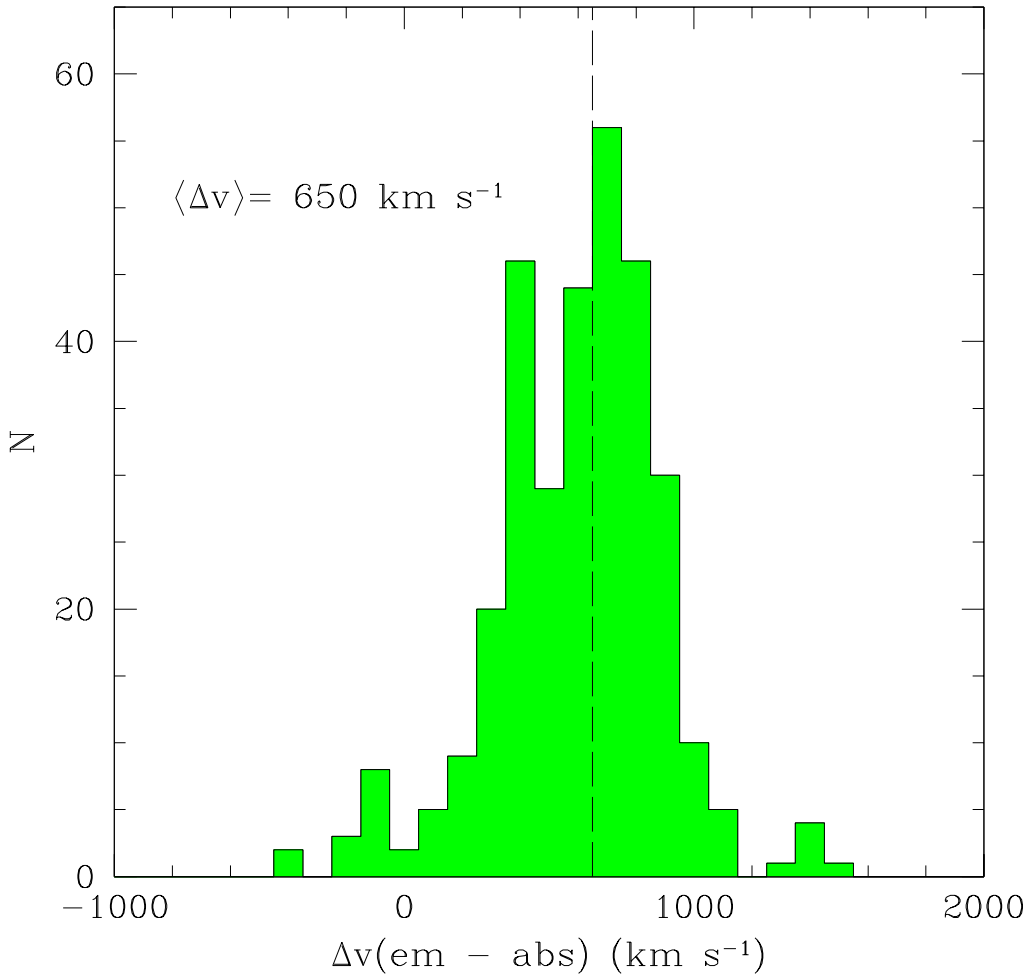

Figure 5.1 The distribution of velocity offsets between Lyα emission and low-ionization interstellar absorption. The most straightforward indication that LBGs are experiencing large-scale outflows of their interstellar material is the velocity offset measured in individual spectra between Lyα emission and interstellar absorption lines. This histogram shows the distribution of velocity offsets for the 323 galaxies with spectra in which both types of features are detected. The mean velocity offset (redshift difference) is $\Delta v = 650$ km s^{-1}($\Delta z = 0.008$).

Since the only features that can be detected in individual LBG spectra seem to trace outflow kinematics, the outflows complicate our effort to assign systemic redshifts. In general, stellar systemic redshifts cannot be measured for individual galaxies because UV photospheric features from hot stars are much too weak to see in typical LBG spectra. In order to estimate stellar systemic redshifts for individual galaxies, we applied the formulae presented in Adelberger et al. (2003), which predict a value of the systemic redshift for three separate cases: when there is only a Lyα emission redshift; when there is only an interstellar absorption redshift; and when there are both Lyα emission and interstellar absorption redshifts.

While no reference was made to stellar photospheric features in the estimate of the systemic redshifts of individual galaxies, the rest-frame composite spectrum presented in the next section indicates a mean systemic velocity of $\Delta v = -10 \pm 35$ km s^{-1} for the three strongest stellar features, which we have identified as C III λ1176, O IV λ1343, and S V λ1501. [1] It is worth noting possible contributions to the O IV λ1343 absorption from Si III λ1341, and to the S V λ1501 absorption from Si III λ1501, if there is a significant B-star component in the composite spectrum. However, at least the Si III λ1501 contribution will not change the inferred negligible systemic velocity of the feature that we have identified as S V λ1501. The insignificant velocities of the stellar features demonstrate the success of the systemic redshift estimates for the LBGs included in composite spectra, at least on average. Also, since the stellar features appear at roughly zero velocity, the redshifts and blueshifts of other sets of spectral features measured relative to the rest-frame of the composite spectrum should offer a true representation of the average kinematic properties of the large-scale galactic outflows in LBGs. The establishment of the velocity zeropoint from the stellar lines in composite spectra represents a significant improvement over the kinematic information contained in individual rest-frame UV spectra, where only the strongest interstellar outflow-related features are detected.

5.4 LBG Rest-frame UV Spectroscopic Features

Figure 5.2 shows a composite spectrum that is the average of our entire spectroscopic sample of 811 LBGs, combined in the manner described in section 5.3. Rest-frame UV spectra of LBGs are dominated by the emission from O and B stars with masses higher than $10 M_{\odot}$ and $T \geq 25000K$. The overall shape of the UV spectrum is modified by dust extinction internal to the galaxy, and, at rest wavelengths shorter than 1216 Å, by inter-galactic HI absorption along the line of sight. Composite spectra contain the average of many different lines of sight through the IGM. Therefore, spectral features that are intrinsic to the galaxy at wavelengths shorter than Lyα, and which can be completely wiped out by individual Lyα forest systems along a specific line of sight, become visible in the composite spectra. While we regain spectroscopic information by averaging over many different

[1] The precise wavelengths are C III λ1175.71, O IV λ1343.35, which is a blend of lines at $\lambda = 1342.99$ and $\lambda = 1343.51$, and S V λ1501.76.

sightlines, we still, however, see the average decrement of the Lyα forest, D_A. In the following section, we describe the spectroscopic features contained in the composite spectrum of Figure 5.2, which trace the photospheres and winds of massive stars, neutral and ionized gas associated with large-scale outflows, and ionized gas in H II regions where star formation is taking place.

5.4.1 Stellar Features

The C III 1176, O IV 1343, and S V 1501 stellar photospheric lines discussed in section 5.3.1 are marked in Figure 5.2. Also of note (though not marked) is the large number of weak absorption features between 1400 and 1500 Å. These include blends of Fe V, Si II, Si III, and C III photospheric absorption lines from O and B stars (Bruhweiler et al., 1981; de Mello et al., 2000). In addition to photospheric absorption features, the spectra of the most massive hot stars indicate the presence of stellar winds of 2000-3000 km s^{-1} due to radiation pressure (Groenewegen et al., 1989). These wind features appear as broad blue-shifted absorption for weaker winds, or as a P-Cygni type profile if the wind density is high enough (Leitherer et al., 1995). The most prominent stellar wind features are N V $\lambda\lambda 1238, 1242$, Si IV $\lambda\lambda 1393, 1402$, C IV $\lambda\lambda 1548, 1550$, and He II $\lambda 1640$. The shape of the N V wind profile, especially the absorption component, is affected by its close proximity to the Lyα region of the spectrum, and is therefore difficult to characterize in detail, though we do see both emission and absorption qualitatively consistent with a P-Cygni type profile. While clear of the large-scale continuum effects of Lyα, the Si IV and C IV transitions contain the combination of stellar wind and photospheric absorption, plus a strong interstellar absorption component, which are difficult to disentangle. The stellar wind feature only becomes apparent in Si IV for blue giant and supergiant stars, while, in contrast, the C IV wind feature is strong in main sequence, giant, and supergiant O stars (Walborn & Panek, 1984). Consequently, the interstellar, rather than the wind component, seems to dominate the Si IV doublet in the LBG composite spectrum, while the C IV feature exhibits both the blue-shifted broad absorption and redshifted emission associated with stellar winds, in addition to a strong, narrower, interstellar absorption component. The redshifted emission indicates the presence of stars with $M \geq 30 M_{\odot}$ (Leitherer et al., 1995; Pettini et al., 2000). In Figure 5.3, a Starburst99 model spectrum (Leitherer et al., 1999) is plotted over the zoomed-in C IV $\lambda\lambda 1548, 1550$ region of the LBG composite spectrum for comparison. The model spectrum is for a 300 Myr old episode of continuous star formation (the median stellar population age inferred from the optical/near-IR colors of LBGs, Shapley et al. 2001), and is constructed from a library of *Hubble Space Telescope (HST)* FOS and STIS observations of massive hot stars in the Magellanic Clouds with a mean metallicity $Z = 0.25 Z_{\odot}$ (consistent with the limited information on LBG metallicities). The model and data agree quite well in the emission component of the P-Cygni profile. However, the model overpredicts the strength of the broad wind absorption. This discrepancy may be due to a combination of age and metallicity effects.

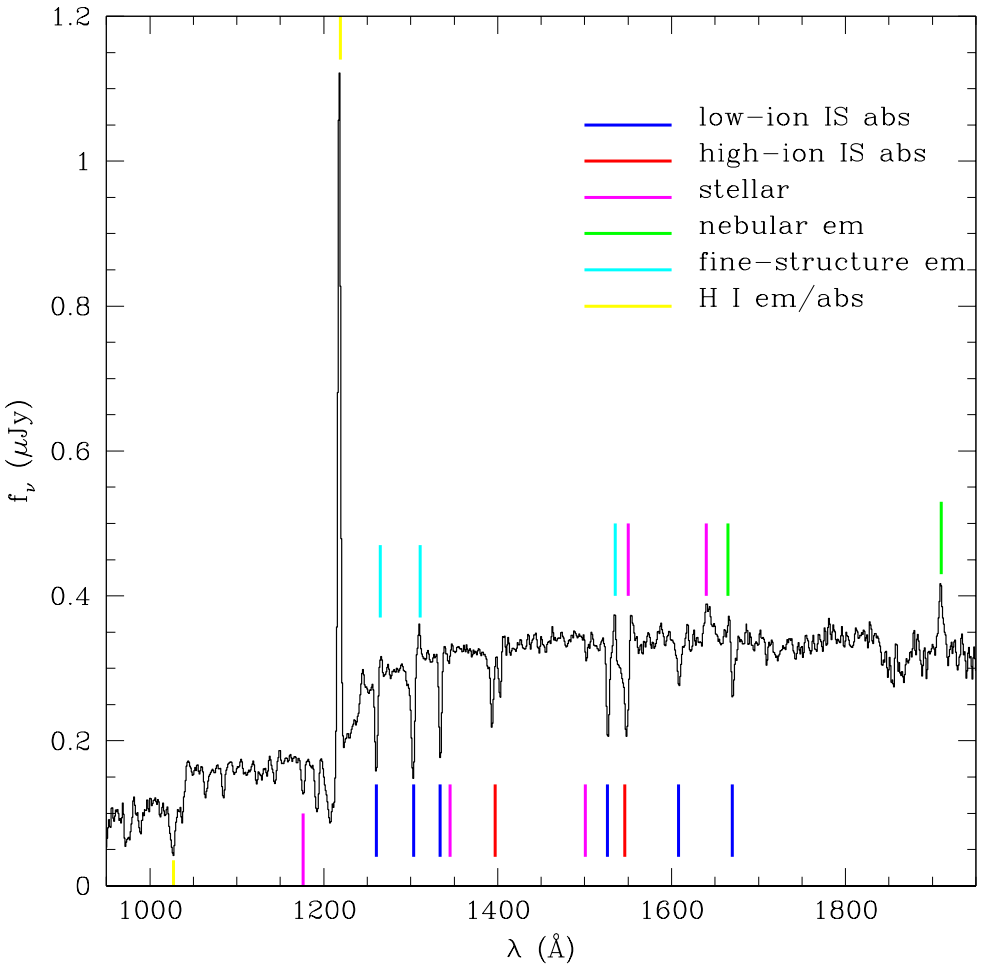

Figure 5.2 A composite rest-frame UV spectrum constructed from 811 individual LBG spectra. Dominated by the emission from massive O and B stars, the overall shape of the UV continuum is modified shortward of Lyα by a decrement due to inter-galactic HI absorption. Several different sets of UV features are marked: stellar photospheric and wind, interstellar low- and high-ionization absorption, nebular emission from H II regions, Si II* fine-structure emission whose origin is ambiguous, and emission and absorption due to interstellar HI (Lyα and Lyβ). There are numerous weak features which are not marked, as well as several features bluewards of Lyα which only become visible by averaging over many sightlines through the IGM. The composite LBG spectrum is available in electronic form from http://www.astro.caltech.edu/~aes/lbgspec/.

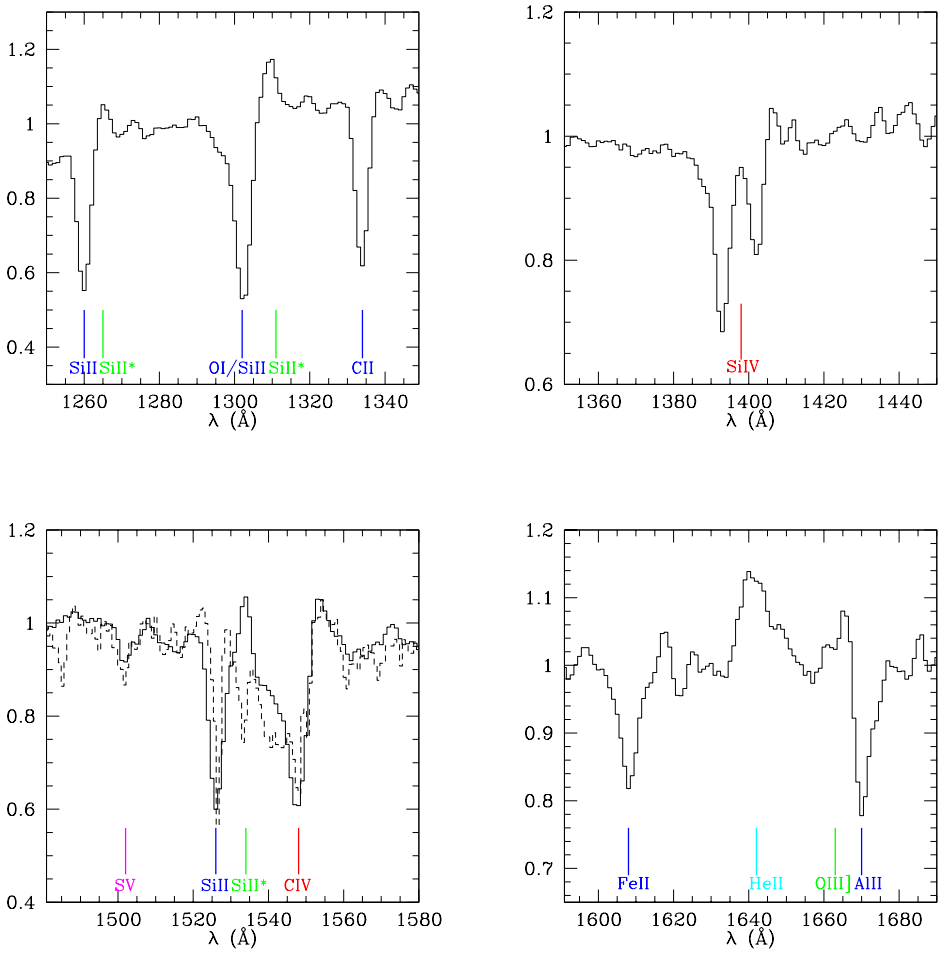

Figure 5.3 Four zoomed-in regions from the composite spectrum of Figure 5.2. The zoomed-in vertical scale allows a more detailed look at weak emission features such as Si II* $\lambda\lambda\lambda 1265, 1309, 1533$, and O III] $\lambda\lambda 1661, 1666$. The lower left-hand box shows the zoomed-in region near C IV $\lambda\lambda 1548, 1550$. The observed composite spectrum is plotted as a solid line, while the dashed line is a Starburst99 model spectrum for 300 Myr of continuous star-formation with $Z = \frac{1}{4} Z_{\odot}$ (Leitherer et al., 1999, 2001). The model and data agree well for the emission component of the C IV P-Cygni stellar wind line, but the model overpredicts the amount of broad, blue-shifted absorption. This may be due to the lower average metallicity or older age of the LBGs included in the composite spectrum, relative to the model. The lower right-hand box shows the zoomed-in region near the He II $\lambda 1640$ stellar wind line, whose large strength we have trouble reproducing using Starburst99 models with reasonable parameters.

The composite LBG spectrum also shows He II λ1640 emission which is quite strong compared with observations in local starburst galaxies (Heckman et al., 1998). Narrow He II λ1640 emission is seen in galaxy spectra with strong nebular emission. If massive stars are forming in He III regions, He II λ1640 can appear as a nebular recombination emission line (from supernovae remnants or superbubbles) (Leitherer et al., 1995). The He II λ1640 emission in the composite LBG spectrum, though, is quite broad, with FWHM $\sim$ 1500 km s^{-1}. This is visibly broader than the most of the other weak emission lines in the spectrum originating in H II nebular regions, so we favor a stellar wind origin for the He II feature. Broad stellar He II emission is predominantly produced in fast, dense winds from Wolf-Rayet (W-R) stars, which are the evolved descendants of O stars more massive than $M > 20 - 30 M_{\odot}$. Therefore, the strength of the He II emission should provide information about the ratio of W-R to O stars (Schaerer & Vacca, 1998).

In order to interpret the He II line, we use Starburst99 population synthesis codes (Leitherer et al., 1999). Model UV spectra of both solar and 0.25 $\times$ solar metallicity are produced by Starburst99. The solar metallicity spectrum extends from 1200 $-$ 1800 Å, which includes the He II line, but the sub-solar metallicity model only extends from 1200 $-$ 1600 Å. While the current best estimates of LBG metallicities (Pettini et al., 2002, 2001) are closer to $Z = 0.25 Z_{\odot}$, we can still use the solar metallicity model spectra to make some interesting inferences. The observed strength of the LBG He II emission line can be matched using a 3 Myr old instantaneous burst model with a standard Salpeter IMF. This is the brief period, following a burst of star formation, when the fractional contribution of Wolf-Rayet stars to the integrated UV luminosity reaches a maximum. Such young burst ages have indeed been derived for Wolf-Rayet galaxies, whose strong optical and UV He II emission lines indicate the presence of numerous high-mass stars and a high W-R/O star ratio (Conti et al., 1996; Leitherer et al., 1996). It is not clear which average stellar population is represented by the composite spectrum in Figure 5.2, but since LBG rest-frame UV/optical SEDs indicate a wide range of properties and ages, and are generally not well-represented by instantaneous burst models (Shapley et al., 2001; Papovich et al., 2001), it seems extremely unlikely that the 3 Myr old burst model can be representative of the whole population and accordingly we rule out this interpretation.

If we then consider 300 Myr continuous star-formation models (based on the median age derived from SED-fitting), the only way to produce a high enough W-R/O star ratio is to invoke an IMF slope much flatter than the standard Salpeter form of $N(m) \propto m^{-\alpha}$ with $\alpha = 2.35$. Slopes of $\alpha \leq 1$ match the He II strength, but then the C IV P-Cygni emission is overproduced by a factor of ≥ 4. The discrepancy will be even worse for the sub-solar metallicity models. The ratio of W-R/O stars decreases as a strong function of decreasing metallicity, since the lower-limit on the masses of O stars that evolve into W-R stars moves towards higher masses as the metallicity decreases (Maeder, 1991; Meynet, 1995). Theoretical predictions of W-R line luminosities (Schaerer & Vacca, 1998; Leitherer et al., 1999) show that, for a given IMF, 300 Myr continuous star-formation models with

$Z = 0.25Z_{\odot}$ have He II λ1640 line strengths only half as strong as in the case of solar-metallicity. A more drastic adjustment to the slope of the IMF would be required for the sub-solar metallicity model to match the He II emission strength, which would then lead to an even larger discrepancy for the C IV P-Cygni emission (since, empirically, we measure that the C IV P-Cygni emission does not depend very significantly on metallicity). Clearly, current population synthesis models do not simultaneously reproduce the C IV and He II stellar wind features in LBGs for reasonable choices of star-formation history, age, metallicity, and IMF slope. We will be able to test this discrepancy better with high-quality spectra for individual LBGs whose stellar population ages and star-formation histories we know more accurately than our rough estimate of the stellar population represented by the composite of all the LBGs.

5.4.2 Outflow-related Features

The large-scale outflow of interstellar material appears to be a generic feature of LBGs, one implied both by the typical LBG star-formation rate per unit area, and also by the fairly ubiquitous observed offset in velocity between Lyα emission and interstellar absorption lines when both sets of lines are seen. Spectral features probing neutral outflowing gas are H I Lyα and Lyβ, and neutral and singly ionized metal absorption lines. More highly ionized metal lines probe the ionized phase of the outflow (Heckman et al., 2001b; Pettini et al., 2002). While the interstellar absorption lines in $\sim 70\%$ of individual LBG spectra are strong enough that an absorption redshift can be assigned to at least one low- or high-ionization feature, it is not possible to obtain robust equivalent width measurements for multiple features due to the typical low S/N (and prevalent sky-subtraction residuals). However, in composite spectra containing hundreds of LBGs, these features are detected with high significance. In this section, we describe the average properties of the spectral features related to the large-scale outflows in LBGs.

5.4.2.1 Low-ionization Lines Associated with Neutral Gas

The strongest low-ionization interstellar lines probing outflowing interstellar material are marked in Figure 5.2, and include Si II λ1260, O I+Si II λ1303 (a blend at the spectral resolution of our sample), C II λ1334, Si II λ1526, Fe II λ1608, and Al II λ1670. While there are additional interstellar absorption lines at wavelengths shorter than Lyα, as well as a host of other, weaker, low-ionization interstellar absorption lines, we confine the analysis in Chapter 6 to these six strongest features redward of Lyα, which we detect at very high significance. The features marked have been well-studied in local starburst galaxies (Gonzalez Delgado et al., 1998; Heckman et al., 1998), as well as in the lensed LBG, MS1512-cB58 (Pettini et al., 2000, 2002). Relative to the stellar, systemic redshift, we measure an average blueshift for the strong low-ionization interstellar features of $\Delta v = -150 \pm 60\,\mathrm{km\ s^{-1}}$. Using the C II λ1334 and Si II λ1526 features, which we assume to

be the least affected by blends, and assuming an effective spectral resolution of 2.6 Å for the LBG composite spectrum, we compute the average deconvolved velocity full-width [2] for the low-ionization interstellar (LIS) lines, FWHM(LIS) = 560 ± 150 km s^{-1}. The largest uncertainty affecting this measurement is the uncertainty of the effective spectral resolution of the composite spectrum, which we conservatively estimate to range between $2 - 3.25$ Å (roughly $400 - 700$ km s^{-1}). The upper bound on the spectral resolution is set by the minimum FWHM value measured for any of the strong interstellar absorption lines. The lower bound of 2 Å is set by our estimate of the spectral resolution provided by the optimum observing conditions.[3]

We list rest-frame equivalent widths and relative systemic redshifts for the six strongest low-ionization interstellar absorption lines in Table 5.1. The strength of these features makes them ideal for measuring interstellar absorption redshifts in noisy individual spectra. However, they are not useful for measuring chemical abundances, due to the fact that all of the strong lines are saturated. The saturation of the strong lines is most easily demonstrated by comparing the equivalent widths for two different Si II transitions: Si II λ1260 and λ1526. On the linear part of the curve of growth, $W \propto Nf\lambda^2$, where N is the column density of the ionic species and λ is the rest-frame wavelength of the transition. According to the relative oscillator strengths and wavelengths of the two Si II transitions, the ratio $W_0(1260)/W_0(1526) > 5$ on the linear part of the curve of growth. We measure $W_0(1260)/W_0(1526) = 0.95$, consistent with a ratio of unity, given the uncertainties, thus demonstrating that the Si II transitions are optically thick. There are weaker features detected in the composite LBG spectrum which probe the linear part of the curve of growth, and which have been used to derive metal abundances in the outflow of MS1512-cB58 (Pettini et al., 2000, 2002). These include S II $\lambda\lambda\lambda$1250, 1253, 1259, Si II λ1808, Fe II λ1144, Ni II λ1317, λ1370, λ1703, λ1709, λ1741, and λ1751. Most of these features are detected with only marginal significance in the composite LBG spectrum due to low spectral resolution. An abundance determination also requires an estimate of the H I column density, which is not easily measured from the composite spectrum, due to the way in which it was combined. In this paper, the analysis of the low ions in the outflowing gas is confined to the properties of the strong transitions.

5.4.2.2 High-ionization Lines Associated with Ionized Gas

In addition to the low-ionization features associated with neutral outflowing gas, we detect high-ionization interstellar features such as Si IV $\lambda\lambda$1393, 1402, C IV $\lambda\lambda$1548, 1550, and N V $\lambda\lambda$1238, 1242. These features predominantly trace gas at $T \gtrsim 10^4 K$, which has been ionized by a combination of

[2] By deconvolved velocity full-width, FWHM$_{int}$, we mean the square-root of the difference in quadrature between the observed full-width, FWHM$_{obs}$ and the instrumental resolution, FWHM$_{inst}$: FWHM$_{int}$ = (FWHM$^2_{obs}$ − FWHM$^2_{inst}$)$^{1/2}$.

[3] The spectra were obtained through 1.″4 slits, which is much larger than the LBG size in typical seeing conditions ($0.''5 - 1.''0$). Under such conditions, the spectral resolution was dictated by the angular sizes of objects falling within slits (i.e., the seeing), rather than by the slit-width.

radiation from massive stars and collisional processes associated with the outflow. We also detect O VI $\lambda\lambda 1032, 1038$ in absorption. If the radiation field is dominated by the spectrum of hot stars, rather than an AGN, O VI is likely to arise in collisionally ionized gas, indicating the presence of an even hotter phase with $T \gtrsim 10^5 K$ (Heckman et al., 2001b).

Section 5.4.1 included a discussion of the stellar winds indicated by the Si IV, C IV, and N V profiles. In this section we consider the properties of the interstellar contributions to the same high-ionization transitions. Again, the proximity of N V to Lyα prevents us from studying this transition in detail, though we do see evidence for an interstellar absorption component. Also, it is difficult to characterize the properties of the hot phase traced by O VI, due to the fact that the O VI absorption is fairly weak, blended with C II $\lambda 1036$ absorption, and resides in the red wing of the strong Lyβ profile. However, we measure $\Delta v = -180$ km s^{-1} for both members of the Si IV transition, which has a doublet ratio of roughly 2:1, indicating that the lines are on the linear part of the curve of growth. We measure $\Delta v = -390$ km s^{-1}, for what we isolate as the interstellar component of the C IV absorption, assuming a saturated doublet ratio of 1:1 and therefore a rest-frame centroid of $\lambda = 1549.479$ Å. The measurement of the C IV interstellar velocity is fairly uncertain, due to the combination of P-Cygni emission and broad absorption, possible nebular emission, and interstellar absorption all superposed on one another. The properties of the Si IV and C IV interstellar absorption lines are listed in Table 5.1.

In light of the complexities associated with the C IV doublet, we emphasize the comparison between the Si IV doublet and the low-ionization lines. The blueshift of the Si IV doublet ($\Delta v = -180$ km s^{-1}) agrees quite well with the average blueshift of the strong low-ionization interstellar lines ($\Delta v = -150$ km s^{-1}). Furthermore, the average deconvolved velocity full-width for the two members of the Si IV doublet is FWHM(Si IV) $= 590 \pm 140$ km s^{-1}, very similar to the average FWHM for the low-ionization lines. The deconvolved velocities associated with either the Si IV or low-ionization lines are very uncertain due to the uncertainties in spectral resolution. Independent of the resolution of the composite spectrum, however, both the blue-shifts and the un-deconvolved velocity widths of the low and high ionization lines are consistent with each other.

The properties of low and high ionization absorption profiles were compared in the spectrum of the gravitationally lensed LBG, MS1512-cB58, using ~ 10 times higher spectral resolution (Pettini et al., 2002). In the case of cB58, which has much stronger than average low-ionization interstellar absorption lines, saturated Si IV and C IV transitions, and Lyα dominated by a damped absorption profile, absorptions from low-ions and high-ions span the same overall velocity range. Also, the material with the highest optical depth (i.e., where the lines are black) is blueshifted by roughly the same amount for the low ions and the high ions, to within 20 km s^{-1}. One distinction highlighted by Pettini et al. (2002) is that the high-ionization lines show smoother absorption profiles, while the low-ionization profiles break up into a number of discrete components. Composite LBG spectra do

not have sufficient spectral resolution to discern qualities such as profile smoothness or clumpiness. However, the overall agreement between low and high ion stages in mean blueshift and velocity FWHM is consistent with the high-resolution results from cB58. In contrast, Wolfe & Prochaska (2000) find distinct kinematic properties for low and high-ionization transitions associated with damped Lyα absorbers. Specifically, the mean velocities of low and intermediate (Al III) ionization stages differ from those of the high ions, although within each of these two sets of lines there is normally very good internal velocity agreement. Also, in 29 out of 32 cases, the velocity width of the high-ionization absorption exceeds that of the low-ionization absorption. The kinematic differences between LBGs and DLAs are another manifestation of the differing characteristics of these two populations of high redshift galaxies, which also exhibit distinct clustering properties (Adelberger et al., 2003) and metallicities (Pettini, 2002). Such differences will eventually help us clarify the true nature of damped Lyα absorption systems.

5.4.2.3 Lyα

By far the most prominent feature in individual LBG spectra is H I Lyα. The original sources of most Lyα photons are recombinations in H II regions. While the Lyα equivalent width is sensitive to conditions in the H II regions such as temperature, metallicity, star-formation rate, and star-formation history, resonant scattering of Lyα in LBGs by interstellar H I makes the emergent Lyα profile at least as sensitive to the geometry, kinematics, and dust content of the large-scale outflows. When seen in emission, Lyα can be used to measure a redshift. In the composite LBG spectrum shown in Figure 5.2, we measure a Lyα emission redshift of $\Delta v = +360$ km s^{-1}. This relative redshift reflects the fact that a Lyα photon has a much better chance of escaping a galaxy if its last scattering occurs off of an atom which is redshifted with respect to the bulk of the neutral material in the galaxy, imparting a Doppler shift which takes the Lyα photon off resonance. We measure a deconvolved emission full-width of FWHM(Lyα) $= 450 \pm 150$ km s^{-1}. When seen in absorption, the Lyα feature can be quite broad, with blueshifted absorption extending from zero velocity down to $\Delta v \leq -5000$ km s^{-1}. Broad Lyα absorption is therefore not a precise redshift indicator. In spectra with Lyα seen only in absorption, interstellar metal lines can be used to measure the redshift more precisely.

A wide distribution of Lyα profiles is seen in the LBG spectroscopic sample, ranging from damped absorption to emission an order of magnitude stronger than the feature shown in Figure 5.2 (Steidel et al., 2000). In section 6.4, we will discuss how several LBG spectroscopic properties depend on Lyα equivalent width, and what inferences can be drawn about the physical conditions which determine the emergent Lyα profile. The composite spectrum shown in Figure 5.2 has a Lyα feature dominated by emission. The total rest-frame equivalent width is $W_0 = 14.3$ Å which includes both redshifted emission, and much weaker blueshifted absorption. This spectrum is the average of all the LBG

spectra in the spectroscopic sample, yet there are selection effects which depend on both apparent $\mathcal{R}$ magnitude, color, and spectroscopic type, which bias the spectrum relative to a true "average" of the total LBG photometric sample. For example, the spectroscopic sample over-represents bright objects relative to faint objects, and the number of objects with Lyα emission relative to those with only Lyα absorption. As discussed in section 6.2, it becomes much more difficult at fainter magnitudes to identify spectroscopically a galaxy with no Lyα emission. Therefore, as the number of spectroscopically unidentified objects increases at fainter magnitudes, so does the ratio of emission to absorption line galaxies with measured redshifts. Accordingly, the Lyα feature in Figure 5.2 may be biased towards stronger emission than the true average for the total photometric sample. In order to quantify this bias, a more detailed treatment of selection effects is required.

5.4.3 Emission Lines

One of the benefits of producing a high S/N ratio composite spectrum is that it can reveal weak spectral features that would have remained undetected in individual spectra. We detect several weak emission lines, some of which we attribute to nebular regions photoionized by radiation from massive stars, and others whose origin is still ambiguous. The weak emission lines in the LBG composite spectra are: Si II* λ1265, Si II* λ1309, Si II* λ1533, O III] $\lambda\lambda$1661, 1666, and C III] $\lambda\lambda$1907, 1909. We measure a mean velocity of $\Delta v = 100 \pm 35$ km s^{-1} for the Si II* transitions. The centroids of the fine-structure emission lines may be biased to the red by weak fine-structure absorption lines or neighboring saturated resonance absorption features (Si II λ1260, O I+Si II λ1303, and Si II λ1526) associated with the outflow, which attenuate the blue edges of the fine-structure emission profiles. We measure a velocity of $\Delta v = 0$ km s^{-1} for the O III] λ1663 doublet, and a velocity of $\Delta v = 40$ km s^{-1} for the C III] λ1909 transition, both of which agree very well with the stellar systemic velocities (section 5.3.1). O III] λ1663 and C III] λ1909 are both collisionally excited, semi-forbidden transitions, so there is no absorption from these ions in the large-scale outflow of gas. While the Al II λ1670 resonance absorption feature is fairly close to O III], the C III] transition should be clear of any absorption line. There may be a nebular emission component in C IV $\lambda\lambda$1548, 1550, but it is difficult to isolate nebular C IV emission from the stellar P-Cygni emission. The properties of the emission lines are summarized in Table 5.2.

5.4.3.1 AGN Contribution?

Even though all galaxy spectra flagged as narrow- or broad-lined AGN on an individual basis were removed from the LBG composite spectra sample, the presence of weak emission lines in the LBG composite spectrum may reveal some average low-level of nuclear activity in LBGs. To address this issue, we examined the emission line ratios in a composite spectrum of 198 LBGs with rest-frame $W_{\mathrm{Ly}\alpha} \geq 20$ Å in emission (see section 6.4). The nebular emission lines in this composite spectrum

are also stronger than those marked in the total LBG spectrum of Figure 5.2. We compared the emission line ratios in this strong-emission spectrum with those in a composite spectrum of 16 LBGs flagged as narrow-lined AGN on an individual basis (Steidel et al., 2002). The average Lyα emission equivalent width in this strong-emission (yet not AGN-flagged) subsample is only half as large the emission strength in the narrow-line AGN spectrum. The narrow-line AGN spectrum has line intensity ratios of C IV/Lyα $\sim$ 0.25, and C III]/Lyα $\sim$ 0.125, which are very similar to the mean ratios of C IV/Lyα $= 0.21 \pm 0.09$ and C III]/Lyα $= 0.10 \pm 0.05$, measured for a sample of four local Seyfert 2 galaxies by Ferland & Osterbrock (1986). In contrast, the non-AGN spectrum has intensity ratios of C IV/Lyα ≤ 0.02 and C III]/Lyα $= 0.05$. The 2% represents a strict upper limit on the ratio of nebular C IV/Lyα (which is probably much smaller), since the total C IV emission represents the sum of nebular emission plus stellar P-Cygni emission. Clearly, the ratios of both C III] and C IV to Lyα are much smaller in the non-AGN LBG spectrum than in the narrow-line AGN spectrum. Additionally, the ratio of C III]/C IV is significantly higher in the non-AGN spectrum than in the AGN spectrum, indicating a softer photoionizing radiation field, more likely dominated by the emission from hot stars rather than non-thermal processes.

5.4.3.2 C/O Abundance

Ultraviolet spectroscopic observations of H II regions in nearby irregular and spiral galaxies with the *HST* have been used to study how the relative abundances of carbon and oxygen (C/O) depend on oxygen abundance (O/H) (Garnett et al., 1995, 1997, 1999; Kobulnicky & Skillman, 1998). Ranging in O/H from less than 0.1 to 1.0 times $(O/H)_{\odot}$, a compilation of these data is shown in figure 5.4 and demonstrates a clear trend of increasing C/O with increasing O/H (Garnett et al., 1999). For example, in spiral galaxy H II regions, $\log(C/O) \simeq -0.7$ at $\log(O/H) = -4.0$, and increases to $\log(C/O) \simeq -0.2$ at $\log(O/H) = -3.4$[4]. While the behavior at the smallest metallicities is less clear, due the unexpectedly high C/O ratio in the extremely metal-poor galaxy, I Zwicky 18, the H II regions in other sub-solar metallicity irregular galaxies show the same overall trend as the spiral galaxies (Garnett et al., 1995). Stellar evolution models including stellar winds from massive stars predict that the carbon yield from massive stars increases relative to the oxygen yield, with increasing metallicity (Maeder, 1992). These models successfully reproduce both the observed local trend in C/O with O/H, and also C/O abundance gradients in Galactic stars and H II regions (e.g., Carigi 2000). While the rise of C/O with O/H in local star-forming regions is mainly due to yields from massive stars, there is also the fact that oxygen is primarily synthesized in stars with $M > 10M_{\odot}$, whereas carbon is produced in both high and intermediate mass stars $(2 - 8M_{\odot})$, delaying in time the ejection of some fraction of carbon into the ISM, relative to oxygen. In relatively young galaxies at high redshift, the observed C/O ratio may thus also reflect the average time since

[4]The solar oxygen abundance is $\log(O/H)_{\odot} = -3.26$ (Holweger, 2001).

the onset of star-formation. In such circumstances, younger stellar populations may be dominated by the chemical yields from the most massive stars, whereas after a few 100 Myr since the onset of star formation, an increased C/O ratio reflects the fact that intermediate-mass stars have had a chance to release their carbon into the ISM.

Since we detect both C III] λ1909 and O III] λ1663 in the LBG composite spectrum shown in Figure 5.2, we follow the analysis of Garnett et al. (1995), assuming that the electron densities in these H II regions are well below the critical limit for the C III] and O III] transitions. In the low-density limit, we can express the relative abundances of C^{+2} and O^{+2} as:

$$\frac{C^{+2}}{O^{+2}} = \frac{1}{9} \times \frac{\Omega_{\rm OIII]}(^3{\rm P},^5{\rm S}_2)}{\Omega_{\rm CIII]}(^1{\rm S},^3{\rm P})} \times \frac{\lambda_{\rm CIII]1909}}{\lambda_{\rm OIII]1663}} \times e^{-11054/T} \times \frac{I({\rm CIII]}\lambda1909)}{I({\rm OIII]}\lambda1663)} \tag{5.2}$$

In this expression $\Omega_{\rm OIII]}(^3{\rm P},^5{\rm S}_2)$ and $\Omega_{\rm CIII]}(^1{\rm S},^3{\rm P})$ are the multiplet collision strengths for the O III] λ1663 and C III] λ1909 doublets, which have a weak temperature dependence (see Garnett et al. 1995 for specific collision-strength values); the prefactor of $\frac{1}{9}$ represents a combination of statistical weights; $\lambda_{\rm CIII]1909}$ and $\lambda_{\rm OIII]1663}$ are the effective wavelengths of the C III] and O III] doublets; T is the H II region electron temperature; and $I({\rm CIII]}\lambda1909)$ and $I({\rm OIII]}\lambda1663)$ are the line intensities. To compute $I({\rm OIII]}\lambda1663)$ we integrate the flux from both members of the resolved O III] λ1663 doublet (the C III] doublet is unresolved). Strictly speaking, $C/O = C^{+2}/O^{+2} \times {\rm ICF}$, where ICF is an ionization correction factor that takes into account the fact that while C III] and O III] are similar ionization states, C^{+2} has a slightly lower ionization potential than O^{+2}. In practice, Garnett et al. (1995) find ICF only ranges between $1.06 - 1.33$, and so, for lack of any detailed information, we make the approximation ICF = 1 and $C/O \simeq C^{+2}/O^{+2}$. Based on the measured ratio of C III] and O III] line strengths in the total composite LBG spectrum, we measure $\log(C/O) = -0.68 \pm 0.13$. This confidence interval is marked by the horizontal magenta shaded region in Figure 5.4. The quoted uncertainty corresponds to a temperature range $T = 10000 - 20000$ K, but does not include the uncertainty in the determination of the continuum level, which may amount to an additional error of about a factor of two in the determination of C/O. We measure a very similar value of $\log(C/O) = -0.74 \pm 0.14$ in the LBG composite spectrum constructed from the subsample that includes only strong emission-line galaxies (see sections 5.4.3.1, 6.4). Similar C/O ratios are found by Garnett et al. (1999) for galaxies with $O/H \sim 0.2 \times (O/H)_\odot$. There are large uncertainties associated with the LBG C/O measurements. However, we note that the corresponding O/H values are consistent with—if towards the low-end of the confidence interval of—the O/H metallicity determinations for LBGs based on the ratio of rest-frame optical nebular [O II], [O III], and Hβ emission lines ($\sim 0.1 - 1 \times (O/H)_\odot$) (Pettini et al., 2001).[5] The range in log(O/H) deduced

[5]The galaxies with rest-frame optical spectroscopic observations were drawn from the bright end of the LBG UV luminosity function. It is not clear how this selection criterion limits the range of metallicities probed, relative to the abundance range in the LBG sample as a whole.

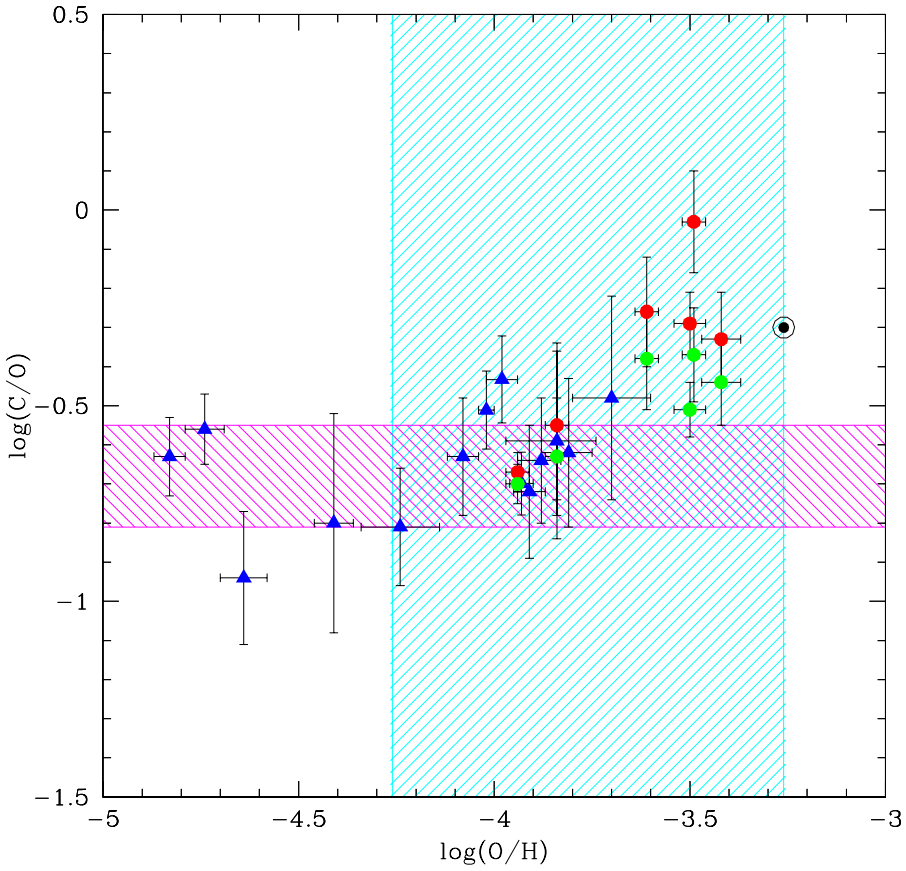

Figure 5.4 log(C/O) vs. log(O/H) for local H II regions. Blue triangles are data from dwarf irregular galaxies and the Magellanic Clouds (Garnett et al., 1995, 1997; Kobulnicky & Skillman, 1998). Spiral galaxy data are shown with circles (Garnett et al., 1999). Red symbols assume a shallow ($R_V = 3.1$) Milky Way extinction curve, whereas green symbols indicate a steeper ($R_V = 5.0$) one. The solar abundances (Holweger, 2001; Allende Prieto et al., 2002) are indicated by the large bulls-eye. The horizontal (magenta) shaded area indicates the log(C/O) confidence region derived from the total composite LBG spectrum. The vertical (cyan) shaded area indicates the range of log(O/H) implied by the ratio of [O III], [O II], and Hβ line-strengths in a small sample of bright LBGs (Pettini et al., 2001).

by Pettini et al. (2001) is marked by the vertical cyan shaded region in Figure 5.4. In view of the large uncertainties associated with both C/O and O/H determinations in LBGs, we do not interpret these results any further, except to point out that the comparison of C and O emission strengths will be an interesting diagnostic of chemical evolution and stellar populations at high-redshift in future, higher-quality data.

5.4.3.3 Si II* Lines

In addition to C III] and O III], which have been studied in local star-forming regions, we also detect lines that we identify as Si II* fine-structure emission lines. Unfortunately, our spectral resolution is too coarse to determine if we detect C II* λ1335 Å emission as well (the C II λ1334 resonance absorption line from outflowing neutral gas swamps any signal at that wavelength). A literature search of local ultraviolet observations reveals very few references to Si II* fine-structure emission lines. The *International Ultraviolet Explorer* (*IUE*) atlas of star-forming galaxies compiled by Kinney et al. (1993) contains a census of ultraviolet emission lines associated with nebular objects such as H II regions, planetary nebulae, and supernova remnants, but does not include the Si II* features. The spectral resolution of *IUE* is ~ 1000 km s^{-1}, coarser than the resolution of the LBG composite spectra. When the LBG composite spectra are smoothed to the resolution of the *IUE* data, the Si II* lines are still visible at 5% to 10% above the continuum level. Presumably, the individual *IUE* spectra contained in the Kinney et al. (1993) atlas are of insufficient S/N to see these features. However, the Si II* features are also not detected in composite starburst spectra containing 20 individual galaxy spectra drawn from the *IUE* atlas, each of which has continuum S/N of at least 10 (Heckman et al., 1998).

The Einstein A coefficients associated with the Si II* transitions range from $10^8 - 10^9$ s^{-1}, more than six orders of magnitude larger than the A-values for the semi-forbidden O III] and C III] transitions. Only in very high-density environments ($N_e = 10^9 - 10^{13}$ cm^{-3}) are the Si II excited level populations determined by collisional excitations and de-excitations (Keenan et al., 1992). In H II regions, where the electron densities are typically $N_e = 10^2 - 10^3$ cm^{-3}, collisions are therefore not the dominant mechanism governing the Si II level populations. Also, when $T \sim 10^4$ K and Si II and Si III have comparable abundances (as appropriate here), it can be shown that the recombination rate of Si III into the excited Si II levels is of the same order as the Si II collisional excitation rates (Shull & van Steenberg, 1982). In order to understand the origin of the Si II* emission lines in a more systematic way, we modeled all observed LBG nebular emission lines using the CLOUDY96 software package (Ferland et al., 1998). The observational constraints are the average rest-frame optical strengths of [O III], [O II], and Hβ (Pettini et al., 2001), as well as the rest-frame UV O III] and C III] strengths (section 5.4.3.2). We found that *any* model which provides a satisfactory fit to the O, C, and Hβ line ratios simultaneously predicts Si II* emission line strengths that are more than

an order of magnitude weaker than observed. This result seems to exclude an origin in photoionized H II regions for the Si II* emission lines.

An alternative explanation for these lines is that they are produced in the large-scale outflows in LBGs. UV photons with $\lambda = 1260, 1304, 1526$ are absorbed by ground state Si II in the outflowing neutral gas, as indicated by the saturated Si II resonance absorption transitions. Each photon absorbed in a resonance or fine-structure transition is re-emitted in a transition either to the ground state or the excited ground state, with the relative probabilities determined by the Einstein A-coefficients for the different transitions. In the absence of dust extinction, and if the slit used to observe the galaxy/outflow system is as large as the region emitting in Si II and Si II*, the sum of the resonant and fine-structure emission equivalent widths should be equal in strength to the absorption from the same transitions. This is clearly not the case, in that the Si II *λ1265, 1309, 1533 fine-structure emission lines are an order of magnitude weaker than the Si II λ1260, 1304, 1526 resonant absorption lines. We don't even detect any resonant Si II emission, as saturated blue-shifted Si II absorption dominates over emission at $\Delta v = +100\,\mathrm{km\ s^{-1}}$, the mean velocity of the Si II* emission lines. The dominance of resonant absorption over fine-structure emission may be due to dust attenuation of Si II photons during resonant scattering. It also may indicate that the slit used in LBG spectroscopic observations only subtends a small fraction of the Si II* emitting region. One problem with interpreting the Si II* emission lines as being produced in the outflowing gas is their kinematic properties. The outflow is optically thin to Si II* (negligible absorption is detected in these transitions), so we expect Si II* emission lines produced in outflowing gas to probe the full range of approaching and receding velocities ($\geq$ 1000 km s^{-1}). In fact, the Si II* lines are barely resolved in the composite spectrum, with FWHM $\leq$ 500 km s^{-1}. While Si II* emission may be biased towards positive velocities by blue-shifted fine-structure, or even broad resonance, absorption, we expect that it should be at least as broad as the Lyα emission, which is attenuated on the blue edge by much stronger absorption over a wider range of velocities. However, the Si II* lines are narrower than the Lyα emission line, which extends to much more redshifted velocities. In summary, both the outflow and H II region models of the Si II* features fail to explain all of the observed properties of the emission lines, whose true nature remains to be determined.

Table 5.1. Strong LBG Interstellar Absorption Features

Ion	$\lambda_{\rm lab}$[a] (Å)	f[b]	W_0[c] (Å)	σ[c] (Å)	Δv[d] (km s^{-1})
Si II	1260.4221	1.007	-1.63	0.10	-110
O I	1302.1685	0.04887	-2.20[e]	0.12[e]	$[-270]$[e]
Si II	1304.3702	0.094	-2.20[e]	0.12[e]	$[-270]$[e]
C II	1334.5323	0.1278	-1.72	0.11	-150
Si IV	1393.76018	0.5140	-1.83	0.16	-180
Si IV	1402.77291	0.2553	-0.81	0.10	-180
Si II	1526.70698	0.130	-1.72	0.18	-110
C IV	1548.204	0.1908	-3.03[f]	0.21[f]	$[-390]$[f]
C IV	1550.781	0.09522	-3.03[f]	0.21[f]	$[-390]$[f]
Fe II	1608.45085	0.058	-0.91	0.15	-60
Al II	1670.7886	1.833	-1.04	0.15	-100

[a]Vacuum wavelengths.

[b]Transition oscillator strengths as in Pettini et al. (2002).

[c]Rest-frame equivalent width and 1σ error. The error takes into account both sample variance and the S/N of the composite spectrum (see section 6.3).

[d]Relative velocity measured in the systemic rest frame of the composite spectrum, equivalent to the rest frame of the stars.

[e]W_0, σ, and Δv values listed for O I λ1302 and Si II λ1304 refer to the total measured for the blend of these two features. The value of Δv assumes that the rest wavelength of the blend is $\lambda = 1303.2694$ Å.

[f]W_0, σ, and Δv values listed for both members of the C IV $\lambda 1548, 1550$ doublet refer to the blend of these two features. There may be a contribution to W_0 from stellar wind absorption which has not been subtracted out. The value of Δv assumes that the rest wavelength of the blend is $\lambda = 1549.479$ Å.

Table 5.2. Weak LBG Emission Features

Ion	$\lambda_{\rm lab}$[a] (Å)	A_{ul}[b] ($10^8 {\rm s}^{-1}$)	W_0[c] (Å)	σ[c] (Å)	Δv[d] (km s^{-1})
Si II*	1264.738	2.30e+01	0.34	0.09	+130
Si II*	1309.276	7.00e+00	0.35	0.10	+50
Si II*	1533.431	7.40e+00	0.21	0.09	+110
O III]	1660.809	2.20e−06	0.23[e]	0.13[e]	+40
O III]	1666.150	5.48e−06	0.23[e]	0.13[e]	−50
CIII]	1908.734	1.14e−06	1.67	0.59	+40

[a]Vacuum wavelengths.

[b]Einstein A-coefficients from the NIST Atomic Spectra Database (http://physics.nist.gov/cgi-bin/AtData/main_asd).

[c]Rest-frame equivalent width and 1σ error. The error takes into account both sample variance and the S/N of the composite spectrum (see section 6.3).

[d]Relative velocity measured in the systemic rest frame of the composite spectrum, equivalent to the rest frame of the stars.

[e]W_0 and σ values are given for the flux integrated over the whole O III] doublet.

Chapter 6

Trends in Lyman Break Galaxy Spectra

6.1 Introduction

We have characterized the basic features of the composite spectrum formed from the $z \sim 3$ LBG spectroscopic sample. We are now ready to examine how these spectroscopic features vary across the sample as functions of different galaxy parameters. Some of the parameters which can be measured for individual galaxies are: redshift, z; rest-frame UV apparent magnitude, $\mathcal{R}$; rest-frame UV color corrected for IGM absorption, $(G-R)_0$, which can be parameterized in terms of a reddening, $E(B-V)$, given an assumed form for the intrinsic spectrum; Lyα rest-frame equivalent width, $W_{\mathrm{Ly}\alpha}$; and interstellar kinematics, $\Delta v_{\mathrm{em-abs}}$. Our spectroscopic sample is large enough that we can divide the total sample into several subgroups based on each of the above parameters, and still create a high S/N composite spectrum for each subgroup. Individual spectra are not of sufficient S/N to be able to reliably measure low- and high-ionization interstellar absorption equivalent widths, W_{LIS} and W_{HIS}. Therefore, we do not bin the sample according to interstellar absorption line strength, but we can measure the interstellar absorption strengths with high significance in all of the composite spectra.

6.2 Selection Effects

Before considering LBG spectroscopic trends, we must isolate which parameters are sensitive to the variance in the underlying galaxy population and which are more sensitive to our photometric and spectroscopic selection criteria. To illustrate the importance of selection effects, we consider how our photometric and spectroscopic biases limit the range of galaxy parameter space that can be sampled as a function of z and $\mathcal{R}$ magnitude.

First, we examine biases resulting from the LBG photometric selection criteria. One of the

LBG color criteria is $G - \mathcal{R} \leq 1.2$, which affects the range of intrinsic UV colors selected with the LBG technique as a function of redshift. The reason for this effect is that absorption by HI in the IGM attenuates the flux in the G-band for galaxies with $z \geq 2.4$. The average amount of attenuation is an increasing function of redshift, ranging from $\Delta G = 0$ magnitudes at $z = 2.4$ to $\Delta G = 0.2$ magnitudes at $z = 3.0$, to as much as $\Delta G = 0.5$ magnitudes at $z = 3.4$. Since LBGs are photometrically pre-selected on the basis of observed $G - R$ color, which includes the effect of IGM absorption, the range of intrinsic colors which can be included in the LBG sample is a strong function of redshift. As discussed in section 6.5, the rest-frame UV colors of continuously star-forming galaxies are largely determined by the amount of reddening affecting the stellar continuum, so the intrinsic UV color, $(G - R)_0$ can also be parameterized in terms of $E(B - V)$, once a form of the attenuation curve is assumed (Calzetti, 1997; Calzetti et al., 2000). In subsequent discussion, we use $E(B - V)$ to represent both intrinsic UV color and the amount of dust extinction, since there is almost a one-to-one correspondence between the two parameters. Figure 6.1 shows $E(B - V)$ vs. z for the LBG spectroscopic sample, demonstrating the strong apparent correlation of UV color with redshift, induced by our photometric selection effects.

There are also important photometric selection effects associated with apparent $\mathcal{R}$ magnitude. Due to the nature of LBG color criteria, and the fact the U_n images have finite depth, the dynamic range in $G-\mathcal{R}$ color is limited on average to bluer colors at fainter $\mathcal{R}$ magnitudes. Accordingly, there is a weak apparent correlation between $\mathcal{R}$ and $E(B - V)$, in the sense that fainter LBGs are bluer on average. However, Adelberger (2002) demonstrates that, once selection effects are accounted for, $\mathcal{R}$ and $E(B - V)$ are consistent with being independently distributed. The biases against UV color as a function of z and $\mathcal{R}$ magnitude result from the LBG photometric selection criteria and uncertainties, and have been discussed extensively and quantified for the purpose of constructing the LBG rest-frame UV luminosity function (Steidel et al., 1999; Adelberger & Steidel, 2000; Adelberger, 2002).

There are two additional spectroscopic sources of incompleteness that affect the sample under consideration. First, not all galaxies in the photometric sample were assigned to slitmasks and observed spectroscopically. This incompleteness is primarily a function of $\mathcal{R}$ magnitude, i.e., a larger fraction of bright galaxies in the photometric sample were observed spectroscopically, relative to the fraction of faint galaxies. The distribution of $G - \mathcal{R}$ colors of spectroscopically observed galaxies is relatively unbiased with respect to the photometric sample. Second, not all galaxies observed spectroscopically had successfully measured redshifts. This type of incompleteness also depends on $\mathcal{R}$ magnitude, but the subtlety lies in the fact that that galaxies with different spectroscopic types (i.e., those with and without Lyα emission) have different spectroscopic success rates as a function of $\mathcal{R}$ magnitude. Figure 6.2 shows the spectroscopic incompleteness as a function of magnitude, and Figure 6.3 shows the incompleteness as a function of both magnitude and spectral type.

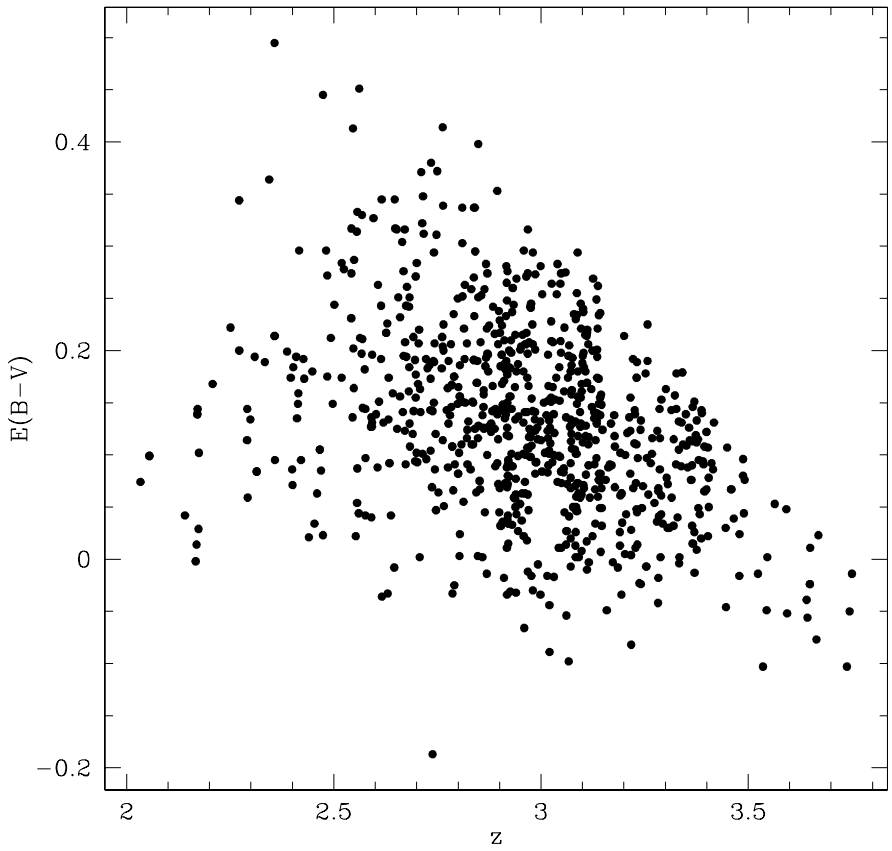

Figure 6.1 The distribution of $E(B-V)$ values as a function of z. Due to the way in which LBGs are color-selected to have *observed* $G-\mathcal{R}$ colors which lie within a specific range, the increased IGM absorption affecting the G-band flux as a function of z limits the range of *intrinsic* colors of LBGs (parameterized by $E(B-V)$) at higher z.

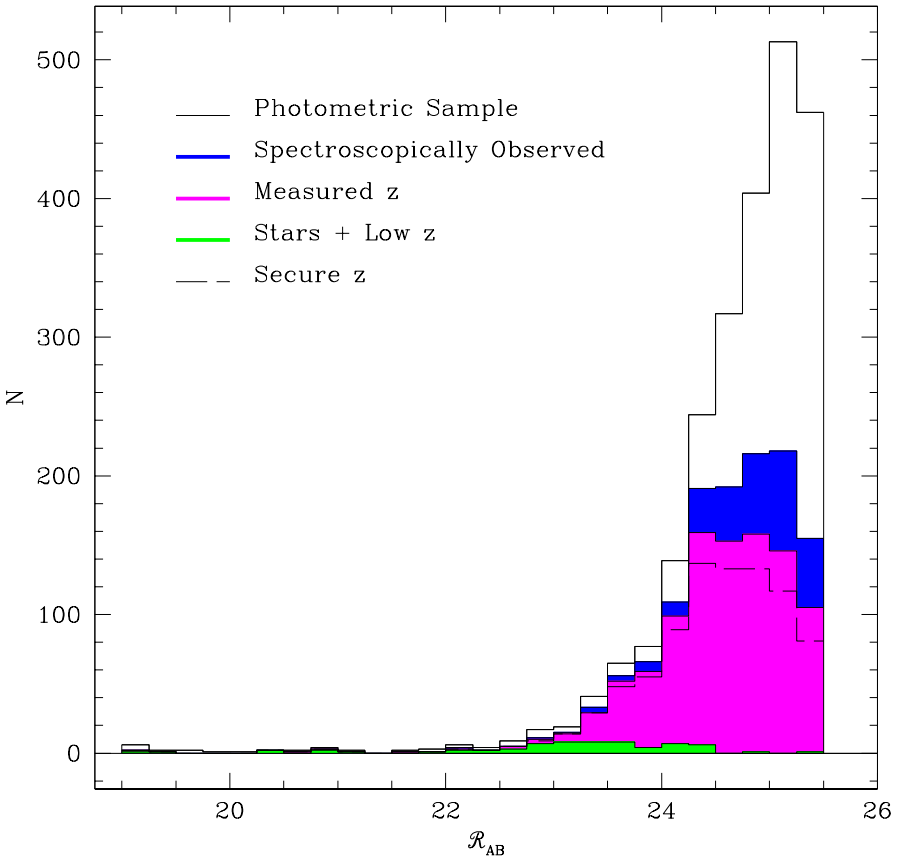

Figure 6.2 Photometric and spectroscopic incompleteness of the LBG sample as a function of $\mathcal{R}$ magnitude. The empty histogram represents galaxies photometrically selected by their colors to be at $z \sim 3$. The blue histogram consists of galaxies from the photometric sample which were observed spectroscopically. The pink histogram indicates spectroscopically observed objects for which a redshift was successfully measured. The green histogram shows the small fraction of spectroscopically confirmed objects ($\sim 4\%$) which turn out to be stars or low-z galaxies. The dashed histogram shows the subset of spectroscopically confirmed objects which have secure redshifts confirmed by at least two independent members of our group. Non-AGN objects in this secure-z sample with $z > 2$ were included in composite spectra.

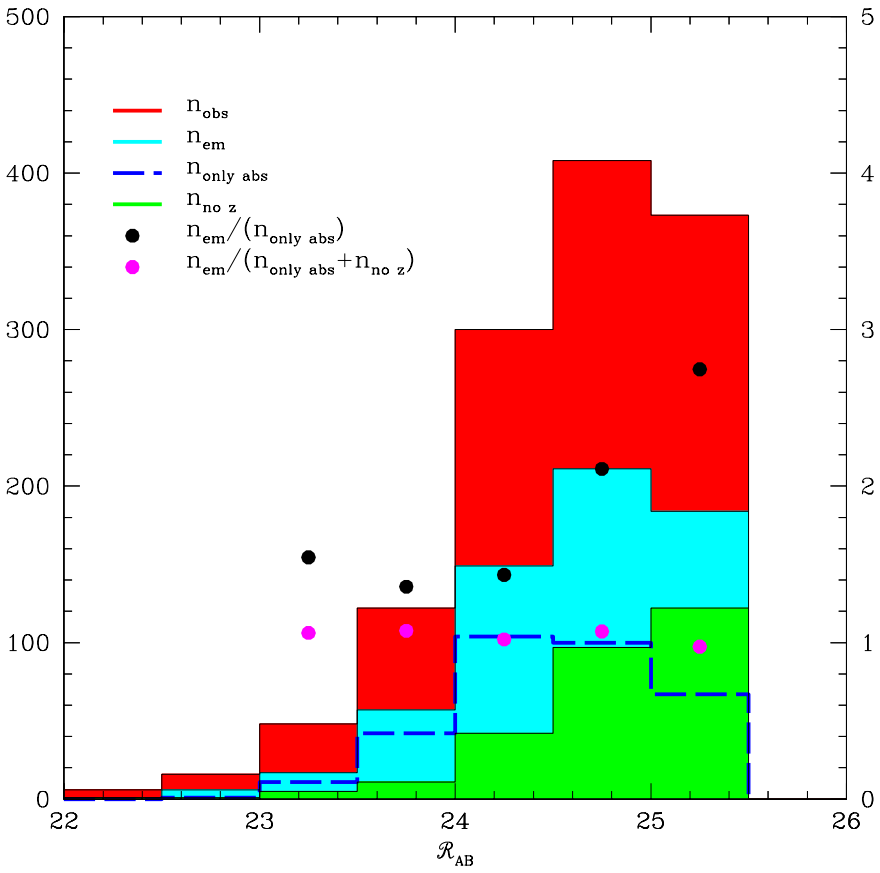

Figure 6.3 Photometric and spectroscopic incompleteness of the LBG sample as a function of $\mathcal{R}$ magnitude and spectroscopic type. The red histogram shows the number of galaxies observed spectroscopically. The cyan histogram shows the number of galaxies with redshifts measured from features which include Lyα emission. The blue dashed histogram shows the number of objects with no detectable Lyα emission and redshifts measured only from interstellar absorption lines. The green histogram shows the number of objects for which no redshift was successfully measured. The black dots indicate the ratio of galaxies with Lyα emission to those with only absorption line redshifts, which increases steeply as a function of $\mathcal{R}$ magnitude. Based on the assumption that the unidentified objects in the green histogram are $z \sim 3$ galaxies that have $W_{\mathrm{Ly}\alpha} < 0$ and spectra with insufficient S/N to identify absorption features, we see that the ratio of objects with Lyα emission to those with only absorption features remains roughly constant as a function of magnitude (pink dots).

There are three subgroups identified in Figure 6.3: spectra for which the redshift was measured with Lyα emission (some of which also have interstellar absorption redshifts, but which have at least one identifiable emission line); spectra for which the redshift was only measured with interstellar absorption lines; spectra for which no redshift was measured. Not surprisingly, the fraction of galaxies with spectroscopic failures increases from $\sim 10\%$ at $\mathcal{R} = 24$ to $> 30\%$ at $\mathcal{R} = 25 - 25.5$. The fraction of spectroscopic successes for which the redshift was measured from features including Lyα emission increases from $\sim 60\%$ at $\mathcal{R} = 24$ to $\sim 75\%$ at $\mathcal{R} = 25 - 25.5$. Simultaneously, the fraction of successes for which the redshift was measured only from absorption lines decreases from $\sim 40\%$ at $\mathcal{R} = 24$ down to $\sim 25\%$ at $\mathcal{R} = 25 - 25.5$. These percentages reflect the somewhat obvious fact that it is easier to measure a redshift from an emission line than from an absorption line at fainter magnitudes. As a result, the observed fractions of spectroscopically confirmed objects with and without emission lines in the faintest magnitude bin of Figure 6.3 do not represent the true underlying fractions, in the sense that emission line objects are overrepresented. We can try to draw inferences about the underlying proportion of emission and absorption objects from the fraction of objects without measured spectroscopic redshifts. The simplest possible assumption is that these galaxies must have Lyα emission fluxes below some limiting value as a function of magnitude. This limiting Lyα flux depends on other factors in addition to $\mathcal{R}$ magnitude, most notably time-dependent observing conditions such as sky transparency and seeing. It is difficult to quantify these effects exactly, so we use the conservative assumption that the galaxies without redshifts have $W_{\mathrm{Ly}\alpha} < 0$, i.e., no Ly$\alpha$ emission, and that if redshifts had been measured for these galaxies they would have only been measured from interstellar absorption lines. If the fraction of galaxies with no redshifts is added to the fraction of galaxies with only interstellar absorption redshifts, we see that the implied true proportion of emission and absorption objects remains roughly constant and equal as a function of magnitude (pink dots in Figure 6.3), in contrast to the observed proportion (black dots in Figure 6.3). This exercise gives a rough indication of the degree to which objects with Lyα emission lines are overrepresented relative to absorption-line-only objects within the spectroscopic sample as a function of magnitude.

The photometric and spectroscopic biases presented above affect determinations of both the total LBG spectrum and of the ways in which spectroscopic properties depend on galaxy parameters. Luminosity and redshift are especially prone to these selection effects. Therefore, the discussion of LBG spectroscopic trends is limited to the parameters $W_{\mathrm{Ly}\alpha}$, $E(B-V)$, and $\Delta v_{\mathrm{em-abs}}$. There are highly significant patterns in the spectroscopic properties of LBGs as functions of these parameters. With simple arguments, we show why the strong dependences in the spectroscopic parameters reflect the physical conditions in LBGs, and not the nature of our selection effects.

6.3 Uncertainties

In order to assess the significance of the spectroscopic trends in the sample, it is necessary to assign error bars to the spectroscopic measurements from each composite spectrum. The uncertainty on an equivalent width measurement from a composite spectrum includes not only the finite S/N of the composite spectrum, but also the range of equivalent widths in the sample of galaxies used to construct the composite. While Lyα equivalent widths were measured for almost all of the individual galaxies in the spectroscopic sample, only a subset of the strong interstellar absorption lines was detectable in typical individual spectra. In fact, in 231 cases Lyα emission was the only spectroscopic feature identified. Additionally, the Si II*, C III], and O III] nebular emission lines are far too weak to be measured in individual spectra.

Given that most of the spectroscopic features analyzed in the composites could not be measured reliably in individual spectra, we estimated the sample variance for these features using bootstrap techniques, as follows. For each composite spectrum, we generated 500 fake composite spectra, each one constructed from a sample of galaxies drawn with replacement from the sample used for the real composite spectrum ($\sim 37\%$ of the sample is replaced with duplicates). Using a measurement technique identical to the analysis applied to the real composite spectrum, we continuum normalized each fake composite spectrum, and measured the equivalent widths of Lyα, the six strongest low-ionization interstellar absorption lines, the Si IV and C IV high-ionization interstellar absorption lines, and the weak nebular emission lines. To take into account the noise in each fake composite spectrum, each fake equivalent width measurement was perturbed by an amount drawn from a Gaussian distribution with standard deviation $\sigma = \frac{\sqrt{n}}{S/N}$, where n is the number of pixels over which the equivalent width was measured, and S/N is the signal-to-noise ratio of the real composite spectrum, measured in a relatively featureless portion of the continuum. For the strong interstellar absorption lines and weak emission lines, the contributions to the uncertainty from sample variance and finite S/N were roughly comparable, while in the case of Lyα, sample variance dominated the uncertainty estimate. The total uncertainty for each real equivalent width measurement was then equal to the standard deviation of the distribution of 500 perturbed fake equivalent width measurements (which were distributed around the actual measured value with no systematic offset). The uncertainties for all quantities measured from composite spectra were derived with the above technique. Bootstrap techniques can also be used to estimate the uncertainty in the mean continuum properties such as $E(B-V)$ and $\mathcal{R}$ magnitude, of each composite sample. [1]

[1] Of course, it is also possible to estimate the uncertainty in the mean, $\langle x \rangle$, as $\sigma_{\langle x \rangle} = \frac{\sigma_x}{\sqrt{N_x}}$, where σ_x is the standard deviation of the distribution of x, and N_x is the number galaxies in the sample from which x was measured. This technique yields roughly the same uncertainty in $E(B-V)$ and $\mathcal{R}$ magnitude for each composite sample as the value estimated from the bootstrap method.

6.4 Lyα Dependences

One of the most striking characteristics of the LBG spectroscopic sample is the broad distribution of Lyα strengths and profile-types, ranging from pure damped absorption, to emission plus absorption, to pure strong emission. There is a large body of theoretical and observational work concerning the physical processes that determine the emergent Lyα profile in local and high-redshift star-forming galaxies. In local star-forming galaxies, early observations indicated Lyα emission equivalent widths much smaller than expected from recombination theory, given the star-formation rates inferred from optical Balmer emission lines (Meier & Terlevich, 1981; Hartmann et al., 1984, 1988). Additionally, these observations offered evidence for a correlation between Lyα/Hβ and metallicity (measured from the nebular oxygen abundance, O/H), in the sense that galaxies with lower Lyα/Hβ also had higher O/H (Hartmann et al., 1988; Charlot & Fall, 1993). The observations were first explained with the presence of interstellar dust in a uniform medium, which preferentially destroys Lyα photons relative to non-resonant UV continuum photons, due to the increased path-length traversed by the resonantly scattered Lyα photons. In addition to affecting Lyα photons produced by recombinations in H II regions, dust extinction can also attenuate stellar continuum photons in the immediate vicinity of Lyα, which are also resonantly scattered (Charlot & Fall, 1993; Chen & Neufeld, 1994). The combination of resonant scattering and dust attenuation was thought to significantly reduce the emergent Lyα emission.

The models of a uniform scattering medium clearly oversimplify the structure of the ISM in star-forming galaxies. There are other factors that introduce complexity into the description of Lyα radiative transfer, including the geometry and kinematics of the ISM. As described by Neufeld (1990) and Charlot & Fall (1993), the relative geometries of interstellar H I and H II regions significantly affect the transfer of resonantly scattered photons, but in ways which can either suppress or enhance the Lyα line relative to the continuum. The importance of the geometry of the neutral phase of the ISM is emphasized by the observational results of Giavalisco et al. (1996a). A lack of correlation between the equivalent width of Lyα and the UV continuum slope, β (a measure of continuum extinction), is interpreted as evidence for the decoupling of the reddening of line and continuum photons. This decoupling can occur if the neutral ISM (where the dust resides) is inhomogeneous. Due to resonant scattering, for example, Lyα photons can propagate into paths with less than average gas and dust and escape, whereas the continuum photons reflect the average dust obscuration along the line of sight. The kinematics of the the neutral ISM can also affect the emergent Lyα profile. Inspired by such examples as the metal-poor local starburst I Zwicky 18, which has Lyα only in absorption (Kunth et al., 1994), and the dustier and more metal-rich Haro 2 which shows a redshifted P-Cygni Lyα emission feature (Lequeux et al., 1995), Kunth et al. (1998) survey a small sample of local starburst galaxies in the UV, and find that the objects with Lyα only in absorption also

have interstellar absorption lines (O I λ1302 and Si II λ1304) which are at rest with respect to the H II regions, whereas galaxies with Lyα emission exhibit asymmetric, P-Cygni Lyα profiles, with redshifted Lyα emission, and blueshifted interstellar absorption lines. These observations support a picture in which Lyα photons mainly escape when they are produced by—or scatter off of—material which is offset in velocity from the bulk of the scattering neutral medium. If the neutral ISM is static with respect to the sources of Lyα photons, then the covering factor of the neutral gas becomes important (Kunth et al., 1998). Using such observational evidence, Tenorio-Tagle et al. (1999) have developed a detailed model for the way in which outflow kinematics determine the emergent Lyα profile in starburst galaxies.

At high redshift, a representative subsample of LBG Lyα equivalent widths (Steidel et al., 2000) show that only $\sim 20-25\%$ of LBGs at $z \sim 3$ at a given UV luminosity have Lyα emission lines strong enough to be flagged as narrow-band excess objects, given typical high-redshift Lyα emission line search sensitivities (Cowie & Hu, 1998; Hu et al., 1998). As discussed below, LBGs with such strong emission have certain properties which make them distinct from the population of LBGs as a whole. Narrowband searches are frequently used to probe redshifts higher than $z \sim 3$, so it is important to understand how the properties of narrow-band-selected objects relate to those of general population of star-forming galaxies at similar epochs.

Extending the work of Steidel et al. (2000), we have now measured Lyα equivalent widths for the entire LBG spectroscopic sample. [2] Figure 6.4 shows the rest-frame $W_{\mathrm{Ly}\alpha}$ distribution, which has a median of ~ 0 Å and ranges from < -50 Å in absorption to > 100 Å in emission. The precise measurement of absorption equivalent widths is difficult, given the broad nature of Lyα absorption, the presence of strong metal absorption lines at nearby wavelengths (Si III λ1206 and Si II $\lambda\lambda 1190, 1193$), and the uncertainty in determining the continuum level on the blue side of the line due to Lyα forest absorption. The typical uncertainties in absolute equivalent widths can be larger than $\sim 50\%$ for absorption profiles, while emission equivalent widths are better determined, with $\sim 30\%$ uncertainties. The Lyα profiles for 38% of the galaxies consist of a combination of both emission and absorption. For galaxies characterized by this type of profile, two equivalent widths were measured: a total equivalent width representing the sum of the emission and absorption components, and also an emission equivalent width representing the emission alone. The intrinsic rest-frame UV color, and implied dust extinction, $E(B-V)$, were computed by correcting the observed $G-\mathcal{R}$ color for both the total Lyα equivalent width, and also the average IGM absorption along the line of sight.

[2] There are actually 17 galaxies in the spectroscopic sample for which we did not measure the Lyα equivalent width. Most of these galaxies are towards the low-redshift end of the LBG redshift distribution such that Lyα was not contained in the spectral format of the LRIS detector. Additionally there are galaxies for which Lyα fell on top of some defect in the two dimensional spectral image, precluding us from robustly measuring an equivalent width.

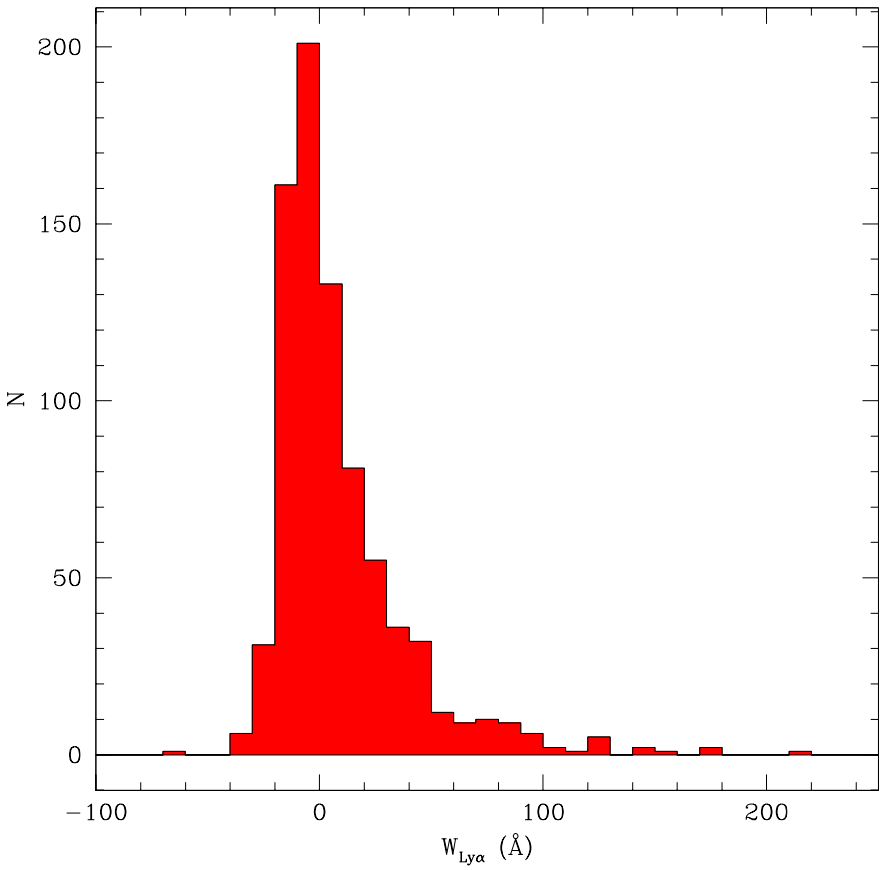

Figure 6.4 The distribution of Lyα equivalent widths for the LBG spectroscopic sample. This sample contains a broad range of equivalent widths with a median of ~ 0 Å. Only 25% of the sample has rest-frame $W_{\mathrm{Ly}\alpha} \geq 20$ Å, large enough to be selected by narrow band excess techniques, given the depth of current surveys. There is a correlation between Lyα emission equivalent width and $\mathcal{R}$ magnitude among sources with $W_{\mathrm{Ly}\alpha} \geq 20$ Å, such that fainter galaxies have larger $W_{\mathrm{Ly}\alpha}$.

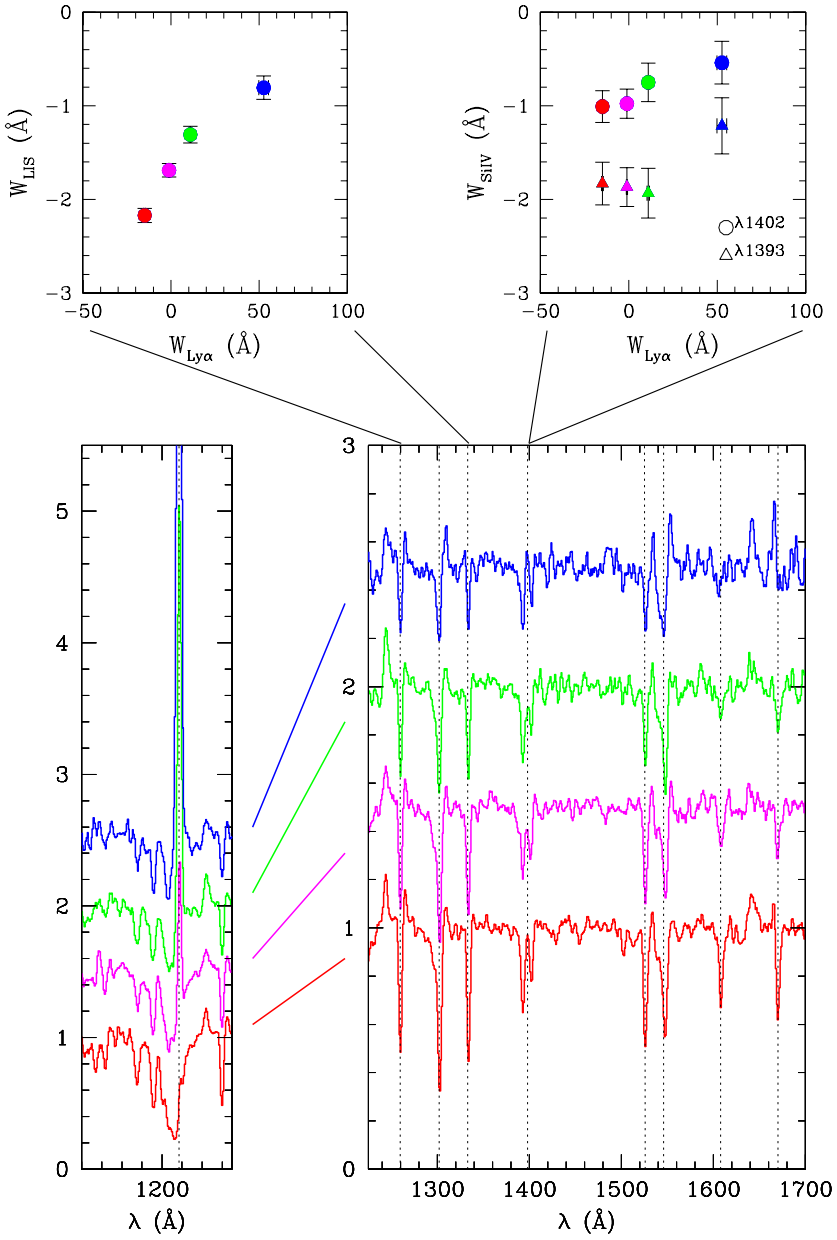

Figure 6.5 Bottom: A sequence of 4 continuum-normalized composite spectra, constructed from the 4 quartiles of LBG spectroscopic sample grouped according to Lyα equivalent width. The spectra have been offset by regular vertical intervals for easier viewing, in order of increasing $W_{\mathrm{Ly}\alpha}$. The lower left-hand panel zooms in on the region near Lyα, while the right-hand panel focuses on the region redwards of Lyα, where the strongest features are blue-shifted low-ionization and high-ionization interstellar absorption features associated with large-scale outflows of interstellar material. Top: The behavior of low- and high-ionization interstellar absorption lines as a function of Lyα equivalent width. These plots confirm quantitatively what the bottom panels indicate visually: the average low-ionization absorption equivalent width, W_{LIS}, decreases dramatically as $W_{\mathrm{Ly}\alpha}$ varies from strong absorption to strong emission, while the high-ionization Si IV absorption equivalent width, W_{SiIV}, remains roughly constant (except in the quartile of the sample with strong Lyα emission, in which W_{HIS} is slightly weaker).

In order to understand the factors which determine the emergent Lyα profile in LBGs, we binned the sample of 794 individual spectra with Lyα measurements according to $W_{\mathrm{Ly}\alpha}$ into 4 subsamples of equal size. A composite spectrum was constructed from each subsample. The large number of galaxies contained in each bin insured that the resulting composite spectrum had very high S/N, yet there were also enough separate bins that the Lyα properties of the subsamples at each extreme were quite distinct: the bin at one extreme was characterized by objects with strong absorption, while the other extreme bin was dominated by objects with large emission equivalent widths. We obtain several striking results from binning the sample according to $W_{\mathrm{Ly}\alpha}$ and measuring the features of the resulting composite spectra. These measurements are summarized in Table 6.1.

As shown in Figure 6.5, the average absorption equivalent width of the 6 strongest low-ionization interstellar lines, W_{LIS}, decreases in strength by almost a factor of three as $W_{\mathrm{Ly}\alpha}$ varies from -15 Å in absorption to 50 Å in emission. Even in the spectrum with the strongest Lyα emission and weakest absorption lines, the ratio of Si II λ1260 and λ1526 absorption equivalent widths is roughly unity. This indicates that the lines are still saturated and that the change in low-ionization equivalent width across the sample is not primarily due to a change in metallicity. There is no significant change in the absorption strength of the high-ionization interstellar absorption lines, W_{SiIV} and W_{CIV}, as $W_{\mathrm{Ly}\alpha}$ varies from strong absorption to strong emission, except in the quartile of galaxies with $W_{\mathrm{Ly}\alpha} \geq 20$ Å, which has line strengths smaller than the other three quartiles by 50% (still a much less significant change than what is seen in the low ions). Additionally, the Si IV doublet ratio is consistent with the transition being optically thin in all four subsamples.

Another important result is that the UV continuum slope becomes significantly bluer as $W_{\mathrm{Ly}\alpha}$ varies from strong absorption to strong emission. This result is most dramatically illustrated by the left-hand box of Figure 6.6, which shows how the strong-absorption and strong-emission composite spectra, normalized at 1100 Å, diverge at longer wavelengths. To support this visual picture, the right-hand box of Figure 6.6 shows that the mean $E(B-V)$ value for each of the four subsamples decreases as a function of increasing $W_{\mathrm{Ly}\alpha}$ in emission.

Furthermore, Figure 6.7 shows that with increasing Lyα emission strength, the kinematic offset implied by the relative redshifts of Lyα emission and low-ionization interstellar absorption lines decreases monotonically from $\Delta v_{\mathrm{em-abs}} = 800$ km s^{-1} to $\Delta v_{\mathrm{em-abs}} = 480$ km s^{-1}. The kinematic offsets were measured directly from the composite spectra. Weak Lyα emission is detected even in the spectrum composed of the quartile of galaxies with strong absorption and no emission on an individual basis. Therefore, a kinematic offset can be estimated even for this absorption sample.

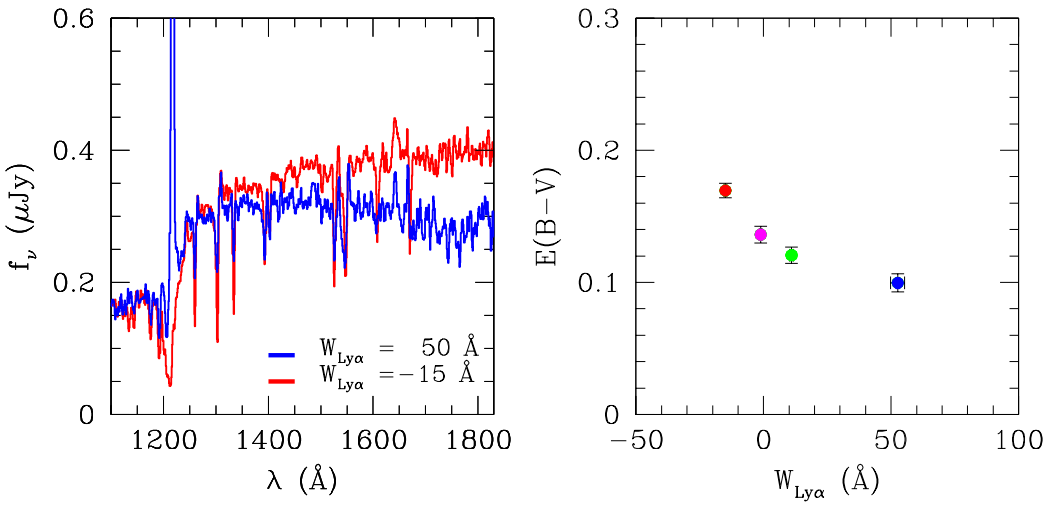

Figure 6.6 The dependence of UV continuum shape on Lyα equivalent width. Left: Plotted in blue, the composite spectrum of the quartile of galaxies with the strongest Lyα emission and the weakest low-ionization interstellar absorption lines is also significantly bluer in spectral slope than the composite spectrum of the quartile of galaxies with the strongest Lyα absorption and strongest low-ionization interstellar absorption lines, which is plotted in red. Right: The visual difference between the two extreme spectra in the left-hand panel is confirmed by the mean $E(B-V)$ for each of the four Lyα quartiles, which decreases as a function of increasing Lyα emission.

Now we focus on the composite spectrum of the quartile of galaxies with $W_{\rm Ly\alpha} \geq 20$ Å, which is strong enough to be selected by current narrow-band emission line search techniques (Hu et al., 1998; Rhoads et al., 2000). This composite spectrum has significantly stronger C III] and O III] nebular emission line strengths than the composite spectra with weaker Lyα emission (see Figure 6.8). In contrast to the strong low-ionization and high-ionization absorption lines, which probe conditions in the foreground, outflowing interstellar medium, the nebular lines act as probes of H II regions where stars are forming. The strength of these features should be independent of conditions in the foreground gas and associated orientation effects, and more sensitive to the nebular temperature and metallicity, and the nature of the stellar population.

The sample with $W_{\rm Ly\alpha} \geq 20$ Å in emission is much more complete as a function of $\mathcal{R}$ magnitude than the spectroscopic sample as a whole, since we don't fail spectroscopically on objects with observed equivalent widths of $W_{\rm Ly\alpha,obs} \geq 80$ Å (the same as rest-frame $W_{\rm Ly\alpha} \geq 20$ Å at $z \sim 3$). Therefore, this sample is ideal to test for the dependence of Lyα emission strength on apparent UV luminosity. We divide the galaxies with $W_{\rm Ly\alpha} \geq 20$ Å into three groups according to $\mathcal{R}$ magnitude, and compare the three distributions of Lyα equivalent widths. The mean $W_{\rm Ly\alpha}$ increases towards fainter magnitudes, and a one-dimensional K-S test shows that there is only a 0.1% chance that the brightest distribution of $W_{\rm Ly\alpha}$ could be drawn from the same parent population as the faintest sample. Since any individual $W_{\rm Ly\alpha}$ measurement has a significant uncertainty, especially at faint magnitudes, we check this statistical result by constructing composite spectra of the faintest third

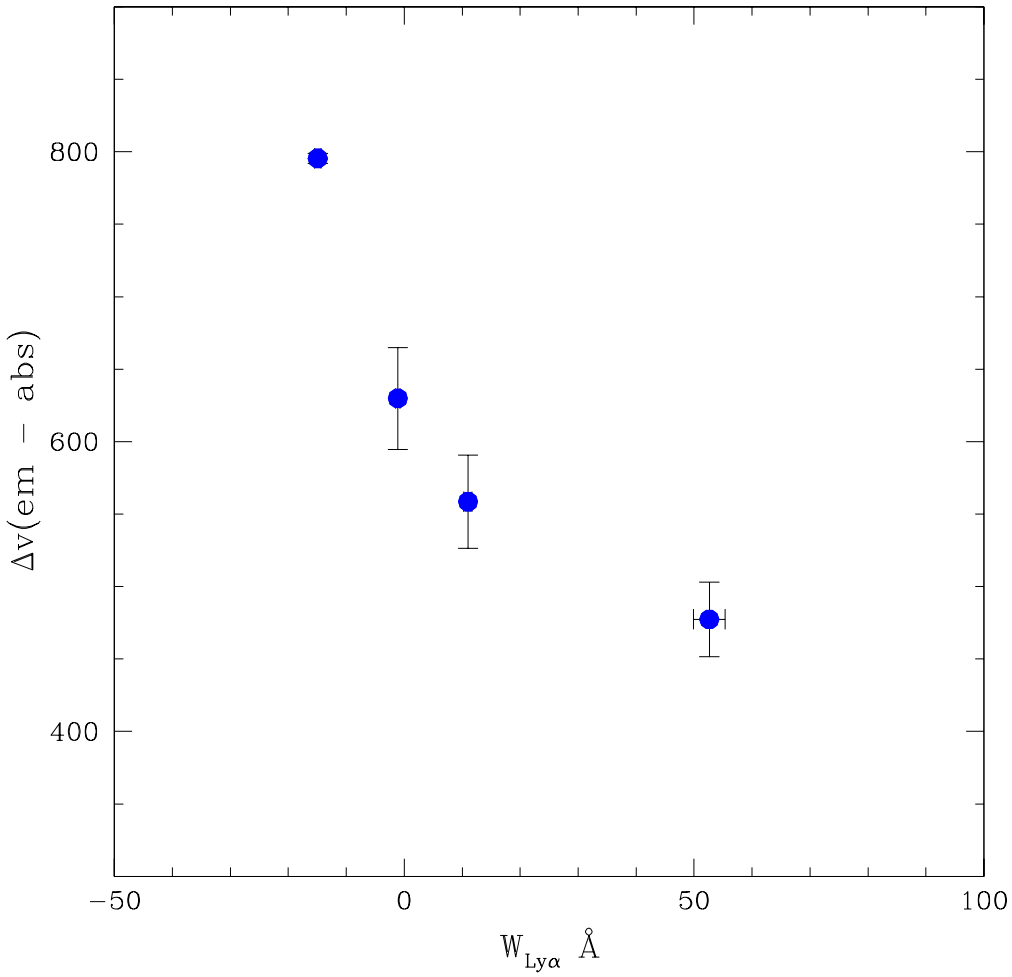

Figure 6.7 The dependence of $\Delta v_{\rm em-abs}$ on Lyα equivalent width. Velocity offsets between Lyα emission and the strongest low-ionization interstellar absorption lines were measured directly from the composite spectra of each of the four Lyα subsamples. As Lyα emission strength increases, the kinematic offset decreases. The error bars on the velocity offsets represent the scatter among the velocities of the different individual interstellar absorption features.

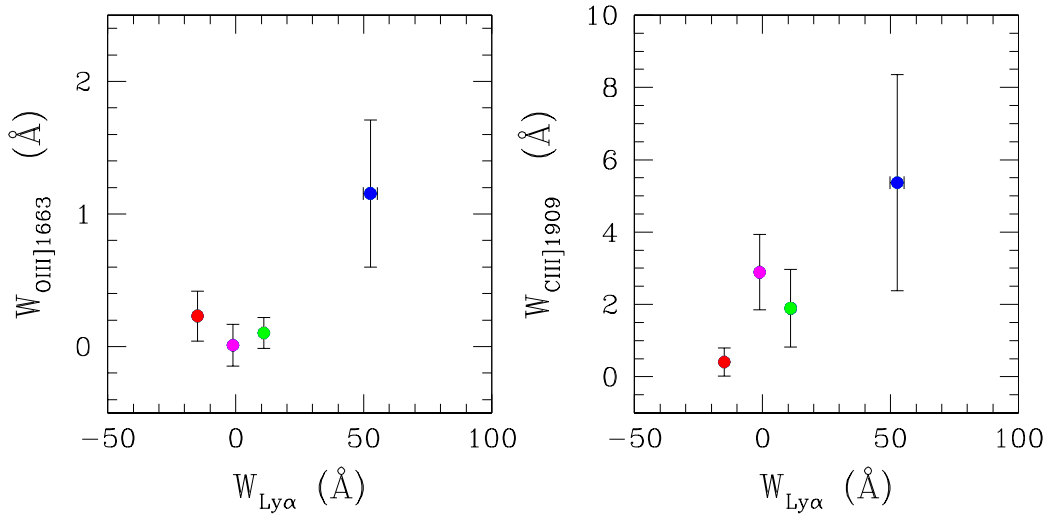

Figure 6.8 The dependence of O III] and C III] nebular emission strength on Lyα equivalent width. The composite spectrum constructed from the quartile of galaxies with $W_{\mathrm{Ly}\alpha} \geq 20$ Å has significantly stronger nebular emission than the rest of the sample.

and brightest third of the subsample with $W_{\mathrm{Ly}\alpha} \geq 20$ Å. Measured directly from the bright and faint composite spectra, which are shown in Figure 6.9, the Lyα equivalent widths are $W_{\mathrm{Ly}\alpha}(\mathrm{bright}) = 43$ Å and $W_{\mathrm{Ly}\alpha}(\mathrm{faint}) = 65$ Å. Even in the faintest subsample, which has the strongest Lyα emission of any LBG subsample, the average value of $W_{\mathrm{Ly}\alpha}(\mathrm{faint}) = 65$ Å is still well below what is expected for Case B recombination, given a stellar population continuously forming stars with a Salpeter IMF for ≤ 1 Gyr (Charlot & Fall, 1993). Therefore, the escape of Lyman continuum photons from LBG star-forming regions is not ruled out by the strength of Lyα emission, and the escape fraction from LBGs is probably determined much more by the covering fraction of outflowing neutral clouds at larger radii (Heckman et al., 2001a; Steidel et al., 2001).

At least in part due to selection effects, the quartile of the sample with the strongest Lyα emission is significantly fainter on average than the quartile with the strongest Lyα absorption. The mean apparent magnitude of the strong absorption quartile is $\mathcal{R} = 24.44$, while the mean apparent magnitude of the strong emission quartile is $\mathcal{R} = 24.85$. Since grouping the sample by $W_{\mathrm{Ly}\alpha}$ also segregates to a certain degree by $\mathcal{R}$ magnitude, it is important to show that the significant spectroscopic trends hold at fixed apparent UV luminosity, especially at an apparent magnitude where all spectroscopic "types" are sampled equally. Therefore, we zero in on the range $\mathcal{R} = 24-24.5$, and bin the 207 galaxies in this magnitude range into four equal subsamples according to $W_{\mathrm{Ly}\alpha}$. As shown in Figure 6.10, the same strong Lyα-dependent trends hold at fixed magnitude: as Lyα changes from strong absorption to strong emission, the average W_{LIS} significantly decreases, and the UV continuum slope becomes significantly bluer; simultaneously, the average W_{SiIV} and W_{CIV} remain roughly independent of $W_{\mathrm{Ly}\alpha}$. The fixed-magnitude Lyα sample is roughly 4 times

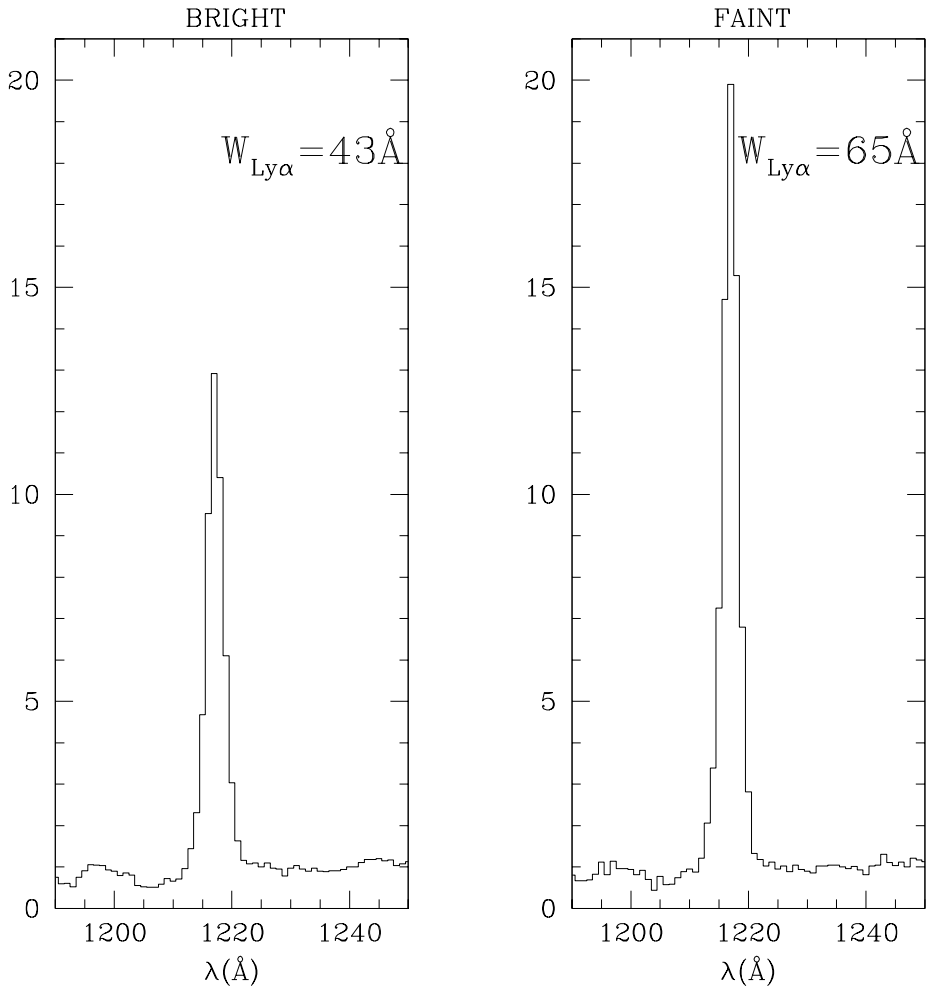

Figure 6.9 The dependence of $W_{\rm Ly\alpha}$ on apparent UV luminosity. Restricting the comparison to galaxies with $W_{\rm Ly\alpha} \geq 20$ Å, which should not be prone to magnitude-dependent selection effects, we construct composite spectra for faint (right panel) and bright (left panel) galaxies. Equivalent widths are measured directly from the continuum-normalized composite spectra and indicate that fainter galaxies have larger Lyα emission equivalent widths than brighter galaxies.

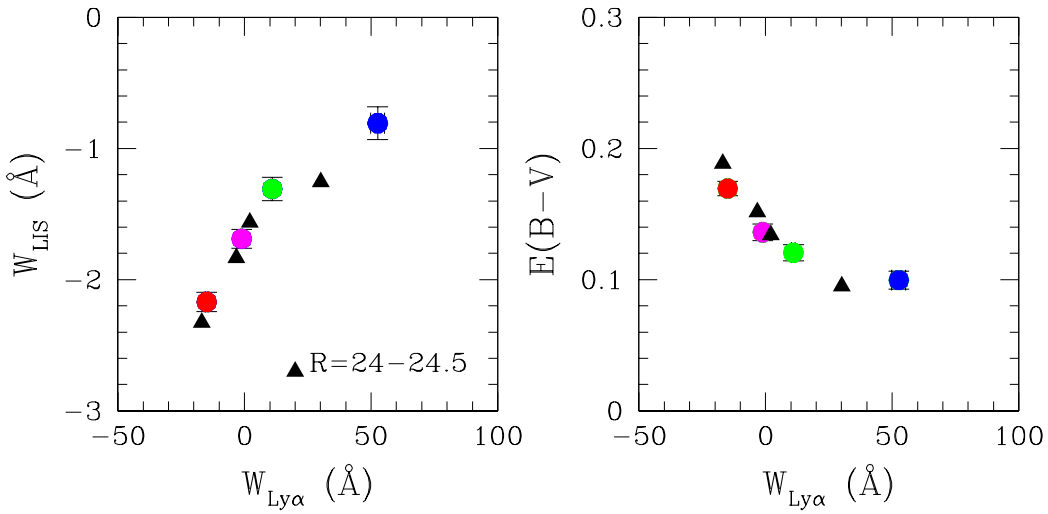

Figure 6.10 Strong Lyα-dependent trends at fixed $\mathcal{R}$ magnitude. Galaxies with $\mathcal{R} = 24 - 24.5$ are divided into four subsamples based on Lyα equivalent width, and black triangles indicate measurements from the corresponding composite spectra. Left: $W_{\rm Ly\alpha}$ vs. $W_{\rm LIS}$. Colored symbols are as in Figure 6.5. Galaxies with $\mathcal{R} = 24 - 24.5$ follow the same trend as the total sample. Right: $E(B-V)$ vs. $W_{\rm Ly\alpha}$. Colored symbols are as in Figure 6.6, and galaxies with $\mathcal{R} = 24 - 24.5$ obey the same correlation.

smaller than the total Lyα sample, and therefore weak nebular emission lines are not detected with much significance. The same significant Lyα-dependent trends are found to apply as well for fixed-magnitude bins of $\mathcal{R} = 24.5 - 25$ and $\mathcal{R} = 25 - 25.5$. LBG photometric and spectroscopic selection effects should not introduce a correlation between $W_{\rm Ly\alpha}$ and $W_{\rm LIS}$, or between $W_{\rm Ly\alpha}$ and UV continuum slope. The consistency of the trends at different $\mathcal{R}$ magnitudes provides direct evidence that magnitude-dependent selection effects have not spuriously introduced correlations; we consider the physical significance of these trends in Chapter 7.

6.5 UV Color Dependences

At $z \sim 3$, the intrinsic UV color, $(G-\mathcal{R})_0$, is determined by correcting the observed $G-\mathcal{R}$ color for the observed Lyα equivalent width, and the redshift-dependent average Lyα forest opacity (Madau, 1995). A stellar population continuously forming stars (an appropriate model of the UV colors and spectra of most LBGs) has an unreddened UV spectral energy distribution shape that remains fairly constant for ages between 10 Myr and 1 Gyr. [3] Therefore, the range of LBG $(G-\mathcal{R})_0$ colors can be parameterized in terms of $E(B-V)$, the amount of dust extinction reddening the intrinsic UV continuum. In order to convert $(G-\mathcal{R})_0$ to $E(B-V)$, we assume for the unreddened stellar population a 300 Myr old continuous star-formation model—the median age for a subsample

[3] If the spectral energy distribution is parameterized as $F_\lambda \propto \lambda^\beta$, β only ranges between -2.6 and -2.1 for continuous star-formation ages between 10 Myr and 1 Gyr (Leitherer et al., 1999).

of LBGs with optical-IR colors (Shapley et al., 2001). We also assume a relatively grey form for the dust extinction law, which accurately describes the dust properties of local starburst galaxies (Calzetti, 1997; Calzetti et al., 2000; Meurer et al., 1999). While the evidence at high redshift is still preliminary, multi-wavelength observations show that the starburst extinction law predicts the properties of LBGs at X-ray and radio wavelengths much better than extinction laws appropriate for the SMC or Ultra-Luminous Infrared Galaxies (ULIRGs) (Seibert et al., 2002; Meurer et al., 1999; Nandra et al., 2002).

Based on the range of UV colors of LBGs, and the types of assumptions described above, Adelberger & Steidel (2000) find that the UV luminosities of LBGs are attenuated on average by a factor of ~ 7 due to dust extinction, and that this factor ranges from $0 - 100$. Additionally, LBGs with more dust extinction have higher intrinsic star-formation rates and younger stellar populations (Adelberger & Steidel, 2000; Shapley et al., 2001). The role played by star-formation induced outflows in the evolution of the dust properties of LBGs was addressed qualitatively by Shapley et al. (2001), but without the benefit of detailed spectroscopic analysis. Here, we fold in spectroscopic information to gain a more complete picture of the relationship between dust extinction and outflows.

As presented in section 6.4, when Lyα varies from strong absorption to strong emission: 1) the strength of the low-ionization interstellar absorption lines decreases 2) the dust-sensitive UV continuum becomes bluer. Given the strong interdependence of $W_{\mathrm{Ly}\alpha}$, W_{LIS}, and $E(B-V)$, it is interesting to consider which correlations among the three variables are stronger, and therefore fundamental, and which arise as a by-product of the more fundamental correlations. When the sample is divided into $E(B-V)$ quartiles, we confirm the same interdependence of $W_{\mathrm{Ly}\alpha}$, W_{LIS}, and $E(B-V)$. Figure 6.11 also demonstrates that W_{LIS} is more strongly dependent on $W_{\mathrm{Ly}\alpha}$ than on $E(B-V)$. Though W_{LIS} becomes significantly weaker (a factor of 1.6) as $E(B-V)$ decreases from the reddest to the bluest quartile, there is a more significant change in W_{LIS} (a factor of 2.7) as $W_{\mathrm{Ly}\alpha}$ varies from strong absorption to strong emission. The variance in W_{LIS} as a function of $E(B-V)$ cannot be accounted for entirely by the change in $W_{\mathrm{Ly}\alpha}$, however; $W_{\mathrm{Ly}\alpha}$ only changes from $W_{\mathrm{Ly}\alpha}(\mathrm{red}) = 5$ to $W_{\mathrm{Ly}\alpha}(\mathrm{blue}) = 20$ Å as $E(B-V)$ decreases from the reddest to the bluest quartile (in contrast to the change from $W_{\mathrm{Ly}\alpha}(\mathrm{abs}) = -15$ Å to $W_{\mathrm{Ly}\alpha}(\mathrm{em}) = 50$ Å in the four Lyα subsamples). According to the relationship between $W_{\mathrm{Ly}\alpha}$ and W_{LIS} presented in section 6.4, we would predict a smaller difference between $W_{\mathrm{LIS}}(\mathrm{red})$ and $W_{\mathrm{LIS}}(\mathrm{blue})$ to accompany the difference between $W_{\mathrm{Ly}\alpha}(\mathrm{red})$ and $W_{\mathrm{Ly}\alpha}(\mathrm{blue})$. We therefore infer a direct statistical link between the absorbing gas and the reddening of the UV continuum, as well as between the absorbing gas and the Lyα profile.

Due to selection effects, the bluest quartile is fainter ($\langle\mathcal{R}\rangle = 24.75$) than the reddest quartile ($\langle\mathcal{R}\rangle = 24.51$). To remove the effects of luminosity, we again examine whether the trends still hold

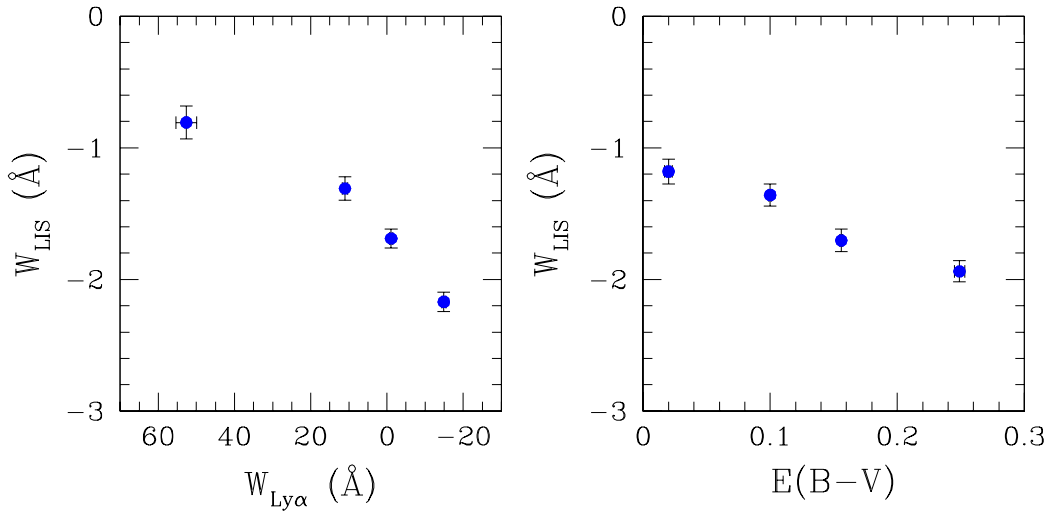

Figure 6.11 The dependence of low-ionization interstellar absorption strength, $W_{\rm LIS}$, on both Lyα equivalent width and dust reddening. These plots show the results of dividing LBG spectroscopic sample into quartiles, according to either Lyα equivalent width (left) or $E(B-V)$ (right). While $W_{\rm LIS}$ depends strongly on both $W_{{\rm Ly}\alpha}$ and $E(B-V)$, there is more variance in $W_{\rm LIS}$ when the sample is sorted by $W_{{\rm Ly}\alpha}$. This suggests a stronger statistical link between $W_{\rm LIS}$ and $W_{{\rm Ly}\alpha}$, though the correlation between $W_{\rm LIS}$ and $E(B-V)$ is strong enough that there may be a direct physical connection among all three quantities.

when we look in fixed magnitude ranges: $\mathcal{R} = 24-24.5, 24.5-25, 25-25.5$. The strength of correlations with $E(B-V)$ is independent of magnitude, though there is a systematic offset in the "zeropoints," such that galaxies of a given $E(B-V)$ have stronger Lyα and weaker low-ionization interstellar absorption lines at fainter $\mathcal{R}$ magnitudes. The qualitative similarity of the $E(B-V)$ correlations at all magnitudes confirms their connection to actual physical conditions, rather than to luminosity-dependent selection effects. For LBGs in general, and especially for LBGs in a fixed magnitude range, the dependence of spectroscopic properties on dust extinction is roughly equivalent to the dependence on (slightly model-dependent) dust-corrected star-formation rate. Therefore, galaxies with redder UV continua, stronger interstellar absorption lines, and weaker Lyα emission, also have larger star-formation rates.

6.6 Kinematic $\Delta v_{\rm em-abs}$ Dependences

The multi-wavelength properties of "superwinds" in local starburst galaxies have been studied with spatially resolved imaging and spectroscopy (Heckman et al., 2000, 2001b). Also, the hydrodynamics of different phases of the outflowing ISM have been modeled numerically (Strickland & Stevens, 2000). Due to their small angular sizes and faint magnitudes, there is very little two-dimensional morphological information or spatially resolved spectroscopy of $z \sim 3$ star-forming galaxies. However, the one dimensional spectroscopic properties of LBGs indicate the presence of large velocity

fields, consistent with the outflow conditions seen in local starbursts. In individual spectra, the Lyα and interstellar redshift differ, with an average offset of $\Delta v_{\rm em-abs} = 650$ km s^{-1}, ranging from less than 0 km s^{-1}to greater than 1000 km s^{-1}(sections 5.3.1, 5.4.2, Figure 5.1). The composite spectrum of the total LBG spectroscopic sample, at rest with respect to stars and H II regions, has Δv(Lyα) = +360 km s^{-1}and Δv(LIS) = $-$150 km s^{-1}, implying $\Delta v_{\rm em-abs}$ = 510 km s^{-1}. This offset is smaller than the average $\Delta v_{\rm em-abs}$ measured from individual spectra, but we actually expect the total sample to have a smaller average $\Delta v_{\rm em-abs}$ than the subsample of objects with both emission and absorption redshifts. This is because the total composite spectrum has stronger Lyα emission than the composite spectrum constructed only from objects with individual $\Delta v_{\rm em-abs}$ measurements, and section 6.4 demonstrated a correlation between $W_{\rm Ly\alpha}$ and $\Delta v_{\rm em-abs}$.

Since the $\Delta v_{\rm em-abs}$ distribution for the 323 galaxies with both Lyα emission and interstellar absorption redshifts is fairly broad, it affords sufficient dynamic range for us to consider how other galaxy properties depend on outflow kinematics. Studies of the radiative transfer of Lyα in local starburst galaxies (Kunth et al., 1998) stress the importance of ISM kinematics on the emergent Lyα profile. With our sample, we can directly test the link between Lyα equivalent width and ISM kinematics. Also, $\Delta v_{\rm em-abs}$ should be related to the velocity FWHM of the outflowing gas. The FWHM of blue-shifted gas will determine the range of wavelengths of Lyα photons that are scattered. Blue-shifted gas with a larger velocity dispersion will scatter Lyα photons with a larger range of wavelengths, pushing the observed centroid of Lyα emission to longer wavelengths, and causing a larger apparent $\Delta v_{\rm em-abs}$ for the same outflow velocity (see Figure 3 of Adelberger et al. 2002a). Ideally, we would like to examine the relationship between $\Delta v_{\rm em-abs}$ and the intrinsic FWHM of the strong low-ionization interstellar absorption lines. We are hampered in this effort by the uncertainty in the effective spectral resolution of our composite spectra. Even when all of the spectra are shifted into the absorption rest frame to minimize the effects of redshift errors, the FWHM measurements are quite noisy and difficult to interpret. However, a comparison between the much better determined $W_{\rm LIS}$ and $\Delta v_{\rm em-abs}$ may help to isolate the kinematic contribution to the saturated absorption equivalent widths.

The galaxies with $\Delta v_{\rm em-abs}$ measurements are divided into three subsamples, with $\langle \Delta v_{\rm em-abs} \rangle = 340, 620, 890$ km s^{-1}, and a composite spectrum is constructed for each subsample. Due to the requirement that both emission and absorption features are present in order to compute $\Delta v_{\rm em-abs}$, the kinematic sample is biased towards brighter objects. However, there should be no biases that prevent us from including certain types of objects as a differential function of $\Delta v_{\rm em-abs}$. Consistent with the results of section 6.4, we find that $W_{\rm Ly\alpha}$ is weakly dependent on $\Delta v_{\rm em-abs}$ (Figure 6.12). While statistically significant, the difference between $W_{\rm Ly\alpha}(\Delta v = 340)$ and $W_{\rm Ly\alpha}(\Delta v = 890)$ is small compared to the large range of $W_{\rm Ly\alpha}$ seen in the entire sample. Also, $W_{\rm LIS}$ marginally increases with increasing $\Delta v_{\rm em-abs}$, though the difference is not significant, and may arise as a result of the strong

correlation between Lyα and the interstellar absorption lines (Figure 6.12). Somewhat surprisingly, the sample with $\langle \Delta v_{\rm em-abs} \rangle = 890$ km s^{-1} has very strong *high*-ionization equivalent widths, though the Si IV doublet ratio indicates that Si IV is still optically thin. Relative to the average values for the total LBG sample (section 5.4.2.2), the high Δv sample has $W_{\rm Si\ IV}$ and $W_{\rm C\ IV}$ that are 50% higher. Finally, the UV continuum becomes bluer with increasing velocity width (Figure 6.12). None of the correlations with $\Delta v_{\rm em-abs}$ is as significant as the trends among $W_{\rm Ly\alpha}$, $W_{\rm LIS}$, and $E(B-V)$.

6.7 Comparison with Local Starburst Results

A systematic analysis of the UV spectroscopic properties of local starburst galaxies was carried out by Heckman et al. (1998), intended to guide the interpretation of UV spectroscopic properties of high-redshift star-forming galaxies. Several starburst parameters were considered, including UV continuum slope, UV and bolometric luminosity, UV low-ionization interstellar equivalent width, high-ionization stellar wind equivalent width, and nebular metallicity. One of the parameters carrying a lot of the variance of the properties of local starbursts is metallicity, measured from the nebular oxygen abundance, O/H. More metal-rich starbursts have more dust extinction, higher star-formation rates, and stronger UV absorption lines. Since there are nebular O/H measurements for only a handful of LBGs, and the C/O measurements from the composite spectra are very uncertain, it is not possible to make a direct comparison to the metallicity-dependent results for local starbursts. Moreover, a large part of the analysis in the present work addresses the factors that control the emergent Lyα profile in LBGs, which is, ironically, much harder to study at low redshift due to contamination from geocoronal Lyα, and therefore not included in the Heckman et al. analysis. However, we can directly compare the local and high-redshift results for the relationship between UV continuum reddening and interstellar absorption line strengths. Both in local starbursts and LBGs, there is a strong correlation between $W_{\rm LIS}$ and UV continuum reddening. Since the absorption lines are saturated in both samples, variations in their equivalent widths reflect changes in the combination of neutral gas covering fraction and velocity dispersion, rather than in metal abundance. For the local starbursts, the correlation is interpreted as resulting from the mutual dependence of both $W_{\rm LIS}$ and dust extinction on the velocity dispersion of the absorbing neutral gas. As described more fully in section 7.2, we offer a different interpretation of this trend.

We can compare the $z \sim 3$ results about Lyα emission with other local studies. In contrast to the apparent decoupling between Lyα extinction and continuum reddening found in local starburst galaxies (Giavalisco et al., 1996a) we find a significant correlation between UV continuum extinction and $W_{\rm Ly\alpha}$. Either this difference between the local starbursts and LBGs points to a significant difference between the geometries of dusty neutral gas in star-forming galaxies at low and high-redshift, or else the low-redshift sample suffered from the vagaries of small sample statistics. In the

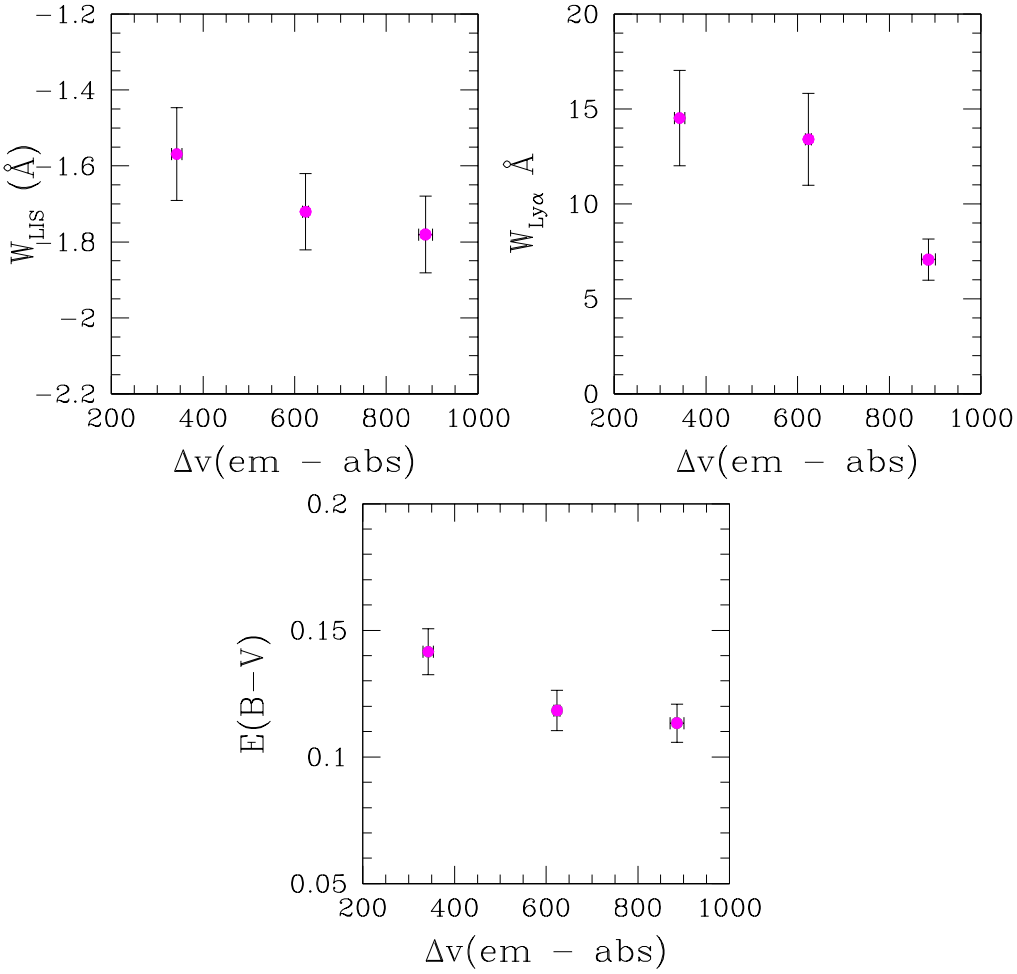

Figure 6.12 Dependences of $W_{\rm LIS}$, $W_{{\rm Ly}\alpha}$, and $E(B-V)$ on $\Delta v_{\rm em-abs}$. These plots show the average $W_{\rm LIS}$, $W_{{\rm Ly}\alpha}$, and $E(B-V)$ values measured from each of the 3 subsets of galaxies sorted by $\Delta v_{\rm em-abs}$, and their associated composite spectra. $W_{\rm LIS}$ and $E(B-V)$ are not significantly dependent on Δv, while $W_{{\rm Ly}\alpha}$ is smaller for the subsample with the highest Δv ($\geq$ 800 km s^{-1})). This trend is consistent with the fact that the Δv measured in the composite spectrum with the strongest Lyα absorption is larger than the Δv measured in the spectrum with the strongest Lyα emission. However, the change in $W_{{\rm Ly}\alpha}$ with Δv is small compared with the total variance of Lyα across the whole LBG spectroscopic sample.

work of Kunth et al. (1998), strong Lyα absorption is seen in cases where the interstellar absorption lines are static with respect to the galaxy systemic velocity, whereas Lyα emission is detected in galaxies with blue-shifted interstellar absorption lines. The blue-shift of interstellar absorption lines is ubiquitous in the LBG spectroscopic sample, even in galaxies with strong Lyα absorption. In contrast to the evidence at low redshift, the presence of an outflow in LBGs is not a sufficient criterion for detecting Lyα emission. In fact, it appears that the Lyα emission equivalent width *increases* as the velocity offset between Lyα and the interstellar absorption lines decreases.

In local starbursts, the UV nebular emission lines such as C III] λ1909 are stronger in starbursts of lower metallicity (Heckman et al., 1998). This effect is most likely due to a decrease in the nebular electron temperature of higher metallicity gas, which causes more of the nebular cooling from collisionally excited lines to occur in the infrared rather than the UV. Collisionally excited C III] and O III] nebular emission lines are stronger than average in the composite spectrum of LBGs with $W_{\mathrm{Ly}\alpha} \geq 20$ Å. By analogy with the local results, this subsample may be composed of objects with lower than average LBG metallicites. The C/O ratio in the strong emission composite spectrum implies an O/H abundance that is lower than the average O/H observed in the small sample of LBGs with rest-frame optical spectroscopic measurements (Pettini et al., 2001), though the uncertainties in both measurements are large. Important future observations include nebular metallicity measurements of statistical samples of LBGs, when multi-object rest-frame optical spectroscopy becomes possible. Also important are outflow metallicity measurements from unsaturated interstellar absorption lines, which will be possible with higher S/N and resolution rest-frame UV spectra.

Table 6.1. Spectroscopic Properties of Lyα Subsamples

	Group 1[a]	Group 2[a]	Group 3[a]	Group 4[a]
N_{gal}	199	198	199	198
$W_{\mathrm{Ly}\alpha}$[b]	-14.92 ± 0.56	-1.10 ± 0.38	11.00 ± 0.71	52.63 ± 2.74
$W_{\mathrm{SiII,1260}}$[b]	-1.85 ± 0.16	-1.59 ± 0.16	-1.36 ± 0.19	-1.05 ± 0.22
$W_{\mathrm{OI+SiII,1303}}$[b]	-3.24 ± 0.16	-2.71 ± 0.16	-1.98 ± 0.19	-1.21 ± 0.21
$W_{\mathrm{CII,1334}}$[b]	-2.34 ± 0.16	-1.91 ± 0.15	-1.43 ± 0.19	-0.83 ± 0.23
$W_{\mathrm{SiII,1526}}$[b]	-2.38 ± 0.19	-1.82 ± 0.19	-1.33 ± 0.23	-1.21 ± 0.33
$W_{\mathrm{FeII,1608}}$[b]	-1.57 ± 0.21	-1.03 ± 0.18	-0.69 ± 0.25	-0.59 ± 0.34
$W_{\mathrm{AlII,1670}}$[b]	-1.64 ± 0.22	-1.08 ± 0.20	-1.07 ± 0.25	0.04 ± 0.44
$W_{\mathrm{SiIV,1393}}$[b]	-1.83 ± 0.23	-1.87 ± 0.21	-1.93 ± 0.27	-1.22 ± 0.30
$W_{\mathrm{SiIV,1402}}$[b]	-1.01 ± 0.17	-0.98 ± 0.16	-0.75 ± 0.21	-0.54 ± 0.23
$W_{\mathrm{CIV,1549}}$[b]	-3.56 ± 0.30	-2.97 ± 0.32	-3.22 ± 0.39	-2.43 ± 0.47
$W_{\mathrm{OIII],1663}}$[b]	0.23 ± 0.19	0.01 ± 0.16	0.10 ± 0.12	1.16 ± 0.56
$W_{\mathrm{CIII],1909}}$[b]	0.41 ± 0.39	2.89 ± 1.04	1.90 ± 1.07	5.37 ± 2.99
$E(B-V)$[c]	0.169 ± 0.006	0.136 ± 0.006	0.120 ± 0.006	0.099 ± 0.007
β[c]	-0.73 ± 0.03	-0.88 ± 0.04	-0.98 ± 0.03	-1.09 ± 0.05
Δv_{em-abs} (km s^{-1})	795 ± 3	630 ± 35	560 ± 30	475 ± 25
$\mathcal{R}_{AB}$	24.44 ± 0.04	24.49 ± 0.04	24.64 ± 0.04	24.85 ± 0.04
SFR$_0$ ($h^{-2} M_\odot$ yr^{-1})[d]	52 ± 5	38 ± 2	29 ± 3	25 ± 3

[a]Groups 1–4 are the four quartiles of the LBG spectroscopic sample, divided according to Lyα equivalent width.

[b]Rest-frame equivalent width in Å, measured from the composite spectra. Positive values indicate emission, while negative values indicate absorption. Uncertainties are calculated as described in section 6.3.

[c]Estimates of reddening, based on the intrinsic UV color, $(G-\mathcal{R})_0$. $E(B-V)$ assumes the Calzetti law for dust extinction, and an underlying stellar population with 300 Myr of constant star-formation. β is derived directly from the $(G-\mathcal{R})_0$ color, assuming that the UV spectrum can be described by the form, $F_\lambda \propto \lambda^\beta$.

[d]Dust-corrected star-formation rate, derived from the apparent $\mathcal{R}$ magnitude, the redshift, and the amount of UV extinction inferred from the $(G-\mathcal{R})_0$ color.

Chapter 7

A Physical Picture Implied by the Spectra of Lyman Break Galaxies

7.1 Summary of Observational Results

We have presented a summary of the spectroscopic features contained in LBG rest-frame UV spectra, and the important trends among UV continuum reddening; outflow kinematics; and the equivalent widths of Lyα, low- and high-ionization interstellar absorption, and nebular emission. The most important results are:

1. LBGs with stronger Lyα emission have bluer UV continua, weaker low-ionization interstellar absorption lines, smaller kinematic offsets between Lyα emission and interstellar absorption lines, and lower star-formation rates (the last property may be due in part to selection effects).

2. Low- and high-ionization absorption equivalent widths exhibit different behaviors as functions of other spectral properties.

3. Galaxies with rest-frame $W_{\mathrm{Ly}\alpha} \geq 20$ Å in emission have weaker than average high-ionization lines, and nebular emission lines which are significantly stronger than in the rest of the sample. In the subsample with strong emission lines, which is itself fainter than average for the spectroscopic sample, there is evidence that Lyα emission strength increases towards fainter magnitudes (and lower star-formation rates). To study the dependence of the full distribution of Lyα equivalent widths on luminosity, a more careful treatment of photometric and spectroscopic incompleteness is required.

7.2 A Physical Picture

Ultimately, these spectroscopic trends are not very interesting unless we consider what they imply about the physical conditions in LBGs and their outflows. Here we offer a picture which is consistent with all of the observations, and highlight empirical results which still require further explanation. In high-resolution optical and near-IR images, LBGs have typical half-light radii of $1.6h^{-1}$ kpc

(Giavalisco et al., 1996b). This typical half-light radius represents the scale of the H II regions where massive star formation takes place. The UV stellar continuum, photospheric and wind features, and UV and optical nebular emission lines are produced here. Negligible systemic velocities of nebular emission lines with respect to stellar photospheric absorption features indicate that the massive stars and H II regions are at rest with respect to each other (sections 5.3.1 and 5.4.3.2). Also produced in the H II regions through recombinations of ionized hydrogen are the original Lyα photons which subsequently diffuse through frequency space and through dusty neutral gas at larger radii.

A generic feature of galaxies selected with Lyman Break color criteria is a star-formation surface density high enough that the mechanical energy input from the resulting large number of Type II supernova explosions drives a large bubble of hot gas out of the galaxy (Heckman, 2002). This superbubble expands at several hundred km s^{-1}, and may eventually escape the galactic gravitational potential, possibly without radiating away most of the mechanical energy input from supernovae (Adelberger, 2003). The location, relative to the central star-formation regions, of the neutral and ionized gas giving rise to strong blueshifted absorption is an important component of any physical picture describing the spectra of LBGs.

Neutral gas displays a range of blue-shifted line-of-sight velocities with an average of $\Delta v \sim -200$ km s^{-1}, but extending to $\Delta v \sim -600$ km s^{-1}(Pettini et al., 2002). If cold neutral interstellar clouds are entrained and accelerated by the flow of hot gas, they may reside at smaller distances, r, than the expanding shock front of the superbubble. A plausible lower limit to r is the typical LBG half-light radius, $1.6h^{-1}$ kpc, given that the majority of LBG rest-frame UV spectra exhibit such strong absorption lines. If the absorbing gas were at much smaller radii, more mixed in with the stars, we would expect a much smaller covering factor, and weaker absorption on average. An upper limit on r may be obtained from consideration of close pairs of LBGs, by searching for absorption from the lower redshift member of a pair in the spectrum of the higher redshift one. There are 17 LBG pairs with projected separations of $r_\theta < 160h^{-1}$ comoving kpc. When the spectra of the higher-redshift pair members are shifted into the rest-frame of the lower-redshift galaxies and averaged, little Lyα or metal absorption is detected. The mean impact parameter in these pairs is $110h^{-1}$ kpc, which puts an upper limit of $r \lesssim 25h^{-1}$ proper kpc on the physical dimensions of the gas giving rise to strong blue-shifted absorption in LBG spectra (Adelberger et al., 2003).

Along with neutral material, there is also ionized gas with a similar mean blueshift and range of velocities over which absorption takes place. Blue-shifted Si IV and C IV absorption features are produced in this gas, which has been ionized by a mixture of radiation and collisional processes. In contrast to the low-ionization features, the Si IV doublet appears to be optically thin. While the neutral and ionized phases have comparable kinematic properties, this similarity does not necessarily constrain their relative physical distributions. In alternate scenarios consistent with the kinematics of the low and high ions, 1) the Si IV and C IV absorption may be produced in the outer ionized

regions of the outflowing clouds giving rise to low-ionization absorption, or 2) it may originate in more diffuse, but still outflowing, ionized gas in which the outflowing neutral clouds are embedded. There may also be evidence for a third, hotter phase of gas at $T \sim 3{\times}10^5$ K, if the O VI that produces absorption is collisionally ionized. In the future, it will be interesting to compare the kinematics of the O VI absorption with that of the low-ions and other high-ions, using higher spectral resolution data.

Heckman et al. (2001b) and Strickland & Stevens (2000) have considered the outflow scenario in detail for local starbursts, and Adelberger (2003) and Pettini et al. (2002) have done the same for LBGs at $z \sim 3$. The composite LBG spectra provide some new results about outflows at high redshift. The low-ionization interstellar absorption lines are the most direct probe of the outflowing neutral gas, and there is clearly a direct link between $W_{\rm LIS}$ and the emergent Lyα profile. Quite strikingly, the interstellar absorption strength monotonically decreases as the Lyα emission strength increases. Also important is the decoupling of the behavior of neutral and ionized absorbing gas. When the sample is divided according to $W_{\rm Ly\alpha}$, $W_{\rm LIS}$ varies by almost a factor of three, whereas $W_{\rm SiIV}$ stays roughly constant except for the sample with strong Lyα emission, in which the high-ions are 50% weaker. The difference between the behavior in low and high ion line strengths is especially intriguing since the two sets of lines have similar mean blue-shifts and velocity FWHMs. This result may be evidence for a variable neutral gas covering fraction in the outflow, whereas the ionized gas maintains a more constant covering fraction. It also favors the scenario in which patchy neutral clouds are embedded in an ionized gas phase with unity covering fraction, rather than the one in which Si IV and C IV absorption are produced in the outer regions of the patchy neutral clouds.

Dust has been observed in the outflows from local star-forming galaxies (Heckman et al., 2000). In this work, we also find strong evidence for dust in the outflowing neutral clouds at $z \sim 3$. The correlation between the $W_{\rm LIS}$ and $E(B-V)$ is most naturally explained if some fraction of the reddening of the stellar continuum takes place in the outflowing gas. The strong correlation between $W_{\rm LIS}$ and $E(B-V)$ also argues for an outflow geometry that is at least comparable in size to the galaxy half-light radii—i.e., the absorbing neutral clouds must be distributed in front of the entire face of the galaxy, affecting the total region of UV continuum surface brightness, and not only a small central region. LBGs differ from local galaxies hosting starbursts in terms of two important geometrical properties, which may also distinguish the nature and evolution of LBG outflows from local ones. First, local starbursts often occur in a central nuclear region with $r_* \leq 1$ kpc, which is small compared to the galaxy half-light radius, whereas LBGs indicate high star-formation surface-densities over a larger size-scale. Second, local star-forming galaxies often have large gas disks. Superwinds expand perpendicular to these disks, in the direction of the steepest pressure gradient (Heckman et al., 2000; Heckman, 2002). Based on the morphological information about LBGs and models of galaxy formation, such disks were probably not in place at $z \sim 3$.

7.3 The Absorbing Gas

The properties of the blue-shifted neutral gas are crucial in determining the appearance of LBG rest-frame UV spectra. The equivalent widths of these low-ionization lines correlate strongly with two key spectroscopic properties: $W_{\mathrm{Ly}\alpha}$ and $E(B-V)$. An important question is: what physical parameter of the low-ionization gas governs the equivalent widths? As stated before, the four strongest low-ionization lines must be saturated based on the ratio of equivalent widths of different Si II transitions. Therefore, the change in average equivalent width by a factor of ~ 3 reflects a change in the neutral clouds' velocity dispersion, covering fraction, or both. Using all of the available information, we attempt to infer which of these properties is reflected by the change in W_{LIS}.

Since W_{LIS} is so strongly correlated with $W_{\mathrm{Ly}\alpha}$, we focus on the properties of the composite spectra described in section 6.4, constructed from subsamples sorted by $W_{\mathrm{Ly}\alpha}$. This is, for practical purposes, equivalent to sorting by W_{LIS}, which we would like to do, but cannot, given the quality of the individual spectra. The relevant measurements are the observed residual intensities and FWHMs of the low-ionization interstellar absorption lines. For saturated lines, the deconvolved residual intensity is an empirical estimate of the gas covering fraction, (i.e., $I = 1 - C_f$, where I is the residual intensity, and C_f is the covering fraction). The observed residual intensities smoothly increase as $W_{\mathrm{Ly}\alpha}$ increases from strong absorption to strong emission (Figure 6.5). Also, the observed FWHMs of the composite spectrum with the strongest Lyα emission are narrower than those in the strongest absorption composite, though there is not a smooth trend with $W_{\mathrm{Ly}\alpha}$.

Ideally, we would like to determine simultaneously the deconvolved FWHMs and residual intensities of the low-ionization interstellar absorption lines. The deconvolved quantities depend very sensitively on the effective spectral resolutions of the four Lyα composite spectra, however, and these four spectral resolutions may not even be equivalent. For example, spectra with Lyα emission could have been spectroscopically identified under conditions of worse atmospheric seeing than absorption-only spectra. Another effect is that the systemic redshift formulae from Adelberger et al. (2003) have different levels of precision for different types of spectra. The effective spectral resolution is only constrained to be between $\Delta\lambda \sim 2.0 - 3.2$ Å for the four spectra, which is of the same order as the intrinsic FWHMs. When the spectral resolution is so uncertain, yet comparable to the intrinsic FWHMs, resolution effects are degenerate with both intrinsic FWHM and residual intensity. Thus, we can only say that there is a significant reduction in the *product* of covering fraction and velocity spread as the absorption lines decrease in equivalent width,

Without a quantitative determination of the relative significance of velocity FWHM and covering fraction in moderating W_{LIS}, we offer two pieces of circumstantial evidence that covering fraction may be the more important effect of the two. First, we compare the spectroscopic properties of the two brightest spectroscopically confirmed LBGs that are not AGN: MS1512-cB58 ($\mathcal{R} = 20.6$) and

Q0000-D6 ($\mathcal{R} = 22.88$). cB58 is in the quartile of LBGs with the strongest Lyα and low-ionization interstellar absorption. In contrast, Q0000-D6 has $W_{\rm Ly\alpha}$ and $W_{\rm LIS}$ that place it in the second highest quartile of $W_{\rm Ly\alpha}$ emission. As shown in Figure 7.1, the difference in Lyα properties of the two objects is reflected in the difference in low-ionization equivalent widths, which are ~ 1.6 times stronger in cB58 than in Q0000-D6 (though, just as in the composite spectra, the high-ionization line-strengths are roughly the same strength). In this case, we explicitly measure the velocity widths of the low-ionization lines in cB58 and Q0000-D6. The C II λ1334 FWHM is measured directly from the high-resolution spectrum of cB58 as FWHM(cB58)=655 km s^{-1}. Based on a careful analysis of the spatial extent of the object along the slit in the 2D spectrogram of the low-resolution spectrum of Q0000-D6, we estimate a rest-frame resolution of $\Delta\lambda = 2.5$ Å and the deconvolved C II λ1334 velocity width is FWHM(D6)=665 km s^{-1}. In this case, cB58 and Q0000-D6 have the same low-ionization velocity dispersions, and the difference in equivalent width can only be explained as a difference in the covering fraction of blueshifted neutral clouds. While the cB58 C II line has a residual intensity of ~ 0, implying a unity covering fraction, the intrinsic residual intensity in Q0000-D6 is 0.4, implying a covering fraction of only 60%. The second piece of circumstantial evidence is the strong correlation between $W_{\rm LIS}$ and $E(B-V)$ (sections 6.4 and 6.5). Heckman et al. (1998) attribute this correlation in local starbursts to the fact that the velocity dispersion in the absorbing gas must be larger in galaxies with more dust extinction. This explanation is plausible in that galaxies with higher star-formation rates can drive winds with larger velocity spreads (Heckman et al., 2000), and they are also dustier (Adelberger & Steidel, 2000; Shapley et al., 2001). However, a more direct explanation for the correlation results if the blue-shifted neutral gas is dusty. Accordingly, galaxies with a larger covering fraction of dusty clouds suffer more extinction of the UV stellar continuum, as well as exhibiting larger saturated equivalent widths, and weaker Lyα emission.

7.4 Lyman Continuum Leakage

One of the reasons we have devoted so much of the discussion to the covering fraction of neutral gas is that this property may determine how optically thick LBGs are to their own H I-ionizing radiation. The optical depth of LBGs to Lyman continuum photons is a cosmologically interesting question, given the controversy surrounding the contribution of galaxies to the ionizing background at $z \sim 3$. Escaping Lyman continuum flux was apparently detected by Steidel et al. (2001) in a composite spectrum of 29 LBGs drawn from the high-redshift tail of the current spectroscopic sample. This spectrum is very similar to the composite spectrum of the total LBG spectroscopic sample (Figure 5.2) in terms of $W_{\rm Ly\alpha}$, $W_{\rm LIS}$ and $W_{\rm HIS}$, though it indicates less reddening by dust ($\langle E(B-V)\rangle = 0.07$ for the galaxies in the Lyman continuum sample, and $\langle E(B-V)\rangle = 0.13$ for galaxies in the total LBG sample). As discussed before, the composite spectrum of the total

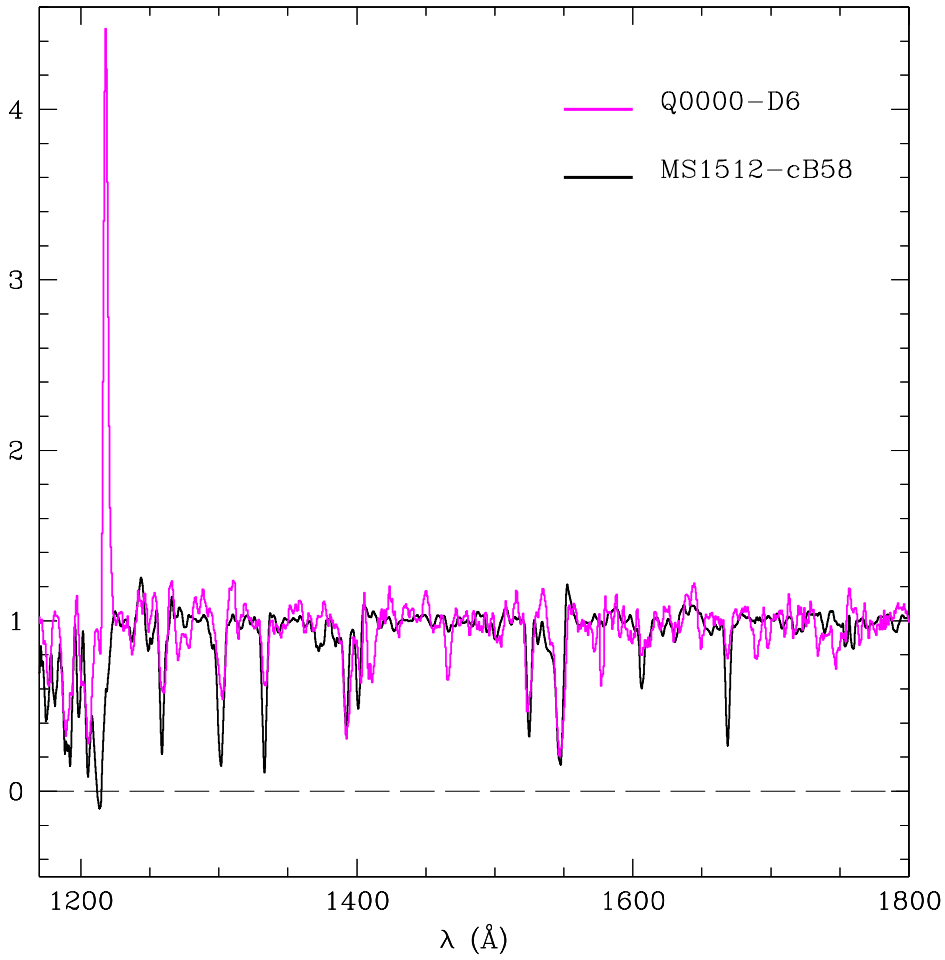

Figure 7.1 Continuum-normalized spectra of the two highest S/N LBGs in the spectroscopic sample: MS1512-cB58 and Q0000-D6. cB58 (plotted in black) belongs in the quartile of LBGs with the strongest Lyα absorption, while Q0000-D6 (plotted in magenta) is in the 30% of the sample with the strongest Lyα emission. The contrast between Lyα profiles is clear, as is the contrast between $W_{\rm LIS}$ absorption strengths. On the other hand, the strength of the high-ionization absorption lines is roughly comparable. In this case, where we know the spectral resolution accurately for both spectra, we can show that the intrinsic velocity widths of the absorption lines are comparable, and that the difference in $W_{\rm LIS}$ between cB58 and Q0000-D6 is due to a difference in the covering fraction of neutral gas.

LBG sample suffers from its own selection biases with respect to the LBG UV luminosity function. Therefore, the similarity of the Lyman continuum composite spectrum to the total LBG composite spectrum is not proof that the Lyman continuum spectrum represents a true "average" $z \sim 3.4$ galaxy spectrum.

Furthermore, in contradiction to the apparent detection of Lyman continuum emission, Giallongo et al. (2002) derive an upper limit for the escape fraction in two bright LBGs which is four times lower than the Steidel et al. (2001) detection. One of these two galaxies is Q0000-D6, (section 7.3), which apparently has only 60% covering fraction of gas capable of producing significant low-ionization metal absorption lines! If there are indeed no unresolved saturated components in the low-ionization features which are missed due to finite spectral resolution, the case of Q0000-D6 may imply that low-ionization lines which do not reach zero intensity are a necessary but not sufficient condition for the escape of Lyman continuum emission. For example, we note that the cores of the high-ionization lines in the spectrum of Q0000-D6 are black (when viewed at sufficient spectral resolution using the Keck Echelle Spectrograph and Imager). If these transitions arise in gas with sufficient neutral hydrogen column density to be optically thick to Lyman continuum photons, very little ionizing radiation will escape from Q0000-D6. It is clearly of great interest to push the Lyman continuum observations of this galaxy to more sensitive limits than those achieved so far.

In order to arrive at the global contribution of LBGs to the ionizing background, high-resolution spectra are necessary to measure the neutral gas velocity dispersions and covering fractions without degeneracy as a function of $W_{\mathrm{Ly}\alpha}$, W_{LIS}, W_{HIS}, $E(B-V)$, and $\Delta v_{\mathrm{em-abs}}$. Once it is understood how the gas covering fraction depends on other spectroscopic parameters, we need to construct an unbiased estimate of the average spectrum of the light associated with LBGs. Proper weighting of each individual spectrum as a function of its $\mathcal{R}$ magnitude and Lyα equivalent width should compensate for all of the photometric and spectroscopic biases presented in section 6.2 yielding the true average spectrum. Based on the spectroscopic properties of the average spectrum, the average LBG neutral gas covering fraction can be inferred. The final step is to use direct observations of the Lyman continuum region to calibrate the relationship between gas covering fraction and Lyman continuum leakage. If it is possible to calibrate this relationship, the average LBG covering fraction can be converted into a true average Lyman continuum escape fraction.

7.5 Future Observations

While this work has illuminated the range of rest-frame UV spectroscopic properties of LBGs, there are many limitations in the data which prevented us from drawing quantitative conclusions, and which highlight the need for several specific future observations. Data of higher spectral resolution are necessary to measure the velocity distribution and covering fraction of the absorbing neutral gas

without degeneracy. Properties such as stellar population age should be folded into the analysis to search for temporal evolution in the UV spectroscopic properties. Comparing the *HST* morphologies of galaxies of different spectroscopic types will also aid in understanding the effects of geometry and orientation. With such observations we will truly be able to characterize the detailed effects of star formation at $z \sim 3$, both on galaxies and the intergalactic medium.

We wish to extend special thanks to those of Hawaiian ancestry on whose sacred mountain we are privileged to be guests. Without their generous hospitality, most of the observations presented herein would not have been possible. We also thank Mark Dickinson, Mauro Giavalisco, Mindy Kellogg, Matthew Hunt, and Dawn Erb, who assisted in the observations and reductions, and the referee, Claus Leitherer for careful and helpful suggestions which improved the quality of the paper. CCS and AES have been supported by grant AST-0070773 from the U.S. National Science Foundation and by the David and Lucile Packard Foundation. KLA acknowledges support from the Harvard Society of Fellows.

Part III

Epilogue

Chapter 8

A Deep Spectroscopic Survey of Lyman Break Galaxies

8.1 Introduction

In order to quantify the amount of mass, energy, and metals deposited into the IGM at $z \sim 3$ due to star-formation feedback in LBGs, we would like to characterize the physical properties of large-scale outflows in LBGs. These properties include the fraction of the continuum source covered by outflowing gas, the full range of velocities over which outflowing gas is absorbing relative to the stellar systemic velocity, the neutral hydrogen column density and metal content of the absorbing gas, and the way in which the geometry of the absorbing gas allows for the leakage of ionizing radiation from the galaxies. We would also like to understand how these properties relate to other aspects of the galaxies hosting the star formation, including the rest-frame UV and optical morphologies, and the stellar population ages and star-formation histories.

As described in Chapter 7, several limitations of the LBG composite spectra prevented us from making more quantitative conclusions about the nature of large-scale outflows in LBGs. The first and probably most significant limitation was the low (and somewhat uncertain) spectral resolution of the composite spectra, which limited our ability to interpret strong changes in low-ionization interstellar equivalent widths. Second, we were unable to measure true stellar systemic redshifts for typical individual galaxies whose spectra were included in the composites, due to the weak nature of such features. [1] As a result, when investigating spectroscopic trends involving outflow kinematics, we were only able to bin the sample of LBGs according to the velocity offset between Lyα emission and interstellar absorption lines, rather than the more physically meaningful parameter, outflow speed, which would have required knowledge of the stellar systemic velocity for individual galaxies. Third, we were unable to measure the average H I column-density of outflowing neutral gas because of the manner in which the composite spectra were constructed (the column density measured from

[1] We did, however, make educated guesses of the systemic redshifts based on the formulae presented in Adelberger et al. (2003), which appeared to be fairly accurate, at least on average.

the average spectrum is not equivalent to the average column density of the spectra being combined). We were also unable to place useful constraints on the column densities of heavy elements contained in outflowing gas due to the low spectral resolution of the composite spectra. These limitations prevented us from placing useful constraints on the amount of neutral hydrogen and metal content escaping from the galaxies. Fourth, observations of the Lyman Continuum region were lacking for galaxies with the exception of a small, intrinsically blue sample drawn from the high-redshift end of the LBG selection function (Steidel et al., 2001), preventing us from linking information about the leakage of Lyman Continuum emission to the properties of the strong interstellar features probing the outflow. Finally, most of the composite spectra were constructed from the average of hundreds of individual LBG spectra in order to characterize the rest-frame UV spectroscopic characteristics with high S/N. As a result, it was difficult to connect the composite rest-frame UV spectroscopic properties to specific characteristics of a stellar population such as age or morphology.

In this chapter, we describe a spectroscopic survey of a small sample of bright LBGs, designed to address some of the questions remaining from our previous study of composite spectra. This new survey utilizes the unique capabilities of the new double-armed incarnation of the LRIS spectrograph on the Keck I telescope. We use the blue arm to make sensitive observations of the Lyman-Continuum region for $z \sim 3$ LBGs, while simultaneously covering the interstellar lines redwards of Lyα with the red arm at twice the spectral resolution used in typical LBG discovery spectra. In § 8.2, we describe the sample and observations. The data reductions are discussed in § 8.3, while § 8.4 presents some early results and future prospects for the survey.

8.2 Sample and Observations

For this deep spectroscopic survey of LBGs, we targeted galaxies in the SSA22a field at RA=22:17:34.2, DEC=+00:15:01 (J2000). This field contains 146 photometric LBG candidates, 57 of which were spectroscopically confirmed (Steidel et al., 2003) at the time we planned the deep survey. Our primary targets for deep observations were 20 bright galaxies with $23.0 <= \mathcal{R} < 24.5$. Fifteen of these 20 galaxies already had known redshifts based on their LBG discovery spectra, and, with the fairly high S/N observations, we were able to measure redshifts for an additional three galaxies.

The data were obtained during the course of 5 separate observing runs in the interval October 2000 - August 2002, using the Low Resolution Imaging Spectrometer (LRIS; Oke et al., 1995) on Keck I, in its newly outfitted (as of September 2000) dichroic capability. Two different slit mask configurations were used in the course of data collection. The two slit masks had different sky position angles, but significant overlap in targeted objects (9 objects were in common between the setups), and both used $1\farcs2$ slits. On the October 2000 observing run, the slit mask had a sky position angle of $\theta = 172$ degrees. The "d560" dichroic beam splitter was used to direct light bluer

than $\sim$ 5600 Å towards the LRIS blue channel, while longer wavelength light was sent to the red channel. The blue light was dispersed by a 400 lines mm^{-1} grism blazed at 3400 Å, leading to a dispersion of 1.7 Å/pixel on the engineering-grade Tektronix 2K $\times$ 2K UV/AR-coated CCD, while the red light was dispersed by a 600 lines mm^{-1} grating blazed at 7500 Å, yielding a dispersion of 1.28 Å/pixel on the red side Tektronix 2K $\times$ 2K CCD. Most slitlets had complete wavelength coverage spanning from the atmospheric cutoff at 3200 Å to redder than 7500 Å.

On all subsequent observing runs (June 2001, July 2001, June 2002, and August 2002) a slit mask with a sky position angle of $\theta = -50$ degrees was used. The "d500" dichroic beam splitter was used to split the incoming light beam at $\sim$ 5000 Å. The blue light was dispersed by the same 400 lines mm^{-1} grism blazed at 3400 Å, while the red light was dispersed by a 600 lines mm^{-1} grating blazed at 5000 Å. For the final two observing runs (June 2002 and August 2002), the new science-grade Marconi 4K $\times$ 4K CCD mosaic was used for the blue-side observations. The new blue camera has smaller pixels, yielding a dispersion of $\sim$ 1.06 Å/pixel when used together with the 400-line grism. For this second setup, most slitlets had complete wavelength coverage spanning from the atmospheric cutoff to redder than 7000 Å.

Our typical observing strategy consisted of taking a series of 1800 second exposures simultaneously on the red and blue sides. The telescope was dithered slightly ($\sim$ 1 arc second) between exposures in order to sample different parts of the detectors. We obtained 6 hours of total integration time for both red and blue side observations in October 2000, $\sim$ 3 hours in June 2001, $\sim$ 5 hours in July 2001, $\sim$ 2 hours in June 2002, and $\sim$ 8 hours in August 2002. The resulting total integration time for the 9 objects in common to both slit mask setups is $\sim$ 24 hours, while for an additional 5 objects only included in the second slit mask setup, we have $\sim$ 18 hours of integration time. Finally, for 6 objects observed only in October 2000, we have 6 hours of integration time. [2] Table 8.1 lists the $\mathcal{R}$ magnitudes, $G - \mathcal{R}$ colors, redshifts, total LRIS red-channel exposure times and instrumental configuration for the sample of 20 objects targeted with deep spectroscopy.

Flat fields for the red side data were obtained at the end of an observing sequence using an internal halogen lamp. Internal flat fields were not used for the blue side data taken with the engineering-grade detector, though spectroscopic twilight flat fields were obtained during the August 2002 observing run using the new blue detector, which is in greater need of flat fielding. An observation of internal arc lamps (Hg, Ne, Ar, Kr, Xe for the October 2000 run, and Hg, Ne, Ar, Zn, Cd for all subsequent runs) was also obtained at the end of each observing sequence for the purpose of wavelength calibration.

[2] The two galaxies whose redshifts have not yet been identified were only observed in October 2000.

8.3 Data Reductions

To date, the red side observations have been fully reduced, though the blue side observations of the Lyman Continuum region have not yet been completely processed. Here we present the details of the red side reductions. The data were reduced using IRAF tasks, with scripts customized for cutting up the multi-object slit mask images into individual slitlets and flatfielding each slitlet using the proper image section of the flat-field image. After flat-fielding, cosmic rays in individual slitlet exposures were flagged and added to corresponding bad pixel masks. First-pass background subtraction was performed by fitting a Legendre polynomial function to the background level at each dispersion point whose order was typically between 3 and 5. In the case of very long slits, a 7th order polynomial was used. Offsets between exposures in the spatial direction were determined from the spatial locations of the object continuum, whereas offsets in the wavelength direction were determined from the wavelength positions of bright night sky lines. The multiple background-subtracted exposures were brought into registration based on the computed offsets, and averaged with the exclusion of bad pixels flagged in the individual cosmic ray masks.

Due to the fact that the first-pass background subtraction did not take into account the location of the object at each dispersion point, the polynomial function fit to the background was often biased high near the location of the object, resulting in a background-subtracted exposure with a trough surrounding the object continuum in the spatial direction. This problem is only manifest at wavelengths in the object spectrum where the continuum is strong, and not at the locations of strong absorption lines (where, for the purposes of background subtraction, there is no object). Therefore, if the spatial region affected by object flux at each dispersion point is not masked out during the estimate of the background level, the overall continuum level will be biased low relative to its true value, and the depths of absorption lines relative to the continuum will be measured incorrectly. [3] To address this issue, for each slitlet, we traced the path of the object in the first-pass averaged two-dimensional spectrogram, produced a mask indicating the location of the object at every dispersion point, applied offsets to this mask in a manner appropriate for each individual de-registered exposure, and performed the background subtraction on the original cosmic-ray-zapped exposures, with reference to the object mask. Thus, the spatial region affected by object flux at each dispersion point was not included in the estimate of the background level, and the bias mentioned above was greatly reduced.

For each slitlet, the second-pass background-subtracted exposures were summed using the previously determined offsets. The object continuum in the two-dimensional slitlet spectrogram was traced and extracted to a one-dimensional spectrum using optimal weighting techniques to increase the S/N. The two-dimensional arc spectrum for each slitlet was extracted to one-dimension using the

[3] Given the scientific goals of this survey, incorrectly estimating the observed depths of absorption features represents a serious concern.

corresponding object trace. Wavelength solutions were then obtained by fitting a 3rd-order Legendre polynomial to the arc-lamp spectra. Typical residuals were $\sim 0.05-0.1$ Å. If necessary, a slight grey shift was applied to the wavelength solutions to make bright night-sky lines appear at the correct wavelengths (such shifts are indicative of either differences in the slit illumination of the internal arc and on-sky science spectra, or slight instrument flexure between the arc and science exposures). An approximate flux-calibration was applied using long-slit observations of spectrophotometric standard stars, observed with the same dichroic and grating/grism configuration as the science data. Finally, the data were reduced to vacuum-heliocentric wavelengths.

The above procedure was applied to data from individual observing runs. After the data from each run was fully processed to one-dimensional, wavelength-calibrated, flux-calibrated, vacuum-heliocentric spectra, we combined the spectra from different observing runs for individual objects. For a given object, the spectra obtained on different observing runs ranged in S/N by as much as a factor of $\sim 3-4$. Therefore, in constructing the final summed spectrum for each object, we weighted the spectrum from each observing run by the square of its S/N. Redshifts were measured from the high S/N combined spectra. Then, the spectra were de-redshifted into the systemic rest frame, and continuum normalized. Figures 8.1 and 8.2 show some representative examples of rest-frame continuum-normalized spectra. These spectra do not include data taken in October 2000 with the different instrumental configuration, and therefore represent a total of ~ 18 hours of integration time. The spectra shown in Figures 8.1 and 8.2 have S/N per resolution element ranging from $\sim 10-25$. The remaining 6 galaxies in the sample with ≥ 18 hours of integration time which are not shown in Figures 8.1 and 8.2 have slightly lower S/N (ranging from $\sim 7-10$ per resolution element), but still represent a significant improvement relative to the typical quality of LBG discovery spectra.

8.4 Early Results

The spectra plotted in Figures 8.1 and 8.2 exhibit a large range of properties. We defer a full quantitative analysis of the equivalent widths, velocity FWHMs, and intrinsic depths of the strong interstellar absorption features, as well as a measurement of the full velocity field of stars and outflowing gas. Such an analysis will be reserved for future work, which will also include information from the LRIS blue arm spectra about the Lyα profile, H I column-density, and the escape fraction of Lyman Continuum emission. But, for the present discussion, we would like to highlight some initial qualitative observations which can be made from the spectra.

Figure 8.1 contains spectra whose low-ionization interstellar absorption lines reach zero or almost-zero intensity at line-center, indicating a complete coverage of the continuum source by outflowing neutral gas. In contrast, the spectra contained in Figure 8.2 have weaker interstellar absorption features, which, in the most extreme case, have depths of only half of the continuum level. With

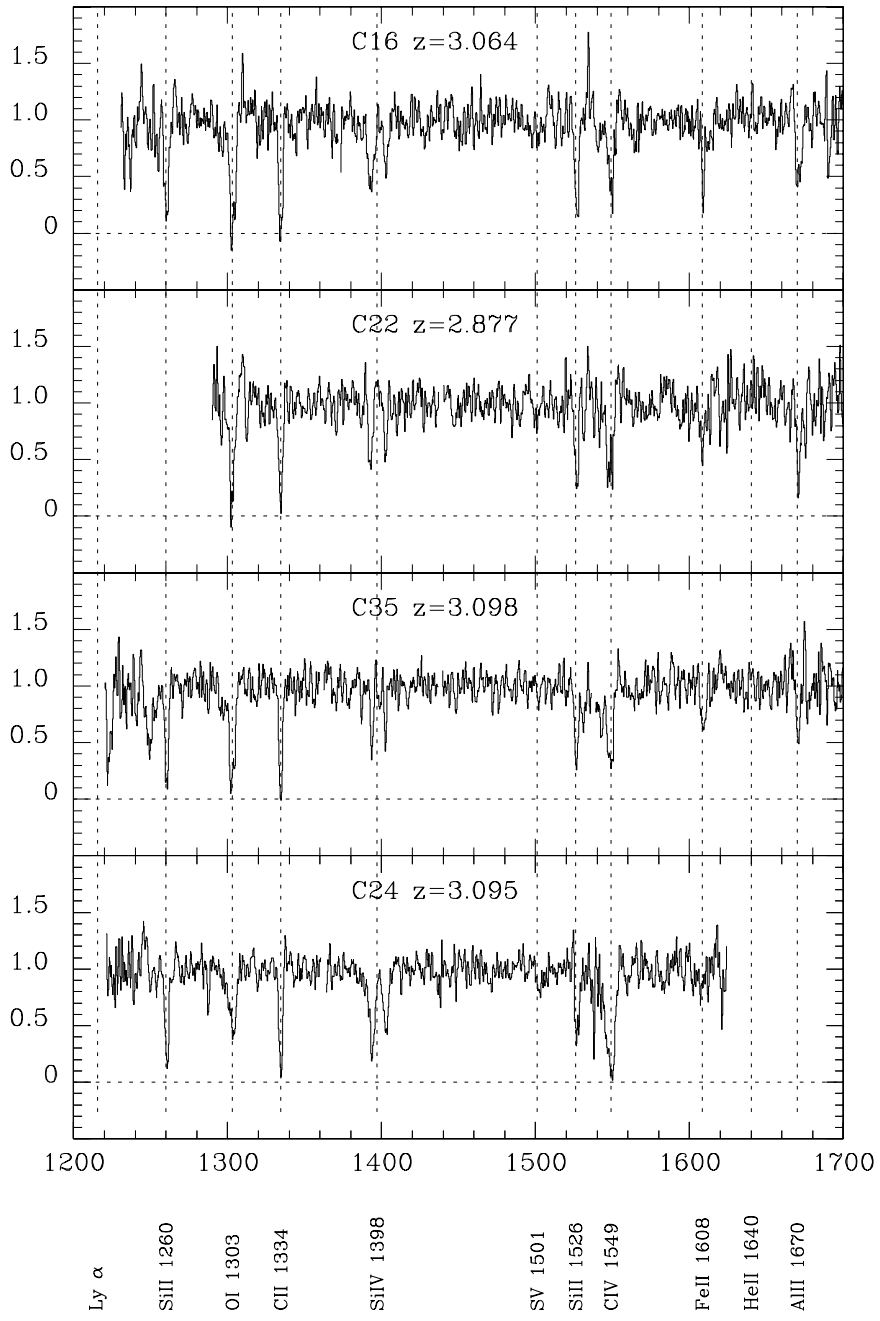

Figure 8.1 Four examples of deep LRIS-R spectra. Each spectrum represents a total of 18 hours of integration time, and has been shifted into the rest frame and continuum-normalized. This figure contains spectra with strong low-ionization interstellar absorption lines, at least one of which in each spectrum reaches zero intensity at line center. The object name and interstellar absorption redshift are indicated at the top of each figure. Both low- and high-ionization interstellar absorption features are indicated with dotted lines, and the weak S V stellar photospheric absorption line is indicated as well. One striking property of these spectra is the large variation in the widths of the high-ionization Si IV absorption features.

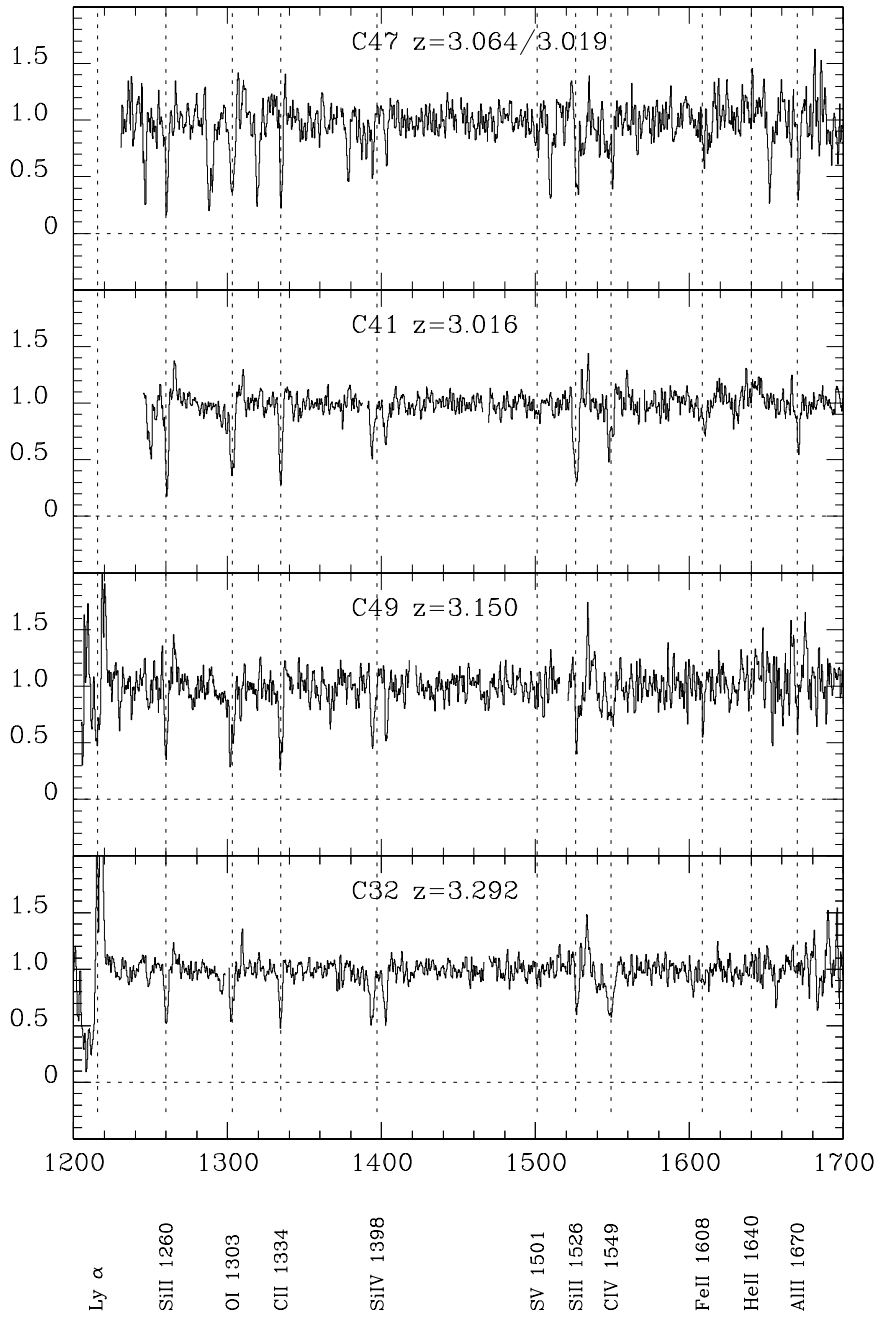

Figure 8.2 Four examples of deep LRIS-R spectra. Each spectrum represents a total of 18 hours of integration time, and has been shifted into the rest frame and continuum-normalized. This figure contains spectra with weaker low-ionization interstellar absorption lines than those shown in Figure 8.1. The weakest lines are observed in the spectrum of SSA22a-C32 (bottom), with depths at line-center barely reaching down to 50% of the continuum level. The object name and interstellar absorption redshift are indicated at the top of each figure. Both low- and high-ionization interstellar absorption features are indicated with dotted lines, and the weak S V stellar photospheric absorption line is indicated as well. Of special note is the spectrum of SSA22a-C47 (top), which actually contains two redshifts. We have adopted the rest frame of the $z = 3.064$ galaxy and marked the spectral features accordingly, but a set of strong absorption lines is apparent for the $z = 3.019$ galaxy as well.

the exception of the Lyα equivalent width, the average equivalent width of the saturated low-ionization interstellar absorption lines was the parameter whose variance was characterized with the highest significance in our study of the lower-resolution composite LBG spectra (Shapley et al., 2003). However, it is clear, even from the preliminary data presented here, that we will be able to measure variation in other, more physically meaningful parameters from the new higher-resolution LBG spectra.

Figure 8.3 zooms in on the spectral region containing three strong low-ionization interstellar absorption lines: Si II λ1260, O I+Si II λ1303, and C II λ1334. Spectra for the two objects SSA22a-C16 and SSA22a-C32 are plotted. As measured from the discovery spectra, SSA22a-C16 has a Lyα absorption equivalent width which places it in the quartile of LBGs with the strongest Lyα absorption and low-ionization interstellar absorption equivalent widths, whereas SSA22a-C32 has Lyα emission which puts it in the half of the sample with stronger Lyα emission and weaker interstellar absorption lines. Figure 8.3 shows that the absorption lines in C32 are not only significantly shallower at line center than those in C16, but also significantly narrower. Though narrower, the lines in C32 are clearly resolved with our observational setup. While this pair of galaxies represents only a single example of a difference in velocity width, the full range of low-ionization velocity widths displayed in Figures 8.1 and 8.2 will enable us to measure how differences in the velocity widths of the low-ionization absorption lines—and not simply their equivalent widths—correlate with other spectral properties in the galaxies with deep spectroscopic observations.

Also already apparent from the spectra plotted in Figures 8.1 and 8.2 is the fact that the velocity width of the members of the Si IV $\lambda\lambda 1393, 1402$ doublet varies significantly across the sample, and that differences in the Si IV velocity width do not necessarily trace differences in the velocity structure of low-ionization absorption lines. To demonstrate, Figure 8.4 zooms in on the spectral region containing both the low-ionization absorption line, C II λ1334, and the high-ionization doublet, Si IV $\lambda\lambda 1393, 1402$. The spectra of SSA22a-C24 and SSA22a-C35 are both plotted. C24 and C35 have almost identical strong-absorption C II profiles, in terms of depth and velocity width, however the Si IV lines are almost three times broader in C24 than they are in C35. In the composite LBG spectra, and in the spectrum of MS1512-cB58, low- and high-ionization absorption features exhibited comparable velocity widths and blueshifts relative to the stellar systemic velocity (Shapley et al., 2003; Pettini et al., 2002). In contrast, the deep spectra demonstrate that the similarity in low- and high-ionization velocity width does not always hold. Determining the origin of this difference will shed light on the relative distributions of neutral and ionized gas in starburst-driven outflows.

Also detected in the deep spectra are weak stellar photospheric lines including S V λ1501 and O IV λ1343. The only stellar photospheric feature marked in Figures 8.1 and 8.2 is S V, but in several cases O IV is also detected. There are several other stellar features contained in the wavelength range covered by the deep spectra, and we will attempt to identify them as well to determine an

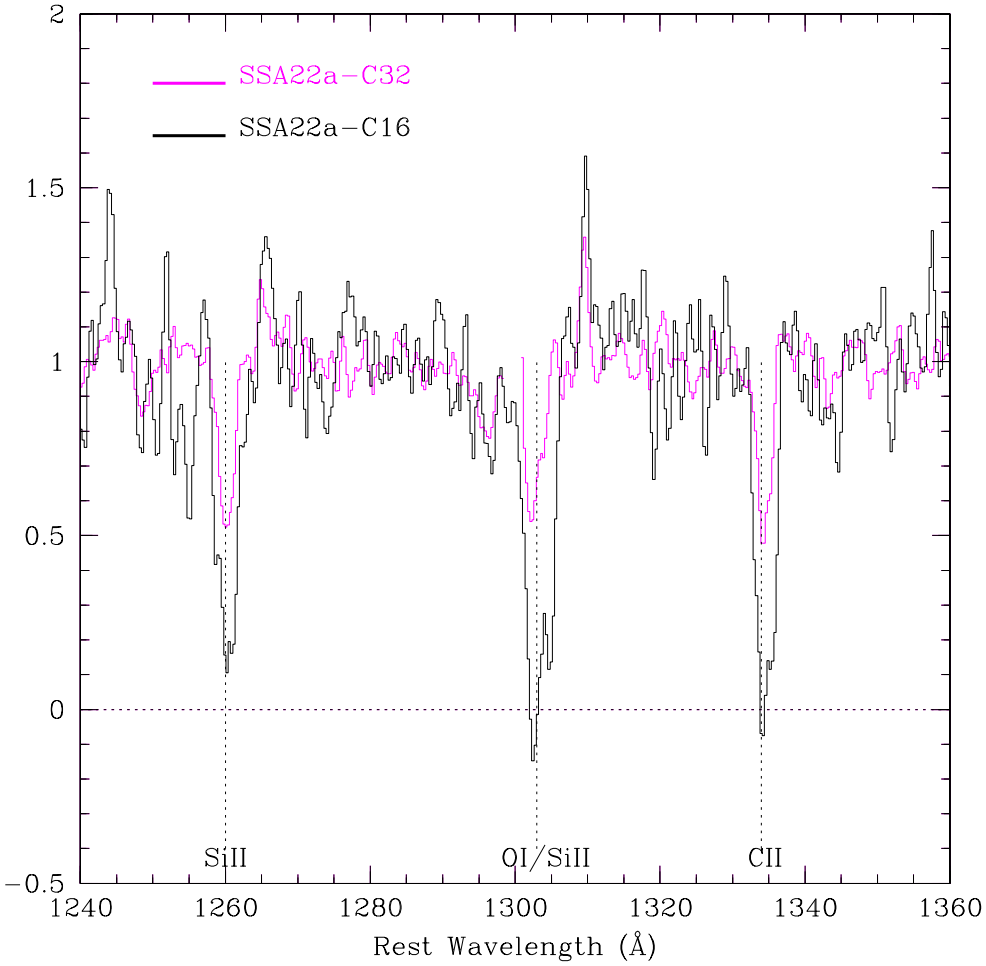

Figure 8.3 A comparison of low-ionization velocity widths. This figure illustrates the difference in low-ionization absorption profiles for two galaxies with deep spectroscopic observations: SSA22a-C16 (plotted in black), and SSA22a-C32 (plotted in magenta). The absorption features in the spectrum of C32 are not only significantly shallower, but also significantly narrower than the features in the spectrum of C16. This difference cannot be attributed to differences in spectral resolution.

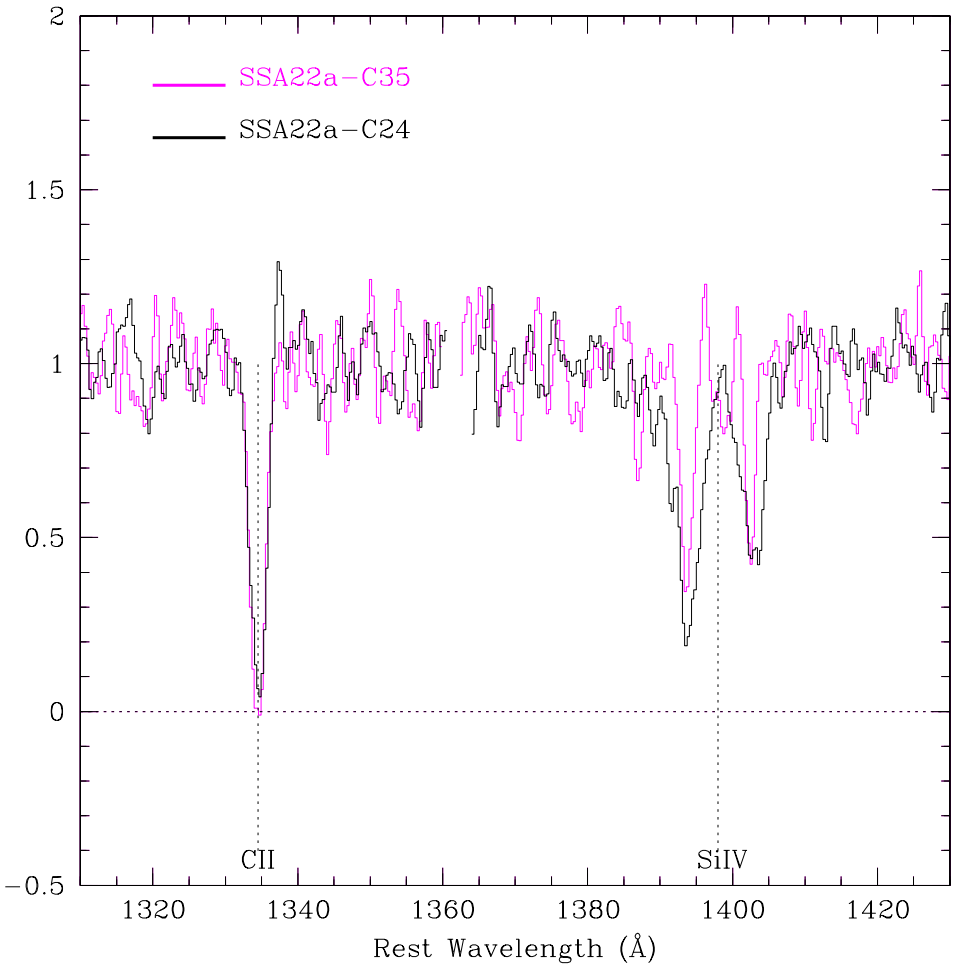

Figure 8.4 A comparison of high-ionization velocity widths. This figure illustrates the difference in high-ionization absorption profiles for two galaxies with deep spectroscopic observations and very similar low-ionization absorption profiles: SSA22a-C24 (plotted in black), and SSA22a-C35 (plotted in magenta). While the C II low-ionization profiles are almost identical in the spectra of C24 and C35, the widths of the Si IV absorption profiles are almost 3 times larger in the spectrum of C24.

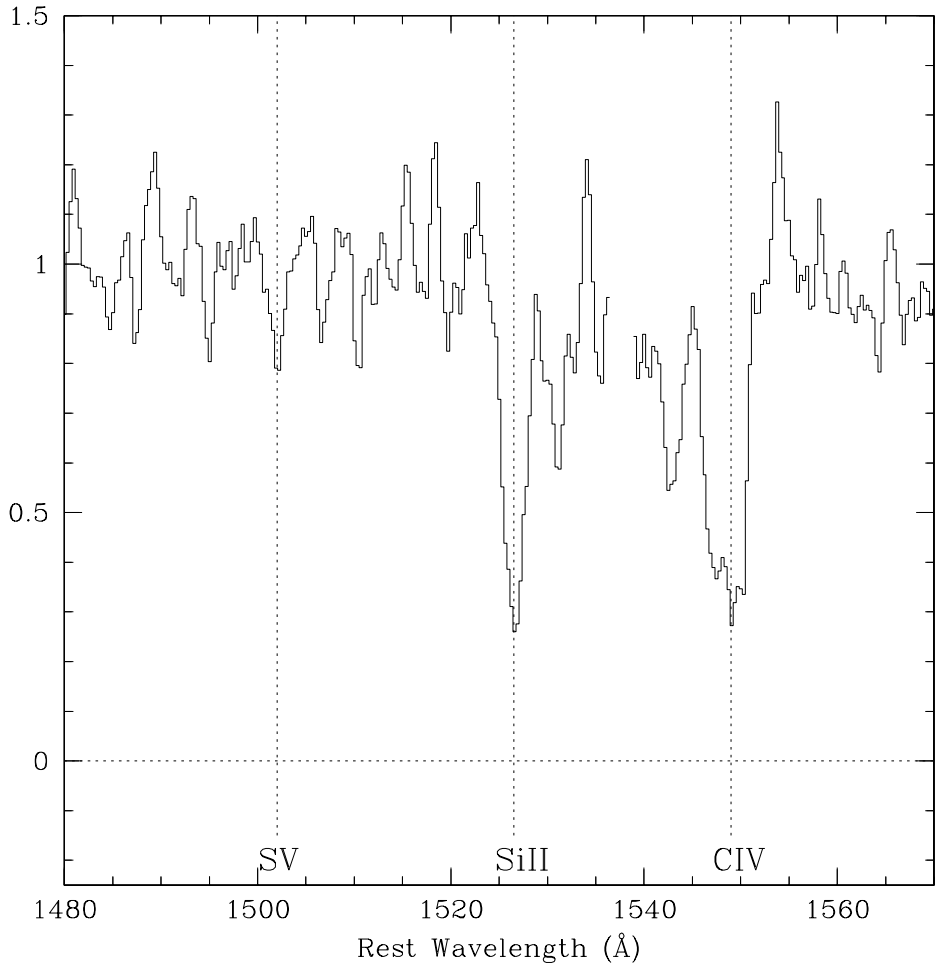

Figure 8.5 Zoomed-in region of the spectrum of SSA22a-C35 at $z = 3.098$. We detect the stellar photospheric line, S V λ 1501, in this spectrum, along with several other stellar features. Measuring the redshifts of the stellar features allows us to characterize the complete velocity field of the outflowing neutral and ionized gas, referenced to the systemic velocity of the stars.

average stellar systemic velocity. Figure 8.5 zooms in on the region near S V for SSA22a-C35. With the establishment of the stellar systemic velocity, we will be able to determine the offsets of low-ionization and high-ionization interstellar absorption lines, and Lyα emission, all relative to the stars. With such information, we will be able to estimate outflow velocities on a case by case basis.

One further aspect of the deep spectra is that we have a very good estimate of the spectral resolution of each spectrum, based on the dispersion of the 600-line grating and the atmospheric conditions during each exposure that determined the apparent size of the object in the slit (see footnote in § 5.4.2). With accurate knowledge of the spectral resolution of each spectrum, we will be able to deconvolve both the apparent depths and velocity FWHM's of the low- and high-ionization absorption lines, and derive the intrinsic values for both of these physical quantities. The intrinsic

depths and widths of the strong absorption lines were only poorly determined in the systematic study of LBG composite spectra (Shapley et al., 2003). We also hope that the increased S/N and resolution of the deep spectra will enable us to measure outflow metal column densities from weaker, unsaturated transitions.

Finally, we mention a couple of serendipitous observations which should further aid in our understanding of LBG outflows. First, the galaxy SSA22a-C47 did not have a measured redshift at the time it was placed on the slit mask for deep observations, and received a total of 24 hours of integration time. Once the data were summed for this object, it became immediately apparent that the spectrum contained, not one, but two redshifts indicated by the presence of strong interstellar absorption features. The two redshifts are $z = 3.064$ and $z = 3.019$, which imply a velocity separation of $\Delta v = 3300$ km s^{-1}—too large to indicate any kind of physical association between the two galaxies. As yet, we have not definitively identified a second imaging counterpart, though there is a faint object on the C47 slitlet, at a separation of $\sim 2\farcs5$. The spectrum of the faint nearby object is of too low S/N to determine a redshift. We will follow up the issue of the counterpart of C47 in more detail, in order to establish the impact parameter between the pair of galaxies giving rise to the redshifts, and therefore to use the higher-redshift galaxy as a probe of the galacto-centric radius at which strong metal absorption is taking place in the lower-redshift galaxy. Second, the galaxy SSA22a-D3 (not shown in Figures 8.1 and 8.2) is clearly double in its two-dimensional spectrogram. The strong low-ionization interstellar absorption lines in D3 clearly indicate shear (seen as a tilt in the absorption as a function of position) as they cut across both continuum components. We have extracted individual spectra for both of the components of D3, and hope that a detailed comparison of the spectra of the two components will provide further insight into the geometry of LBG outflows. Finally, the higher spectral resolution and S/N of the deep LBG spectra have enabled the identification of several examples of complex Lyα profiles, including double and spatially extended emission. We will include this Lyα profile information along with our analysis of all of the other spectral features.

The LRIS red-channel deep spectra are incredibly rich with high-quality information, given the faint apparent magnitudes of the objects observed. The addition of the LRIS blue-channel deep spectra will provide complementary information about the Lyman Continuum opacity and outflow neutral hydrogen column-density for most objects in the sample. We will also fold in morphological and stellar population information for those objects with *HST* and near-IR images. This survey will provide unprecedented insight into the physical properties of Lyman Break Galaxies.

Table 8.1. LRIS-R Observations of Bright Lyman-Break Galaxies in the SSA22a Field

Object Name	$\mathcal{R}_{\rm AB}$	$(G-\mathcal{R})_{\rm AB}$	$z^{\rm a}$	Obs. Run	Exptime	Dichroic	Grating
SSA22a-C11	24.20	0.47	3.097	Oct 2000	21600	d560	600/7500
				Jun 2001	10600	d500	600/5000
				Jul 2001	17900	d500	600/5000
				Jun 2002	6900	d500	600/5000
				Aug 2002	29200	d500	600/5000
SSA22a-C16	23.64	0.98	3.064	Oct 2000	21600	d560	600/7500
				Jun 2001	10600	d500	600/5000
				Jul 2001	17900	d500	600/5000
				Jun 2002	6900	d500	600/5000
				Aug 2002	29200	d500	600/5000
SSA22a-C24	23.86	0.78	3.095	Oct 2000	21600	d560	600/7500
				Jun 2001	10600	d500	600/5000
				Jul 2001	17900	d500	600/5000
				Jun 2002	6900	d500	600/5000
				Aug 2002	29200	d500	600/5000
SSA22a-C32	23.68	0.67	3.292	Oct 2000	21600	d560	600/7500
				Jun 2001	10600	d500	600/5000
				Jul 2001	17900	d500	600/5000
				Jun 2002	6900	d500	600/5000
				Aug 2002	29200	d500	600/5000
SSA22a-C35	24.18	0.95	3.098	Oct 2000	21600	d560	600/7500
				Jun 2001	10600	d500	600/5000
				Jul 2001	17900	d500	600/5000
				Jun 2002	6900	d500	600/5000
				Aug 2002	29200	d500	600/5000
SSA22a-C41	23.80	0.18	3.016	Oct 2000	21600	d560	600/7500
				Jun 2001	10600	d500	600/5000
				Jul 2001	17900	d500	600/5000
				Jun 2002	6900	d500	600/5000
				Aug 2002	29200	d500	600/5000
SSA22a-C47[b]	23.84	0.60	3.064	Oct 2000	21600	d560	600/7500
			3.019	Jun 2001	10600	d500	600/5000
				Jul 2001	17900	d500	600/5000
				Jun 2002	6900	d500	600/5000
				Aug 2002	29200	d500	600/5000
SSA22a-D17	24.27	0.45	3.066	Oct 2000	21600	d560	600/7500
				Jun 2001	10600	d500	600/5000

Table 8.1 (cont'd)

Object Name	$\mathcal{R}_{\rm AB}$	$(G-\mathcal{R})_{\rm AB}$	z[a]	Obs. Run	Exptime	Dichroic	Grating
				Jul 2001	17900	d500	600/5000
				Jun 2002	6900	d500	600/5000
				Aug 2002	29200	d500	600/5000
SSA22a-MD23	24.14	0.46	3.077	Oct 2000	21600	d560	600/7500
				Jun 2001	10600	d500	600/5000
				Jul 2001	17900	d500	600/5000
				Jun 2002	6900	d500	600/5000
				Aug 2002	29200	d500	600/5000
SSA22a-C22	24.46	0.54	2.877	Jun 2001	10600	d500	600/5000
				Jul 2001	17900	d500	600/5000
				Jun 2002	6900	d500	600/5000
				Aug 2002	29200	d500	600/5000
SSA22a-C49	23.85	0.59	3.150	Jun 2001	10600	d500	600/5000
				Jul 2001	17900	d500	600/5000
				Jun 2002	6900	d500	600/5000
				Aug 2002	29200	d500	600/5000
SSA22a-D7	23.50	0.62	2.757	Jun 2001	10600	d500	600/5000
				Jul 2001	17900	d500	600/5000
				Jun 2002	6900	d500	600/5000
				Aug 2002	29200	d500	600/5000
SSA22a-MD14	24.14	0.86	3.097	Jun 2001	10600	d500	600/5000
				Jul 2001	17900	d500	600/5000
				Jun 2002	6900	d500	600/5000
				Aug 2002	29200	d500	600/5000
SSA22a-D3[c]	23.37	0.97	3.065	Jun 2001	10600	d500	600/5000
				Jun 2002	6900	d500	600/5000
				Aug 2002	29200	d500	600/5000
SSA22a-C30	24.22	0.82	3.097	Oct 2000	21600	d560	600/7500
SSA22a-D13	20.84	0.74	3.353	Oct 2000	21600	d560	600/7500
SSA22a-M38	24.11	1.15	3.288	Oct 2000	21600	d560	600/7500
SSA22a-MD38[d]	24.10	0.53	···	Oct 2000	21600	d560	600/7500
SSA22a-MD46	23.30	0.42	3.080	Oct 2000	21600	d560	600/7500
SSA22a-MD52[d]	23.63	0.66	···	Oct 2000	21600	d560	600/7500

[a]Redshifts for all objects (with the exception of the broad-lined AGN, SSA22a-D13) are measured from the strong low-ionization interstellar absorption features, which are detected with high significance. The stellar absorption redshift is slightly higher in general.

[b]The absorption features from two galaxies at similar redshifts are detected in the spectrum of SSA22a-C47. We list both redshifts here.

[c]While included in the mask design for the July 2001 observing run, the SSA22a-D3 slit is located at the edge of the slit mask corresponding to the bottom edge of the LRIS red-channel detector. Unfortunately, during the July 2001 observing run, the footprint of the mask on the LRIS red-channel detector was shifted in such a way that light from the D3 slitlet did not fall on the detector. Therefore, there is no July 2001 integration time listed for D3.

[d]As indicated by the exposure times, SSA22a-MD38 and SSA22a-MD52 were only observed for the 6 hours of the October 2000 run. We have not yet measured redshifts for these galaxies, whose spectra are of inferior quality relative to those of other galaxies in the sample.

Bibliography

Adelberger, K. L. 2002, PhD thesis, California Institute of Technology

—. 2003, ApJ, submitted.

Adelberger, K. L. & Steidel, C. C. 2000, ApJ, 544, 218

Adelberger, K. L., Steidel, C. C., Giavalisco, M., Dickinson, M., Pettini, M., & Kellogg, M. 1998, ApJ, 505, 18

Adelberger, K. L., Steidel, C. C., Shapley, A. E., & Pettini, M. 2003, ApJ, 584, 45

Allende Prieto, C., Lambert, D. L., & Asplund, M. 2002, ApJ, 573, L137

Alton, P. B., Davies, J. I., & Bianchi, S. 1999, A&A, 343, 51

Baugh, C. M., Cole, S., Frenk, C. S., & Lacey, C. G. 1998, ApJ, 498, 504

Binney, J. & Merrifield, M. 1998, Galactic Astronomy (Princeton, NJ : Princeton University Press)

Blanton, M. R., Dalcanton, J., Eisenstein, D., Loveday, J., Strauss, M. A., SubbaRao, M., Weinberg, D. H., Anderson, J. E., Annis, J., Bahcall, N. A., Bernardi, M., Brinkmann, J., Brunner, R. J., Burles, S., Carey, L., Castander, F. J., Connolly, A. J., Csabai, I., Doi, M., Finkbeiner, D., Friedman, S., Frieman, J. A., Fukugita, M., Gunn, J. E., Hennessy, G. S., Hindsley, R. B., Hogg, D. W., Ichikawa, T., Ivezić, Ž., Kent, S., Knapp, G. R., Lamb, D. Q., Leger, R. F., Long, D. C., Lupton, R. H., McKay, T. A., Meiksin, A., Merelli, A., Munn, J. A., Narayanan, V., Newcomb, M., Nichol, R. C., Okamura, S., Owen, R., Pier, J. R., Pope, A., Postman, M., Quinn, T., Rockosi, C. M., Schlegel, D. J., Schneider, D. P., Shimasaku, K., Siegmund, W. A., Smee, S., Snir, Y., Stoughton, C., Stubbs, C., Szalay, A. S., Szokoly, G. P., Thakar, A. R., Tremonti, C., Tucker, D. L., Uomoto, A., Vanden Berk, D., Vogeley, M. S., Waddell, P., Yanny, B., Yasuda, N., & York, D. G. 2001, AJ, 121, 2358

Bruhweiler, F. C., Kondo, Y., & McCluskey, G. E. 1981, ApJS, 46, 255

Bruzual, G. & Charlot, S. 1996, private communication (BC96 manual)

Calzetti, D. 1997, AJ, 113, 162

Calzetti, D., Armus, L., Bohlin, R. C., Kinney, A. L., Koornneef, J., & Storchi-Bergmann, T. 2000, ApJ, 533, 682

Chapman, S. C., Scott, D., Steidel, C. C., Borys, C., Halpern, M., Morris, S. L., Adelberger, K. L., Dickinson, M., Giavalisco, M., & Pettini, M. 2000, MNRAS, 319, 318

Charlot, S. & Fall, S. M. 1993, ApJ, 415, 580

Chen, W. L. & Neufeld, D. A. 1994, ApJ, 432, 567

Cole, S., Norberg, P., Baugh, C. M., Frenk, C. S., Bland-Hawthorn, J., Bridges, T., Cannon, R., Colless, M., Collins, C., Couch, W., Cross, N., Dalton, G., De Propris, R., Driver, S. P., Efstathiou, G., Ellis, R. S., Glazebrook, K., Jackson, C., Lahav, O., Lewis, I., Lumsden, S., Maddox, S., Madgwick, D., Peacock, J. A., Peterson, B. A., Sutherland, W., & Taylor, K. 2001, MNRAS, 326, 255

Conti, P. S., Leitherer, C., & Vacca, W. D. 1996, ApJ, 461, L87

Cowie, L. L. & Hu, E. M. 1998, AJ, 115, 1319

Davies, J. I., Alton, P., Bianchi, S., & Trewhella, M. 1998, MNRAS, 300, 1006

de Mello, D. F., Leitherer, C., & Heckman, T. M. 2000, ApJ, 530, 251

Dickinson, M. 2000, Philosophical Transactions of the Royal Society of London, Series A, Vol. 358, no. 1772, p.2001, 358, 2001

Dickinson, M. & Giavalisco, M. 2002, astro-ph/0204213

Ferland, G. J., Korista, K. T., Verner, D. A., Ferguson, J. W., Kingdon, J. B., & Verner, E. M. 1998, PASP, 110, 761

Ferland, G. J. & Osterbrock, D. E. 1986, ApJ, 300, 658

Folkes, S., Ronen, S., Price, I., Lahav, O., Colless, M., Maddox, S., Deeley, K., Glazebrook, K., Bland-Hawthorn, J., Cannon, R., Cole, S., Collins, C., Couch, W., Driver, S. P., Dalton, G., Efstathiou, G., Ellis, R. S., Frenk, C. S., Kaiser, N., Lewis, I., Lumsden, S., Peacock, J., Peterson, B. A., Sutherland, W., & Taylor, K. 1999, MNRAS, 308, 459

Franx, M., Illingworth, G. D., Kelson, D. D., van Dokkum, P. G., & Tran, K. 1997, ApJ, 486, L75

Fukugita, M., Hogan, C. J., & Peebles, P. J. E. 1998, ApJ, 503, 518

Garnett, D. R., Shields, G. A., Peimbert, M., Torres-Peimbert, S., Skillman, E. D., Dufour, R. J., Terlevich, E., & Terlevich, R. J. 1999, ApJ, 513, 168

Garnett, D. R., Skillman, E. D., Dufour, R. J., Peimbert, M., Torres-Peimbert, S., Terlevich, R., Terlevich, E., & Shields, G. A. 1995, ApJ, 443, 64

Garnett, D. R., Skillman, E. D., Dufour, R. J., & Shields, G. A. 1997, ApJ, 481, 174

Giallongo, E., Cristiani, S., D'Odorico, S., & Fontana, A. 2002, ApJ, 568, L9

Giavalisco, M. & Dickinson, M. 2001, ApJ, 550, 177

Giavalisco, M., Koratkar, A., & Calzetti, D. 1996a, ApJ, 466, 831

Giavalisco, M., Steidel, C. C., Adelberger, K. L., Dickinson, M. E., Pettini, M., & Kellogg, M. 1998, ApJ, 503, 543

Giavalisco, M., Steidel, C. C., & Macchetto, F. D. 1996b, ApJ, 470, 189

Gonzalez Delgado, R. M., Leitherer, C., Heckman, T., Lowenthal, J. D., Ferguson, H. C., & Robert, C. 1998, ApJ, 495, 698

Gray, D. F. 1976, The Observation and Analysis of Stellar Photospheres (New York : Wiley)

Groenewegen, M. A. T., Lamers, H. J. G. L. M., & Pauldrach, A. W. A. 1989, A&A, 221, 78

Hartmann, L. W., Huchra, J. P., & Geller, M. J. 1984, ApJ, 287, 487

Hartmann, L. W., Huchra, J. P., Geller, M. J., O'Brien, P., & Wilson, R. 1988, ApJ, 326, 101

Heckman, T. M. 2002, in ASP Conf. Ser. 254: Extragalactic Gas at Low Redshift, 292

Heckman, T. M., Armus, L., & Miley, G. K. 1990, ApJS, 74, 833

Heckman, T. M., Lehnert, M. D., Strickland, D. K., & Armus, L. 2000, ApJS, 129, 493

Heckman, T. M. & Leitherer, C. 1997, AJ, 114, 69

Heckman, T. M., Robert, C., Leitherer, C., Garnett, D. R., & van der Rydt, F. 1998, ApJ, 503, 646

Heckman, T. M., Sembach, K. R., Meurer, G. R., Leitherer, C., Calzetti, D., & Martin, C. L. 2001a, ApJ, 558, 56

Heckman, T. M., Sembach, K. R., Meurer, G. R., Strickland, D. K., Martin, C. L., Calzetti, D., & Leitherer, C. 2001b, ApJ, 554, 1021

Holweger, H. 2001, in AIP Conf. Proc. 598: Joint SOHO/ACE workshop "Solar and Galactic Composition", 23

Hu, E. M., Cowie, L. L., & McMahon, R. G. 1998, ApJ, 502, L99

Keenan, F. P., Cook, J. W., Dufton, P. L., & Kingston, A. E. 1992, ApJ, 387, 726

Kinney, A. L., Bohlin, R. C., Calzetti, D., Panagia, N., & Wyse, R. F. G. 1993, ApJS, 86, 5

Kobulnicky, H. A. & Skillman, E. D. 1998, ApJ, 497, 601

Kunth, D., Lequeux, J., Sargent, W. L. W., & Viallefond, F. 1994, A&A, 282, 709

Kunth, D., Mas-Hesse, J. M., Terlevich, E., Terlevich, R., Lequeux, J., & Fall, S. M. 1998, A&A, 334, 11

Leitherer, C., Leão, J. R. S., Heckman, T. M., Lennon, D. J., Pettini, M., & Robert, C. 2001, ApJ, 550, 724

Leitherer, C., Robert, C., & Heckman, T. M. 1995, ApJS, 99, 173

Leitherer, C., Schaerer, D., Goldader, J. D., Delgado, R. M. G., Robert, C., Kune, D. F., de Mello, D. F., Devost, D., & Heckman, T. M. 1999, ApJS, 123, 3

Leitherer, C., Vacca, W. D., Conti, P. S., Filippenko, A. V., Robert, C., & Sargent, W. L. W. 1996, ApJ, 465, 717

Lejeune, T. & Cuisinier, F. 1996, GISSEL96 CD-ROM.

Lejeune, T., Cuisinier, F., & Buser, R. 1997, A&AS, 125, 229

Lequeux, J., Kunth, D., Mas-Hesse, J. M., & Sargent, W. L. W. 1995, A&A, 301, 18

Lin, H., Kirshner, R. P., Shectman, S. A., Landy, S. D., Oemler, A., Tucker, D. L., & Schechter, P. L. 1996, ApJ, 464, 60

Liu, M. C., Charlot, S., & Graham, J. R. 2000, ApJ, 543, 644

Lowenthal, J. D., Koo, D. C., Guzman, R., Gallego, J., Phillips, A. C., Faber, S. M., Vogt, N. P., Illingworth, G. D., & Gronwall, C. 1997, ApJ, 481, 673

Madau, P. 1995, ApJ, 441, 18

Madau, P., Ferguson, H. C., Dickinson, M. E., Giavalisco, M., Steidel, C. C., & Fruchter, A. 1996, MNRAS, 283, 1388

Maeder, A. 1991, A&A, 242, 93

—. 1992, A&A, 264, 105

Martin, C. L. 1999, ApJ, 513, 156

Matthews, K. & Soifer, B. T. 1994, in ASSL Vol. 190: Astronomy with Arrays, The Next Generation, 239

Meier, D. L. & Terlevich, R. 1981, ApJ, 246, L109

Meurer, G. R., Heckman, T. M., & Calzetti, D. 1999, ApJ, 521, 64

Meurer, G. R. & Seibert, M. 2001, in Starburst Galaxies: Near and Far, 272

Meynet, G. 1995, A&A, 298, 767

Mihos, J. C. & Hernquist, L. 1996, ApJ, 464, 641

Mo, H. J., Mao, S., & White, S. D. M. 1999, MNRAS, 304, 175

Nandra, K., Mushotzky, R. F., Arnaud, K., Steidel, C. C., Adelberger, K. L., Gardner, J. P., Teplitz, H. I., & Windhorst, R. A. 2002, ApJ, 576, 625

Neufeld, D. A. 1990, ApJ, 350, 216

Oke, J. B., Cohen, J. G., Carr, M., Cromer, J., Dingizian, A., Harris, F. H., Labrecque, S., Lucinio, R., Schaal, W., Epps, H., & Miller, J. 1995, PASP, 107, 375

Papovich, C., Dickinson, M., & Ferguson, H. C. 2001, ApJ, 559, 620

Persson, S. E., Murphy, D. C., Krzeminski, W., Roth, M., & Rieke, M. J. 1998, AJ, 116, 2475

Pettini, M. 2002, in "Cosmochemistry: The Melting Pot of Elements", 23

Pettini, M., Kellogg, M., Steidel, C. C., Dickinson, M., Adelberger, K. L., & Giavalisco, M. 1998, ApJ, 508, 539

Pettini, M., Rix, S. A., Steidel, C. C., Adelberger, K. L., Hunt, M. P., & Shapley, A. E. 2002, ApJ, 569, 742

Pettini, M., Shapley, A. E., Steidel, C. C., Cuby, J., Dickinson, M., Moorwood, A. F. M., Adelberger, K. L., & Giavalisco, M. 2001, ApJ, 554, 981

Pettini, M., Steidel, C. C., Adelberger, K. L., Dickinson, M., & Giavalisco, M. 2000, ApJ, 528, 96

Rhoads, J. E., Malhotra, S., Dey, A., Stern, D., Spinrad, H., & Jannuzi, B. T. 2000, ApJ, 545, L85

Sawicki, M. & Yee, H. K. C. 1998, AJ, 115, 1329

Schaerer, D. & Vacca, W. D. 1998, ApJ, 497, 618

Seibert, M., Heckman, T. M., & Meurer, G. R. 2002, AJ, 124, 46

Shapley, A. E., Steidel, C. C., Adelberger, K. L., Dickinson, M., Giavalisco, M., & Pettini, M. 2001, ApJ, 562, 95

Shapley, A. E., Steidel, C. C., Pettini, M., & Adelberger, K. L. 2003, ApJ, in press.

Shull, J. M. & van Steenberg, M. 1982, ApJS, 48, 95

Somerville, R. S., Primack, J. R., & Faber, S. M. 2001, MNRAS, 320, 504

Steidel, C. C., Adelberger, K. L., Dickinson, M., Giavalisco, M., Pettini, M., & Kellogg, M. 1998, ApJ, 492, 428

Steidel, C. C., Adelberger, K. L., Giavalisco, M., Dickinson, M., & Pettini, M. 1999, ApJ, 519, 1

Steidel, C. C., Adelberger, K. L., Shapley, A. E., Pettini, M., Dickinson, M., & Giavalisco, M. 2000, ApJ, 532, 170

—. 2003, ApJ, in press.

Steidel, C. C., Giavalisco, M., Dickinson, M., & Adelberger, K. L. 1996a, AJ, 112, 352

Steidel, C. C., Giavalisco, M., Pettini, M., Dickinson, M., & Adelberger, K. L. 1996b, ApJ, 462, L17

Steidel, C. C. & Hamilton, D. 1993, AJ, 105, 2017

Steidel, C. C., Hunt, M. P., Shapley, A. E., Adelberger, K. L., Pettini, M., Dickinson, M., & Giavalisco, M. 2002, ApJ, 576, 653

Steidel, C. C., Pettini, M., & Adelberger, K. L. 2001, ApJ, 546, 665

Steidel, C. C., Pettini, M., & Hamilton, D. 1995, AJ, 110, 2519

Strickland, D. K. & Stevens, I. R. 2000, MNRAS, 314, 511

Tenorio-Tagle, G., Silich, S. A., Kunth, D., Terlevich, E., & Terlevich, R. 1999, MNRAS, 309, 332

Trentham, N., Kormendy, J., & Sanders, D. B. 1999, AJ, 117, 2152

Walborn, N. R. & Panek, R. J. 1984, ApJ, 280, L27

Williams, R. E., Blacker, B., Dickinson, M., Dixon, W. V. D., Ferguson, H. C., Fruchter, A. S., Giavalisco, M., Gilliland, R. L., Heyer, I., Katsanis, R., Levay, Z., Lucas, R. A., McElroy, D. B., Petro, L., Postman, M., Adorf, H., & Hook, R. 1996, AJ, 112, 1335

Wolfe, A. M. & Prochaska, J. X. 2000, ApJ, 545, 591

Yee, H. K. C., Ellingson, E., Bechtold, J., Carlberg, R. G., & Cuillandre, J.-C. 1996, AJ, 111, 1783